

# C

---

## CALIBRATION AND VALIDATION

---

Andreas Colliander  
Jet Propulsion Laboratory, California Institute of  
Technology, Pasadena, CA, USA

### Definition

*Calibration.* The process of quantitatively defining the system responses, under specified conditions, to known, controlled signal inputs. The result of a calibration permits either the assignment of values of measurands to the system output or the determination of corrections with respect to the system output (Joint Committee for Guides in Metrology JCGM (includes ISO) 2008; Randa et al., 2008; CEOS Working Group on Calibration and Validation, 2012).

*Validation.* The process of assessing, by independent means, the quality of the data products derived from the system outputs. The quality is determined with respect to the specified requirements (Joint Committee for Guides in Metrology JCGM (includes ISO) 2008; Randa et al., 2008; CEOS Working Group on Calibration and Validation, 2012).

### Introduction

The value of remotely sensed data products, in the scientific sense in particular, is determined by how well the characteristics of a product are known (e.g., Platt and Sathyendranath, 1988; Wentz and Schabel, 2000; Atlas and Hoffman, 2000; Jung et al., 2010). These characteristics generally include long- and short-term deviation of the product value from the true value corresponding to the measurement, which is estimated through independent means (e.g., Wehr and Attema, 2001), and accuracy of the geographic location assigned to the product

(e.g., Wolfe et al., 2002; Small et al., 2004). The process of determining these characteristics for a particular remote sensing product is referred to as validation. However, before a data product is validated, it needs to be calibrated. Therefore, the calibration and validation processes are very closely linked together although they are distinctively two separate processes (see the Definition). This entry discusses calibration and validation in terms of characterization against the true value; geolocation aspect of the validation is a separate topic with specific challenges and solutions.

Remote sensing missions have requirements for the data products they are tasked to produce (e.g., Barre et al., 2008). The aim of the calibration and validation process of a particular mission is then to show that it meets its stated requirements (e.g., Delwart et al., 2008). Since the requirements are typically assigned based on expected scientific utilization of the data, the calibration and validation processes are generally regarded as a scientific function. Furthermore, the science community commonly contributes to calibration and validation efforts of data products independently from the missions in their research, due to the importance of knowing the characteristics and quality of the data (e.g., Donlon et al., 2002; Wang and Key, 2003; Mears and Wentz, 2005; Flanner et al., 2010).

The challenges of calibration and validation are specific to the mission and the data product. However, there are some general challenges concerning most of the remote sensing products. The most common and general issues causing concern are (1) establishment of accurate reference sites where the true value corresponding to the measurement can be estimated independently and accurately (e.g., Cosh et al., 2004) and (2) representing the entire measurement domain, which is often global, with a finite number of these sites (e.g., Morisette et al., 2002). It is typical the calibration and validation effort of a given mission

continues during the entire lifetime of a mission and even beyond (e.g., Xu and Ignatov, 2010).

Remote sensing data products can be divided into sensor products and geophysical products. Sensor product refers to output of an instrument after translating the instrument counts to a desired quantity, such as normalized radar cross section (e.g., Srivastava et al., 1999) or radiance (e.g., Abrams, 2000). Geophysical products refer to data products which contain geophysical parameters, such as wind speed (e.g., Liu et al., 1998) or leaf area index (e.g., Yang et al., 2006), retrieved based on the sensor products (and usually with some additional ancillary data). The calibration and validation of the sensor and geophysical products differ in some aspects and are discussed separately in the subsequent text.

International cooperation is in a key role to satisfy the requirements of calibration and validation of typical remote sensing products with very large domains. Committee on Earth Observation Satellites (CEOS) (CEOS Working Group on Calibration and Validation, 2012) is one international organization which has been active in promoting calibration and validation efforts. The Working Group on Calibration and Validation of CEOS has formulated a general approach for calibration and validation of remote sensing products and has established a validation hierarchy based on different stages of extent of validation efforts (see the end of this text).

### Historical perspective

At the beginning of the satellite remote sensing era (e.g., Nimbus-1 in 1964 and Landsat-1 in 1972), the calibration and validation activities were mostly limited to activities carried out directly by the space agencies. The current form of utilization of remote sensing data products started roughly with the launch of NASA's Nimbus-7 satellite in 1978. The new data policy of this mission enabled engagement of wider science community in more rapid manner after the launch of the satellite (Goddard Space Flight Center, National Aeronautics and Space Administration 2004). This also contributed to the start of the community-wide pre-and postlaunch calibration and validation efforts of remote sensing data products (e.g., Austin, 1980; Hovis, 1982; Stowe, 1982; Bernstein and Chelton, 1985; Stowe et al., 1988). After this, most NASA Earth observation satellites have followed the similar data policy. However, other space agencies have highly varying policies regarding data dissemination, which directly affects the extent of the calibration and validation activity.

Currently, it is common that a launch of each new remote sensing instrument initiates the science community to seek opportunities to participate in the calibration and validation activities. Naturally, the increased number of instruments and accumulated experience on the calibration and validation of satellite data products is another main reason for the increasing activity in the calibration and validation front. However, the calibration and validation efforts of remote sensing products have maintained

very similar features from the earlier days of remote sensing (e.g., compare (Hilland et al., 1985) with (O'Carroll et al., 2008)). At the same time, new instruments and new applications do require new methods for successful calibration and validation of remote sensing products.

### Sensor products

Calibration and validation of the sensor products of a mission is the critical part in ensuring the usefulness of the mission data. The quality of the sensor products typically dominates the quality of the geophysical products. Each remote sensing instrument has an algorithm which is used to translate the raw instrument counts to the desired quantity. The complexity of the algorithm depends on the instrument implementation and the properties of the desired quantity. For example, retrieval of normalized radar cross section requires measurement geometry in addition to instrument parameters (Ulaby et al., 1982), whereas antenna temperature of radiometer is independent of the measurement geometry (Ulaby et al., 1981). In principle, the features of the algorithm dictate the requirements for the calibration effort (i.e., parameters to be adjusted), and the quantity itself determines the requirements for the validation effort (i.e., proper target representing the quantity).

Instrument calibration usually includes some sort of internal calibration sources (e.g., Xiong and Barnes, 2006; Brown et al., 2007). While these sources can be used to remove the effects of some instrument non-idealities, they do not provide reference for the full instrument measurement chain (e.g., Butler and Barnes, 1998). There are different approaches for external calibration: use of an onboard reference target (e.g., Yamaguchi et al., 1998; Twarog et al., 2006); measurement of celestial targets, such as moon or cosmic microwave background radiation (e.g., Sun et al., 2003; Jones et al., 2006); or establishment of a reference target on the ground. Dedicated efforts to improve the stability of the observations (e.g., Gopalan et al., 2009; Eymard et al., 2005) and studies to correct errors caused by the antenna of an instrument (e.g., Njoku, 1980; McKague et al., 2011) are also typical for calibration of remote sensing instrument. Intercalibration between the remote sensing instruments is an important aspect for extending a data record either in time, to lengthen the time series and/or increase the fidelity of the time series, or in space to increase coverage (e.g., Cavalieri et al., 2012; Xiong et al., 2008).

There are areas on the surface of the Earth which provide well-defined response for some types of remote sensing measurements. Therefore, the target on the ground may be a natural scene suitable for calibration purposes (e.g., rain forests for microwave scatterometers (Long and Skouson, 1996)) or it can also be a target built for this specific reason (e.g., corner reflector for synthetic aperture radar (Shimada et al., 2009)). Some of the natural targets can provide relative well-defined absolute reference

value; others are more suitable for just tracking stability of the instrument. Examples of Earth scenes used as vicarious references for spaceborne remote sensing instrument calibration are Antarctica ice sheets (e.g., Macelloni et al., 2007, 2011), Amazon rain forests (e.g., Shimada, 2005), oceans (Ruf et al., 2006), deserts (e.g., Slater et al., 1987), and dry lake beds (e.g., Helder et al., 2010). Utility of man-made structures has also been demonstrated, such as a large asphalt field in Biggar et al., (2003).

Validation of sensor data products is usually done by using on-ground reference targets discussed above, since this represents the relevant measurement plane for the scientific utilization of the measurements. After the sensor product has been calibrated, it is compared against selected targets to establish the uncertainty of the product. This process may lead to further calibration too in which case the residual deviation from the targets becomes the result of the validation. Ideally, of course, the targets used for calibration and validation should be different. However, the use of the same targets is the reason why sometimes the nomenclature of sensor cal/val process refers only to calibration and does not include references to validation, even though it is clearly part of the process.

### Geophysical products

The retrieval algorithms of geophysical parameters are highly varying in their approach to determine the value of the desired parameter. Regardless of the approach, however, each algorithm requires calibration in order to optimize the correctness of its output. In order for the calibration process to be successful, the structure and error contributions of the algorithm need to be known (e.g., Pulliainen et al., 1993; Keihm et al., 1995; Wentz, 1997; Njoku et al., 2003; Brando and Dekker, 2003). Several algorithms include forward models that require detailed calibration before application to the inverse processing (e.g., Wigneron et al., 2007). In order to accomplish the calibration of an algorithm field, measurements and additional remote sensing measurements are typically exploited to determine the parameter values of the algorithm (e.g., Kelly et al., 2003; Njoku et al., 2003).

The validation process of geophysical products requires knowledge of the true value of the geophysical parameter within the effective measurement area with uncertainty less than the required uncertainty of the product. The following subsection discusses the issues related to scaling the in situ truth measurement to the footprint scale in spatial domain. Even in the absence of the spatial scaling issues, the uncertainty of the actual in situ measurement must be less than the uncertainty requirement of the product (e.g., Emery et al., 2001; Bailey and Werdell, 2006; Henocq et al., 2010). The establishment of these validation sites depends naturally a great deal on the geophysical parameter: The general approach and requirements for wind speed (e.g., Dobson et al., 1987) or chlorophyll a (e.g., Ruiz-Verdu et al., 2008) measurement are completely different from snow water equivalent

(e.g., Tedesco and Narvekar, 2010) or leaf area index (e.g., Garrigues et al., 2008) measurements, let alone atmospheric water vapor (e.g., Divakarla et al., 2006), or ozone (e.g., Froidevaux et al., 2008) measurements. The objective in each case is nevertheless the same, to find a representative measurement of the parameter so that it can be compared against the remotely sensed value. After appropriately matching up the remotely sensed product and the in situ measurement, the validation results are typically presented as, for example, root mean square error, correlation, and histograms (e.g., Hooker and McClain, 2000; Bourassa et al., 2003; Hilland et al., 1985).

### Spatial scaling

Remote sensing measurements are based on the instrument recordings of interaction of electromagnetic waves with the target. The instruments have a defined sensing area or volume (i.e., footprint) depending on the antenna beam shape and interaction of the measurement signal with the sensed medium. When it comes to calibrating and validating the measurements, the independent reference measurements, in situ measurements in particular, typically do not have the same features as the remotely sensed signal and do not measure the exactly same domain as the footprint represents. The translation of the reference measurements to the remote sensing footprint is often referred to as spatial scaling, and it is a crucial part of the calibration and validation of remote sensing products. Sensor product calibration and validation efforts usually try to utilize homogeneous regions where scaling is not an issue in the same way as with calibration and validation of typical geophysical products.

The challenge of the spatial scaling depends typically on the relationship between the heterogeneity of the measured parameter and the size of the footprint. Scaling of even relative high-resolution (small size) footprint may be challenging for highly heterogeneous parameters (e.g., Liang et al., 2002). Some remote sensing instruments have very low resolution, but if the measured parameter changes slowly over large distances, scaling can be accomplished with relative few resources within the footprint (e.g., Le Vine et al., 2007). The most challenging cases include of course remote sensing measurements of highly heterogeneous parameters with large footprints (e.g., Jackson et al., 2010).

There are several techniques developed for scaling the value of geophysical parameters up to the footprints of remote sensing measurements. As an example, these techniques include aggregation of in situ measurements (e.g., Jackson et al., 2010), model-based techniques (e.g., Chen et al., 1999), timing of the acquisition so that the heterogeneity effect is minimized (e.g., Wang et al., 2008), and temporal stability approach which assumes that single point of the area represents the footprint average (e.g., the challenge then is to find the representative point (Vachaud et al., 1985; Grayson and

Western, 1998)). An important aspect of the upscaling of the in situ measurements is estimation of the error associated with the upscaled value. Several techniques have been proposed and used for accomplishing this, for example: investigating the variance of the subscale measurements (e.g., Tian et al., 2002) and combination of several observation sources (e.g., Hilland et al., 1985; O'Carroll et al., 2008; Caires and Sterl, 2003; Miralles et al., 2010).

### Coverage

Although it is generally accepted that the validation of the geophysical products should be done against in situ measurements, other references are being applied too. The reason for this is that in general, in situ measurements have limited coverage in space and in time, i.e., they do not cover the entire domain, which is often global (the main reason why remote sensing is applied in the first place), and it may not always be possible to make in situ measurements for long periods or with high frequency for a certain location (e.g., consider limitations of radiosondes, dropsondes, and buoys).

Depending on the size of the covered domain, the challenge for the calibration and validation effort is to find a strategy with which it can be claimed that the product is calibrated and validated over the entire domain. Therefore, other remote sensing sources (e.g., Corlett et al., 2006) and models (e.g., Caires and Sterl, 2003) have been used to complement the in situ measurements. It is also typical to divide the entire domain in sub-domains and then find validation sites which represent each sub-domain (e.g., Hilland et al., 1985) or to cover a diversity of conditions with set of sites which can be claimed to represent the conditions over the entire domain (e.g., Ceccato et al., 2002). But only rarely a validation is accepted without some strategy to reference the measurements back to verifiable in situ acquisitions.

### Temporal context

Remote sensing products can be calibrated and validated over a short time period (a few years at most) or a long time period (at least a decade). Calibration and validation of individual missions is usually a short-term effort because the mission requirements are typically set without long-term requirement and, furthermore, the duration of a single mission is seldom long enough to qualify as a long term anyway. Therefore, long-term calibration and validation imply inter-mission effort to extend the calibrated and validated data record to over decade long time frame (e.g., Gallo et al., 2005). Typically high quality long-term data records are required for climate applications (e.g., Flanner et al., 2011; Behrenfield et al., 2006), but also other monitoring and tracking applications require long-term remote sensing observations (e.g., Lepers et al., 2005). The type, quality, and length of remote sensing data records have limited the use of remote sensing data for long-term applications until more recently.

The requirements of calibration and validation process are affected significantly by the climatic temporal context of multiple decades combined with usually very high requirements on the stability. Therefore, a combination of both retrieval intercomparisons and in situ measurements is often necessary to validate the long-term record (e.g., Takala et al., 2009). For example, the importance of [sea surface temperature \(SST\)](#) record for climate studies was understood long time ago (e.g., Harries et al., 1983) and ever since significant effort has been made to establish a well-calibrated long-term SST record (e.g., Stuart-Menteth et al., 2003).

### Prelaunch calibration and validation

It is common that remote sensing missions include calibration and validation activities for both sensor and geophysical retrieval algorithms in the prelaunch phase. Essentially, the objective of these activities is to increase the expectation of the mission success to the level that launching a satellite seems worthwhile. Missions set requirements for the instrument performance based on the intended use of the measurements. In the prelaunch phase, this performance is verified through measurements, analysis, and simulations. The calibration strategy of an instrument may require measurement of certain calibration parameters on the ground, and sometimes, when possible, the instrument is entirely calibrated on the ground already. These activities are often referred to as prelaunch calibration activities. However, it should be emphasized that the eventually applicable calibration is almost always conducted on the orbit.

The development of geophysical retrieval algorithms starts before mission definition in research activities which try to identify potential remote sensing measurements concepts. The prelaunch calibration and validation activities include similar components as retrieval algorithm research such as field campaigns and simulations. However, these activities are driven by particular mission characteristics such as exact observation configuration including measurement frequency, footprint, coverage, and instrument performance figures. The prelaunch efforts can only approximate the actual measurements of the mission, and the actual calibration and validation of the retrieval algorithms and products takes place only after the launch of the mission.

### Validation stages

CEOS (CEOS Working Group on Calibration and Validation, 2012) has put forward a four-stage validation hierarchy which has been adopted by many data providers. The validation stage increases with increasing product maturity and extensiveness of the validation effort.

- Stage 1 validation: Product accuracy is assessed from a small (typically <30) set of locations and time periods by comparison with in situ or other suitable reference data.

- Stage 2 validation: Product accuracy is estimated over a significant set of locations and time periods by comparison with reference in situ or other suitable reference data. Spatial and temporal consistency of the product and with similar products has been evaluated over globally representative locations and time periods. Results are published in the peer-reviewed literature.
- Stage 3 validation: Uncertainties in the product and its associated structure are well quantified from comparison with reference in situ or other suitable reference data. Uncertainties are characterized in a statistically robust way over multiple locations and time periods representing global conditions. Spatial and temporal consistency of the product and with similar products has been evaluated over globally representative locations and periods. Results are published in the peer-reviewed literature.
- Stage 4 validation: Validation results for stage 3 are systematically updated when new product versions are released and as the time series expands.

## Summary

All remote sensing products require calibration and validation, and it is an essential part of the process of making remote sensing products to meet the requirements of scientific utilization. The main challenges in the calibration and validation of almost any data product are how to make corresponding and representative reference measurements and how to extend the validation over the entire measurement domain. These challenges are overcome by careful design of the reference sites and their in situ measurements, which vary greatly depending on the geophysical parameter and on the footprint of the remote sensing product, and strategizing the utilization of diversity of validation sites with augmentation by other remote sensing products and models. Intersensor and inter-product calibration and validation are conducted to increase the length and fidelity of the time series or the coverage of the measurement. This is essential for utilization of remote sensing data for climate change studies.

## Acknowledgments

This research was carried out at the Jet Propulsion Laboratory, California Institute of Technology, under a contract with the NASA.

## Bibliography

- Abrams, M., 2000. The advanced spaceborne thermal emission reflection radiometer (ASTER): data products for the high spatial resolution imager on NASA's terra platform. *International Journal of Remote Sensing*, **21**(5), 847–859.
- Atlas, R., and Hoffman, R. N., 2000. The use of satellite surface wind data to improve weather analysis and forecasting at the NASA data assimilation office. *Elsevier Oceanography Series*, **63**, 57–78.
- Austin, R. W., 1980. Gulf of Mexico, ocean-color surface-truth measurements. *Boundary-Layer Meteorology*, **18**(3), 269–285.

- Bailey, S. W., and Werdell, J. P., 2006. A multi-sensor approach for the on-orbit validation of ocean color satellite data products. *Remote Sensing of Environment*, **102**(1–2), 12–23.
- Barre, H. M. J. P., Duesmann, B., and Kerr, Y. H., 2008. SMOS: the mission and the system. *IEEE Transactions on Geoscience and Remote Sensing*, **46**(3), 587–593.
- Behrenfield, M. J., O'Malley, R. T., Siegel, D. A., McClain, C. R., Sarmiento, J. L., Feldman, G. C., Miligan, A. J., Falkowski, P. G., Letelier, R. M., and Boss, E. S., 2006. Climate-driven trends in contemporary ocean productivity. *Nature*, **444**, 752–755.
- Bernstein, R. L., and Chelton, D. B., 1985. Large-scale sea surface temperature variability from satellite and shipboard measurements. *Journal of Geophysical Research*, **90**(C6), 11619–11630.
- Biggar, S. F., Thome, K. J., and Wisniewski, W., 2003. Vicarious radiometric calibration of eo-1 sensors by reference to high-reflectance ground targets. *IEEE Transactions on Geoscience and Remote Sensing*, **41**(6), 1174–1179.
- Bourassa, M. A., Legler, D. M., O'Brien, J. J., and Smith, S. R., 2003. Seawinds validation with research vessels. *Journal of Geophysical Research*, **108**, C2.
- Brando, V. E., and Dekker, A. G., 2003. Satellite hyperspectral remote sensing for estimating estuarine and coastal water quality. *IEEE Transactions on Geoscience and Remote Sensing*, **41**(6), 1378–1387.
- Brown, S. T., Desai, S., Lu, W., and Tanner, A. B., 2007. On the long-term stability of microwave radiometers using noise diodes for calibration. *IEEE Transactions on Geoscience and Remote Sensing*, **45**(7), 1908–1920.
- Butler, J. J., and Barnes, R. A., 1998. Calibration strategy for the earth observing system (EOS) – AM1 platform. *IEEE Transactions on Geoscience and Remote Sensing*, **36**(4), 1056–1061.
- Caires, S., and Sterl, A., 2003. Validation of ocean wind and wave data using triple collocation. *Journal of Geophysical Research*, **108**, C3.
- Cavalieri, D. J., Parkinson, C. L., DiGirolamo, N., and Ivanoff, A., 2012. Intersensor calibration between F13 SSMI and F17 SSMIS for global sea ice data records. *IEEE Geoscience and Remote Sensing Letters*, **9**(2), 233–236.
- Ceccato, P., Flasse, S., and Gregoire, J.-M., 2002. Designing a spectral index to estimate vegetation water content from remote sensing data: part 2. Validation and applications. *Remote Sensing of Environment*, **82**(2–3), 198–207.
- CEOS Working Group on Calibration and Validation, 2012. Committee on Earth Observation Satellites (Online). Available from <http://www.ceos.org>. Accessed 14 Feb 2012.
- Chen, J. M., Liu, J., Cihlar, J., and Goulden, M. L., 1999. Daily canopy photosynthesis model through temporal and spatial scaling for remote sensing applications. *Ecological Modeling*, **124**(2–3), 99–119.
- Corlett, G. K., et al., 2006. The accuracy of SST retrievals from AATSR: an initial assessment through geophysical validation against in situ radiometers, buoys and other SST data sets. *Advances in Space Research*, **37**(4), 764–769.
- Cosh, M. H., Jackson, T. J., Bindlish, R., and Prueger, J. H., 2004. Watershed scale temporal and spatial stability of soil moisture and its role in validating satellite estimates. *Remote Sensing of Environment*, **92**, 427–435.
- Delwart, S., Bouzinac, C., Wursteisen, P., Berger, M., Drinkwater, M., Martin-Neira, M., and Kerr, Y. H., 2008. SMOS validation and the COSMOS campaigns. *IEEE Transactions on Geoscience and Remote Sensing*, **46**(3), 695–704.
- Divakarla, M. G., Barnett, C. D., Goldberg, M. D., McMillin, L. M., Maddy, E., Wolf, W., Zhou, L., and Liu, X., 2006. Validation of atmospheric infrared sounder temperature and water vapour retrievals with matched radiosonde measurements and forecasts. *Journal of Geophysical Research*, **111**, D09S15.

- Dobson, E., Monaldo, F., Goldhirsh, J., and Wilkerson, J., 1987. Validation of geosat altimeter-derived wind speeds and significant wave heights using buoy data. *Journal of Geophysical Research*, **92**(C10), 10719–10731.
- Donlon, C. J., Minnett, P. J., Gentemann, C., Nightingale, T. J., Barton, I. J., Ward, B., and Murray, M. J., 2002. Toward improved validation of satellite sea surface skin temperature measurements for climate research. *Journal of Climate*, **15**(4), 353–369.
- Emery, W. J., Baldwin, D. J., Schlüssel, P., and Reynolds, R. W., 2001. Accuracy of in situ sea surface temperatures used to calibrate infrared satellite measurements. *Journal of Geophysical Research*, **106**(C2), 2387–2405.
- Eymard, L., Obligis, E., Tran, N., Karbou, F., and Dedieu, M., 2005. Long-term stability of ERS-2 and TOPEX microwave radiometer in-flight calibration. *IEEE Transactions on Geoscience and Remote Sensing*, **43**(5), 1144–1158.
- Flanner, M. G., Shell, K. M., Barlage, M., Perovich, D. K., and Tschudi, M. A., 2010. Radiative forcing and albedo feedback from the northern hemisphere cryosphere between 1979 to 2008. *Nature Geoscience*, **4**, 151–155.
- Flanner, M. G., Shell, K. M., Barlage, M., Perovich, D. K., and Tschudi, M. A., 2011. Radiative forcing and albedo feedback from the northern hemisphere cryosphere between 1979 and 2008. *Nature Geoscience*, **4**, 151–155.
- Froidevaux, L., et al., 2008. Validation of aura microwave limb sounder stratospheric ozone measurements. *Journal of Geophysical Research*, **113**, D15S20.
- Gallo, K., Ji, L., Reed, B., Eidenshink, J., and Dwyer, J., 2005. Multi-platform comparisons of MODIS and AVHRR normalized difference vegetation index data. *Remote Sensing of Environment*, **99**(3), 221–231.
- Garrigues, S., Lacaze, R., Baret, F., Morisette, J. S., Weiss, M., Nickeson, J. E., Fernandes, R., Plummer, S., Shabanov, N. V., Myneni, R. B., Knyazikhin, Y., and Yang, W., 2008. Validation and intercomparison of global leaf area index products derived from remote sensing data. *Journal of Geophysical Research*, **113**, G02028.
- Goddard Space Flight Center, National Aeronautics and Space Administration, 2004. *Nimbus Program History, National Aeronautics and Space Administration*, Greenbelt: MD.
- Gopalan, K., Jones, W. L., Biswas, S., Bilanow, S., Wilheit, T., and Kasparis, T., 2009. A time-varying radiometric bias correction for the TRMM microwave imager. *IEEE Transactions on Geoscience and Remote Sensing*, **47**(11), 3722–3730.
- Grayson, R. B., and Western, A. W., 1998. Towards areal estimation of soil water content from point measurements: time and space stability of mean response. *Journal of Hydrology*, **207**, 68–82.
- Harries, J. E., Llewellyn-Jones, D. T., Minnett, P. J., Saunders, R. W., and Zavody, A. M., 1983. Observations of sea-surface temperature for climate research. *Philosophical Transactions of the Royal Society of London A*, **309**, 381–395.
- Helder, D. L., Basnet, B., and Morstad, D. L., 2010. Optimized identification of worldwide radiometric pseudo-invariant calibration sites. *Canadian Journal of Remote Sensing*, **36**(5), 527–539.
- Henocq, C., Boutin, J., Petitcolin, F., Reverdin, G., Arnault, S., and Lattes, P., 2010. Vertical variability of near-surface salinity in the tropics: consequences for L-band radiometer calibration and validation. *Journal of Atmospheric and Oceanic Technology*, **27**, 192–209.
- Hilland, J. E., Chelton, D. B., and Njoku, E. G., 1985. Production of global sea surface temperature fields for the jet propulsion laboratory workshop comparisons. *Journal of Geophysical Research*, **90**(C6), 11642–11650.
- Hooker, S. B., and McClain, C. R., 2000. The calibration and validation of seaWiFS data. *Progress in Oceanography*, **45**, 427–465.
- Hovis, W., 1982. Results of the CZCS validation program. In *OCEANS 82*. Washington.
- Jackson, T. J., Cosh, M. H., Bindlish, R., Starks, P. J., Bosch, D. D., Seyfried, M., Goodrich, D. C., Moran, S., and Du, J., 2010. Validation of advanced microwave scanning radiometer soil moisture products. *IEEE Transactions on Geoscience and Remote Sensing*, **48**(12), 4256–4272.
- Joint Committee for Guides in Metrology JCGM (includes ISO, Geneva, Switzerland), 2008. *International Vocabulary of Metrology – Basic and General Concepts and Associated Terms (VIM)*.
- Jones, W. L., Park, J. D., Soisuvarn, S., Hong, L., Gaiser, P. W., and St. Germain, K. M., 2006. Deep-space calibration of the windsat radiometer. *IEEE Transactions on Geoscience and Remote Sensing*, **44**(3), 476–495.
- Jung, M., et al., 2010. Recent decline in the global land evapotranspiration trend due to limited moisture supply. *Nature*, **467**, 951–954.
- Keihm, S. J., Janssen, M. A., and Ruf, C. S., 1995. TOPEX/poseidon microwave radiometer (TMR): III. Wet troposphere range correction algorithm and pre-launch error budget. *IEEE Transactions on Geoscience and Remote Sensing*, **33**(1), 147–161.
- Kelly, R. E., Chang, A. T., Tsang, L., and Foster, J. L., 2003. A prototype AMSRE-E global snow area and snow depth algorithm. *IEEE Transactions on Geoscience and Remote Sensing*, **41**(2), 230–242.
- Le Vine, D. M., Lagerloef, G. S. E., Colomb, F. R., Yueh, S. H., and Pellerano, F. A., 2007. Aquarius: an instrument to monitor surface salinity from space. *IEEE Transactions on Geoscience and Remote Sensing*, **45**(7), 2040–2050.
- Lepers, E., Lambin, E. F., Janetos, A. C., DeFries, R., Achard, F., Ramankutty, N., and Scholes, R. J., 2005. A synthesis of information on rapid land-cover change for the period 1981–2000. *BioScience*, **55**(2), 115–124.
- Liang, S., Fang, H., Chen, M., Shuey, C. J., Walthall, C., Daughtry, C., Morisette, J., Schaaf, C., and Strahler, A., 2002. Validating MODIS land surface reflectance and albedo products: methods and preliminary results. *Remote Sensing of Environment*, **83** (1–2), 149–162.
- Liu, T. W., Tang, W., and Polito, P. S., 1998. NASA scatterometer provides global ocean-surface wind fields with more structures than numerical weather prediction. *Geophysical Research Letters*, **25**(6), 761–764.
- Long, D. G., and Skouson, G. B., 1996. Calibration of spaceborne scatterometers using tropical rain forests. *IEEE Transactions on Geoscience and Remote Sensing*, **34**(2), 413–424.
- Macelloni, G., Brogioni, M., Pampaloni, P., and Cagnati, A., 2007. Multifrequency microwave emission from the dome-C area on the east Antarctic plateau: temporal and spatial variability. *IEEE Transactions on Geoscience and Remote Sensing*, **45**(7), 2029–2039.
- Macelloni, G., Brogioni, M., Pettinato, S., Zasso, R., Crepaz, A., Zaccaria, J., Padovan, B., Drinkwater, M., 2011. Multifrequency microwave emission of the east Antarctic plateau. In *Proceedings of IEEE International Geoscience and Remote Sensing Symposium (IGARSS), 2011*, Vancouver: Canada.
- McKague, D. S., Ruf, C. S., and Puckett, J. J., 2011. Beam spilling correction for spaceborne microwave radiometers using the two-point vicarious calibration method. *IEEE Transactions on Geoscience and Remote Sensing*, **49**(1), 21–27.
- Mears, C. A., and Wentz, F. J., 2005. The effect of diurnal correction on satellite-derived lower tropospheric temperature. *Science*, **309**(5740), 1548–1551.
- Miralles, D. G., Crow, W. T., and Cosh, M. H., 2010. Estimating spatial sampling errors in coarse-scale soil moisture estimates derived from point-scale observations. *Journal of Hydrometeorology*, **11**, 1423–1429.

- Morisette, J. T., Privette, J. L., and Justice, C. O., 2002. A framework for the validation of MODIS land products. *Remote Sensing of Environment*, **83**(1–2), 77–96.
- Njoku, E. G., 1980. Antenna pattern correction procedures for the scanning multichannel microwave radiometer (SMMR). *Boundary-Layer Meteorology*, **18**, 79–98.
- Njoku, E. G., Jackson, T. J., Lakshmi, V., Chan, S. T. K., and Nghiem, S. V., 2003. Soil moisture retrieval from AMSR-E. *IEEE Transactions on Geoscience and Remote Sensing*, **41**(2), 215–229.
- O’Carroll, A. G., Eyre, J. R., and Saunders, R. W., 2008. Three-way error analysis between AATSR, AMSR-E, and in situ sea surface temperature observations. *Journal of Atmospheric and Oceanic Technology*, **25**, 1197–1207.
- Platt, T., and Sathyendranath, S., 1988. Oceanic primary production: estimation by remote sensing at local and regional scales. *Science*, **241**, 1613–1620.
- Pulliainen, J., Karna, J.-P., and Hallikainen, M., 1993. Development of geophysical retrieval algorithms for the MIMR. *IEEE Transactions on Geoscience and Remote Sensing*, **31**(1), 268–277.
- Randa, J., Lahtinen, J., Camps, A., Gasiewski, A. J., Hallikainen, M., Le Vine, D. M., Martin-Neira, M., Piepmeier, J., Rosenkranz, P. W., Ruf, C. S., Shiue, J., Skou, N., 2008. *Recommended Terminology for Microwave Radiometry*, National Institute of Standards and Technology. Technical Note 1551.
- Ruf, C. S., Hu, Y., and Brown, S. T., 2006. Calibration of windsat polarimetric channels with a vicarious cold reference. *IEEE Transactions on Geoscience and Remote Sensing*, **44**(3), 470–475.
- Ruiz-Verdu, A., Koponen, S., Heege, T., Doerffer, R., Brockmann, C., Kallio, K., Pyhalahti, T., Pena, R., Polvorinos, A., Heblinski, J., Ylostalo, P., Conde, L., Odermatt, D., Estelles, V., Pulliainen, J., 2008. Development of MERIS lake water algorithms: validation results from Europe. In *Proceedings of 2nd MERIS User Workshop*, Frascati: Italy.
- Shimada, M., 2005. Long-term stability of L-band normalized radar cross section of amazon rainforest using the JERS-1 SAR. *Canadian Journal of Remote Sensing*, **31**(1), 132–137.
- Shimada, M., Isoguchi, O., Tadono, T., and Isono, K., 2009. PALSAR radiometric and geometric calibration. *IEEE Transactions on Geoscience and Remote Sensing*, **47**(12), 3915–3932.
- Slater, P. N., Biggar, S. F., Holm, R. G., Jackson, R. D., Mao, Y., Moran, M. S., Palmer, J. M., and Yuan, B., 1987. Reflectance- and radiance-based methods for the in-flight absolute calibration of multispectral sensor. *Remote Sensing of Environment*, **22**(1), 11–37.
- Small, D., Rosich, B., Meier, E., Uesch, D., 2004. Geometric calibration and validation of ASAR imagery. In *Proceedings of CEOS SAR Workshop*, Ulm: Germany.
- Srivastava, S. K., Hawkins, R. K., Lukowski, T. I., Banik, B. T., Adamovic, M., and Jefferies, W. C., 1999. RADARSAT image quality and calibration – update. *Advances in Space Research*, **23**(8), 1487–1496.
- Stowe, L. L., 1982. Validation of nimbus-7 temperature-humidity infrared radiometer estimates of cloud type and amount. *Advances in Space Research*, **2**(6), 15–19.
- Stowe, L. L., Wellemeyer, C. G., Yeh, H. Y. M., Eck, T. F., The Nimbus-7 Cloud Data Processing Team, 1988. Nimbus-7 global cloud climatology. Part I: algorithms and validation. *Journal of Climate*, **1**(5), 445–470.
- Stuart-Menteth, A. C., Robinson, I. S., and Challenor, P. G., 2003. A global study of diurnal warming using satellite-derived sea surface temperature. *Journal of Geophysical Research*, **108**, C5.
- Sun, J., Xiong, X., Guenther, B., and Barnes, W., 2003. Radiometric stability monitoring of the MODIS reflective solar bands using the moon. *Metrologia*, **40**, S85–S88.
- Takala, M., Pulliainen, J., Metsamaki, S. J., and Koskinen, J. T., 2009. Detection of snowmelt using spaceborne microwave radiometer data in eurasia from 1979 to 2007. *IEEE Transactions on Geoscience and Remote Sensing*, **47**(9), 2996–3007.
- Tedesco, M., and Narvekar, P. S., 2010. Assessment of the NASA AMSR-E SWE product. *IEEE Transactions on Geoscience and Remote Sensing*, **3**(1), 141–159.
- Tian, Y., et al., 2002. Multiscale analysis and validation of the MODIS LAI product I. Uncertainty assessment. *Remote Sensing of Environment*, **83**, 414–430.
- Twarog, E. M., Purdy, W. E., Gaiser, P. W., Cheung, K. H., and Kelm, B. E., 2006. WindSat on-orbit warm load calibration. *IEEE Transactions on Geoscience and Remote Sensing*, **44**(3), 516–529.
- Ulaby, F. T., Moore, R. K., and Fung, A. K., 1981. *Microwave Remote Sensing: Active and Passive*. Norwood: Artech House. Microwave Remote Sensing Fundamentals and Radiometry, Vol. 1.
- Ulaby, F. T., Moore, R. K., and Fung, A. K., 1982. *Microwave Remote Sensing: Active and Passive*. Reading: Addison-Wesley Company. Radar Remote Sensing and Surface Scattering and Emission Theory, Vol. 2.
- Vachaud, G., Passerat de Silans, A., Balabanis, P., and Vauclin, M., 1985. Temporal stability of spatially measured soil water probability density function. *Journal of Soil Science Society of America*, **49**(4), 822–828.
- Wang, X., and Key, J. R., 2003. Recent trends in arctic surface, cloud, and radiation properties from space. *Science*, **299**(5613), 1725–1728.
- Wang, W., Liang, S., and Meyers, T., 2008. Validating MODIS land surface temperature products using long-term nighttime ground measurement. *Remote Sensing of Environment*, **112**(3), 623–635.
- Wehr, T., and Attema, E., 2001. Geophysical validation of envisat data products. *Advances in Space Research*, **28**(1), 83–91.
- Wentz, F. J., 1997. A well-calibrated ocean algorithm for special sensor microwave/imager. *Journal of Geophysical Research*, **102**(C4), 8703–8718.
- Wentz, F. J., and Schabel, M., 2000. Precise climate monitoring using complementary satellite data sets. *Nature*, **403**, 414–416.
- Wigneron, J.-P., Kerr, Y., Waldteufel, P., Saleh, K., Escorihuela, M.-J., Richaume, P., Ferrazzoli, P., de Rosnay, P., Gurney, R., Calvet, J.-C., Grant, J. P., Guglielmetti, M., Hornbuckle, B., Matzler, C., Pellarin, T., and Schwank, M., 2007. L-band microwave emission of the biosphere (L-MEB) model: description and calibration against experimental data sets over crop fields. *Remote Sensing of Environment*, **107**(4), 639–655.
- Wolfe, R. E., Nishihama, M., Fleig, A. J., Kuyper, J. A., Roy, D. P., Storey, J. C., and Patt, F. S., 2002. Achieving sub-pixel geolocation accuracy in support of MODIS land science. *Remote Sensing of Environment*, **83**(1–2), 31–49.
- Xiong, X., and Barnes, W., 2006. An overview of MODIS radiometric calibration and characterization. *Advances in Atmospheric Sciences*, **23**(1), 69–79.
- Xiong, X., Sun, J., and Barnes, W., 2008. Intercomparison of on-orbit calibration consistency between terra and aqua MODIS reflective solar bands using the moon. *IEEE Geoscience and Remote Sensing Letters*, **5**(4), 778–782.
- Xu, F., and Ignatov, A., 2010. Evaluation of in situ surface temperature for use in the calibration and validation of satellite retrievals. *Journal of Geophysical Research*, **115**, C09022.
- Yamaguchi, Y., Kahle, A. B., Tsu, H., Kawakami, T., and Pniel, M., 1998. Overview of advanced spaceborne thermal emission and reflection radiometer (ASTER). *IEEE Transactions on Geoscience and Remote Sensing*, **36**(4), 1062–1071.

Yang, W., Tan, B., Huang, D., Rautiainen, M., Shabanov, N. V., Wang, Y., Privette, J. L., Huemmrich, K. F., Fensholt, R., Sandholt, I., Weiss, M., Ahl, D. E., Gower, S. T., Nemani, R. R., Knyazikhin, Y., and Myneni, R. B., 2006. MODIS leaf area index products: from validation to algorithm improvement. *IEEE Transactions on Geoscience and Remote Sensing*, **44**(7), 1885–1898.

---

## CALIBRATION, MICROWAVE RADIOMETERS

---

Christopher Ruf  
 Department of Atmospheric, Oceanic and Space Sciences,  
 University of Michigan, Ann Arbor, MI, USA

### Definition

*Antenna temperature ( $T_a$ )*. A weighted average of the brightness temperature incident on a radiometer from all directions, where the weighting is the antenna radiation pattern.

*Receiver noise temperature ( $T_{rec}$ )*. The equivalent brightness temperature that would produce the same signal strength as the noise generated by a radiometer's electronics.

*System noise temperature ( $T_{sys}$ )*. The sum of the antenna temperature entering a radiometer plus its receiver noise temperature.

*Antenna radiation pattern*. The sensitivity of an antenna to incoming radiation, usually expressed as a function of angle of arrival in polar coordinates and normalized so that the integral over all angles is unity.

*Antenna mainbeam*. The portion of an antenna radiation pattern localized near the direction of maximum sensitivity.

*Antenna sidelobes*. The antenna radiation pattern away from its mainbeam.

### Overview

A microwave radiometer measures the power associated with a particular polarization component of a propagating electromagnetic wave over a specific portion of the electromagnetic spectrum (see entry *Radiation, Electromagnetic*). The brightness temperature ( $T_b$ ) in the direction from which the wave originated can be inferred from the power measurement. The  $T_b$  is specific to the polarization state and spectral range of the measurement. Raw radiometer power measurements generally contain contributions from other sources than the desired  $T_b$ , including incoming radiation from other directions and polarizations as well as radiation emitted by the radiometer receiver itself. Radiometer calibration consists of an accurate accounting for all significant contributions to the raw measurements and estimation of the desired  $T_b$ .

### Antenna effects

In general, electromagnetic radiation incident on an antenna arrives from all directions and with all possible polarization states. An ideal antenna would selectively receive radiation with only the desired polarization and that arrives only from the desired direction. In practice, an antenna will receive radiation incident from all directions weighted by its radiation pattern. The weighted average of the incident  $T_b$ , weighted by the radiation pattern, is referred to as the antenna temperature ( $T_a$ ). The mainbeam of the radiation pattern is the (typically narrow) range of directions over which the antenna is most sensitive. Calibrated  $T_b$  measurements by a radiometer are generally considered to originate from this range of directions. The sidelobes of the radiation pattern describe its sensitivity to radiation incident from all other directions outside the mainbeam. Typically 1–10% of the total power measured by a radiometer originates from sidelobe directions. Similarly, an antenna will receive radiation from all polarization states, weighted by its sensitivity to each component. An antenna's polarimetric gain matrix describes the sensitivity. Its main diagonal elements specify the sensitivity to the desired polarization, in a manner analogous to the mainbeam for directional sensitivity. The off-diagonal elements play a similar role as the antenna sidelobes, specifying the sensitivity to unwanted polarization states.

Calibration of a radiometer for antenna effects consists of correcting the  $T_a$  measurements for each of the unwanted contributors in order to estimate the  $T_b$  contribution with the desired polarization arriving from the mainbeam direction. Sidelobe corrections are generally made by (1) measuring or modeling the radiation pattern of the antenna; (2) estimating the mean  $T_b$  entering the antenna from its sidelobes; and then (3) subtracting the mean sidelobe  $T_b$ , weighted by the sidelobe sensitivity, from the raw measurements (Njoku et al., 1980). Similarly, polarimetric corrections first require that an antenna's gain matrix be known, usually by direct measurement in a specialized facility. If radiometric measurements are made of all polarization states of the incident radiation, then the gain matrix can be inverted mathematically to correct for the off-diagonal contamination (Gasiewski and Kunkee, 1993). If only some of the states are measured, then the others must be estimated prior to the matrix inversion.

### Receiver effects

A radiometer antenna collects incident radiation and converts it to a voltage on a transmission line. A radiometer receiver amplifies that voltage to a more measurable signal strength, typically with transistor amplifiers, and then measures the time average of the square of the voltage. This measurement is directly proportional to the power in the signal. The measured power contains one component due to the antenna temperature and another due to thermal emission by the antenna and receiver. The latter

component is called the receiver noise temperature ( $T_{rec}$ ), and the sum of the two is referred to as the system noise temperature ( $T_{sys}$ ), that is,  $T_{sys} = T_a + T_{rec}$ . The raw power measurement made by a radiometer is equal to  $T_{sys}$  multiplied by the receiver gain.  $T_{rec}$  originates primarily from three sources. Both the antenna and the transmission line connecting it to the amplifier are typically made of a highly conducting metal. However, because the conductivity is finite, there will be a small resistive loss in power experienced by the signal as its current flows along the metal. The metal will reradiate its own thermal emission in order to remain in local thermodynamic equilibrium. This reradiation contributes to  $T_{rec}$ . The amplifier also generates its own emission, due in part to resistive losses at its input stage as well as other noise generation mechanisms within the transistor. Other noise sources are also present in the receiver after its first amplifier, but they have a relatively small effect on  $T_{rec}$  because the  $T_a$  portion of the signal has been significantly amplified at that point.

Calibration of receiver effects consists of estimating the receiver gain and  $T_{rec}$  and then subtracting  $T_{rec}$  from  $T_{sys}$  to obtain  $T_a$ .  $T_{rec}$  can be estimated in different ways, depending on the radiometer hardware architecture. Many radiometer antennas are mechanically scanned to sweep their mainbeam across a  $T_b$  scene and generate an image. In this case, it is common to place a pair of calibration targets with known  $T_b$  values at opposite edges of the scan (Hollinger et al., 1990). Their measurement allows for the determination of both the receiver gain and  $T_{rec}$ . Some radiometers are not mechanically scanned and it is impractical to place calibration targets in front of the antenna, especially in spaceborne deployments. In these cases, receiver gain can be estimated by intermittently adding a known noise source to  $T_{sys}$  and measuring the resulting change in power. To estimate  $T_{rec}$ , a calibration switch is often used, which redirects the input to the receiver from the antenna to a calibration target with a known  $T_b$  (Ruf and Warnock, 2007). This approach can be less accurate and stable because the calibration switch itself is a source of power loss and thermal noise and because the resistive losses in the antenna and the portion of the transmission line between it and the receiver are now outside of the calibrated portion of the receiver.

## Conclusion

Calibration of a microwave radiometer is the process by which the  $T_b$  arriving from a particular direction at a particular polarization is estimated from its raw measurements. The raw measurements can be explained by considering the action of the radiometer antenna on the incident radiation and then considering the action of the radiometer receiver on the signal generated by the antenna. The principle instrumental effects that are corrected for by the calibration process are the sensitivity of the antenna to incident radiation from undesirable directions and at undesirable polarizations, the addition

of thermal emission to the measurement by the receiver itself, and the magnitude of the signal amplification by the receiver.

## Bibliography

- Gasiewski, A. B., and Kunkee, D., 1993. Calibration and applications of polarization correlating radiometers. *IEEE Transactions on Microwave Theory Techniques*, **29**(6), 1449.
- Hollinger, J. P., Pierce, J. L., and Poe, G. A., 1990. SSM/I instrument evaluation. *IEEE Transactions on Geoscience and Remote Sensing*, **28**, 781–790.
- Njoku, E. G., Christensen, E. J., and Cofield, R. T., 1980. The SeaSat scanning multichannel microwave radiometer (SMMR): antenna pattern correction – development and implementation. *IEEE Journal of Oceanic Engineering*, **OE-5**, 125.
- Ruf, C. S., and Warnock, A. M., 2007. GEOSAT follow on water vapor radiometer: performance with a shared active/passive antenna. *IEEE Transactions on Geoscience and Remote Sensing*, **45**, 970–977.

## Cross-references

[Microwave Radiometers](#)  
[Radiation, Polarization, and Coherence](#)

---

## CALIBRATION, OPTICAL/INFRARED PASSIVE SENSORS

---

Carol Bruegge  
 Jet Propulsion Laboratory, California Institute of  
 Technology, Pasadena, CA, USA

## Definition

*Calibration.* A set of operations that establish, under specified conditions, the relationship between values indicated by a measuring instrument and the corresponding known values of a standard. For remote sensors, this typically implies the radiometric, spectral, and geometric characterization of an instrument as needed to understand the impact of the instrument's performance on the data or the derived data products.

Calibration factors are determined by comparison with a standard whose output is known in accepted physical units as part of the *Système International d'Unités* (abbreviated SI). Units are based on the metric-kilogram-second (mks) system and include the Kelvin, for temperature, and Watt, for power. Derived radiometric parameters are listed in [Table 1](#).

The calibration parameters derived for a sensor must be reported with the associated uncertainty and confidence level. The uncertainty analysis needs to establish both the precision and absolute uncertainty. The *precision* of the calibration is the consistency with repeated measurements. The *absolute calibration* is determined by the sensor's response to stable standards. These should be related to international or national standards through an unbroken chain of comparisons.

**Calibration, Optical/Infrared Passive Sensors, Table 1**  
Common radiometric parameters

Entity	Symbol	Units
Spectral irradiance (radiant flux density at a surface)	$E_\lambda$	$\text{W m}^{-2} \mu\text{m}^{-1}$
Spectral radiance	$L_\lambda$	$\text{W m}^{-2} \text{sr}^{-1} \mu\text{m}^{-1}$
Spectral reflectance (reflected flux/incident flux)	$\rho_\lambda$	Unitless

The *confidence level* is an interval about the result of a measurement within which the true value is expected to lie, as determined from an uncertainty analysis with a specified probability. A  $3\sigma$  (sigma) confidence level implies that the stated uncertainty is achieved with 99 % probability.

## Introduction

During the sensor development phase, the science and engineering teams first agree to set calibration requirements and a calibration approach. Absolute calibration requirements of 3–5 % ( $1\sigma$ ) uncertainty are considered state of the art. Higher accuracy is typically specified for channel-relative or pixel-relative measurements. The accuracy is limited due to instrument-specific attributes, such as stray-light, out-of-field response, polarization sensitivity, scan-mirror sensitivity, linearity, signal-to-noise, temperature sensitivity, dark offset, and long-term stability. Radiometric uncertainty is increased when these effects alter the imagery and recorded signals in unpredictable ways.

Testing is conducted throughout the lifetime of the sensor. Characterizations of the filter and detector components provide early assurance that design requirements will be met. Preflight testing at the instrument level, before assembly onto the spacecraft, allows many parameters to be determined, which cannot be established on-orbit. This testing period is crucial to understanding the as-built performance. Following this, the program must commit to an on-orbit calibration plan. This allows response degradation, due to the browning of the optical elements or throughput change due to radiation damage, to be monitored. An adequate on-orbit calibration program will allow accurate radiance products to be reported even in the presence of sensor degradation. Both preflight and on-orbit calibrations are essential. An overview of the preflight testing for the Multi-angle Imaging SpectroRadiometer (MISR) is given by Bruegge et al. (2002).

## Spectral response function

Most remote sensing systems measure incident light using several channels, where each channel is designed with a specified color sensitivity. That is, the instrument's per-channel output is designed to be a function of both the amount of incident light, as well as its wavelength. The color selection may be achieved by using spectral

filters within the instrument, or may be accomplished by use of a grating that disperses light according to the wavelength. In either case, the *spectral response function* (SRF) must be determined for each channel. This is a measure of the instrument's output as a function of the incident wavelength of light. The distribution only needs to be known in a relative sense, and is typically normalized to unity at the wavelength of peak response.

The SRF is measured using a test setup that can illuminate an instrument with monochromatic light, and where the wavelength of light can be varied during the test. The characterization should measure both the in-band response, near the region of peak sensitivity, and also the far-wing response. The hardware used is most commonly a monochromator. For instruments with very narrow spectral response functions, a tunable diode laser can be used, or Fourier Transform Interferometer (Strow et al., 2003). In either case, it is imperative that the system response be measured. It is insufficient to substitute the filter transmittance for this response, as all optical components, as well as the detector itself, contribute to the SRF.

It is common practice to summarize a sensor's spectral properties by tabulating the center wavelength and spectral width. This has been done by quoting the wavelength-of-peak response and full-width at half-maximum (FWHM). The latter is the wavelength at which the response falls to half of its peak value. These parameters can be misleading in cases where the SRF may be double peaked, asymmetric, or have a large out-of-band response. A better representation can be obtained from an equivalent square-band response analysis (Palmer, 1984). Here the sensor spectral response function is replaced with a function of equivalent area, but with an effective amplitude  $R_n$  and a throughput of 0 at wavelengths less than a computed minimum wavelength or greater than a computed maximum wavelength. Figure 1 gives an example of an SRF and square-band equivalent. The example is of Landsat-4, TM band 2 channel.

## Radiometric calibration

### Band-averaged radiances

Typically, raw data (digital numbers, or  $DN$ ) from a sensor are converted to radiance units by knowledge of the gain coefficient. An example might be

$$DN - DN_0 = \bar{L}_\lambda \cdot G \quad (1)$$

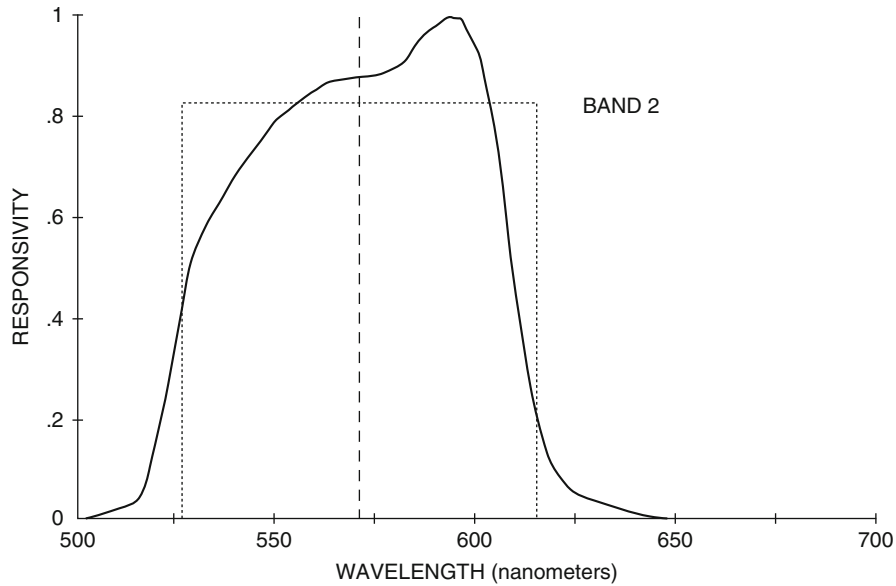
where

$DN$  is the sensor output count

$DN_0$  is the dark-scene output count

$\bar{L}_\lambda$  is the band-weighted spectral radiance incident onto the sensor ( $\text{W m}^{-2} \text{sr}^{-1} \mu\text{m}^{-1}$ )

and  $G$  is the radiometric response coefficient ( $DN/[\text{W m}^{-2} \text{sr}^{-1} \mu\text{m}^{-1}]$ )



**Calibration, Optical/Infrared Passive Sensors, Figure 1** Spectral response function and moments-derived center wavelength and width for a typical detector.

A precise determination of the band-weighted radiance would require knowledge of both the spectral content of the incident light as well as the sensor spectral response function,  $R_\lambda$ . The band-weighted incident radiance is as follows:

$$\bar{L}_\lambda = \frac{\int L_\lambda R_\lambda \partial \lambda}{\int R_\lambda \partial \lambda} \quad (2)$$

For calibration, the gain,  $G$ , is computed with complete knowledge of the SRF and source spectral radiance. For radiance retrieval and science product generation, where output digital numbers are converted into radiances, the spectral content of the scene is not retrieved, rather only a band-weighted average.

### Standards

The test equipment associated with a radiometric calibration requires an extended, spatially uniform, and spectrally smooth light source. A blackbody radiator is the most widely used source for infrared calibration. Its use in the visible, UV, and near-IR is limited. For these wavelengths, an integrating sphere or lamp and diffuse reflector fixture is more typical. The source must be larger than the geometric field of view of the sensor to be tested. This is to capture stray and diffracted light that will contribute to the output. Point sources of light are suitable for measuring a system's point spread function response, but are not suitable as radiometric targets.

If the source is an integrating sphere, its output needs to be calibrated by use of a transfer detector. The detector is, in turn, calibrated against a source standard. Standard

filament lamps are commercially available. The manufacturer typically seasons them by operating for 30 h. Lamps with output fluctuations are discarded. Suitable lamps are calibrated against a working standard that has a calibration traceable to national standards. These lamps can have accuracies approaching 1 % ( $2\sigma$ ). Schneider and Goebel (1984) provide a review of standards.

### On-orbit calibration

In-flight calibration is best accomplished using multiple technologies. Data from an on-board calibrator (OBC), for one, can provide the most frequent verification of sensor performance and stability. These systems can be used to make frequent checks on performance. Sampling dark current or the response to an attenuated view of the sun, for example, can be made once per orbit. As the OBC can itself degrade on-orbit, scene-viewing techniques are also required. Although considered the definitive validation of sensor performance, measurements are less frequent due to constraints associated with imagery collection. Scene studies can be as simple as observations of an un-instrumented desert site, or a highly accurate measurement of a site's in situ observations, and involving a field team or a network. Coastlines and contrast edges can be used to confirm channel geolocation and co-registration. The SeaWiFS sensor makes use of lunar observations to track relative degradation changes (Eplee et al., 2001). Finally, cross-comparisons with sensors of similar footprints and bandpasses provide convincing error estimations. The comparison of radiances as determined from all techniques allows radiance uncertainty to be determined.

### On-board calibrators

Examples of on-board calibrators can be found on EOS/Terra spacecraft sensors. The Multi-angle Imaging SpectroRadiometer (MISR) makes use of two deployable Spectralon diffuse targets. These are used to reflect sunlight into the earth-observing cameras. The panels have proven to be radiometrically stable on-orbit (Chrien et al., 2002). This is attributed to cleanliness and proper handling procedures that avoid exposure to contaminants (Stiegman et al., 1993). The panels are monitored by detector standards. Both radiation-resistant and high-quantum efficient detectors are utilized. The latter are intended to provide a measure of the incident light based upon physical principles, rather than transfer calibration using a standard source. In practice, detector stability has proven to be the driving criteria for detector selection.

The MODerate resolution Imaging SpectroRadiometer (MODIS), also on the Terra spacecraft, makes use of several on-board calibrator systems. These include a blackbody (BB) radiator, solar diffuser (SD), a solar-diffuse stability monitor, and the spectroradiometric calibration assembly (SRCA). The BB is the prime calibration source for the thermal bands located from 3.5 to 14.4  $\mu\text{m}$ , while the SD provides a diffuse, solar-illuminated calibration source for the visible, near-infrared, and shortwave infrared bands ( $0.4 \mu\text{m} \leq \lambda < 2.2 \mu\text{m}$ ). The SDSM tracks changes in the reflectance of the SD via reference to the sun so that potential instrument changes are not incorrectly attributed to changes in this calibration source. The SRCA is a very complex, multifunction calibration instrument that provides in-flight spectral, radiometric, and spatial calibration.

### Unattended desert sites

The Sahara desert sites are considered stable with time. These sites have only small amounts of vegetation, are sparsely populated, and are typically found with clear-sky and low-aerosol conditions. Many instrument teams use these targets to monitor sensor degradation with time (Cosnefroy et al., 1996). Routine observations of sites such as Egypt\_1 (26.10 East longitude, 27.12 North latitude) can be trended in order to determine the response degradation for a channel with time. Data are normalized by cosine of the solar zenith angle and the Earth–Sun distance. Observations are trended that are acquired at a fixed observation angle. This reduces error due to surface bidirectional reflectance factor (BRF) differences with view angle.

### Vicarious calibration

Vicarious calibration (VC) is a process that is based upon in situ measurements acquired over a large, homogeneous desert site. With these data, the top-of-atmosphere spectral radiance can be computed and compared to those reported by the sensor as it simultaneously images the test site. Agreement constitutes

validation of the sensor's calibration. The in situ observations determine aerosol optical depths, surface spectral reflectance and BRF, and water vapor column amount. The top-of-atmosphere radiances are computed using a radiative transfer code such as MODTRAN. Vicarious calibrations can have uncertainties as small as 3 % ( $1\sigma$ ). Key to the success of these measurements is the site selection. Western US desert sites, such as Railroad Valley, Nevada, are typically cloud-free and low in aerosols, minimizing errors in the radiative transfer calculation (Thome et al., 2003). It is for this reason that the vicarious calibration data is considered the radiometric standard for MISR, with the on-board calibrator adjusted to provide consistent calibrations (Bruegge et al., 2004).

Vicarious calibration requires visits by a field team to collect surface and atmospheric measurements at times necessarily coincident with a sensor over-flight. With the creation of an autonomous calibration facility, vicarious calibration data can be made available to the sensor community without the need for each research group to deploy its own field team. One example of an autonomous site is the LSpec (LED Spectrometer) automatic facility (Kerola et al., 2009). The facility is located at Frenchman Flat, within the Nevada Test Site. An array of eight LED spectrometers perform the autonomous function of recording surface reflectances at 5 min intervals, thereby permitting accurate and continual real-time scaling to a high-resolution characterization of the surface. Also resident at the LSpec site is a Cimel sun photometer, used to make atmospheric transmittance measurements. The Cimel is part of the Aerosol Robotic Network (AERONET; <http://aeronet.gsfc.nasa.gov/index.html>). Measurements made by the LSpec Cimel are used by AERONET to derive values of aerosol optical depths. From continuous in situ measurement of spectral reflectance of the playa surface, along with acquired aerosol optical depths and ozone optical depths (obtained from the Ozone Mapping Instrument OMI; <http://jwocky.nasa.gov>), the LSpec database provides all physical measurements needed to compute top-of-radiance with the same accuracy as traditional vicarious experiments. Data products are available to the public, and are available via a web-based interface at (<http://LSpec.Jpl.Nasa.Gov>).

### Cross-calibration

The comparison of radiances from two or more sensors having similar passbands, acquired over a common target at near-coincident times can be a powerful validation exercise. In reality, the constraints on the measurements can be relaxed by making use of a radiance model for the site. That is, if the top-of-atmosphere spectral radiance can be determined, these data can be used to estimate the band-averaged radiance for a given sensor, at its SRF and for its time of observation. This is repeated for one or more sensors. The comparison of the first sensor

differenced to its model with the second sensor differenced to its model constitutes the cross-calibration (Thome et al., 2003).

### Summary

There is an increasing demand for higher accuracy calibration. This is driven by the desire to have long-term data records that span multiple satellite programs. In an effort to establish best practices and minimize sensor-to-sensor biases, many international working groups and national standard laboratories are in collaboration. Information on the Committee on Earth Observation Satellites (CEOS) calibration/validation group can be obtained at <http://wgcv.ceos.org/>.

### Acknowledgment

This research was carried out at the Jet Propulsion Laboratory, California Institute of Technology, under a contract with the NASA.

### Bibliography

- Bruegge, C. J., Chrien, N. L., Ando, R. R., Diner, D. J., Abdou, W. A., Helmlinger, M. C., Pilorz, S. H., and Thome, K. J., 2002. Early validation of the multi-angle imaging spectroradiometer (MISR) radiometric scale. *IEEE Transactions on Geoscience and Remote Sensing*, **40**(7), 1477–1492.
- Bruegge, C. J., Abdou, W. A., Diner, D. J., Gaitley, B. J., Helmlinger, M. C., Kahn, R. A., and Martonchik, J. V., 2004. Validating the MISR radiometric scale for the ocean aerosol science communities. In Morain, S. A., and Budge, A. M. (eds.), *Post-Launch Calibration of Satellite Sensors*. Leiden: A.A. Balkema, pp. 103–115.
- Chrien, N. L., Bruegge, C. J., and Ando, R. R., 2002. Multi-angle imaging spectroradiometer (MISR) on-board calibrator (OBC) in-flight performance studies. *IEEE Transactions on Geoscience and Remote Sensing*, **40**(7), 1493–1499.
- Cosnefroy, H., Briottet, X., and Leroy, M., 1996. Selection and characterization of Sahara and Arabian desert sites for the calibration of optical satellite sensors. *Remote Sensing of Environment*, **58**(1), 101–114.
- Eplee, R. E., Robinson, W. D., Bailey, S. W., Clark, D. K., Werdell, P. J., Wang, M., Barnes, R. A., and McClain, C. R., 2001. Calibration of SeaWiFS. II. Vicarious techniques. *Applied Optics*, **40**, 6701–6718.
- Kerola, D. X., Bruegge, C. J., Gross, H. N., and Helmlinger, M. C., 2009. Vicarious calibration of visible-near infrared earth remote sensors using LED Spectrometer (LSpec) facility measurements in conjunction with radiative transfer models. *IEEE Transactions on Geoscience and Remote Sensing*, **47**(4), 1244–125.
- Palmer, J. M., 1984. Effective bandwidths for LANDSAT-4 and LANDSAT-D' multispectral scanner and thematic mapper subsystems. *IEEE Transactions on Geoscience and Remote Sensing*, **GE-22**(3), 336–338.
- Schneider, W. E., and Goebel, D. G., 1984. Standards for calibration of optical radiation measurement systems. *Laser Focus*, **20**(99), 82–96.
- Stiegman, A. E., Bruegge, C. J., and Springsteen, A. W., 1993. Ultraviolet stability and contamination analysis of Spectralon diffuse reflectance material. *Optical Engineering*, **32**(4), 799–804.
- Strow, L. L., Hannon, S. E., Weiler, M., Overoye, K., Gaiser, S. L., and Aumann, H. H., 2003. Prelaunch spectral calibration of the

atmospheric infrared sounder (AIRS). *IEEE Transactions on Geoscience and Remote Sensing*, **41**(2), 274–286.

Thome, K. J., Biggar, S. F., and Wisniewski, W., 2003. Cross comparison of EO-1 sensors and other Earth resources sensors to Landsat-7 ETM+ using Railroad Valley Playa. *IEEE Transactions on Geoscience and Remote Sensing*, **41**(6), 1180–1188.

### Cross-references

[Calibration and Validation](#)  
[Remote Sensing, Physics and Techniques](#)

---

## CALIBRATION, SYNTHETIC APERTURE RADARS

---

Anthony Freeman  
 Jet Propulsion Laboratory, California Institute of  
 Technology, Pasadena, CA, USA

### Synonyms

Imaging radar calibration

### Definition

*Synthetic aperture radar (SAR)*. A type of radar that forms high-resolution images of surfaces (planetary and terrestrial) using a technique known as aperture synthesis.

*SAR calibration*. Encompasses all of the necessary steps taken to convert SAR image pixel values to fundamental units such as (normalized) radar cross section, measured in units of (m<sup>2</sup>/m<sup>2</sup>), or relative phase, measured in degrees.

*SAR calibration performance*. An assessment of how well the calibrated SAR image pixel values correspond to the desired fundamental units.

*Relative calibration performance (precision)*. An assessment of the relative errors between measurements made by a sensor of the same quantity separated in time or space.

*Absolute calibration performance (accuracy)*. An assessment of the error in any single measurement made by a sensor as compared with an accepted, standard reference value.

### Introduction

Synthetic aperture radar (SAR) was first conceived and demonstrated from aircraft in 1953 (Wiley, 1965). SARs are generally radars mounted on aircraft or satellite platforms and pointed sideways. The radar illuminates an area (referred to as its footprint) on the planet's surface down and off to the side of the platform track, and as the platform moves, this footprint traces out a swath that will eventually form the SAR image. SARs achieve high-resolution through aperture synthesis, a technique that combines radar returns collected from multiple (many) vantage points. This is done through signal processing, which generally occurs after the "raw" data has been sent down to the ground.

Early SARs were used to simply produce high-resolution images for military mapping purposes and later geologic or landform mapping. This was especially valuable in areas that were often cloud-covered and therefore unsuited to electro-optical sensor mapping. Interpretation and analysis of SAR images in this early period was not too different from photointerpretation of aerial photography and was therefore largely qualitative and highly subjective.

In the early 1980s, scientists using SAR data began to consider whether it could be used quantitatively, to allow geophysical quantities such as soil moisture, snow water equivalent, or surface topography (see also entry *Land Surface Topography*), for example, to be estimated directly from SAR measurements. Exciting results were being obtained from field experiments using well-calibrated, ground-based scatterometers with small footprints at around this time (Ulaby et al., 1982), and the expectation was that such local-scale results could be expanded to a global scale using SARs flown in space (Dubois et al., 1992). To achieve this, SAR data would have to be calibrated to standards similar to the ground-based scatterometers and to the same units, which had not happened up to that point. This challenge was vigorously tackled between 1987 and 1994 by scientists and engineers engaged in the field (Freeman, 1992).

As a result of all this effort, the first systematically calibrated SAR data became available to the science community in the late 1980s (van Zyl et al., 1992) from the NASA/JPL airborne SAR system (AIRSAR). This was followed in the early 1990s by calibrated data from the European Space Agency's ERS-1 spaceborne SAR (Attema and Francis, 1991), the Japanese Space Agency's JERS-1 SAR (Shimada, 1993), and NASA/JPL's SIR-C system in 1994 (Freeman et al., 1995). Since that time, calibrated SAR data has been the accepted norm, and systems such as the Canadian Space Agency's Radarsat or the Japanese Space Agency's PalSAR routinely deliver high-quality, calibrated SAR data to a broad science community.

### External SAR calibration

During the 1980s, several groups around the world conducted experiments designed to calibrate SAR data collected over a given site. Examples include some of the field campaigns in support of the SIR-A (1981) and SIR-B (1984) missions, which carried a SAR in the payload bay of the space shuttle. Data from the SIR-A and SIR-B missions was largely uncalibrated, except for a few sites where calibration targets of known radar cross section were deployed and later used to estimate the radar cross section across the image (Way and Smith, 1991; Curlander and McDonough, 1991). This is referred to as external calibration. Calibration targets typically used in such experiments include trihedral corner reflectors, which resemble upturned pyramids in appearance and have a well-determined radar cross section, and

transponders, which can be tuned to have a range of radar cross sections and characteristics (Freeman et al., 1990).

Valuable as these field experiments were, it is of course impractical to deploy corner reflectors in every scene where one wants calibrated SAR data. Consider also that plans were under way in the 1980s to obtain high-resolution radar measurements of the surface of Venus and Titan by flying SARs on the Magellan and Cassini missions. What was needed was an approach that would allow systematic calibration of all data generated by a SAR sensor, without the need for calibration targets within the scene.

### Internal SAR calibration

In the late 1980s, engineers began to adapt internal calibration methods developed for scatterometers (Ulaby et al., 1982), to allow the systematic conversion of all SAR image pixel values to fundamental units such as radar cross section. Internal calibration involved first constructing an error budget for the system that identifies all possible calibration error sources and their likely magnitudes. The next step is to design and build a radar system that is as stable as possible. All elements of the radar system that contribute to the calibration error budget and could therefore affect the final calibration performance are first characterized on the ground. Examples include the RF power measured in watts, which is transmitted by the radar when it illuminates the ground, and the gain of the receiver used to collect the reflected echoes from the area illuminated by the antenna footprint. SAR systems are somewhat unique in that the processing that turns the "raw" signal data collected by the SAR into high-resolution image data can also affect the calibration, so this therefore has to be factored into the error budget and characterized (Freeman and Curlander, 1989).

Preflight characterization of the individual elements of the SAR system is used to verify the system error budget. During flight operations, test signals are injected at reasonable intervals to check that the performance of the radar system is consistent with this preflight characterization. Examples of test signals are sinusoids or Gaussian noise sources covering a given RF frequency range, which are fed into the receiver. The RF power transmitted by the radar is also measured frequently. Some systems include capabilities to actively monitor the radar antenna performance (gain and pointing).

Putting all this together, systematic calibration of SAR data involves using the characterization of the end-to-end radar system from preflight and in-flight measurements, to arrive at a formula to convert the SAR image pixel values into fundamental units. The system error budget is then used to estimate the calibration performance for the final product. This calibration performance is verified using external calibration over sites containing calibration targets, or natural surfaces with sufficiently well-known radar reflectivity, such as the Amazon rain forest, or vegetation-free surfaces such as bare soil or open ocean.

## Polarimetric SAR

One of the most challenging types of SAR data to calibrate comes from polarimetric radars, in which SAR images are collected simultaneously at several different polarizations. A typical polarimetric SAR system, such as NASA/JPL's AIRSAR, collects polarimetric SAR data by first transmitting a horizontally polarized radar waveform, then measuring the reflected energy from the surface in both horizontal (H) and vertical (V) polarizations. This produces radar images in what is termed HH and HV polarizations (H-transmit, H-receive and H-transmit, V-receive). The radar also transmits a vertically polarized waveform to produce images in VV and VH polarizations. H and V polarizations are orthogonal, and if one collects radar reflectivities in all four polarizations in this basis (i.e., HH, HV, VH, VV), then it is possible to synthesize what one would have seen with a radar configured with circular polarizations, for example (Zebker et al., 1987).

Polarimetric SAR data, besides allowing such polarization synthesis, are incredibly rich in information, and researchers have mined such data to retrieve estimates of soil moisture (Dubois et al., 1995), vegetation biomass (Dobson et al., 1992), and to differentiate between agricultural crops (Freeman et al., 1994). Polarimetric SAR data, when well-calibrated, can also be used to bound the underlying physics of the radar wave's interaction with the surface (Freeman and Durden, 1998) and to estimate structural characteristics (e.g., roughness scales) and electrical properties (dielectric constant or conductivity) of the surface under investigation (Oh et al., 1992).

Calibration of polarimetric SAR has its own particular set of challenges, one of which is that it is impossible to build a radar antenna that transmits or receives pure H or V polarizations. There is always some small contribution from the orthogonal polarization, termed cross talk, which has to be corrected or accounted for. van Zyl, (1990) was the first to derive a polarimetric calibration algorithm that used characteristics of naturally occurring surfaces to successfully correct for system cross talk. Another challenge is that the relative phase between polarizations (e.g., HH versus VV) contains significant information. Thus, approaches have been developed to calibrate relative phase between measurements (Sheen et al., 1989). Finally, interactions of the radar waveform with the ionosphere, particularly the effect of Faraday rotation (which changes the polarization of the radar waveform), are a significant source of calibration error at some wavelengths. Techniques to calibrate SAR data subject to Faraday rotation and at the same time other system effects appeared in the literature in 2004 (Freeman, 2004) and have since been validated using PalSAR data (Nicoll et al., 2007). Recently, interest has surfaced in a novel form of dual-polarized measurements known as compact or hybrid polarimetry, which carries less information than fully polarimetric SAR but has some advantages in terms of system design. Calibration of compact polarimetry systems presents some interesting challenges (Freeman et al., 2008).

## Interferometric SAR

Interferometric SAR systems collect data from two different vantage points, and the relative phase between the two measurements is compared to estimate surface elevations or surface motion. Comparison of the relative phase between measurements allows observation of very subtle surface variations of the order of a fraction of the radar wavelength. Calibration of interferometric SAR then requires excellent phase calibration between measurements. These measurements may be made at the same time or over a time separation of years, in what is known as repeat-pass observations. This latter requirement introduces a long-term phase stability requirement into the system design.

Calibration of topography data derived from interferometric SAR data generated by the spaceborne radar topography mission (SRTM) was achieved by Rodriguez et al. (2006). Calibration of interferometric SAR data from different time periods was first demonstrated using ERS-1 data and has been demonstrated on a number of SAR missions since then. The largest calibration uncertainty in such repeat-pass observations stems from uncertainties in the relative location of the vantage points for each observation. The vector joining these two points is known as the interferometric baseline for that pair of observations. This baseline can vary from pass to pass, depending on the orbital characteristics of the platform and the degree to which the flight track can be controlled.

In recent years, techniques combining polarimetric and interferometric SAR have received a lot of attention (e.g., Dubois-Fernandez et al., 2005), with scientists publishing estimates of forest height derived from such data (termed PoLinSAR), using algorithms such as the random volume over ground model (Treuhaf et al., 1996). These techniques open up a new set of challenges for SAR calibration.

## Conclusion

Since the late 1980s, calibrated SAR data has become the norm rather than the exception. Scientist using SAR data now expect it to be calibrated and to within known calibration uncertainties. Challenges exist in the calibration of SAR data from longer wavelength systems, subject to ionospheric effects, and when polarimetry and interferometry are combined. New science applications tend to push for better calibration performance, which also presents a challenge for the calibration engineer.

## Acknowledgments

This research was carried out at the Jet Propulsion Laboratory, California Institute of Technology, under a contract with the NASA.

## Bibliography

Attema, E., and Francis, R., 1991. ERS-1 calibration and validation. *ESA Bulletin*, 65, 80–86.

- Curlander, J. C., and McDonough, R. N., 1991. *Synthetic Aperture Radar Systems and Signal Processing*. New York: Wiley. Wiley Series in Remote Sensing.
- Dobson, M. C., et al., 1992. Dependence of radar backscatter on conifer forest biomass. *IEEE Transactions on Geoscience and Remote Sensing*, **30**, 3.
- Dubois, P. D., Evans, D., and van Zyl, J., 1992. Approach to derivation of SIR-C science requirements for calibration. *IEEE Transactions on Geoscience and Remote Sensing*, **30**, 6.
- Dubois, P. C., van Zyl, J., and Engman, T., 1995. Measuring soil moisture with imaging radars. *IEEE Transactions on Geoscience and Remote Sensing*, **33**, 4.
- Dubois-Fernandez, P., Dupuis, X., and Garestier, F., 2005. PollnSAR calibration of deramp-on-receive system: example with the RAMSES airborne system. *Canadian Journal of Remote Sensing*, **31**, 1.
- Freeman, A., 1992. SAR calibration: an overview. *IEEE Transactions on Geoscience and Remote Sensing*, **30**, 6.
- Freeman, A., 2004. Calibration of linearly polarized polarimetric SAR data subject to Faraday rotation. *IEEE Transactions on Geoscience and Remote Sensing*, **42**, 8.
- Freeman, A., and Curlander, J. C., 1989. Radiometric correction and calibration of SAR images. *Photogrammetric Engineering and Remote Sensing*, **55**, 1295–1301.
- Freeman, A., and Durden, S., 1998. A three-component scattering model for polarimetric SAR data. *IEEE Transactions on Geoscience and Remote Sensing*, **36**, 3.
- Freeman, A., Shen, Y., and Werner, C. L., 1990. Polarimetric SAR calibration experiment using active radar calibrators. *IEEE Transactions on Geoscience and Remote Sensing*, **28**, 2.
- Freeman, A., Villaseñor, J., Klein, J. D., Hoogeboom, P., and Groot, J., 1994. On the use of multifrequency and polarimetric radar backscatter features for classification of agricultural crops. *International Journal of Remote Sensing*, **15**, 9.
- Freeman, A., et al., 1995. SIR-C data quality and calibration results. *IEEE Transactions on Geoscience and Remote Sensing*, **33**, 4.
- Freeman, A., Dubois, P. C., and Truong-Loi, M-L., 2008. Compact polarimetry at longer wavelengths – calibration. In *Proceedings of EUSAR 2008*. Friedrichshafen.
- Nicoll, J., Meyer, F., and Jehle, M., 2007. Prediction and detection of Faraday rotation in ALOS PALSAR data. In *Proceedings of Geoscience and Remote Sensing Symposium*. Barcelona.
- Oh, Y., Sarabandi, K., and Ulaby, F. T., 1992. An empirical model and an inversion technique for radar scattering from bare soil surfaces. *IEEE Transactions on Geoscience and Remote Sensing*, **30**, 2.
- Rodríguez, E., Morris, C. S., and Belz, J. E., 2006. A global assessment of the SRTM performance. *Photogrammetric Engineering and Remote Sensing*, **72**, 3.
- Sheen, D. R., Freeman, A., and Kasischke, E. S., 1989. Phase calibration of polarimetric radar images. *IEEE Transactions on Geoscience and Remote Sensing*, **GE-27**, 719–731.
- Shimada, M., 1993. J-ERS-1 SAR calibration and validation. In *Proceedings of CEOS SAR calibration workshop*. Noordwijk, The Netherlands.
- Treuhaft, R., Madsen, S., Moghaddam, M., and van Zyl, J., 1996. Vegetation characteristics and underlying topography from interferometric radar. *Radio Science*, **31**, 6.
- Ulaby, F. T., Moore, R. K., and Fung, A. K., 1982. *Microwave Remote Sensing: Active and Passive*. London: Addison-Wesley. Remote Sensing.
- van Zyl, J. J., 1990. Calibration of polarimetric radar images using only image parameters and trihedral corner reflector responses. *IEEE Transactions on Geoscience and Remote Sensing*, **28**, 3.
- van Zyl, J. J., Carande, R., Lou, Y., Miller, T., and Wheeler, K., 1992. The NASA/JPL three-frequency polarimetric AIRSAR system. In *Proceedings of IGARSS '92*. Houston.
- Way, J., and Smith, E. A., 1991. The evolution of synthetic aperture radar systems and their progression to the EOS SAR. *IEEE Transactions on Geoscience and Remote Sensing*, **29**, 6.
- Wiley, C. A., 1965. Pulsed doppler radar methods and apparatus. U.S. Patent 3,196,436, Filed August 13 1954.
- Zebker, H. A., van Zyl, J. J., and Held, D. N., 1987. Imaging radar polarimetry from wave synthesis. *Journal of Geophysical Research*, **92**, 683–701.

## Cross-references

[Electromagnetic Theory and Wave Propagation](#)  
[Radar, Synthetic Aperture](#)  
[Radiation, Polarization, and Coherence](#)

---

## CALIBRATION, SCATTEROMETERS

---

David Long

Department of Electrical and Computer Engineering,  
 BYU Center for Remote Sensing, Brigham Young  
 University, Provo, UT, USA

## Definitions

*Radar scatterometer*. A calibrated radar designed to measure the radar backscatter cross section of a target, which is generally an area on the earth's surface.

*Wind scatterometer*. A scatterometer designed to measure the ocean's surface backscatter at multiple azimuth angles in order to estimate the near-surface vector wind. It is also used for ice melt/freeze, soil moisture, and vegetation remote sensing.

*Normalized radar cross section*. Area-normalized radar backscatter, which is the ratio of the incident and reflected radar signal power. Equivalent to the radar albedo. Often represented by  $\sigma^0$  or sigma-o.

*Geophysical model function (GMF)*. An empirical or analytic relationship between radar backscatter and geophysical quantity, that is, sigma-o is a function of the vector wind, polarization, and other parameters,

$$\sigma^0 = F(S, \chi, p, \dots)$$

where  $S$  is the neutral-stability wind speed (typically at 10 m height),  $\chi$  is the relative angle between the radar illumination angle and the wind direction,  $p$  is the polarization ( $h$  or  $v$ ), and  $\dots$  represents other parameters such as the wave field, temperature, salinity, etc.

## Introduction

A scatterometer is a carefully calibrated radar designed to measure the radar backscatter cross section (usually as the normalized radar backscatter coefficient) of a target, which is frequently part of a natural scene. Accurate calibration of the scatterometer-measured backscatter is critical to the utility of the scatterometer data, and much effort is expended to insure precise calibration of the radar. Scatterometer backscatter measurements are generally

used to infer geophysical properties about the target scene, for example, the near-surface wind speed, soil-moisture, or snow wetness. This is typically done with the aid of a geophysical model function (GMF) or functional relation that relates the parameter of interest to the radar backscatter. Thus, scatterometer calibration can also refer to the determination of this model function and the verification of the geophysical estimation from the scatterometer backscatter measurements. Note that radar parameters and the geometry used to collect the backscatter measurements must be accounted for in the GMF and that uncertainties in these parameters lead to errors in parameter estimation.

### Scatterometer calibration fundamentals

Microwave scatterometers operate by transmitting a microwave signal toward the target and measuring the reflected or backscattered power; the radar cross section is computed from the backscattered power measurement. Due to thermal noise in the radar receiver and Rayleigh fading, the signal power measurement is corrupted by noise. A separate measurement of the receive-only noise power is made and subtracted from the signal-plus-noise measurement to estimate the signal power measurement. The signal-to-noise ratio (SNR) may vary from very low (less than  $-20$  dB) to high (20 dB or more).

For areal (scene) targets, the backscattered signal power is related to the normalized radar cross section ( $\sigma^0$ ) via the radar equation (Ulaby et al., 1981), which can be written as

$$\sigma^0 = P_s X \quad (1)$$

where  $P_s$  is the received backscatter power, and the backscatter conversion factor  $X$  (in simplified form) is

$$X = g P_t G^2 \lambda^2 A_c / (4\pi)^3 R^4 L \quad (2)$$

where processor  $g$  is a calibration correction,  $P_t$  is the transmitted power,  $G$  is antenna gain,  $\lambda$  is the wavelength of the transmitted microwave signal,  $A_c$  is the illuminated footprint area,  $R$  is the slant range to the surface, and  $L$  represents system losses, including processing losses. A key goal in scatterometer calibration is ensuring accurate computation of the backscatter cross section by selecting appropriate values for  $g$  and  $X$ .

More accurate expressions for  $X$  include an integral of the radar equation parameters over the surface, for example,

$$X = \frac{P_t \lambda}{(4\pi)^3 L} \iint g(x, y) G(x, y) / R^4(x, y) dx dy \quad (3)$$

where the integral is defined over the non-negligible antenna gain and  $x$  and  $y$  are orthogonal surface coordinates. (Other forms may be more convenient for a given application such as expressing the integral in terms of antenna angles.)

The parameters in  $X$  can be split into two categories: those that depend on the observation geometry ( $G$ ,  $A_c$ ,  $R$ , and possible contributions to  $g$  and  $L$ ) and those that depend on the radar design and RF system gain ( $P_t$ ,  $\lambda$ , and possible contributions to  $g$  and  $L$ ). Thus, scatterometer backscatter calibration requires both geometric and radar parameter procedures. The parameters  $g$  and  $L$  include factors such as signal spill-over and clipping loss from the radar range gates, signal processing filters, the processing scheme employed, etc. These parameters are highly instrument-specific; techniques for determining them must be adapted for each sensor.

### Backscatter calibration

The scatterometer backscattered signal from the target scene consists of distance-attenuated, time-delayed, frequency-shifted copies of the transmitted signal. The time delay arises due to finite speed of light and the distance (sometimes referred to as the slant range) between the radar and the scene. Variations in the time delay due to spacecraft pointing, topography, and orbit can result in signal power loss by the range gate. The relative motion of the radar with respect to the scene introduces Doppler frequency shift, and variations in Doppler can introduce power variations due to nonideal filters. These must be accounted for in computing  $X$ . Uncertainties or errors in computing  $X$  affect both the mean and variance of the  $\sigma^0$  measurement. Scatterometer  $\sigma^0$  measurement calibration includes insuring that both the mean and variance in the estimated  $\sigma^0$  error in the measurement are minimized. This is complicated by measurement errors due to radiometric noise and Rayleigh fading, which results from time-fluctuation of the self-interference in the echo signal (Ulaby et al., 1981, 1990).

A model for the measured backscatter  $\sigma_m^0$  observed by the scatterometer is

$$\sigma_m^0 = \sigma^0 (1 + K_p v) \quad (4)$$

where  $\sigma^0$  is the true or expected backscatter of the surface,  $K_p$  is the normalized standard deviation (sometimes referred to as the radiometric accuracy) of the measurement error, and  $v$  is typically a normally distributed Gaussian random variable. The multiplicative noise model in Eq. 4 arises, in part, as a result of speckle noise, an inherent limitation in coherent radars. The measurement variability  $K_p$  can be expressed as (see also Yoho and Long, 2003, 2004)

$$K_p^2 = K_{pc}^2 + K_{pr}^2 + K_{pm}^2 \quad (5)$$

where  $K_{pc}$  is the ‘‘communications’’ variability due to radiometric noise,  $K_{pr}$  is the calibration uncertainty and variability, and  $K_{pm}$  is the modeling variability. A key goal in scatterometer calibration is to minimize  $K_{pr}$  and  $K_{pm}$ .  $K_{pc}$  can be written as a quadratic function of the true signal-to-noise ratio ( $\text{SNR} = P_s/P_n$  where  $P_s = X_t \sigma^0$  is

the signal power,  $X$ , the true value of  $X$ , and  $P_n$  is the noise power),

$$K_p^2 = \alpha + \beta/\text{SNR} + \gamma/\text{SNR}^2 \quad (6)$$

where  $\alpha$ ,  $\beta$ , and  $\gamma$  depend on the radar hardware and the signal processing used (e.g., Fischer, 1972; Long and Mendel, 1991; Naderi et al., 1991; Yoho and Long, 2003, 2004).

Accurate ground-based calibration of the RF hardware is required to compute amplifier and antenna gains, filter responses, timing, and other parameters affecting  $X$  and the  $K_p$  parameters  $\alpha$ ,  $\beta$ , and  $\gamma$ . Scatterometers employ carefully designed and calibrated signal feedback paths that attenuate the transmit signal and feed it into the receiver. This permits monitoring and frequent internal calibration of the end-to-end RF system gain. Separate calibration and characterization of the antenna gain pattern must be performed prelaunch.

Once on-orbit, the total system gain including the antennas can be verified by using ground calibration stations. Receive-only, receive/transmit, and transponder ground stations have been used. Transponder stations receive the signal, amplify it by a fixed amount, (optionally) frequency-shift it, and retransmit it toward the orbiting instrument. This provides a signal that stands out against the ordinary backscatter in the measurement data, which enables the system signal timing and ground station received power to be checked against predicted values. As the sensor flies overhead, data from a fixed ground station provides a “slice” through the antenna pattern and measurement swath. Multiple stations enable multiple simultaneous slices to verify and calibrate antenna gain along fan-beam antenna patterns. Typically, ground stations use broad-beam horn antennas that are steered toward the scatterometer as it flies overhead in order to minimize possible signal gain variations in the ground station antennas. With care, absolute system calibration can be accomplished. However, while ground stations are effective in verifying calibration and providing on-orbit adjustments to antenna patterns, achieving the desired high-precision absolute system calibration (better than 0.1 dB) can be difficult since the calibration precision of the ground station is difficult to achieve and maintain.

A widely used alternate approach to system calibration is the use of natural targets. These regions have been used as calibration transfer standards to ensure accurate cross-calibration of multiple instruments. Distributed area targets that have a spatially uniform, temporally stable backscatter response are desired. Rain forests have been widely used for scatterometer calibration due to their wide areal extent and low seasonal variation, but other regions have also been used, including firm at the summits of Greenland and Antarctica and (during certain seasons) deserts and Asiatic steppes. The absolute backscatter of these regions is not known precisely, so natural scenes are generally used for relative calibration of the

backscatter versus observation geometry (such as azimuth angle or intra-footprint) over the scatterometer measurement swath. Rain forests have proven to be the most effective in intersensor calibration and as transfer standards in cross-calibrating difference sensors. Such areas are useful for long-term monitoring of sensor drift.

In the case of dense vegetation, the radar cross section is primarily dependent on the canopy density and varies nearly linearly (in dB) with measurement incidence angle. Carefully selecting homogenous areas within the rain forests that have minimal seasonal variations provides constant regions with the desired calibration characteristics. While the Amazon and Congo rainforests have been widely used, the rainforests of Borneo have proven less suitable for scatterometer calibration due to the mountainous terrain. Seasonal and daily variations in canopy moisture content, particularly daily cycles of dew, introduce some variability in the forest backscatter. For a fixed time of day, the areal average backscatter variation is estimated to be  $\pm 0.15$  dB at both Ku- and C-band (Long and Skouson, 1995; Long, 1998). Excluding measurements made in areas with recent (within 24–48 h) rain reduces the variability. Considerations for incidence and azimuth angle variations are essential, particularly in deserts and snow-covered areas, due to the presence of dunes that exhibit strong azimuthally dependent scattering characteristics.

We note that because of its narrow footprint, pencil-beam scatterometers such as SeaWinds on QuikSCAT receive-only measurements can function as radiometer observations useful for detecting rain. Calibrating QuikSCAT radiometric measurements requires converting the receive-only power measurements into brightness temperature values. Prelaunch RF calibration provides key receive system calibration parameters. Post-launch, comparisons of collocated brightness temperatures measured over extended area targets by conventional radiometers are used in order to complete the calibration process (Jones et al., 2000).

### GMF calibration

Scatterometers are designed to accurately measure  $\sigma^0$  in order to infer geophysical properties from the  $\sigma^0$  measurements with the aid of a GMF that relates  $\sigma^0$  with its observation geometry and the geophysical property of interest, for example, the near-surface ocean wind. An important component of scatterometer calibration is thus to ensure the accuracy of this indirect estimation process by “calibrating” the GMF. In this context, “calibration” refers to validating the accuracy of the estimated geophysical property, for example, the surface wind, by comparison to independent measurements, for example, from buoys. The GMF or backscatter calibration is adjusted to minimize the error (and variance) of the estimated geophysical parameter.

GMF calibration is conducted with the aid of campaigns to collect surface parameter data that is

compared to spatially and temporally collocated backscatter measurements. An extensive literature exists on this topic. Ideally, the surface measurements span the expected range of the parameter of interest and parameters that may affect it. For example, for wind calibration, buoy and/or ship measurements are collected at multiple locations with varying sea-surface temperature, wave conditions, and locations within the scatterometer swath. The comparison data is segmented in various ways in order to evaluate potential sensitivity to unmodeled factors, for example, sea-surface temperature or significant wave height. Near-surface wind measurements are controlled or adjusted to similar heights, fetch, and atmospheric stability conditions using bulk corrections. Assumptions of ergodicity are required comparing buoy point measurements to areal average scatterometer measurements. Rain and land proximity adversely affect the accuracy of scatterometer-derived wind estimates and so only open ocean and no-rain surface data are considered in wind GMF calibration. The size of the scatterometer footprint alters the distribution of the backscatter, particularly in low-wind conditions that can result in very low backscatter. At the other extreme, high winds can saturate the GMF, leading to reduced wind estimate accuracy.

An alternate GMF calibration approach relies on comparison of winds generated from numerical weather prediction (NWP) models and collocated scatterometer backscatter values. While all NWP models have accuracy limitations, the underlying assumption of the alternate approach is that if enough collocated backscatter measurements and NWP winds are collected, the NWP errors “average out,” enabling estimation of an empirical GMF by binning the backscatter data according to the NWP output value. Though not without limitation, this technique has proven highly successful for scatterometer GMF calibration. GMFs, to support simultaneous wind and rain estimation from scatterometer backscatter measurements, rely on both NWP winds and collocated measurements from other sensors, such as radiometers or rain radars, to derive rain-effect and correction models.

## Conclusion

Scatterometry has proven to be a very useful tool for operational wind measure and monitoring and studying the earth. Scatterometer data complements the data from other sensors in long-term studies. An essential element in the success of scatterometry is the precise calibration of the data, which accounts for the detail and attention scatterometer calibration is given.

## Bibliography

Anderson, C., Bonekamp, H., Wilson, J., Figa, J., de Smet, J., and Duff, C., 2007. Calibration and validation of ASCAT backscatter. In *Proceedings of the Joint 2007 EUMETSAT Meteorological Satellite Conference and the 15th Satellite Meteorology & Oceanography Conference of the American Meteorological Society*, Amsterdam.

- Fischer, R. E., 1972. Standard deviation of scatterometer measurements from space. *IEEE Transactions on Geoscience Electronics*, **GE-10**(2), 106–113.
- Grantham, W. L., Bracalente, E. M., Britt, C. L., Wentz, F. J., Jr., Jones, W. L., Jr., and Schroeder, L. C., 1982. Performance evaluation of an operational spaceborne scatterometer. *IEEE Transactions on Geoscience and Remote Sensing*, **GE-20**(3), 250–254.
- Jones, W. L., Merhershahi, R., Zec, J., and Long, D. G., 2000. SeaWinds on QuikSCAT radiometric measurements and calibration. In *Proceedings of the International Geoscience and Remote Sensing Symposium*, July 24–28, 2000, Honolulu, HI, pp. 1027–1029.
- Long, D. G., 1998. Comparison of TRMM and NSCAT observations of surface backscatter over the Amazon rainforest. In *Proceedings of the International Geoscience and Remote Sensing Symposium*, July 6–10, 1998, Seattle, WA, pp. 1879–1881.
- Long, D. G., and Mendel, J. M., 1991. Identifiability in wind estimation from wind scatterometer measurements. *IEEE Transactions on Geoscience and Remote Sensing*, **29**(2), 268–276.
- Long, D. G., and Skouson, G. B., 1995. Calibration of spaceborne scatterometers using tropical rainforests. *IEEE Transactions on Geoscience and Remote Sensing*, **34**(2), 413–424.
- Naderi, F., Freilich, M. H., and Long, D. G., 1991. Spaceborne radar measurement of wind velocity over the ocean—an overview of the NSCAT scatterometer system. *Proceedings of the IEEE*, **79**(6), 850–866.
- Offiler, D., 1994. The calibration of ERS-1 satellite scatterometer winds. *Journal of Atmospheric and Oceanic Technology*, **11**(4), 1002–1017.
- Quilfen, Y., and Bentamy, Y., 1994. Calibration/validation of ERS-1 scatterometer precision products. In *Proceedings of the Geoscience and Remote Sensing Symposium*, August 8–12, 1994, Pasadena, CA, pp. 945–947.
- Spencer, M. W., Wu, C., and Long, D. G., 2000. Improved resolution backscatter measurements with the SeaWinds pencil-beam scatterometer. *IEEE Transactions on Geoscience and Remote Sensing*, **38**(1), 89–104.
- Tsai, W. Y., Graf, J. E., Winn, C., Huddleston, J. N., Dunbar, S., Freilich, M. H., Wentz, F. J., Long, G. J., and Jones, W. L., 1999. Postlaunch sensor verification and calibration of the NASA scatterometer. *IEEE Transactions on Geoscience and Remote Sensing*, **37**(3), 1517–1542.
- Ulaby, F. T., Moore, R. K., and Fung, A. K., 1981. *Microwave Remote Sensing – Active and Passive*. Reading, MA: Addison-Wesley, Vols. 1 and 2.
- Ulaby, F. T., Moore, R. K., and Fung, A. K., 1990. *Microwave Remote Sensing – Active and Passive*. Reading, MA: Addison-Wesley, Vol. 3.
- Verspeek, J., Stoffelen, A., Portabella, M., Verhoef, A., and Vogelzang, J., 2007. ASCAT scatterometer Cal/Val. In *Proceedings of the Joint 2007 EUMETSAT Meteorological Satellite Conference and the 15th Satellite Meteorology & Oceanography Conference of the American Meteorological Society*, Amsterdam.
- Yoho, P. K., and Long, D. G., 2001. Model-based ground station calibration for SeaWinds on QuikSCAT. In Barnes, W. L. (eds.), *Earth observing systems IV, Proceedings of SPIE*, Vol. 4483, 29 July–3 August, San Diego, CA.
- Yoho, P. K., and Long, D. G., 2003. An improved simulation model for spaceborne scatterometer measurements. *IEEE Transactions on Geoscience and Remote Sensing*, **41**(11), 2692–2695.
- Yoho, P. K., and Long, D. G., 2004. Correlation and covariance of satellite scatterometer measurements. *IEEE Transactions on Geoscience and Remote Sensing*, **42**(6), 1176–1187.
- Zec, J., Jones, W. L., and Long, D. G., 1999. NSCAT normalized radar backscattering coefficient biases using homogenous

land targets. *Journal of Geophysical Research*, **104**(C5), 11557–11568.

Zec, J., Jones, W. L., and Long, D. G., 2000. SeaWinds beam and slice balance using data over Amazonian rainforest. In *Proceedings of the International Geoscience and Remote Sensing Symposium*, July 24–28, 2000, Honolulu, HI, pp. 2215–2217.

## Cross-references

[Radar, Scatterometers](#)

---

## CLIMATE DATA RECORDS

---

Eric F. Wood  
Department of Civil and Environmental Engineering,  
Princeton University, Princeton, NJ, USA

### Definition

Following NRC (2004), a climate data record (CDR) is defined as *a time series of measurements of sufficient length, consistency, and continuity to determine climate variability and change*. For satellite-based CDR, these can be further defined as *fundamental CDRs (FCDRs)*, which are calibrated and quality-controlled sensor data that have been improved over time, and *thematic CDRs (TCDRs)*, which are geophysical variables derived from the FCDRs, such as [sea surface temperature](#) and cloud fraction.

Applying the nomenclature that a satellite record meets the standard of a CDR implies that the products were generated and maintained with attention to data stewardship and management, with developed access and dissemination policies. CDR often requires updating and reprocessing to maintain consistency and quality, which implies that the underlying datasets and information used in their creation, such as metadata, are preserved indefinitely in formats that promote easy access. Products deemed a CDR requires commitment for long-term data storage, access, and management.

### Key elements of a climate data record activity

#### CDR organizational elements

1. An advisory and review team to provide input to development of a CDR (FCDR) from satellite data, to review the theoretical basis for the CDR (FCDR) algorithm, and to review the generated CDR (FCDR) products.
2. An advisory and review team for a fundamental CDR should have specific expertise for that product. For thematic CDRs (TCDRs), advisory and review teams should reflect broad disciplinary theme areas.

#### CDR generation elements

1. FCDRs must be generated with the highest possible accuracy and stability.
2. Sensors must be thoroughly characterized before and after launch, and their performance should be continuously monitored throughout their lifetime.

3. Sensors should be thoroughly calibrated, including nominal calibration of sensors in orbit, vicarious calibration with in situ data, and satellite-to-satellite cross-calibration.
4. TCDRs should be selected based on well-defined criteria established by the advisory and review team.
5. Validated TCDRs must have well-defined levels of uncertainty.
6. An ongoing program of correlative in situ measurements is required to validate TCDRs.

### Sustaining CDR elements

1. Resources should be made available for reprocessing the CDRs as new information and improved algorithms are available, while also maintaining the forward processing of data in near real time.
2. Provisions should be included to receive feedback from the scientific community.
3. A long-term commitment of resources should be made to the generation and archival of CDRs and associated documentation and metadata.

### Acknowledgments

The material in this section was drawn from NRC (2004).

### Bibliography

NRC, 2004. *Climate Data Records from Environmental Satellites: Interim Report (2004)*. Washington, DC: Committee on Climate Data Records from NOAA Operational Satellites/National Research Council/National Academies Press. 150 p, 7 x 10.

### Cross-references

[Sea Surface Temperature](#)

---

## CLIMATE MONITORING AND PREDICTION

---

Mathew R. P. Sapiano  
University of Maryland - College Park, College Park,  
MD, USA

### Definition

*Climate*. Time average of atmospheric properties. The objective of the temporal averaging is to establish a background state of behavior that is the most likely state of the atmosphere at any given time. Weather variations are considered to be superimposed on the background climate, while at any given location the climate is viewed as changing through the year; thus, a location has a different climate state for each month of the year. Spatial averaging is generally used as well, but if sufficiently detailed observations are available, microclimates of any desired scale can be defined. Climate variability is the year-to-year change in climate at a given location and time of year; if temporal and/or spatial coherence can be identified in

these variations, coherent modes of climate variability such as the El Niño/Southern Oscillation (ENSO) or the North Atlantic Oscillation (NAO) may be described.

*Climate monitoring.* The practice of describing the current state of the climate system and the status of coherent aspects of climate variability, generally through the use of temporally averaged atmospheric observations.

*Climate prediction.* Prediction of the future state of the climate system on seasonal to interannual timescales, often distinguished from climate change projections on longer timescales. An overlap exists between these concepts on timescales of several years to several decades.

## Introduction

Mark Twain provided the most succinct definition of climate by defining its relationship with weather: “Climate is what we expect, Weather is what we get.” Contrasting weather with climate is perhaps the best approach to defining climate. The weather we observe is deterministic and dynamical; there is a single realization of the weather that is/was actually observed, albeit subject to some measurement error. Climate, on the other hand, is inherently statistical and is often thought of as the *mean state of the weather*, where this mean can be either in time or space (and commonly both). Additionally, weather can be thought of as being deterministic and climate is probabilistic, in that it is the most likely outcome out of some range of possible values (note that the mean usually satisfies the criteria of being the most likely outcome). For example, we might know that it rained on some given day (although there is, of course, measurement error on such an estimate), but the climate estimate of whether it rained on any given day might be a probability of rain rather than an outright answer. For climate monitoring and prediction, the mean underlying state of the Earth system at some given timescale (say the seasonal scale) is of prime interest.

In practical terms, weather monitoring, climate monitoring, and climate change monitoring are often differentiated by the timescale of the signal of interest which is important as a control of the allowable noise/error levels in the data. Weather scales include high-frequency variations and are typically defined as being between zero and 10 days, with longer timescales being more typically associated with climate signals. Climate change signals are generally small and low frequency and are defined as occurring over multiple decades or centuries. Climate monitoring includes scales longer than a few days but still within the period of a few months or years and generally involves the averaging of multiple weather events. Examples of this might be an enhanced hurricane season, a prolonged drought, or even a more expansive hole in the ozone layer.

Despite the many engineering and technical challenges associated with remote sensing datasets, they play a vital role in climate monitoring. Before remote sensing,

observations were limited to single point locations which were generally made in well-populated areas. Remote sensing through radar and satellite observations provides far increased spatial coverage as well as enhanced temporal sampling. This has allowed exploration of the climate in areas of little or no knowledge as well as an understanding of the processes acting at sub-daily timescales. The latency (time until availability) of remotely sensed is also ideal for climate monitoring. Traditionally, climate monitoring products were compiled months after the fact, but remotely sensed data is often available in real time so that global monitoring datasets can be available in mere hours. The construction of climate monitoring datasets from radar networks provides a significant technical challenge and few exist (a notable exception is the Stage IV US gauge-corrected radar precipitation estimates; Lin and Mitchell, 2005). Satellite observations, however, have proven crucial in both climate monitoring and climate change studies and have filled significant gaps in our records most notably, the global oceans.

For the purposes of this entry, we characterize remotely sensed observations in four groups in order from the most direct to the least direct:

1. Direct measurements of climate parameters, specifically the radiation budget at the top of atmosphere
2. Inferred measurements of the current state of important climate characteristics, such as clouds, SST, vegetation, and moisture
3. Contributions to the definition of the initial state of the climate system for prediction or reanalysis models
4. Verification data to for the assessment of climate models and other products and their ability to predict characteristics of the climate system

These groupings are by no means mutually exclusive, with the third and fourth making considerable use of direct and inferred measurements of climate parameters from the first and second group.

We will give examples of the first three groups in the following sections; the fourth is neglected since this is not directly relevant to climate monitoring and prediction, although it is a necessary part of product development. The vast majority of climate monitoring is achieved using inferred observations which fall under the second group, so this section is the largest and has several examples. Remotely sensed data is used in a wide range of different monitoring and prediction capacities; thus, a full survey of all possible activities is impossible. Likewise, each monitoring or prediction product utilizes different techniques, sensors, and algorithms which are too varied to allow for simple classification.

## Measurements of the radiation budget

Spaceborne remotely sensed observations directly measure emitted or reflected radiation at the top of the atmosphere (TOA). Thus, the most direct measurements available from satellites are of the radiation budget which

includes the surface albedo, reflected shortwave radiation from the Sun, and emitted long-wave radiation (usually from the Earth's surface or clouds). While the albedo is fixed for a given surface type, the latter two are modulated by the Earth system. The TOA radiation budget is known to be critically important for climate: Global climate change is a reaction to changes in the energy budget due to increased greenhouse gas concentrations in the atmosphere. Despite the importance of the radiation budget to the climate system, it is still not fully understood how short-term perturbations affect the climate, and, as such, radiation balance estimates are not directly used in climate monitoring. However, estimates of the radiation budget are used to assess the performance of climate models, and so these observations are directly used in that context.

#### Example 1: total solar irradiance

Estimates of incoming solar radiation were traditionally made through the proxy of sunspot counts (see *Radiation, Solar and Lunar*). Sunspots are magnetic disturbances on the Sun's surface that have lower temperatures than their surroundings and lead to slight variations in solar activity with a regular 11 year cycle. Total solar irradiance (TSI) is a more direct measurement of solar activity and is defined as the wavelength-integrated solar radiation received by a surface at an average distance from the Sun at the top of Earth's atmosphere. Measurements of TSI are not possible from Earth's surface due to the effects of the atmosphere on radiation and so measurement of TSI was only made possible with the advent of satellite observations. The historical record of TSI is comprised of several different radiometers aboard different missions (see Fröhlich and Lean, 2004 or Fröhlich, 2007, for details). Multiple combinations of these datasets are available, each with different calibrations (Fröhlich, 2007). The most recent sensor to be launched is the Total Irradiance Monitor aboard the Glory satellite (Mishchenko et al., 2007) which will continue the record of TSI measurements into the future.

TSI is an example of a parameter which is primarily monitored for climate change detection and attribution studies. The "standard" value of TSI is approximately  $1,366 \text{ Wm}^{-2}$  although absolute calibration of sensors is extremely challenging and disagreement exists over the mean value. Over the course of the solar cycle, small variations occur of the order of  $2 \text{ Wm}^{-2}$  (de Toma et al., 2004; Rottman, 2006). Variations in TSI are known to affect climate, and there has been much debate as to whether trends in TSI (or other measures of solar activity such as spectral changes or changes in cosmic rays) could explain recent increases in global temperature. The IPCC AR4 Report (Forster et al., 2007) showed that the contribution of TSI is small and that it is not the main driver of observed changes, although TSI does account for some of the increase.

While TSI affects almost all climate parameters, its effects are greatly obscured by its indirect nature: Solar radiation is the primary driver of the Earth system but it

is modulated by that system. Daily data are routinely available from the web, such as data from the Solar Radiation and Climate Experiment (SoRCE), and can be used in conjunction with other data to understand major solar events such as solar flare activity (e.g., Woods et al., 2004) which impact the Earth. Despite the direct link with the Earth system, it is unclear as to whether TSI variations are large enough to affect the Earth system in a medium-range sense and how to interpret and use these observations for climate monitoring.

#### Measurements of climate parameters

Estimates of Earth system parameters derived from satellites are based on inferences made from measurements of TOA radiation in different channels. The exact nature of these inferred measurements is different for each parameter, mission, sensor, and orbit type. Many parameters require the use of several channels to derive a more accurate estimate, and multiple satellites are often used. For instance, precipitation estimates usually use a mixture of geostationary infrared and polar-orbiting passive microwave estimates to achieve the best global estimate. Multisatellite estimates are commonly used in climate monitoring since these are often superior for surface parameters. The following examples are arranged in order from TOA to the surface and are not intended to be exhaustive, but it is hoped that they are sufficient to provide the interested reader with a foundation for further reading.

#### Example 2: ozone

In the latter part of the twentieth century, before the concept of global climate change had entered the public psyche, there was great public alarm over the discovery of a decline in *stratospheric ozone* and the existence of a hole above Antarctica in the thin ozone layer (see *Stratospheric Ozone*). Ozone is a gas residing primarily in the stable part of the atmosphere above the turbulent troposphere called the stratosphere. Stratospheric ozone occurs naturally at 15–35 km above Earth's surface where ultraviolet (UV) radiation from the Sun fuels a constant cycle of creation and destruction which keeps ozone levels in equilibrium. The ozone layer therefore absorbs nearly all UV radiation which can be harmful to human life, leading to a range of issues including forms of skin cancer. It was discovered in the 1970s that some man-made substances including chlorofluorocarbons (CFCs) were reaching the stable stratosphere and destroying ozone faster than it could be replenished. The Montreal Protocol was established in 1987 (and amended several times since) with the aim of phasing out the use of certain man-made chemicals known to destroy ozone. The treaty has been widely hailed as a success, and global stratospheric ozone levels have begun to recover, although the seasonal Antarctic ozone hole continues to exist and is not expected to recover to pre-1980 levels until midway through the twenty-first century (WMO, 2007).

This ongoing environmental issue is an example of how climate monitoring can have a major impact on society. In situ observations were made throughout the twentieth century, but the emergence of satellite observations with near-global coverage gave the data required to force policy makers into action. The Solar Backscatter Ultraviolet instrument (SBUV/2) aboard the NOAA series of satellites measures scattered UV rays to produce estimates of the total ozone as well as the vertical profile (Bhartia et al., 1996). The European Space Agency (ESA) Global Ozone Monitoring Experiment (GOME) instrument also provides total column ozone and the ozone vertical profile (Burrows et al., 1999) based on backscattered UV radiation.

The United Nations Environment Programme (UNEP) Ozone Secretariat is the primary international body for ozone monitoring. They have produced several assessment documents including the *Scientific Assessment of Ozone Depletion* series of reports which form the basis of global ozone monitoring. Other agencies such as the NOAA Climate Prediction Center (CPC) and other country-level meteorological agencies monitor the current state of stratospheric ozone.

Ozone is also found in much lower concentrations at low levels from anthropogenic sources. This so-called tropospheric ozone is regarded as a pollutant and can lead to serious, direct human health repercussions such as respiratory problems. The mechanisms leading to the formation of tropospheric ozone are different to those of stratospheric ozone, but similar techniques can be employed to retrieve estimates from remotely sensed information. While these estimates are not used in a climate monitoring sense, they are used in air quality forecasting.

### Example 3: precipitation

Accurate measurements of precipitation are challenging because of the high variability of rainfall in both time and space (see *Rainfall*). Significant individual rainfall events can be as short as a few minutes in the case of highly localized convection or last several hours or days and be spread over a large area, as is the case for large-scale stratiform events. Differences in the relative skill of these precipitation estimates are frequently related to the ability to continuously sample precipitation so as not to miss short or small events. For that reason, gauges are usually considered the best source of precipitation data since they provide a time-integrated observation and have few calibration errors. However, gauges can be biased by wind-induced under-catch or other external factors, and coverage is often limited to populated areas where observers can access them. Ground radar estimates give good sampling over a limited area, but calibration issues preclude their combination to form a truly global dataset (the Stage IV radar dataset is a notable exception for the United States only). Satellite estimates of precipitation have larger sampling errors than either gauges or ground radar estimates but give the only estimates over the ocean. Satellite precipitation estimates are based on either

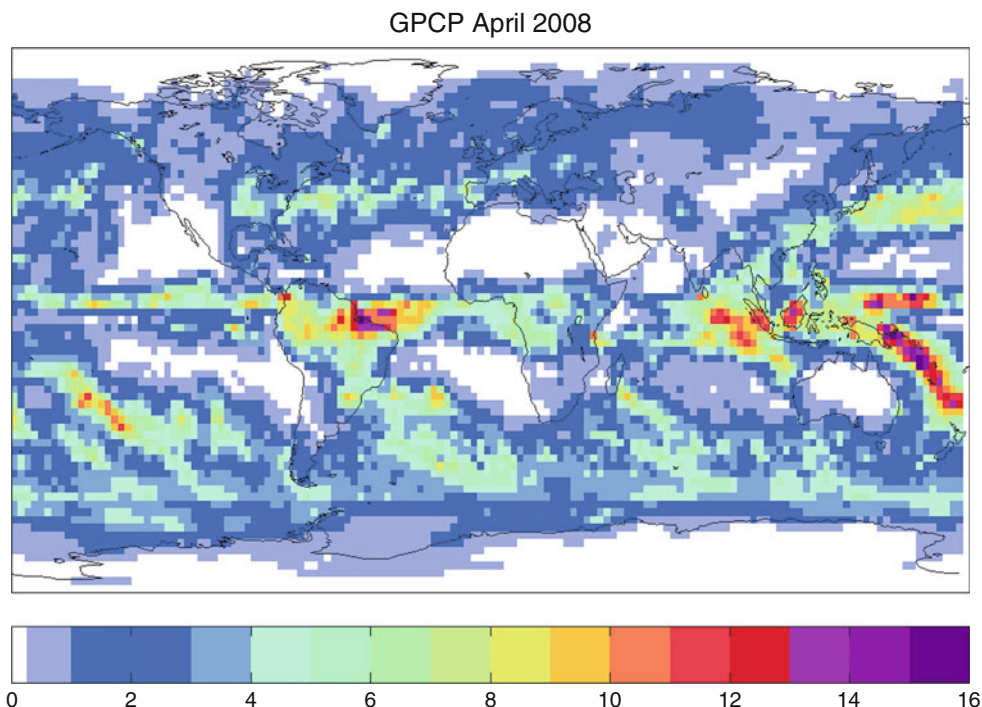
polar-orbiting passive microwave (PMW) or geosynchronous infrared (IR), where the more direct methods of the former generally give superior estimates. Additionally, the NASA Tropical Rainfall Monitoring Mission (TRMM; Kummerow et al., 1998) Precipitation Radar (Iguchi et al., 2000) also provides precipitation estimates, but these are limited to the tropics and the temporal sampling is insufficient for climate monitoring or prediction at the present time.

Despite the advantage of global coverage, satellite-only precipitation estimates are generally considered inferior to combinations of gauge data. Therefore, the most widely used precipitation datasets are combinations of multiple types of data. The two most commonly used precipitation datasets are the Global Precipitation Climatology Project (GPCP; Huffman et al., 1997; Adler et al., 2003) and the CPC Merged Analysis of Precipitation (CMAP; Xie and Arkin, 1997). Both datasets are global, monthly, 2.5° combinations of IR, PMW, and gauge data and a single month of GPCP is shown in Figure 1. A significant barrier to the use of these datasets for real-time monitoring is that the gauge components are not immediately available. The suite of GPCP outputs therefore includes a provisional product which contains most of the combined satellite data and a slightly different, less comprehensive gauge analysis which is available in near real time, but with slightly reduced accuracy which is suitable for climate monitoring. As well as use for the general monitoring of precipitation, these large-scale estimates can also be used in derived products as a key predictor. One particularly useful application is in public health where precipitation has been used for disease risk mapping through disease vector prediction (e.g., Lobitz et al., 2000).

Before the launch of the TRMM mission, there were insufficient polar-orbiting PMW satellites to provide better than daily temporal resolution, but this sampling has been greatly improved with the addition of TRMM (which includes the TRMM Microwave Imager) along with several other PMW instruments such as the Advanced Microwave Sounding Unit (AMSU; Weng et al., 2003) and the Advanced Microwave Scanning Radiometer (AMSR; Wilheit et al., 2003). Several datasets have merged the available PMW estimates with the lower quality but more frequently sampled IR data. These datasets have near-global coverage with resolutions as fine as 8 km every half hour (CMORPH; Joyce et al., 2004) and can include gauge data through a monthly bias correction (TRMM Multi-satellite Precipitation Analysis; TMPA; Huffman et al., 2007). These high-resolution precipitation products are used in a number of climate monitoring situations for near-term predictions such as flash flood prediction (Gupta et al., 2002; Harris et al., 2007) and landslide prediction (Hong et al., 2006, 2007).

### Example 4: vegetation

The most commonly used remotely sensed vegetation product is the normalized difference vegetation index



**Climate Monitoring and Prediction, Figure 1** GPCP V2 mean precipitation for April 2008, in  $\text{mm day}^{-1}$ .

(NDVI; Tucker, 1979) (see Vegetation). NDVI is based on near-infrared (NIR) and Red channels and is simply defined as  $(\text{NIR} - \text{Red}) / (\text{NIR} + \text{Red})$  which is normalized to range from  $-1$  to  $1$ . NDVI is well correlated with the health of vegetation and is based on how green the vegetation is within each observed pixel. Most surfaces equally absorb or reflect in the Vis and NIR channels and give a near zero value of NDVI. Chlorophyll, however, absorbs in the Vis channel while leaves reflect in the NIR channel so that large differences usually denote healthier (or more green) vegetation within a pixel. The most commonly used instrument for the estimation of NDVI has been the Advanced Very High resolution Radiometer (AVHRR) which has flown aboard several missions and continues to provide high-resolution data with near-global coverage. NDVI estimates are used in agricultural and drought monitoring where the health of the crops and vegetation is the primary monitoring target. An important attribute of satellite remote sensing is that observations transcend traditional international boundaries. This is an important characteristic for drought and crop monitoring, as NDVI products can be used to observe countries where ground observations are not available, but where food aid might be required. Derived products are also available, and systems have been developed which forecast disease outbreaks based on NDVI and other variables (Linthicum et al., 1999; Hendrickx et al., 2001; Anyamba et al., 2002).

In general, these studies are based on the use of NDVI and the health of plants as a proxy for the health of disease vectors.

#### Example 5: sea ice

Observations of sea ice extent and concentration are required for both climate change studies and seasonal monitoring (see [Sea Ice Concentration and Extent](#)). The cryosphere is known to be particularly sensitive to changes in global temperature, and the signs of climate change have been most visible in the diminishing Arctic sea ice and the alarming and spectacular breakup of Antarctic ice sheets. However, sea ice also plays an important role in several other climate monitoring datasets, and monitoring products are commonly used in a range of other remotely sensed products to screen out areas where retrievals are either not possible or require modification. Sea ice extent is estimated using a number of different techniques based on passive microwave and infrared observations as well as some limited in situ observations. The NOAA/NESDIS Interactive Multisensor Snow and Ice Mapping System (IMS; Helfrich et al., 2007) is a commonly used merged satellite sea-ice extent product. A single day of the IMS snow (white) and ice (light gray) product is shown in [Figure 2](#). Snow and ice cover are determined by a human forecaster based on remotely sensed data from all sources. Such products are useful

IMS 24km 15 April 2008



**Climate Monitoring and Prediction, Figure 2** IMS Northern Hemisphere snow and ice cover (at 24 km resolution) for 15th April 2008.

for precipitation products where retrievals are often not possible in the presence of snow/ice and ice masks are sometimes used to remove erroneous values. Analyses of sea-surface temperature (SST), such as the Reynolds and Smith (1994) analysis discussed later on, use sea ice products to infer temperature over ice-covered surfaces.

As well as ice extent (or snow cover), the concentration or thickness of ice is of interest, as is the age of the ice (whether the ice is new or has existed for multiple years). Sea ice concentration can be inferred from the Quick Scatterometer (QuikSCAT), the Special Sensor Microwave/Imager (SSM/I), the Scanning Multichannel Microwave Radiometer (SMMR), and, more recently, the Advanced Microwave Scanning Radiometer (AMSR). Such measurements are critically important for climate change monitoring such as the estimation of the depletion of sea ice (e.g., Nghiem et al., 2006). More recently, the Gravity Recovery and Climate Experiment (GRACE) has been used to estimate ice sheet mass inferred from measurements of Earth's gravity.

#### Example 6: sea surface temperature

Estimates of [sea surface temperature](#) (SST) are used in both a climate change monitoring and a seasonal climate monitoring capacity (see [Sea Surface Temperature](#)). For climate change, estimates of SST are important as an indicator of observed changes but also for understanding the global response to carbon dioxide. In a monitoring sense, global SST estimates serve a wide range of functions.

One of the most important indicators of global climate is the El Niño/Southern Oscillation (ENSO) which is chiefly associated with changes in the location and extent of the Tropical-Pacific warm pool and is hence often defined as an average of sea surface temperatures. ENSO variability is associated with a broad range of global weather phenomena and is a dominant component of many climate predictions (further discussion appears later in this section). SST is also an important consideration in hurricane monitoring and prediction since warmer SSTs are required for the initiation of convection and are thus a key component for predicting areas where strengthening of tropical storms is more likely. One of the most widely used gridded SST analyses is the Reynolds and Smith (1994) optimal interpolation (OI; also known as Kriging) of available ship observations and satellite estimates. A single month of this SST estimate is shown in [Figure 3](#). The original dataset used only estimates from the five-channel Advanced Very High Resolution Radiometer (AVHRR) instrument which became operational aboard NOAA-7 in 1981, although it has been updated in successive years. As with many other parameters, merged IR/PMW estimates of SST are quickly becoming the standard and allow for superior estimates. One such dataset is the high-resolution version of the Reynolds and Smith (1994) SSTs which is available at 0.25° daily resolution and uses remotely sensed data from the pathfinder AVHRR from 1981 onward and a mix of AVHRR and Advanced Microwave Scanning Radiometer (AMSR) after its launch in 2002 (Reynolds et al., 2007). SST data have been directly or indirectly used for a variety of monitoring purposes including monitoring of the thermohaline circulation (Latif et al., 2004), as an input for malaria prediction models (Thomson et al., 2005) and as an input for models of coral bleaching (Maynard et al., 2008).

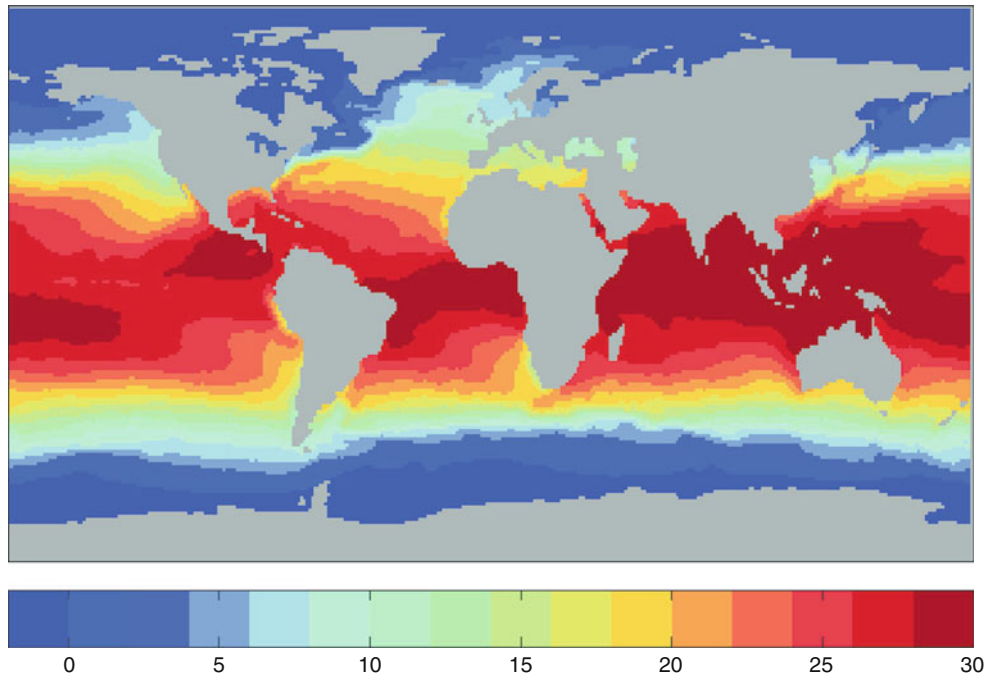
#### Climate prediction and reanalysis

Remotely sensed observations have become an important input to numerical weather and climate models as a main constituent of the analysis of the initial conditions. Numerical forecasts work by propagating a set of initial conditions according to the theoretical physics of the system. The process of estimating the initial condition is called *data assimilation* and involves collecting all of the inputs and merging them. A substantial part of the error in the model predictions is due to errors in the initial condition, and satellites have helped to reduce this error considerably through enhanced spatial and temporal sampling.

#### Reanalysis data

An issue common to all observations is that complete spatial and temporal coverage is not possible. In situ observations are frequently made at a point and are usually unevenly spaced in, at least, space. Remotely sensed observations tend to be more systematically sampled in space and time, but coverage is frequently not global and the sampling is often insufficient. Furthermore, satellite

OI V2 SST April 2008



**Climate Monitoring and Prediction, Figure 3** NOAA OI SST V2 mean sea surface temperature for April 2008, in °C (Reynolds and Smith, 1994).

estimates are nearly always instantaneous whereas our interest for climate is in averages of the data. A polar-orbiting satellite might give a single measurement at a given location once each day, but climate studies require estimates for the whole day. In such cases, a model is often required to obtain estimates which are valid for the whole day.

In the last decade, model reanalysis data has become commonplace in climate science. Such reanalysis techniques are adapted from the data assimilation schemes of operational numerical [weather prediction models](#) and facilitate the combination of multiple observations of multiple parameters and the interpolation of these observations to data-sparse regions in four-dimensional space. Additionally, model forecasts (or nowcasts) can also be made to predict parameters not traditionally measured. Global reanalysis systems therefore provide rich new datasets which can provide data from anywhere in the four-dimensional system (within the model resolution constraints) based on all available in situ and remotely sensed observations. Current reanalysis is still somewhat limited in resolution due to constraints in processing capacity, but are ideal for a range of climate problems.

The first reanalysis to be widely used was the NCAR/NCEP reanalysis (Kalnay et al., 1996) which is still used for a range of purposes and is well suited for many climate monitoring purposes since it is available in near real time. Note that an updated version is now available, the NCEP-DOE AMIP-II Reanalysis (Kanamitsu et al., 2002), which

uses many of the same inputs but corrects a number of issues with the original dataset. The NCAR/NCEP reanalysis directly assimilated radiances from operational TOVS sounders once available (after 1979). Additional remotely sensed datasets were also indirectly used in the analysis as boundary fields. The Reynolds and Smith (1994) SST analysis was used after 1982 when AVHRR data became available and sea ice based on SMMR/SSM/I was used (as well as other non-remote sensing datasets). Another commonly used reanalysis is the European Centre for Medium Range [Weather Forecasting](#) (ECMWF) ERA-40 project which directly assimilated more satellite records than the NCAR/NCEP reanalysis. However, ERA-40 is not available in real time: Analyses from the ECMWF forecast assimilation scheme are available, but the ERA-40 product is not meant for climate monitoring.

The NCAR/NCEP reanalysis starts in 1946, and the ECMWF ERA-40 reanalysis starts in 1958, but much of the satellite data used in both assimilations starts in 1979. This discrepancy has led to discontinuities in the data (Bromwich and Fogt, 2004) which could lead to spurious trend estimates. More recent reanalysis products such as the Japanese JRA-25 (Onogi et al., 2007) and NASA's Modern Era Retrospective Reanalysis (MERRA; <http://gmao.gsfc.nasa.gov/research/merra/>) start in 1979 since remotely sensed observations of the atmosphere make this a far more data-rich period. At present, the ERA-40 reanalysis is not run operationally making it unsuitable for climate monitoring (although the ECMWF

does produce a similar assimilation for their operational model). Additionally, time required for data acquisition and processing make these data unsuitable for some monitoring activities.

### Climate prediction

Whether physically or statistically based, predictions of the weather or climate are usually obtained by propagating a set of initial conditions forward to some given time point. In the case of weather forecasting (typically at scales less than 10 days), the focus is on the prediction of the most likely state (e.g., temperature) and individual weather events (e.g., precipitation) (see *Weather Prediction*). In contrast, climate prediction is focused on prediction of the mean state over the next few months, years, or decades. The bulk of all climate models is intended for prediction of climate change effect at the decadal or century scale (Randall et al., 2007). These models are not explored here, and we instead focus on models for seasonal predictions (between 10 days and several months).

Seasonal climate forecasts are made using one of two distinct approaches. The first is to use a dynamical, numerical model such as that used in operational models (see Goddard et al., 2001, for a review). Such models use a physical-based, dynamical representation of the atmosphere similar to those used for numerical weather forecasting. Forecasts are made by using simplified versions of the basic atmospheric and/or oceanic equations to propagate an initial field, usually based on observations. This initial field is largely based on remotely sensed observations, which are assimilated along with other, in situ observations. Seasonal climate predictions made with dynamical models are traditionally deterministic in nature, meaning that a single (hopefully optimal) answer is obtained. However, it is becoming increasingly common for ensemble approaches to be used whereby multiple realizations of the initial conditions are run through the model to assess the effect of measurement error in the initial conditions on the output. This is particularly useful for climate prediction since errors in the initial conditions are relatively small over a short period, but tend to be amplified for longer forecast lead times, an effect that can lead to forecasts being dominated by noise.

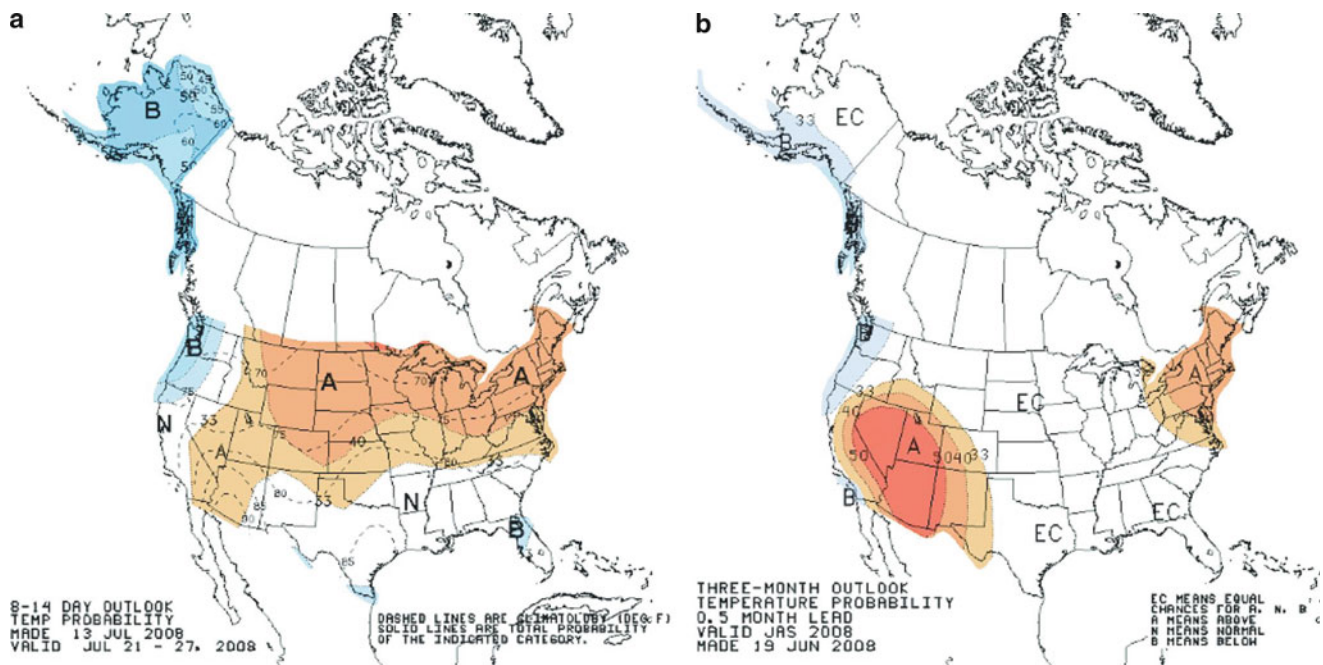
Another difference between weather and climate models is the treatment of the ocean and the inclusion of SSTs, which are intimately linked with atmospheric circulation and weather. SSTs change relatively slowly over time, and these changes are often too slow to make a large difference on weather scales. Weather models therefore tend to use only a dynamical atmosphere with prescribed ocean temperatures which are fixed in time. Within a season, changes in SST become important, and so many climate models (seasonal and decadal) use a dynamical ocean. Since the properties of the ocean and the atmosphere are different, it is common to use separate models and *couple* these models so that information passes between the two at set times. For instance, the ocean model

might be run for a day and then the new values used to update SSTs (or other parameters) for the atmospheric model, which in turn might provide wind estimates for the ocean model. Coupled models are an important tool for seasonal climate prediction that have become widely used at a variety of institutions (Stockdale et al., 1998; Graham et al., 2005; Saha et al., 2006; Luo et al., 2008).

The second commonly used approach for seasonal climate prediction is to use a statistical model to make forecasts based on relationships between some observed data and the quantity to be forecast. Statistical models partition the total variance in the data into that which can be explained by the predictor variables and a residual noise component which is modeled by some assumed error distribution. The advantage to this approach is that a full physical understanding of the system being modeled is not required since any unexplained noise is simply modeled in the residual. In practice, statistical prediction models are constructed by using some set of training parameters to develop a model and estimate the parameters of the model. Estimates of the response data are then generated from this model and standard errors (a measure of how incorrect the estimate is) can be generated based on the assumed distribution of the residual noise. Statistical approaches include a wide range of models from linear regression methods to neural networks and canonical correlation analysis. A common requirement of these models is that a lag relationship be known, whereby the predictors contain information about the future state of the response. Among other sources, climate indices such as ENSO and the North Atlantic Oscillation (NAO) have been found to give this lead information, and the ocean is another common input due to its thermal memory. This provides a logical contrast between statistical and dynamical models: Dynamical models rely on direct knowledge of the climate system to infer its future state, whereas statistical models require no knowledge of the system, instead relying on an indirect relationship between two or more variables.

Remotely sensed products play an important role in seasonal predictions as either a direct input to the models (dynamical or statistical) or in a monitoring capacity where they are used to infer the current mean state of the climate and its most likely tendency. Remotely sensed data is also used in a variety of statistical models. Some examples include models to predict rainfall (Nicholas and Battisti, 2008), SSTs (Landman and Mason, 2001), and prevalence of diseases in humans (Linthicum et al., 1999; Thomson et al., 2005) and plants (Boken et al., 2007). Forecasting of ENSO (Mason and Mimmack, 2002; Coelho et al., 2004) is also important since knowledge of its state helps forecasters infer many other weather characteristics and predictions can be used as the base for other forecasts. Additionally, some statistical models use forecast fields from climate models (which assimilate satellite data) to derive estimates (e.g., Hoshen and Morse, 2004; Thomson et al., 2006).

In practice, information from both statistical and dynamical prediction models is used along with the



**Climate Monitoring and Prediction, Figure 4** CPC probability of above average, below average, or normal temperature for (a) 8–12 days and (b) 3 months for the United States. Downloaded from the NOAA/NCEP/CPC website: <http://www.cpc.ncep.noaa.gov/on> July 14th 2008.

assessment of the current state of the climate system, and seasonal forecast products are usually composites of multiple forecast and monitoring data. As with weather forecasts, a seasonal forecaster usually compiles the information into a single outlook based on the available products and some knowledge of the relative skill of each data source. This final product takes a variety of different forms, although it is common to have separate forecasts for the near and longer term (approximately 10–20 days and 3–6 months, respectively). Each product usually represents a time-integrated product over the period of interest rather than being an instantaneous value for several months time. One example of such a derived product is the CPC temperature probability product shown in Figure 4. Forecasts are shown for 8–12 days and 3 months as a probability of either above/below average or normal rather than an absolute value. Such metrics are common in seasonal climate prediction where the skill is insufficient to give much more than an indication of the likely state of the climate.

## Conclusion

Remote sensing plays a large and varied role in climate monitoring and prediction, providing both the monitoring data and inputs for climate models (statistical or dynamical). At present, our ability to forecast climate is limited by our understanding of the global Earth system and the chaotic nature of the system. While the latter is unlikely to change, it should not be overlooked that current and future research satellite missions have the potential to

improve our understanding and enhance our ability to forecast climate further into the future and with greater accuracy.

## Bibliography

- Adler, R. F., Huffman, G. J., Chang, A., Ferraro, R., Xie, P., Janowiak, J., Rudolf, B., Schneider, U., Curtis, S., Bolvin, D., Gruber, A., Susskind, J., Arkin, P., and Nelkin, E., 2003. The version-2 global precipitation climatology project (GPCP) monthly precipitation analysis (1979-present). *Journal of Hydrometeorology*, **4**(6), 1147–1167.
- Anyamba, A., Linthicum, K. J., Mahoney, R., Tucker, C. J., and Kelley, P. W., 2002. Mapping potential risk of rift valley fever outbreaks in African Savannas using vegetation index time series data. *Photogrammetric Engineering and Remote Sensing*, **68**(2), 137–145.
- Bhartia, P., McPeters, R., Mateer, C., Flynn, L., and Wellemeyer, C., 1996. Algorithm for the estimation of vertical ozone profiles from the backscattered ultraviolet technique. *Journal of Geophysical Research*, **101**(D13), 18793–18806.
- Boken, V. K., Hoogenboom, G., Williams, J. H., Diarra, B., Dione, S., and Easson, G. L., 2007. Monitoring peanut contamination in Mali (Africa) using AVHRR satellite data and a crop simulation model. *International Journal of Remote Sensing*, **29**(1), 117–129.
- Bromwich, D. H., and Fogt, R. L., 2004. Strong trends in the skill of the ERA-40 and NCEP–NCAR reanalyses in the high and midlatitudes of the southern hemisphere, 1958–2001. *Journal of Climate*, **17**, 4603–4619.
- Burrows, J. P., Weber, M., Buchwitz, M., Rozanov, V., Ladstätter-Weißenmayer, A., Richter, A., DeBeek, R., Hoogen, R., Bramstedt, K., Eichmann, K. U., Eisinger, M., and Perner, D., 1999. The global ozone monitoring experiment (GOME):

- mission concept and first scientific results. *Journal of the Atmospheric Sciences*, **56**, 151–175.
- Coelho, C. A. S., Pezzulli, S., Balmaseda, M., Doblas-Reyes, F. J., and Stephenson, D. B., 2004. Forecast calibration and combination: a simple Bayesian approach for ENSO. *Journal of Climate*, **17**, 1504–1516.
- de Toma, G., White, O. R., Chapman, G. A., and Walton, S. R., 2004. Solar irradiance variability: progress in measurement and empirical analysis. *Advances in Space Research*, **34**, 237–242.
- Forster, P., Ramaswamy, V., Artaxo, P., Bernsten, T., Betts, R., Fahey, D. W., Haywood, J., Lean, J., Lowe, D. C., Myhre, G., Nganga, J., Prinn, R., Raga, G., Schulz, M., Van Dorland, R., Ramaswamy, V., Artaxo, P., Bernsten, T., Betts, R., Fahey, D. W., Haywood, J., Lean, J., Lowe, D. C., Myhre, G., Nganga, J., Prinn, R., Raga, G., Schulz, M., and Van Dorland, R., 2007. Changes in atmospheric constituents and in radiative forcing. In Solomon, S., Qin, D., Manning, M., Chen, Z., Marquis, M., Averyt, K. B., Tignor, M., and Miller, H. L. (eds.), *Climate Change 2007: The Physical Science Basis. Contribution of Working Group I to the Fourth Assessment Report of the Intergovernmental Panel on Climate Change*. Cambridge: Cambridge University Press.
- Fröhlich, C., 2007. Solar irradiance variability since 1978. *Space Science Reviews*, **125**(1–4), 53–65.
- Fröhlich, C., and Lean, J., 2004. Solar radiative output and its variability: evidence and mechanisms. *Astronomy and Astrophysics Review*, **12**, 273–320, doi:10.1007/s00159-004-0024-1.
- Goddard, L., Mason, S. J., Zebiak, S. E., Ropelewski, C. F., Basher, R., and Cane, M. A., 2001. Current approaches to seasonal to interannual climate predictions. *International Journal of Climatology*, **21**, 1111–1152.
- Graham, R. J., Gordon, M., Mclean, P. J., Ineson, S., Huddleston, M. R., Davey, M. K., Brookshaw, A., and Barnes, R. T. H., 2005. A performance comparison of coupled and uncoupled versions of the Met Office seasonal prediction general circulation model. *Tellus A*, **57**(3), 320–339.
- Gupta, H., Sorooshian, S., Gao, X., Imam, B., Hsu, K., Bastidas, L., Li, J., and Mahani, S., 2002. The challenge of predicting flash floods from thunderstorm rainfall. *Philosophical Transactions of the Royal Society A: Mathematical, Physical and Engineering Sciences*, **360**(1796), 1363–1371.
- Harris, A., Rahman, S., Hossain, F., Yarborough, L., Bagtzoglou, A. C., and Eason, G., 2007. Satellite-based flood modeling using TRMM-based rainfall products. *Sensors*, **7**, 3416–3427.
- Helfrich, S. R., McNamara, D., Ramsay, B. H., Baldwin, T., and Kasheta, T., 2007. Enhancements to, and forthcoming developments in the interactive multisensor snow and ice mapping system (IMS). *Hydrological Processes*, **21**, 1576–1586.
- Hendrickx, G., Napala, A., Slingenberg, J. H. W., De Deken, R., and Rogers, D. J., 2001. A contribution towards simplifying area-wide Tsetse surveys using medium resolution meteorological satellite data. *Bulletin of Entomological Research*, **91**(5), 333–346.
- Hong, Y., Adler, R., and Huffman, G., 2006. Evaluation of the potential of NASA multi-satellite precipitation analysis in global landslide hazard assessment. *Geophysical Research Letters*, **33**, L22402, doi:10.1029/2006GL028010.
- Hong, Y., Adler, R., and Huffman, G., 2007. An experimental global prediction system for rainfall-triggered landslides using satellite remote sensing and geospatial datasets. *IEEE Transactions on Geoscience and Remote Sensing*, **45**(6), 1671–1680.
- Hoshen, M. B., and Morse, A. P., 2004. A weather-driven model of malaria transmission. *Malaria Journal*, **3**, 32.
- Huffman, G. J., Adler, R. F., Arkin, P. A., Chang, A., Ferraro, R., Gruber, A., Janowiak, J., McNab, A., Rudolf, B., and Schneider, U., 1997. The global precipitation climatology project (GPCP) combined precipitation dataset. *Bulletin of the American Meteorological Society*, **78**(1), 5–20.
- Huffman, G. J., Adler, R. F., Bolvin, D. T., Gu, G., Nelkin, E. J., Bowman, K. P., Hong, Y., Stocker, E. F., and Wolff, D. B., 2007. The TRMM multisatellite precipitation analysis (TMPA): quasi-global, multiyear, combined-sensor precipitation estimates at fine scales. *Journal of Hydrometeorology*, **8**(1), 38–55.
- Iguchi, T., Kozu, T., Meneghini, R., Awaka, J., and Okamoto, K., 2000. Rain-profiling algorithm for the TRMM precipitation radar. *Journal of Applied Meteorology*, **39**, 2038–2052.
- Joyce, R. J., Janowiak, J. E., Arkin, P. A., and Xie, P., 2004. CMORPH: a method that produces global precipitation estimates from passive microwave and infrared data at high spatial and temporal resolution. *Journal of Hydrometeorology*, **5**(3), 487–503.
- Kalnay, E., Kanamitsu, M., Kistler, R., Collins, W., Deaven, D., Gandin, L., Iredell, M., Saha, S., White, G., Woollen, J., Zhu, Y., Leetmaa, A., Reynolds, R., Chelliah, M., Ebisuzaki, W., Higgins, W., Janowiak, J., Mo, K., Ropelewski, C., Wang, J., Jenne, R., and Joseph, D., 1996. The NCEP/NCAR 40-year reanalysis project. *Bulletin of the American Meteorological Society*, **77**, 437–471.
- Kanamitsu, M., Ebisuzaki, W., Woollen, J., Yang, S. K., Hnilo, J. J., Fiorino, M., and Potter, G. L., 2002. NCEP–DOE AMIP-II reanalysis (R-2). *Bulletin of the American Meteorological Society*, **83**, 1631–1643.
- Kummerow, C., Barnes, W., Kozu, T., Shiue, J., and Simpson, J., 1998. The tropical rainfall measuring mission (TRMM) sensor package. *Journal of Atmospheric and Oceanic Technology*, **15**, 809–817.
- Landman, W. A., and Mason, S. J., 2001. Forecasts of near-global Sea surface temperatures using canonical correlation analysis. *Journal of Climate*, **14**, 3819–3833.
- Latif, M., Roeckner, E., Botzet, M., Esch, M., Haak, H., Hagemann, S., Jungclaus, J., Legutke, S., Marsland, S., Mikolajewicz, U., and Mitchell, J., 2004. Reconstructing, monitoring, and predicting multidecadal-scale changes in the North Atlantic thermohaline circulation with Sea surface temperature. *Journal of Climate*, **17**, 1605–1614.
- Lin, Y., and Mitchell, K. E., 2005. The NCEP stage II/IV hourly precipitation analyses: development and applications. In *Preprints, 19th Conference on Hydrology*. San Diego, CA: American Meteorological Society, P1.2.
- Linthicum, K. J., Anyamba, A., Tucker, C. J., Kelley, P. W., Myers, M. F., and Peters, C. J., 1999. Climate and satellite indicators to forecast rift valley fever epidemics in Kenya. *Science*, **285**(5426), 397–400.
- Lobitz, B., Beck, L., Huq, A., Wood, B., Fuchs, G., Faruque, A. S. G., and Colwell, R., 2000. Climate and infectious disease: use of remote sensing for detection of *Vibrio cholerae* by indirect measurement. *Proceedings of the National Academy of Sciences of the United States of America*, **97**(4), 1438–1443.
- Luo, J. J., Masson, S., Behera, S. K., and Yamagata, T., 2008. Extended ENSO predictions using a fully coupled ocean–atmosphere model. *Journal of Climate*, **21**, 84–93.
- Mason, S. J., and Mimmack, G. M., 2002. Comparison of some statistical methods of probabilistic forecasting of ENSO. *Journal of Climate*, **15**, 8–29.
- Maynard, J. A., Turner, P. J., Anthony, K. R. N., Baird, A. H., Berkelmans, R., Eakin, C. M., Johnson, J., Marshall, P. A., Packer, G. R., Rea, A., and Willis, B. L., 2008. ReefTemp: an interactive monitoring system for coral bleaching using high-resolution SST and improved stress predictors. *Geophysical Research Letters*, **35**, L05603, doi:10.1029/2007GL032175.
- Mishchenko, M. I., Cairns, B., Kopp, G., Schueler, C. F., Fafaul, B. A., Hansen, J. E., Hooker, R. J., Itchkawich, T., Maring, H. B., and Travis, L. D., 2007. Accurate monitoring of terrestrial aerosols and total solar irradiance: introducing the glory

- mission. *Bulletin of the American Meteorological Society*, **88**, 677–691.
- Nghiem, S. V., Chao, Y., Neumann, G., Li, P., Perovich, D. K., Street, T., and Clemente-Colón, P., 2006. Depletion of perennial sea ice in the East Arctic Ocean. *Geophysical Research Letters*, **33**, L17501, doi:10.1029/2006GL027198.
- Nicholas, R. E., and Battisti, D. S., 2008. Drought recurrence and seasonal rainfall prediction in the Río Yaqui Basin. *Journal of Applied Meteorology and Climatology*, **47**, 991–1005.
- Onogi, K., Tsutsui, J., Koide, H., Sakamoto, M., Kobayashi, S., Hatsushika, H., Matsumoto, T., Yamazaki, N., Kamahori, H., Takahashi, K., Kadokura, S., Wada, K., Kato, K., Oyama, R., Ose, T., Mannoji, N., and Taira, R., 2007. The JRA-25 reanalysis. *Journal of the Meteorological Society of Japan*, **85**, 369–432.
- Randall, D. A., Wood, R. A., Bony, S., Colman, R., Fichet, T., Fyfe, J., Kattsov, V., Pitman, A., Shukla, J., Srinivasan, J., Stouffer, R. J., Sumi, A., and Taylor, K. E., 2007. Climate models and their evaluation. In Solomon, S., Qin, D., Manning, M., Chen, Z., Marquis, M., Averyt, K. B., Tignor, M., and Miller, H. L. (eds.), *Climate Change 2007: The Physical Science Basis. Contribution of Working Group I to the Fourth Assessment Report of the Intergovernmental Panel on Climate Change*. Cambridge: Cambridge University Press.
- Reynolds, R. W., and Smith, T. M., 1994. Improved global sea surface temperature analyses using optimum interpolation. *Journal of Climate*, **7**, 929–948.
- Reynolds, R. W., Smith, T. M., Liu, C., Chelton, D. B., Casey, K. S., and Schlax, M. G., 2007. Daily high-resolution blended analyses for sea surface temperature. *Journal of Climate*, **20**, 5473–5496.
- Rottman, G., 2006. Measurement of total and spectral solar irradiance. *Space Science Reviews*, **125**(1–4), 39–51.
- Saha, S., Nadiga, S., Thiaw, C., Wang, J., Wang, W., Zhang, Q., Van den Dool, H. M., Pan, H. L., Moorthi, S., Behringer, D., Stokes, D., Peña, M., Lord, S., White, G., Ebisuzaki, W., Peng, P., and Xie, P., 2006. The NCEP climate forecast system. *Journal of Climate*, **19**, 3483–3517.
- Stockdale, T. N., Anderson, D. L. T., Alves, J. O. S., and Balmaseda, M. A., 1998. Global seasonal rainfall forecasts using a coupled ocean–atmosphere model. *Nature*, **392**, 370–373.
- Thomson, M. C., Mason, S. J., Phindela, T., and Connor, S. J., 2005. Use of rainfall and sea surface temperature monitoring for malaria early warning in Botswana. *The American Journal of Tropical Medicine and Hygiene*, **73**(1), 214–221.
- Thomson, M. C., Doblas-Reyes, F. J., Mason, S. J., Hagedorn, R., Connor, S. J., Phindela, T., Morse, A. P., and Palmer, T. N., 2006. Malaria early warnings based on seasonal climate forecasts from multi-model ensembles. *Nature*, **439**(7076), 576–579.
- Tucker, C. J., 1979. Red and photographic infrared linear combinations for monitoring vegetation. *Remote Sensing of Environment*, **8**(2), 127–150.
- Velicogna, I., and Wahr, J., 2006. Acceleration of Greenland ice mass loss in spring 2004. *Nature*, **443**(7109), 329–331.
- Weng, F., Zhao, L., Poe, G., Ferraro, R., Li, X., and Grody, N., 2003. AMSU cloud and precipitation algorithms. *Radio Science*, **338**, 8068–8079.
- Wilheit, T. T., Kummerow, C., and Ferraro, R., 2003. Rainfall algorithms for AMSR-E. *IEEE Transactions on Geoscience and Remote Sensing*, **41**, 204–214.
- WMO (World Meteorological Organization), 2007. *Scientific assessment of ozone depletion: 2006*. Global Ozone Research and Monitoring Project – Report No. 50, Geneva: World Meteorological Organization, 572 pp.
- Woods, T. N., Eparvier, F. G., Fontenla, J., Harder, J., Kopp, G., McClintock, W. E., Rottman, G., Smiley, B., and Snow, M., 2004. Solar irradiance variability during the October 2003 solar storm period. *Geophysical Research Letters*, **31**, L10802, doi:10.1029/2004GL019571.
- Xie, P., and Arkin, P. A., 1997. Global precipitation: a 17-year monthly analysis based on gauge observations, satellite estimates, and numerical model outputs. *Bulletin of the American Meteorological Society*, **78**(11), 2539–2558.

## Cross-references

[Climate Data Records](#)  
[Radiation, Solar and Lunar](#)  
[Sea Surface Temperature](#)  
[Stratospheric Ozone](#)  
[Weather Prediction](#)

---

## CLOUD LIQUID WATER

---

Fuzhong Weng

Center for Satellite Applications and Research (STAR),  
 National Oceanic and Atmospheric Administration,  
 College Park, MD, USA

## Synonyms

CLW; LWP

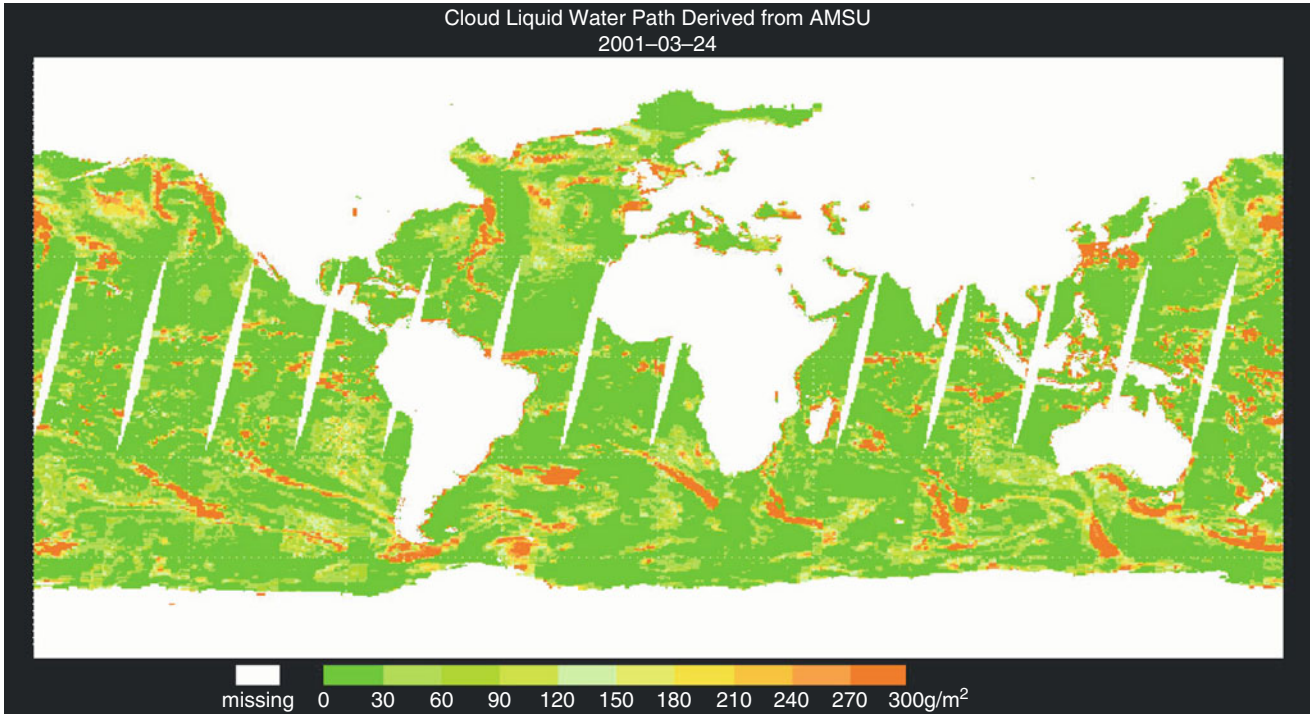
## Definition

Total weight of cloud water in a vertical column of atmosphere for a unit of area.

## Introduction

Clouds play a vital role in modulating climate and the earth's radiation budget. In the atmosphere, the latent heat release or consumption occurs either directly within the clouds or in the precipitation produced from inside the clouds. Clouds strongly affect the radiative fluxes through the atmosphere. Thus, the measurements of hydrometeor variables on clouds in various water phases critically affect the numerical weather prediction (NWP) simulation and climate modeling.

Global measurements of the cloud liquid water path can be determined by satellite-measured microwave brightness temperatures, which quantify the thermal emission of cloud particles. In the early 1970s, the feasibility of the microwave measurement of cloud liquid water was demonstrated by a Nimbus-6 scanning microwave spectrometer. A statistical relationship was first derived between the brightness temperatures at 23 and 31 GHz and cloud liquid water using Nimbus-6 scanning microwave spectrometer data (Grody, 1976). The large-scale distribution of cloud liquid water was obtained over the Pacific Ocean (Grody et al., 1980). This capability was further displayed by Nimbus-7 scanning multichannel microwave radiometer (SMMR) data (Takeda and Liu, 1987). However, more algorithms for cloud liquid water were developed for the Special Sensor Microwave Imager (SSM/I) flown on the defense meteorological



**Cloud Liquid Water, Figure 1** Global cloud liquid water retrieved from NOAA-15 Advanced Microwave Sounding Unit (AMSU). Only satellite descending node data are used in this retrieval. Land and sea ice areas are shown as missing because of the incapability of calculating surface emissivity.

satellite program (e.g., Alishouse et al., 1990; Greenwald et al., 1993; Liu and Curry, 1993; Weng and Grody, 1994; Wentz, 1997). The algorithm was further refined for Advanced Microwave Sounding Unit (AMSU) measurements at 23.8, 31.4 GHz (Weng et al., 2003).

### Algorithm theoretical database

Cloud liquid water is also referred as the liquid water path. It can be measured from both passive and active remote sensing technology deployed in space and on the ground. From satellites, brightness temperatures at lower microwave frequencies directly respond to the emission signals from clouds and raindrops. Over oceans, the brightness temperatures first increase and then become saturated and decrease as cloud liquid water increases. The nonlinear response is a result of emission and scattering from both small cloud droplets and large raindrops. The saturation point normally varies with frequency and is, for example, 8, 3, and 1 kg/m<sup>2</sup> (mm) at 10.65, 18.7, and 36.5 GHz, respectively, for a typical warm rain situation. Since the actual liquid water path ranges within several millimeters, it is necessary to use a composite algorithm (Weng and Grody, 1994) to retrieve cloud liquid water to cover the range from non-raining to raining clouds.

In the absence of scattering from precipitation, brightness temperature at a microwave frequency can be derived as the function (Weng et al., 2003):

$$TB = T_s [1 - (1 - \varepsilon)T^2], \quad (1)$$

where  $\varepsilon$  and  $T_s$  are the surface emissivity and surface temperature, respectively, and the atmospheric transmittance is:

$$T = \exp[-(\tau_o + \tau_v + \tau_l)/\mu], \quad (2)$$

where  $\tau_o$  is the optical thicknesses of oxygen. The optical thicknesses of cloud and water vapor are expressed as  $\tau_L = \kappa_l L$  and  $\tau_v = \kappa_v V$ , respectively, where the liquid water path is  $L = \int_0^{\infty} w(z) dz$  and the water vapor path is  $V = \int_0^{\infty} \rho_v dz$ . The cloud mass absorption

coefficient  $\kappa_l$  is approximated as  $\kappa_l = \frac{6\pi}{\lambda \rho_w} \text{Im} \left\{ \frac{m^2 - 1}{m^2 + 2} \right\}$  through Rayleigh's approximation.

Equation 1 provides a fundamental theory for microwave remote sensing of both atmospheric liquid water and water vapor from space over oceanic conditions. In general, at least two frequencies are required, with one being more sensitive to liquid and the other to water vapor. Note that for land conditions

where the emissivity is normally high (typically greater than 0.9), brightness temperature decreases as cloud liquid water increases. The depression from non-raining clouds is also typically very small, less than several degrees Kelvin. Thus, it is difficult to detect the liquid-phase clouds over land where its emissivity is high and variable.

Using two channel measurements at 23.8 and 31.4 GHz from the Advanced Microwave Sounding Unit (AMSU),  $TB_{23}$  and  $TB_{31}$ , Weng et al. (2003) derived

$$V = a_0\mu[\ln(T_s - TB_{31}) - a_1 \ln(T_s - TB_{23}) - a_2], \quad (3)$$

and

$$V = b_0\mu[\ln(T_s - TB_{31}) - b_1 \ln(T_s - TB_{23}) - b_2], \quad (4)$$

respectively, where the coefficients,  $a_0$  and  $b_0$ , are functions of cloud and water vapor mass absorption coefficients, and  $a_{1,2}$  and  $b_{1,2}$  are functions of surface emissivity and surface temperature, respectively.

The figure below displays a global distribution of cloud liquid water over oceans derived from the use of the AMSU 23.8 and 31.4 GHz measurements. Note that the AMSU measurements during a 24 h period from its descending node do not completely cover the globe because of the presence of orbital gaps. Also, the retrievals are not performed over land, snow, and sea ice conditions due to large emissivity variations. The unit of cloud liquid water is  $\text{g/m}^2$ . Note that low clouds over oceans to the west coast of South America are detected very well and their liquid water path is on the order of  $100 \text{ g/m}^2$ . The weather systems having relatively high amount of cloud liquid water are associated with those frontal systems and the clouds within the inter-tropical convergence zone (ITCZ) (Fig. 1).

## Summary

Satellite passive microwave measurements provide accurate retrievals of cloud liquid water over oceans. It still remains difficult to retrieve cloud liquid water over land from the emission-based algorithms. Further studies will focus on extending the retrievals with more advanced radiative transfer schemes that include scattering from clouds and precipitation. Also, different algorithms should be developed for high and variable emissivity conditions which are typical of land, snow, and sea ice conditions.

## Bibliography

- Alishouse, J. C., Alishouse, J. C., Snider, J. B., Westwater, E. R., Swift, C. T., Ruf, C. S., Snyder, S. A., Vongsathorn, J., and Ferraro, R. R., 1990. Determination of cloud liquid water content using the SSM/I. *IEEE Transactions on Geoscience and Remote Sensing*, **28**, 817–822.
- Greenwald, T. J., Stephens, G. L., and Vonder Haar, T. H., 1993. A physical retrieval of cloud liquid water over the global oceans using special sensor microwave/imager (SSM/I) observations. *Journal of Geophysical Research*, **98**, 18471–18488.
- Grody, N. C., 1976. Remote sensing of atmospheric water content from satellite using microwave radiometry. *IEEE Transactions on Antennas and Propagation*, **24**, 155–162.

- Grody, N. C., Gruber, A., and Shen, W. C., 1980. Atmospheric water content over tropical Pacific derived from the Nimbus-5 Scanner Radiometry. *Journal of Applied Meteorology*, **8**, 986–996.
- Liljegren, J. C., Clothiaux, E. E., Mace, G. G., Mace, G. G., Kato, S., and Dong, X., 2001. A new retrieval of cloud liquid water path using a ground-based microwave radiometer and measurements of cloud temperature. *Journal of Geophysical Research*, **106**, 14485–14500.
- Liu, G., and Curry, J. A., 1993. Determination of characteristic features of cloud liquid water from satellite microwave measurements. *Journal of Geophysical Research*, **98**, 5069–5092.
- Takeda, T., and Liu, G., 1987. Estimation of atmospheric liquid water amount by Nimbus 7 SMMR data: a new method and its application to the western north Pacific region. *Journal of the Meteorological Society of Japan*, **65**, 931–946.
- Weng, F., and Grody, N. C., 1994. Retrieval of cloud liquid water over oceans using special sensor microwave imager (SSM/I). *Journal of Geophysical Research*, **99**, 25535–25551.
- Weng, F., Zhao, L., Ferraro, R., Poe, G., Li, X., and Grody, N., 2003. Advanced microwave sounding unit cloud and precipitation algorithms. *Radio Science*, **38**, 8086–8096.
- Wentz, F. J., 1997. A well-calibrated ocean algorithm for special sensor microwave/imager. *Journal of Geophysical Research*, **102**, 8703–8718.

---

## CLOUD PROPERTIES

---

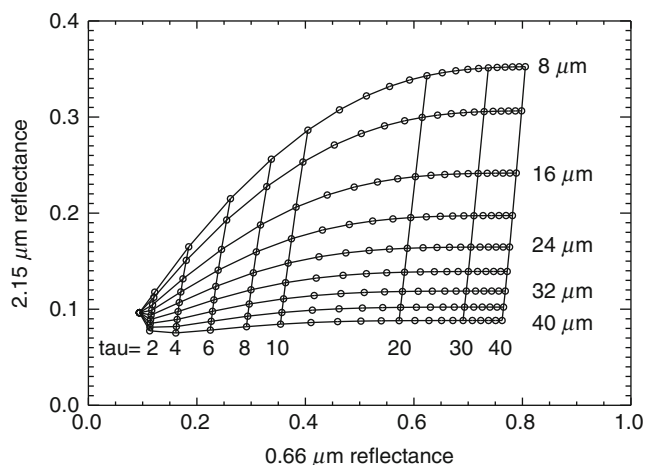
Matthew Lebsock and Steve Cooper  
Jet Propulsion Laboratory, California Institute of  
Technology, Pasadena, CA, USA

## Definitions

- Droplet size distribution.* The number distribution of water droplets as a function of droplet size.
- Cloud optical depth.* A unitless measure of the column integrated radiative extinction of a cloud.
- Water content.* The liquid or ice water content of an atmospheric volume.
- Water path.* The vertical integral of the cloud water content.
- Droplet number concentration.* The number of droplets within an atmospheric volume.
- Droplet effective radius.* A characteristic droplet size defined as the third moment of the droplet size distribution divided by the second moment.
- Radar.* Radio detection and ranging.
- Lidar.* Light detection and ranging.
- Polarization.* A property of electromagnetic radiation that describes the orientation and phase of its oscillations.
- Brightness temperature.* The blackbody temperature that is inferred from a measured spectral intensity.

## Introduction

This entry reviews common remote sensing methods to infer cloud properties. Knowledge of cloud properties is of primary interest because they (1) have a large influence on the reflection and absorption properties of the



**Cloud Properties, Figure 1** Relationship between visible  $0.66\ \mu\text{m}$  and near-infrared  $2.15\ \mu\text{m}$  reflectances for water clouds with optical depths ranging from 0 to 40 and effective radii ranging from 8 to  $40\ \mu\text{m}$  for a case with overhead sun and nadir viewing angle.

atmosphere, thus having a profound effect on the Earth's energy balance, and (2) are related to the turbulent and microphysical processes that govern the lifecycle of clouds and the formation of rainfall, thus influencing the cycling of water within the Earth system.

The overarching goal of cloud property remote sensing is to characterize the droplet size distribution of a cloud. The droplet size distribution is highly variable in space and time, and it is therefore common to approximate its character by the integrated water content and the droplet effective radius, which can then be related to analytic functions such as the log-normal distribution or the gamma distribution. The focus here is on satellite remote sensing of cloud microphysical properties; however, it is noted that similar techniques are used to infer cloud properties from ground-based and airborne platforms as well.

### Visible and near-infrared techniques

Visible and near-infrared techniques have been developed to simultaneously estimate the cloud optical depth and droplet effective radius from measurements of reflected sunlight in a visible and near-infrared channel (Nakajima and King, 1990). The physical basis for these methods lies in the fact that reflected visible radiation is primarily sensitive to the cloud optical depth, whereas the reflection of near-infrared radiation is largely sensitive to the droplet effective radius. Figure 1 shows an example of these dependencies for liquid clouds. Increasing reflectance in the visible channel corresponds to increasing cloud optical depth, whereas increasing reflectance in the near-infrared channel corresponds to decreasing cloud effective radius. The cloud liquid water path may then be derived from the cloud optical depth and effective radius (Stephens, 1978). Analogous methods are used for the

remote sensing of ice clouds. The visible and near-infrared methods are typified by the MODerate resolution Imaging Spectroradiometer (MODIS) cloud retrievals (Platnick et al., 2003). A notable limitation of visible and near-infrared methods is that they rely on reflected sunlight and therefore may only be performed during sunlit hours.

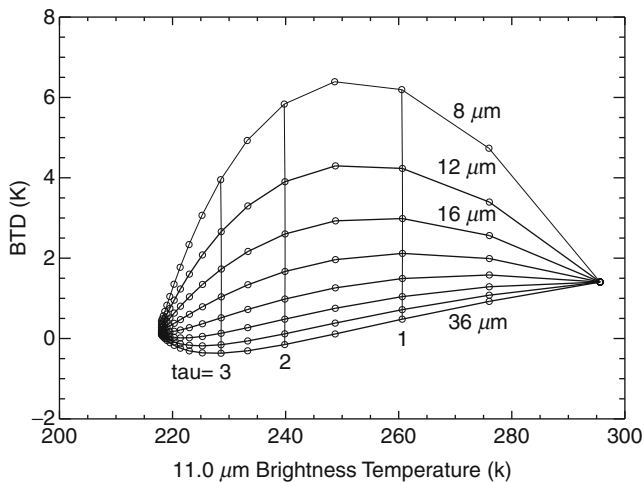
### Microwave techniques

Passive measurements of microwave brightness temperatures have been used to estimate the cloud water path, thus providing a useful integral constraint on the vertical distribution of liquid water content. The physics governing these measurements is that at microwave frequencies, the emission by cloud water may be approximated by the Rayleigh limit (Greenwald, 2009), under which emission is linearly related to cloud water mass. Channels centered near 37 GHz demonstrate the largest signal-to-noise characteristics and dynamic range for the remote sensing of cloud liquid water.

A complication of passive microwave techniques is that the brightness temperatures are also sensitive to the atmospheric temperature and water vapor content as well as the surface temperature and emissivity. Sensitivity to these parameters varies with frequency and measurement polarization. Therefore, passive microwave satellite instruments generally make observations at several frequencies and polarization states, allowing for the simultaneous determination of these properties. The algorithm of Hilburn and Wentz (2008) typifies this approach. A further complication of passive microwave estimates of cloud water path is that they are only possible over oceanic backgrounds where the surface emission is small. The emission from land surfaces is generally large and dominates the much smaller atmospheric emission signal.

### Infrared techniques

An infrared method known as the split-window technique exploits differences in radiative properties of cloud particles at two wavelengths in the atmospheric window to estimate ice cloud properties from satellite-observed brightness temperatures. Small particles less than about  $30\ \mu\text{m}$ , for example, absorb radiation more efficiently at a wavelength of  $12\ \mu\text{m}$  than at  $11\ \mu\text{m}$ . Clouds composed of small particles therefore appear colder at  $12\ \mu\text{m}$  than at  $11\ \mu\text{m}$  from a satellite perspective. Such radiometric signatures were first exploited by Inoue (1985) to detect thin cirrus. Since the ratio of absorption at the two wavelengths is a function of particle size, the technique can also be used to infer cloud effective radius from the brightness temperature difference ( $\Delta T_b$ ) between the two wavelengths (Prabhakara et al., 1988). Infrared radiative transfer (see entry *Radiative Transfer, Theory*) calculations for a set of cloud properties resemble an “arch,” as seen in Figure 2. The right foot of the arch corresponds to the clear-sky emitting temperature of the atmosphere, while the left foot represents an optically thick cloud where observed brightness temperatures approach the



**Cloud Properties, Figure 2** Relationship between TB ( $11\ \mu\text{m}$ ) and BT $\Delta$  ( $11\text{--}12\ \mu\text{m}$ ) for cirrus clouds with optical depths ranging from 0 to 10 and effective radii ranging from 8 to  $32\ \mu\text{m}$ . The clouds are composed of randomly oriented randomized hexagonal ice aggregates (Baran et al., 2003) and have a temperature of 217 K.

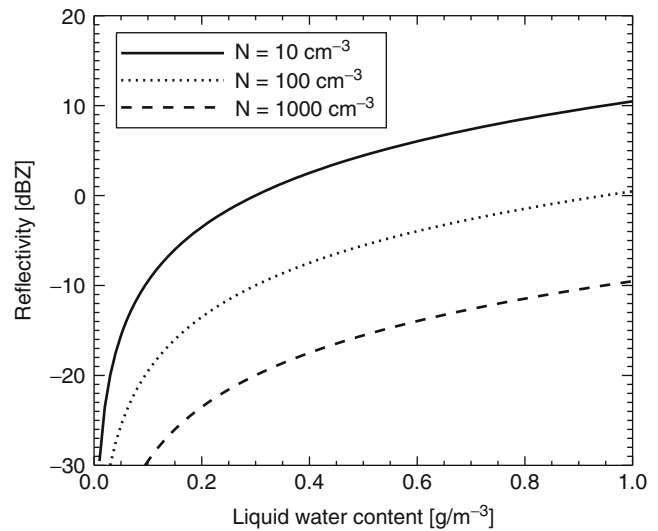
cloud thermodynamic temperature. Intermediate values provide information on cloud properties. Cloud optical depth is found from  $T_{b11}$  along the x-axis and cloud effective radius from  $\Delta T_b$  along the y-axis. Since the technique has sensitivities limited to thin clouds and small particles, it has been applied infrequently at the operational scale. Heidinger and Pavolonis (2009), however, produced a global, multi-decadal set of cloud properties from the split-window technique based upon the AVHRR Pathfinder Atmospheres Extended dataset.

### Visible polarization techniques

The polarization state of reflected visible radiation can be used to determine the effective radius of liquid clouds (Bréon and Goloub, 1998). The physical basis for this technique lies in the observation that at scattering angles between  $150^\circ$  and  $170^\circ$  liquid clouds produce cloud-bow features in the polarized reflection. The angular and spectral characteristics of these cloud-bows may be used to determine the liquid cloud effective radius quite accurately. Use of this technique is limited to sunlit hours over large homogenous cloud layers and is therefore not globally applicable. Despite its limited applicability, it has been used to identify high biases of approximately  $2\ \mu$  in effective radius estimates from the less accurate visible and near-infrared techniques (Bréon and Doutriaux-Boucher, 2005).

### Active techniques

The successful flight of the CloudSat cloud profiling radar and the CALIOP lidar has permitted active techniques for the remote sensing of cloud properties from space. These instruments transmit discrete pulses of radiation and then



**Cloud Properties, Figure 3** Theoretical relationship between liquid water content and reflectivity for three different values of number concentration ( $N$ ) using the equations of Matrosov et al. (2004).

measure the backscattered signal as a function of time from transmission resulting in a vertical profile of backscattered reflectivity. A major advantage of active methods over passive methods is that they provide precise cloud boundaries and observed vertical profiles of the cloud microphysical quantities.

Radar profiling of cloud water content relies on either physical or empirical relationships between the cloud water content or cloud effective radius and the backscattered reflectivity that take the form of a power law (Matrosov et al., 2004). Figure 3 shows some relationships between reflectivity and cloud water content. Note the wide distribution of relationships between the cloud water content and the reflectivity, which results in a large uncertainty in the cloud property retrievals without the addition of an integral constraint. Integral constraints that have been proposed include the cloud optical depth (Austin and Stephens, 2001) or an ancillary passive microwave observation (Dong and Mace, 2003).

Detection of clouds with cloud radar is limited by the radar minimum detectable signal. Clouds that are too thin or composed of small droplets can create reflectivities that lie below the minimum detectable signal. However, the strong lidar backscattering signal permits detection of these clouds. This situation is particularly common with thin cirrus and stratus clouds. Methods analogous to those using radar have been developed to estimate ice cloud microphysical properties from the lidar backscatter when the radar signal falls below the minimum detectable signal (Delanoé and Hogan, 2008). These lidar methods are not feasible for water clouds because of the strong attenuation of the lidar beam by liquid water.

## Summary

This entry reviews the primary methods by which cloud microphysical properties have been estimated from satellite remote sensing. The common methods covered include visible and near-infrared, passive microwave, infrared, visible polarization, and active techniques. Each of these techniques has their own strengths and weaknesses and offers a unique piece of information regarding cloud properties. A topic of current research in cloud remote sensing is understanding the synergies between these various methods and determining how they might best be combined to more accurately estimate cloud properties.

## Acknowledgments

This research was carried out at the Jet Propulsion Laboratory, California Institute of Technology, under a contract with the NASA.

## Bibliography

- Austin, R. T., and Stephens, G. L., 2001. Retrieval of stratus cloud microphysical parameters using millimeter-wave radar and visible optical depth in preparation for CloudSat 1. Algorithm formulation. *Journal of Geophysical Research*, **106** (D22), 28233–28242.
- Baran, A., Havemann, S., Francis, P., and Watts, P., 2003. A consistent set of single-scattering properties for cirrus cloud: tests using radiance measurements from a dual-viewing multi-wavelength satellite-based instrument. *Journal of Quantitative Spectroscopy and Radiative Transfer*, **79**, 549–567.
- Bréon, F.-M., and Doutriaux-Boucher, M., 2005. A comparison of cloud droplet radii measured from space. *IEEE Transactions on Geoscience and Remote Sensing*, **43**(8), 1796–1805.
- Bréon, F., and Goloub, P., 1998. Cloud droplet effective radius from spaceborne polarization measurements. *Geophysical Research Letters*, **25**(11), 1879–1882.
- Delanoë, J., and Hogan, R. J., 2008. A variational scheme for retrieving ice cloud properties from combined radar, lidar, and infrared radiometer. *Journal of Geophysical Research*, **113**, D07204, doi:10.1029/2007JD009000.
- Dong, X., and Mace, G. G., 2003. Profiles of low-level stratus cloud microphysics deduced from ground-based measurements. *Journal of Atmospheric and Oceanic Technology*, **20**, 42–53.
- Greenwald, T. J., 2009. A 2 year comparison of AMSR-E and MODIS cloud liquid water path observations. *Geophysical Research Letters*, **36**, L20805.
- Heidinger, A. K., and Pavolonis, M. J., 2009. Gazing at cirrus clouds for 25 years through a split window. Part I: methodology. *Journal of Applied Meteorology and Climatology*, **48**, 1100–1116.
- Hilburn, K. A., and Wentz, F. J., 2008. Intercalibrated passive microwave rain products from the unified microwave ocean retrieval algorithm (UMORA). *Journal of Applied Meteorology and Climatology*, **47**, 778–794.
- Inoue, T., 1985. On the temperature and effective emissivity determination of semi-transparent cirrus clouds by bispectral measurements in the 10 micron window region. *Journal of the Meteorological Society of Japan*, **63**, 88–99.
- Matrosov, S. Y., Uttal, T., and Hazen, D. A., 2004. Evaluation of radar reflectivity-based estimates of water content in stratiform marine clouds. *Journal of Applied Meteorology*, **43**, 405–419.
- Nakajima, T., and King, M. D., 1990. Determination of the optical thickness and effective particle radius of clouds from reflected

solar radiation measurements. Part I: theory. *Journal of the Atmospheric Sciences*, **47**, 1878–1893.

- Platnick, S., King, M. D., Ackerman, S. A., Menzel, W. P., Baum, B. A., Riedi, J. C., and Frey, R. A., 2003. The MODIS cloud products: algorithms and examples from Terra. *IEEE Transactions on Geoscience and Remote Sensing*, **41**, 459–473.
- Prabhakara, C., Fraser, R. S., Dalu, G., Wu, M. C., Curran, R. J., and Styles, T., 1988. Thin cirrus clouds: seasonal distribution over oceans deduced from nimbus-4 IRIS. *Journal of Applied Meteorology*, **27**, 379–399.
- Stephens, G., 1978. Radiation profiles in extended water clouds. II: parameterization schemes. *Journal of Atmospheric Sciences*, **35**, 2123–2132.

## Cross-references

[Cloud Liquid Water](#)  
[Lidar Systems](#)  
[Microwave Radiometers](#)  
[Radars](#)  
[Rainfall](#)  
[Reflected Solar Radiation Sensors, Polarimetric](#)  
[Water Vapor](#)

---

## COASTAL ECOSYSTEMS

---

Xiaojun Yang  
 Department of Geography, Florida State University,  
 Tallahassee, FL, USA

## Synonyms

Coastal zone; Littoral ecosystems

## Definition

Coastal ecosystems are typically found at a physical region extending from the edge of the continental shelf to the intertidal and nearshore terrestrial area. They include saline, brackish, and freshwaters, as well as coastlines and the adjacent lands that can extend to the entire coastal watershed. Globally, coastal ecosystems comprise a wide array of nearshore terrestrial, intertidal, benthic, and pelagic marine ecosystems.

## Introduction

Coastal ecosystems, by virtue of their position at the interface between truly terrestrial and oceanic ecosystems, belong to the most dynamic and productive ecosystems on Earth. They are among the most important ecosystems, providing numerous ecological, economic, cultural, and aesthetic benefits and services. Although they comprise only 20 % of all land area, coastal areas are now the home of nearly half of the global population (Burke et al., 2001). Increased coastal population and intense development threaten and degrade global coastal ecosystems, placing an elevated burden on organizations responsible for the planning and management of these sensitive areas (Hinrichsen, 1998; Hobbie, 2000; National Research Council, 2000; Selman et al., 2008).

Coastal ecosystem management involves the procedure of monitoring which is based on a reliable information base. Conventional field-based mapping methods are still vital but often logistically constrained. Because of cost-effectiveness and technological soundness, remote sensing has increasingly been used to develop useful sources of information supporting decision making for various coastal applications (e.g., Yang et al., 1999; Yang, 2005a, b, 2008, 2009a, b). But coastal environments challenge the applicability and robustness of remote sensing because they exhibit extreme variations in spatial complexity and temporal variability (Klemas, 2009). Encouragingly, recent innovations in data, technologies, and theories in the wider arena of remote sensing have provided scientists with invaluable opportunities to advance the studies on coastal environments.

Given the above context, this entry will review several major types of coastal ecosystems, followed by a discussion on how remote sensing can be used to characterize coastal waters, submerged aquatic vegetation, benthic habitats, coastal wetlands, and watersheds. It will finally highlight several areas that need further research and development.

### Major coastal ecosystems

Comprehensive reviews on various coastal ecosystem types are given elsewhere (e.g., Mann, 2000; Beatley et al., 2002). Our current discussion targets several types of coastal ecosystems including estuaries, benthic systems, sea grass systems, coastal marshes, and mangroves, because they have been extensively studied by remote sensing. Note that these ecosystems are largely recognized according to the main primary producer with the exception of estuaries. As a rather large ecosystem, estuaries can include the other four as subsystems, but the latter may also occur outside an estuary.

Estuaries are partially enclosed bodies of coastal waters typically found where freshwater from rivers meet with saltwater from the ocean. They are often known as bays, lagoons, harbors, inlets, sounds, or fjords. Estuaries are important ecosystems, providing goods and services that are ecologically, economically, and culturally indispensable. Ecologically, estuaries are not only the “nurseries of the sea,” providing habitats for many marine organisms, but also serve as a natural buffer that filters out much of the sediments and pollutants carried in by terrestrial runoff, creating cleaner water that eventually benefits both human and marine life. Economically, estuaries support significant fisheries, tourism, and other commercial activities and the development of important public infrastructure, such as harbors and ports. Culturally, estuaries are often the focal points for recreation, commerce, scientific research and education, and aesthetic enjoyment.

The benthic system is the community of organisms living on the bottom of oceans in areas not colonized by macrophytes (Mann, 2000). Benthic habitats are virtually bottom environments with distinct physical, chemical, and

biological characteristics. They vary widely depending upon their location, depth, salinity, and sediment. Benthic habitats in areas with depth greater than 200 m have been much less commonly observed and mapped. Estuarine and nearshore benthic habitats can be highly diverse, including submerged mudflats, rippled sand flats, rocky hard-bottom habitats, shellfish beds, and coral reefs. Note that sea grass beds can be described as a benthic system, but they are treated separately (see above). In terms of ecological functioning, the benthic system serves as the site of nutrient regeneration and the site of considerable secondary production that is utilized by important predators, such as bottom-feeding fish and crustaceans (Mann, 2000).

Sea grass are aquatic flowering plants that live fully submerged in the saline coastal environment and are also called “submerged aquatic vegetation.” Sea grass can form extensive beds or meadows, dominated by one or more species. They are distributed worldwide in soft sediments from mean low tide level to the depth limit determined by the penetration of light that permits sea grass plants to photosynthesize. Sea grass beds are a highly diverse and productive ecosystem, and they almost always support more invertebrates and fish than the adjacent areas lacking sea grass (Mann, 2000). Sea grass beds provide coastal zones with a number of ecosystem goods and services, such as fishing grounds, wave protection, oxygen production, and protection against coastal erosion.

Coastal marshes are predominately grasslands that are periodically flooded by tides in the intertidal regions. The salinity from salt or brackish tidal waters creates a salt-stressed aquatic environment where halophytic plants thrive. Coastal marshes may be classified as salt marshes, brackish marshes, and freshwater tidal marshes. They may be associated with estuaries and are also along waterways between coastal barrier islands and the inner coast. Coastal marshes are of great ecological values because they serve as the nursery grounds for fish, habitats for a wide variety of wildlife, and the buffer zones to protect water quality.

The mangrove ecosystem is commonly found in tropical and subtropical tidelands throughout the world. The mangrove family of plants dominates this coastal wetland ecosystem due to their ability to thrive in the saline coastal environment. The three mangrove species commonly grown in the USA are red, black, and white mangroves. The term “mangroves” can narrowly refer to these species but most commonly refers to the habitat and entire plant assemblages. Because mangroves are constantly replenished with nutrients, they sustain a huge population of organisms that in turn feed fish and shrimp, which further support a variety of wildlife; their physical stability helps prevent shoreline erosion, shielding inland areas from damage during severe storms and waves.

### Remote sensing of coastal ecosystems

Modern remote sensing technology began with the invention of the camera more than one century ago, and by now, a large number of remote sensing systems have

**Coastal Ecosystems, Table 1** Characteristics of selected current and future satellite remote sensing systems relevant to coastal environments

Satellite/sensor	Date launched or planned	Spectral range and bands	Spatial resolution	Radiometric resolution (bit)	Revisit (day)	Swath width (km)	Specific coastal applications
OrbView-2/SeaWiFS	1 August 1997	0.402–0.885 $\mu\text{m}$ 8 bands	1.1 km	10	1	2,800	Ocean color, phytoplankton, ocean carbon cycle
ENVISAT/MERIS	1 March 2002	0.390–1.040 $\mu\text{m}$ 15 bands	300–1,200 m	12	3	1,150	Ocean color, phytoplankton, turbidity, sediment, red tides, vegetation
KOMPSAT-1/OSMI	20 December 1999	0.400–0.900 $\mu\text{m}$ 6 bands	850 m	10	2	800	Ocean color, phytoplankton, turbidity
Terra–Aqua/MODIS	18 December 1999 (Terra) 4 May 2002 (Aqua)	0.405–14.385 $\mu\text{m}$ 16 bands	250–1,000 m	12	1	2,330	Sea surface temperature, ocean color, phytoplankton, turbidity, circulation, land cover and vegetation
NOAA POES (NOAA-14 to 18)/AVHRR	30 December 1994 (14) 13 May 1998 (15) 21 September 2000 (16) 24 June 2002 (17) 20 May 2005 (18) 21 November 2000	0.580–12.500 $\mu\text{m}$ 6 bands	1.1 km	10	0.5–1	2,400	Sea surface temperature, turbidity, circulation, land cover and vegetation
EO-1/Hyperion	October 28, 2011	0.400–2.40 $\mu\text{m}$ 220 bands	30 m	16	16	7.5 $\times$ 180	Bathymetry, vegetation, littoral processes
Suomi-NPP/VIIRS	October 28, 2011 (S-NPP)	0.412–12.013 $\mu\text{m}$ 22 bands	370–740 m	12–14	0.5–1	3,000	Ocean color, sea surface temperature, vegetation
GMES-Sentinel-3/OLCI	2014	0.390–1.040 $\mu\text{m}$ 21 bands	300–1200 m	12	2	1,250	Ocean color, sea surface temperature, sea surface topography
Landsat TM/ETM+	16 July 1982 (Landsat 4) 1 March 1984 (Landsat 5) 15 April 1999 (Landsat 7)	0.450–2.350 $\mu\text{m}$ 7 bands (TM) 8 bands (ETM+)	30–120 m (TM) 15–60 m (ETM+)	8	16	185	Bathymetry, water turbidity, littoral processes, land cover and vegetation
SPOT/HRVIR	24 March 1998 (SPOT 4) 4 May 2002 (SPOT 5)	0.500–1.750 $\mu\text{m}$ 5 bands	2.5–20 m	8	1–4	60	Bathymetry, littoral processes, land cover and vegetation, topography

Coastal Ecosystems, Table 1 (Continued)

Satellite/sensor	Date launched or planned	Spectral range and bands	Spatial resolution	Radiometric resolution (bit)	Revisit (day)	Swath width (km)	Specific coastal applications
IRS-1D/LISS	29 September 1997	0.520–1.700 $\mu\text{m}$ 5 bands	5.2–23.5 m	8	24	70–148	Bathymetry, littoral processes, land cover and vegetation
Terra/ASTER	18 December 1999	0.520–11.65 $\mu\text{m}$ 14 bands	15–90 m	8–12	16	60	Littoral processes, sea/land surface temperature, land cover and vegetation
IKONOS	24 September 1999	0.450–0.900 $\mu\text{m}$ 5 bands	1–4 m	11	3–5	11	Bathymetry, water turbidity, littoral processes, land cover and vegetation, topography
QuickBird	18 October 2001	0.450–0.900 $\mu\text{m}$ 5 bands	0.61–2.44 m	11	1–5	20–40	Bathymetry, littoral processes, land cover and vegetation, topography
OrbView-3	26 January 2003	0.450–0.900 $\mu\text{m}$ 5 bands	1–4 m	11	<3	8	Bathymetry, littoral processes, land cover and vegetation, topography
GeoEye-1	6 September 2008	0.450–0.920 $\mu\text{m}$ 5 bands	0.41–1.65 m	11	<3	15.2	Bathymetry, littoral processes, land cover and vegetation, topography
RADARSAT/SAR	4 November 1995 (RADARSAT-1) 14 December 2007 (RADARSAT-2)	C-band HH pol (RADARSAT-1) C-band HH, VV, VH, HV (RADARSAT-2)	6–100 m (RADARSAT-1) 3–100 m (RADARSAT-2)	16	1–4	20–500	Bathymetry, littoral processes, land cover and vegetation, topography
ENVISAT/ASAR	1 March 2002	C-band VV, HH, VV/ HH, HV/HH, VH/VV	30 m	8	<3	50–100	Ocean currents and waves, land topography

been developed to measure energy patterns from different portions of the electromagnetic spectrum (see Jensen, 2007). Many such systems have been originally designed for terrestrial or open-ocean applications, among which some are relevant to coastal environments (Table 1). The following sections will provide an overview on remote sensing of coastal waters, submerged aquatic vegetation, benthic habitats, coastal wetlands, and watersheds. Note that for each application, acquiring accurate and consistent in situ data using ships, buoys, and field instruments is needed in the calibration and validation of remote signals and in algorithm development.

Remote sensing of coastal water quality indicators, such as chlorophyll-*a*, turbidity, dissolved organic matter (DOM), total nitrogen, temperature, and salinity, relies on the use of either a radiative transfer (see entry *Radiative Transfer, Theory*) algorithm or a statistical regression model. Airborne remote sensing systems are most useful for small, shallow, or optically complex coastal waters. Several existing spaceborne color scanners primarily designed for open oceans are of limited usefulness for nearshore coastal waters due to their relatively coarse spatial resolutions. Some researchers have been successful in remote sensing of nearshore coastal and estuarine waters by using satellite data from terrestrial sensors, such as Multispectral Scanner (MSS), Thematic Mapper (TM), Thematic Mapper Plus (ETM+), SPOT HRV, IKONOS, and QuickBird (see Yang, 2005b, 2008, 2009a, b). Compared to multispectral radiometers, hyperspectral sensors offer extremely high spectral resolution that can help discriminate complex bio-optical properties of coastal waters.

Mapping benthic habitats and submerged aquatic vegetation (SAV) can be accomplished through image interpretation or automated classification. The image interpretation approach is particularly suitable for aerial photography or high-resolution satellite imagery. It is based on the synthetic use of various image elements such as tone, pattern, texture, shape, size, and association in the identification and delineation. Individual benthic habitats or SAV polygons can be delineated manually or through an on-screen digitizer. Some field samples obtained through various instruments such as underwater video and still photography are needed to help develop image interpretation keys and verify the mapping accuracy. This image interpretation method can produce accurate results although it is quite labor intensive and highly dependent upon the skills and experience of an interpreter. On the other hand, there are various image classification methods, either supervised or unsupervised, which can be used for benthic habitat or SAV mapping. Image fusion from high-spectral- and high-spatial-resolution sensors can help improve the accuracy of benthic habitat or SAV mapping (Mishra, 2009). Change-detection analysis of benthic habitat or SAV can be made by using change vector analysis, principal component analysis, or map-to-map comparison.

Remote sensing has been used in wetland (including mangroves) mapping for several decades. Early inventories were largely based on the interpretation of aerial

photographs. Automated classification of satellite imagery facilitates the mapping of the spatial distribution of wetlands and the estimation of biomass or net productivity over a large area. Under unfavorable weather conditions, microwave or radar products can be used to help identify broad wetland classes. For species differentiation of wetland plants, broadband remote sensors may be problematic due to their inability to provide sufficient spectral details. Hyperspectral remote sensing allows the detection of subtle differences in canopy density, leaf and canopy structure, and biochemical properties, which can be further used to distinguish coastal wetland plant species. Additionally, LIDAR remote sensing can help estimate canopy structure of shrubs, marsh, grass, and other vegetation found in the littoral zone. The integration of spectral imagery and LIDAR data offer the potential to significantly improve the species classification and structural mapping of coastal plant communities (Nayegandhi and Brock, 2009).

Watershed landscape characterization affects coastal water quality by altering sediment, chemical loads, and hydrology, and therefore information on upstream landscape structure and patterns is indispensable for coastal ecosystem assessment. Remote sensing of coastal watershed landscape structure and patterns generally involves procedures of land cover map production and landscape metrics computation. Aerospace imagery from various terrestrial sensors, especially those equipped with a blue band, can be used to map land cover types in coastal watersheds. The production of an accurate land cover map for a coastal area is not a trivial task, mainly due to the presence of a variety of wetlands and vegetation covers, along with complex urban impervious materials and agricultural lands. Several strategies have been developed to improve automated land cover classification, which include GIS-based hierarchical classification and spatial reclassification, knowledge-based expert systems, artificial neural networks, fuzzy logic, and genetic algorithms. Landscape metrics can be derived from a land cover map, by which the landscape structure and pattern of a coastal watershed can be further assessed (Yang, 2009a).

### Further research

This entry reviews several major coastal ecosystems and discusses how remote sensing can be used to characterize coastal waters, benthic habitats and submerged aquatic vegetation, coastal wetlands (including mangroves), and coastal watershed landscape characteristics.

While some significant progress has been made in remote sensing of coastal ecosystems, there are several major areas that deserve further research. Firstly, the current ocean color scanners are basically designed for offshore waters and are of limited usefulness for optically complex nearshore waters. Further research is needed to help design future ocean color radiometers appropriate for shallow coastal waters. Secondly, most of the algorithms for retrieving water quality measures were originally designed for open-ocean waters, and a significant

area for continuing research is the fundamental understanding of the functional linkage between water constituents and remote reflectance for coastal waters. Thirdly, more research is needed to advance the fundamental understanding of the relationship between the volumetric reflectance, the canopy density of SAV populations, water depth, and bottom reflectance parameters. This will help develop more realistic volumetric reflectance models, thus increasing the likelihood of accurate SAV mapping. Fourthly, there is an increased research demand to develop improved methods and technologies for resolving the spectral confusion between different land cover classes from medium-resolution imagery and for incorporating image spatial characteristics and ancillary data to improve land cover classification from high-resolution imagery. Fifthly, more research is needed to advance the fundamental understanding of the relationship between landscape patterns and ecological processes. Lastly, continuing research efforts are needed to help acquire good and sufficient in situ data for building comprehensive spectral libraries of different coastal plant species and for calibrating remote signals and verifying information extraction algorithms for coastal environments.

## Bibliography

- Beatley, T., Brower, D. J., and Schwab, A. K., 2002. *An Introduction to Coastal Zone Management*, 2nd edn. Washington, DC: Island Press, p. 329.
- Burke, L. A., Kura, Y., Kassem, K., Revenga, C., Spalding, M., and McAllister, D., 2001. *Pilot Analysis of Global Ecosystems: Coastal Ecosystems*. Washington, DC: World Resources Institute, p. 77.
- Council, N. R., 2000. *Clean Coastal Waters: Understanding and Reducing the Effects of Nutrient Pollution*. Washington, DC: National Academy Press, p. 200.
- Hinrichsen, D., 1998. *Coastal Waters of the World: Trends, Threads, and Strategies*. Washington, DC: Island Press, p. 298.
- Hobbie, J. E., 2000. *Estuarine Science: A Synthetic Approach to Research and Practice*. Washington, DC: Island Press, p. 539.
- Jensen, J. R., 2007. *Remote Sensing of the Environment: An Earth Resource Perspective*. Upper Saddle River, NJ: Prentice Hall, p. 592.
- Klemas, V., 2009. Sensors and techniques for observing coastal ecosystems. In Yang, X. (ed.), *Remote Sensing and Geospatial Technologies for Coastal Ecosystem Assessment and Management*. Berlin/Heidelberg: Springer, pp. 17–43.
- Mann, K. H., 2000. *Ecology of Coastal Waters with Implications for Management*, 2nd edn. Malden, Massachusetts: Blackwell Science, p. 406.
- Mishra, D. R., 2009. High-resolution ocean color remote sensing of coral reefs and associated benthic habitats. In Yang, X. (ed.), *Remote Sensing and Geospatial Technologies for Coastal Ecosystem Assessment and Management*. Berlin/Heidelberg: Springer, pp. 171–210.
- Nayegandhi, A., and Brock, J. C., 2009. Assessment of coastal-vegetation habitats using airborne laser remote sensing. In Yang, X. (ed.), *Remote Sensing and Geospatial Technologies for Coastal Ecosystem Assessment and Management*. Berlin/Heidelberg: Springer, pp. 365–390.
- Selman, M., Greenhalgh, S., Diaz, R., and Sugg, Z., 2008. *Eutrophication and Hypoxia in Coastal Areas: A Global Assessment of the State of Knowledge*. Washington, DC: World Resources Institute, p. 6.
- Yang, X., 2005a. Remote sensing and GIS applications for estuarine ecosystem analysis: an overview. *International Journal of Remote Sensing*, **26**(23), 5347–5356.
- Yang, X., 2005b. Special issue: remote sensing and GIS for estuarine and coastal ecosystem analysis. *International Journal of Remote Sensing*, **26**(23), 5163–5356.
- Yang, X., 2008. Theme issue: remote sensing of the coastal ecosystems. *ISPRS Journal of Photogrammetry and Remote Sensing*, **63**(5), 485–590.
- Yang, X., 2009a. Integrating satellite imagery and geospatial technologies for coastal landscape pattern characterization. In Yang, X. (ed.), *Remote Sensing and Geospatial Technologies for Coastal Ecosystem Assessment and Management*. Berlin/Heidelberg: Springer, pp. 461–494.
- Yang, X., 2009b. *Remote Sensing and Geospatial Technologies for Coastal Ecosystem Assessment and Management*. Berlin/Heidelberg: Springer, p. 561.
- Yang, X., Damen, M. C. J., and van Zuidam, R., 1999. Use of Thematic Mapper imagery and a geographic information system for geomorphologic mapping in a large deltaic lowland environment. *International Journal of Remote Sensing*, **20**(4), 568–591.

## Cross-references

[Data Processing, SAR Sensors](#)  
[Fisheries](#)  
[Forestry](#)  
[Geophysical Retrieval, Overview](#)  
[Global Land Observing System](#)  
[Lidar Systems](#)  
[Ocean Data Telemetry](#)  
[Ocean Measurements and Applications, Ocean Color](#)  
[Ocean Modeling and Data Assimilation](#)  
[Ocean Surface Topography](#)  
[Pattern Recognition and Classification](#)  
[Radiative Transfer, Theory](#)  
[Sea Level Rise](#)  
[Sea Surface Salinity](#)  
[Sea Surface Temperature](#)  
[Vegetation Indices](#)  
[Water Resources](#)  
[Wetlands](#)

---

## COMMERCIAL REMOTE SENSING

---

William Gail  
 Global Weather Corporation, Boulder, CO, USA

### Definition

*Commercial*. Pertaining to organizations or activities associated with buying and selling products and services.

### Introduction

Commercial remote sensing is remote sensing that produces information intended for sale on open commercial markets. It is generally performed by companies or through public-private partnerships rather than by governments. The commercial market includes remote sensing performed primarily from aerial and spaceborne

platforms. Due to the strategic nature of remote sensing, commercial interests are nearly always intertwined with national interests, at least for spaceborne systems. Governmental policies authorizing and regulating commercial remote sensing generally reflect objectives for national security, technology development, international relations, and economic positioning. The history of the industry, and its current configuration, reflect this tension between economic and national interests. Demand for commercial remotely sensed data has increased in recent years, in part due to the widespread availability of geographic information systems (GIS) that can display and analyze the imagery and online means for distributing the results.

## History

Aerial commercial remote sensing has been in existence for nearly a century. A significant focus of the industry is photogrammetry, the making of geometrically accurate high-resolution image mosaics covering large areas such as cities and states. Today, such mosaics are routinely produced with image resolutions as good as 15 cm and sometimes better. Until recently, the mosaics were generally panchromatic, but color imagery has become common with the introduction of digital sensors during the 2000s. In addition to optical photogrammetry, commercial remote sensing includes work with synthetic aperture radar (SAR), hyperspectral imagers, and LIDAR sensors. Both SAR and LIDAR are commonly used for measuring topography and related three-dimensional imaging. The aerial remote sensing industry consists of both commercial and government-owned entities, often in competition.

The roots of spaceborne commercial remote sensing extend back to the early 1970s with efforts by the USA, France, and India to provide commercial adjuncts to their national Earth monitoring systems. These early efforts laid the groundwork for today's industry with several dozen commercial systems in operation and a global market that is multibillion dollars (Modello et al, 2004).

In 1972, the USA launched the Earth Resources Satellite 1, which was subsequently renamed Landsat. In part a Cold War effort to demonstrate US leadership in Earth resources monitoring, its commercial value became recognized soon after launch. By the early 1980s, with the various interested parties all seeking a better way to access Landsat's imagery (National Research Council, 1985), a strong effort was made to change the regulatory environment governing Landsat. The result was the Land Remote Sensing Commercialization Act of 1984, which for the first time established the basis for commercial remote sensing operations authorized by the USA. As a result, in 1985 Landsat was partially privatized through a partnership with Earth Observation Satellite Corporation (EOSAT), itself a partnership of Hughes Aircraft and RCA. EOSAT was given a contract to operate the system for 10 years and build follow-on satellites, obtaining rights for commercial sale of the data.

Around the same time, the French *Système pour l'Observation de la Terre* (SPOT) satellite series was being developed. To encourage commercialization, a public-private partnership called Spot Image was created by the French government in 1986. They have since launched a series of increasingly capable satellites, starting with the 10 m resolution SPOT-1 in 1986. In India, the Indian Space Research Organization (ISRO) initiated a commercially oriented Earth-observing program following the success of their early demonstration satellites Bhaskara-1/2 launched in 1979 and 1981. The Indian Remote Sensing (IRS) series of satellites was initiated with the IRS-1 launch in 1988 and continues as a robust program today.

As demand grew and technology improved, these early efforts spurred further commercial interest beginning in the 1990s. The first truly commercial (not public-private partnerships) remote sensing satellite operations were plagued by early failures. EarlyBird was launched by EarthWatch (originally called Worldview and changed in 2001 to DigitalGlobe) in 1997 but functioned for only 3 days. Space Imaging launched their first satellite Ikonos in 1999 but it failed to reach orbit. Space Imaging succeeded with their second Ikonos satellite later in 1999. EarthWatch's second satellite, QuickBird, also suffered a launch failure in 2000, but the third satellite Quickbird-2 succeeded in 2001. ORBIMAGE joined the group in 2003 with the launch of Orbview-3, but only after Orbview-4 was lost on launch. By the early 2000s, these firms had become increasingly dependent on contracts from the US National Geospatial-Intelligence Agency (NGA) for revenue. In 2005, ORBIMAGE acquired Space Imaging for \$58 million after it failed to win the latest rounds of NGA contracts. ORBIMAGE subsequently renamed itself GeoEye.

More recently, the intelligence community has been a significant partner in the development of commercial remote sensing capability. In the USA, large data purchase contracts such as NextView, ClearView, and EnhancedView by NGA have provided anchor funding for commercial remote sensing companies. NextView contracts, for example, are service-level agreements that specify requirements for imagery purchases from satellites still to be developed. They are designed to provide a long-term government partnership commitment that enables the private sector partner to finance and develop new satellites that meet the requirements. To motivate a commercial market, the agreements are nonexclusive, meaning that the companies can sell the same imagery to other customers. A 2007 independent report chartered by the US National Reconnaissance Office (Marino, 2007) defined various approaches for intelligence community use of commercial remote sensing along with the benefits and risks of those approaches.

The Landsat Data Continuity Mission, initiated in the early 2000s as the follow-on to Landsat-7, was originally envisioned as a strong public-private partnership but has since evolved into a more traditional system acquisition with the government retaining responsibility for data

processing and distribution. NASA also used the Sea-viewing Wide Field-of-view Sensor (SeaWiFS) mission to promote commercialization. SeaWiFS was built for NASA under partnership with Orbital Sciences Corporation and launched in 1997. ORBIMAGE (renamed GeoEye), a spin-off from Orbital Sciences, was given the responsibility for operating the satellite (renamed Orbview-2 for commercial purposes) and for selling the data, with NASA itself purchasing data.

The mid-2000s saw the entrance of many new commercial players with innovative approaches to the market. RapidEye, a public-private partnership, developed and launched a series of five satellites designed to provide rapid-refresh multispectral optical imagery. The TerraSAR satellite system owned and operated by InfoTerra, another public-private partnership, focused on SAR imagery. Surrey Satellite Technology Ltd. (SSTL) developed a multi-government collaboration that built and launched a series of small satellites called the Disaster Monitoring Constellation (DMC), each owned and controlled by a different government (Algeria, Nigeria, Turkey, Britain, China, Spain) but operated jointly through a wholly owned subsidiary of SSTL called DMC International Imaging.

Despite today's successes, a number of companies with ambitious commercial business plans have attempted to enter the market and failed. Resource21 was focused on providing short-revisit multispectral imagery for use in agriculture starting in the 1990s. Their plans for a satellite system focused on this market did not proceed. Around the same time, AstroVision began pursuing a new market for imagery taken from geostationary orbit but had not been able to develop the system after more than a decade. In 2011, RapidEye filed for the German equivalent of bankruptcy protection. Even after several decades of market development, spaceborne commercial remote sensing remains a risky business with considerable investment and high likelihood of failure (National Research Council, 2002; Group on Earth Observations, 2005).

### Technology

Of the many spaceborne remote sensing technologies developed over the years for scientific and defense purposes, those that have been commercialized are largely constrained to high-resolution imagery. Initially, this meant panchromatic optical imagers, although inclusion of color bands quickly became routine. One current trend is an increase in the number of color bands and the extension of these bands to infrared wavelengths. Hyperspectral imagers represent the next logical step in this progression, although no company has yet announced plans for doing so. Canada pioneered use of synthetic aperture radar in the commercial realm, with the 1995 launch of Radarsat, and a number of commercial radars are operating now. A significant technology advance occurred with the reduction in size and weight of spacecraft platforms, allowing the introduction of low-cost multi-satellite

constellations such as DMC and RapidEye. A number of companies have built businesses around the sale of satellite systems and technology to nations that do not have the capability to build their own.

Aerial remote sensing technologies have followed a somewhat different path. Because aerial systems allow access to the sensor itself, film remained a viable sensing medium far longer than with spaceborne systems. In the early 2000s, highly capable digital aerial cameras were introduced, and by 2010 most of the industry had transitioned to digital imagery. Related technologies, such as widespread availability of GPS positioning and accurate inertial sensors, made digital sensors even more effective.

### Regulation

Commercial remote sensing is regulated on a nation-by-nation basis, involving both policy and law. In general, the purpose of such regulation is to make data available for legitimate scientific and commercial uses while at the same time protecting national security interests (Gabrynowicz, 2007). A critical aspect of such regulation is the use of licensing that authorizes companies to operate commercial remote sensing systems and defines the constraints on that operation. Central to this are rules for ownership, dissemination, and use of data, particularly with regard to resolution and timeliness of distribution.

The most developed regulatory framework is that of the USA. The earliest formal legislation was the *Land Remote Sensing Commercialization Act of 1984*, a by-product of the Reagan-era policies to promote privatization of government assets. The Act was driven by the specific need to create better access to Landsat imagery, but it also introduced a more general framework for licensing and regulation of commercial remote sensing systems. This was updated through the *Land Remote Sensing Policy Act of 1992*, which reversed the commercialization of Landsat contained in the 1984 Act, but provided further legislation promoting private sector remote sensing.

Despite these legislative acts, uncertainty remained regarding how licensing of commercial remote sensing systems would actually occur. This uncertainty was initially resolved in 1994 through a presidential policy statement known as the *US Policy on Foreign Access to Remote Sensing Space Capabilities* (PDD-23). It stated clearly the dual-purpose policy goal: "the fundamental goal of our policy is to support and to enhance US industrial competitiveness in the field of remote sensing space capabilities while at the same time protecting US national security and foreign policy interests." PDD-23 provided the administrative mechanisms needed to make the 1992 legislative act effective, including four fundamental principles: (a) the presumption that US licenses would only be issued for systems with capability no better than what is commercially available from other suppliers in the world marketplace, (b) tight control of technology exports in the form of satellite systems and components,

(c) management of system capabilities (rather than data distribution) as a means for constraining imagery access by undesirable parties, and (d) “shutter control” that allows the government to stop all commercial remote sensing when appropriate national interests are identified.

Licenses are further constrained by an amendment to the 1997 Defense Authorization Act (known as the Kyl-Bingaman amendment) that specifically limits imagery taken over Israel to no better than that “available from commercial sources.” Throughout much of the 1990s, for example, this limit was set to 2 m. The *Commercial Remote Sensing Policy of 2003* (NSPD-27), which superseded PDD-23, did not change these licensing provisions but strengthened the commercial sector by encouraging drawing on commercial capabilities to the “maximum practical extent” when serving government needs.

Under this framework, authority for licensing commercial remote sensing is allocated to the Department of Commerce. Within the Department of Commerce, the NOAA Office of Space Commercialization provides policy guidance while licenses themselves are issued by the NOAA Commercial Remote Sensing Regulatory Affairs Office. Between 1993 and 2000, 17 licenses were issued. In 2008, a total of 19 licenses were active covering 45 satellites with 10 launched. This office is advised in the effort by an independent board called the Advisory Committee on Commercial Remote Sensing (ACCRES). NOAA is responsible for assessing the state of the industry and determining, for example, the resolution of systems that can be licensed. Among the provisions included originally in licenses is that no imagery can be distributed for at least 24 h after it is collected, a constraint designed to minimize use of US-collected imagery by enemies for targeting US military positions. After lengthy interagency governmental deliberation, this provision was dropped in 2007.

Canada also has a relatively mature and transparent regulatory framework built around the *Canadian Space Agency Act of 1990* and the *Remote Sensing Space Systems Act of 2005*. The USA and Canada have a formal agreement concerning operation of commercial remote sensing systems. India, on the other hand, has no relevant law but rather a comprehensive set of policies (Rao et al., 2002; Gabrynowicz, 2007). In Germany, regulation is provided through the *2008 Satellite Data Security Law*, which specifies that approval for commercial remote sensing activities is applied not to each satellite development but rather to each data request on a case-by-case basis. Japan established a *Basic Space Law* in 2008 and released a *Basic Plan for Space Policy* based on that law in 2009. Other nations tend to have less open or less specific regulatory guidelines or to regulate on a satellite-by-satellite basis (Gabrynowicz, 2007). Some govern commercial remote sensing through general space policies, while others have only informal policies. Only a limited amount of international agreement is available to guide commercial remote sensing. In 1986, the United Nations released

a set of principles concerning remote sensing from space (United Nations, 1986), reflecting the desire for remote sensing activities to be used for the benefit of all nations.

### Current examples

Three recent trends have had enormous impacts on aerial remote sensing. The first is the transition from analog to digital technologies within optical imagers, as discussed previously. Alternate sensing technologies, including radar and LIDAR, are still establishing their niches within overall commercial offerings. The second is advances in computers and software, making it feasible to work with large imagery volumes in professional domains such as GIS and photogrammetry. The third is end-user applications, such as online mapping, that make such imagery and related value-added products accessible to consumers. Today, there is a robust commercial industry dedicated to the collection of aerial remote sensing and related industries for value-added products, software, and instrument development. Despite these technology changes, the industry business models have evolved more slowly and remain characterized by smaller companies. The nature of the industry varies widely by country, with some less robust due to strong competing government capabilities.

For the foreseeable future, high-resolution electro-optical imagery will remain the central focus of spaceborne commercial remote sensing. At the present time, the USA retains leadership in the area of commercial electro-optical imagery, but other nations lead in the area of radar imagery. Considerable innovation is being applied to introduce capabilities such as rapid revisit and advanced multispectral imagery that serve customers beyond those needing the highest resolution.

GeoEye’s latest satellite GeoEye-1 was launched in 2008 and was developed with funding raised in part through an NGA NextView contract. GeoEye-1 provides panchromatic imaging with 0.41 m resolution (although the operating license requires this to be resampled to no better than 0.5 m before distribution) and multispectral imagery with resolution 1.7 m. A second GeoEye satellite is expected sometime by 2013. DigitalGlobe’s Worldview-1 (launched 2007), also funded in part through an NGA contract, produces 0.5 m panchromatic imagery. Worldview-2 (launched 2009) provides 0.46 m panchromatic imagery and 8-band color with 1.8 m resolution. DigitalGlobe also operates the older QuickBird satellite.

Spot Image operates several SPOT satellites and began launching the more advanced Pleiades series beginning in 2011. The Pleiades satellites provide panchromatic imagery at 0.7 m resolution and 4-band color at 2 m resolution. Spot Image also has distribution rights to other national systems, including Korea’s KOMPSAT and Republic of China’s FORMOSAT. Russia launched the Resurs-DK1 satellite, with 0.9 m resolution, in 2006 and markets data through SOVZOND JSC. Russia has also leveraged imagery from older surveillance satellites, digitizing that

imagery and selling it through commercial channels. The Israeli EROS-A/B imagery satellites, launched between 2000 and 2006 with resolution as good as 0.7 m, are owned and operated by an Israeli-founded international company ImageSat International.

The Indian Remote Sensing (IRS) series of satellites is the largest single commercially oriented remote sensing system in the world. It now includes three satellite classes focused on land resources, ocean resources, and cartography. ResourceSat-1/2 satellites, launched in 2003 and 2009, have 6 m pan resolution and 3-band color at the same resolution. OceanSat-2 was launched in 2009 and focused on ocean color imaging, carrying an 8-band multispectral imaging and Ku-band scatterometer. The Cartosat series has had four launches starting in 2005, with pan resolution better than 1 m. Commercial image distribution is the responsibility of ISRO's commercial entity Antrix.

Within eastern Asia, neither China nor Japan has commercial remote sensing capability, though each has a robust remote sensing program. The Korean KOMPSAT-1/2 satellites, launched in 1999 and 2006 by the Korean Aerospace Research Institute (KARI), have resolution of 4-band color with 4 m resolution. The Republic of China FORMOSAT-1/2 series, launched in 1999 and 2004, have a resolution of as good as 1 m and 4-band color with 8 m resolution. The imagery from both KOMPSAR and FORMOSAT is currently marketed by Spot Image.

Several companies have pursued somewhat different approaches to the commercial market, focusing on improved repeat cycles rather than highest resolution. Surrey Satellite Technology Ltd. (SSTL) developed a multi-government collaboration that built and launched a series of small satellites called the Disaster Monitoring Constellation (DMC), each owned and controlled by a different government (Algeria, Nigeria, Turkey, Britain, China, Spain) and operated jointly through a wholly owned subsidiary of SSTL called DMC International Imaging. The German RapidEye satellite constellation, a five-satellite system designed for rapid-refresh multispectral imagery, was developed as a public-private partnership with a diverse set of public and private investors largely from Germany and Canada. The satellites were launched on a single launch vehicle in 2008.

Radar imagery has proven to be of strong commercial interest. Radarsat International was formed in 1989 by a consortium of Canadian companies with the purpose of processing and distributing the data from Radarsat-1, launched in 1995. One of the shareholders, Macdonald Dettwiler and Associates, bought out the others in 1999 and formed a deeper partnership with the Canadian government to build and operate Radarsat-2, launched in 2007. The Radarsat-2 resolution of 3 m substantially improved on the 8 m resolution of Radarsat-1. TerraSAR-X, launched in 2007, is a public-private partnership between EADS (through their InfoTerra company) and the German Aerospace Center (DLR). It produces radar imagery with resolution up to 1 m including a variety of multipolarization and interferometric data

products. A companion satellite, TanDEM-X, was launched in 2010, allowing the system to operate in interferometric mode so as to perform high-resolution topographic mapping. COSMO-SkyMed is a dual-use system of four satellites with 1 m resolution and polarimetric/interferometric capability funded by the Italian Space Agency, the Italian Ministry of Defense, and the commercial company Telespazio. The first launch was in 2007 and the last in 2010.

## Summary

The commercial market today is served by both aerial and spaceborne sectors, with some overlap. Over the last decade, the relative roles of each sector have become more clearly defined within the market. The aerial sector continues to be dominated by smaller companies and governmental entities, with significant national and even regional variability. The spaceborne sector is moving rapidly from an early exploratory phase, in which new technologies, business models, and regulatory environments were being assessed, to a mature phase with well-established success paths. The entire space industry is becoming more commercialized, from launch vehicles to spaceports, establishing a positive context within which remote sensing's own commercialization takes place. The remote sensing industry as a whole is moving from a platform-centric view to a services-centric view in which the features of the data are more important than the features of the sensors. Governments are becoming more focused on remote sensing as an important element of their space programs. They are migrating to smaller but more capable satellites, and they view commercialization or dual use as an important element of their efforts. Capabilities of commercial systems are increasingly diverse, from the growing use of radar to the selection of optical bands to the availability of short-revisit imagery. All trends suggest that the importance of commercial remote sensing will continue to grow in the coming years.

## Bibliography

- Council, N. R., 1985. *Remote Sensing of the Earth from Space: A Program in Crisis*. Washington, DC: The National Academies.
- Council, N. R., 2002. *Toward New Partnerships in Remote Sensing: Government, the Private Sector, and Earth Science Research*. Washington, DC: The National Academies.
- Gabrynowicz, J., 2007. *The Land Remote Sensing Laws and Policies of National Governments: A Global Survey*. Report for U.S. Department of Commerce/National Oceanic and Atmospheric Administration's Satellite and Information Service Commercial Remote Sensing Licensing Program.
- Group on Earth Observations, 2005. *Global Earth Observations System of Systems GEOSS: 10-Year Implementation Plan Reference Document*. Noordwijk: ESA Publications Division.
- Marino, P., 2007. *Independent Study of the Roles of Commercial Remote Sensing in the Future National System for Geospatial-Intelligence (NSG)*. Falls Church, VA: Defense Group.
- Modello, C., Hepner, G. F., and Williamson, R. A., 2004. *10-Year Industry Forecast, Phase I-III - Study Documentation*. Bethesda, MD: ASPRS.
- Rao, M., Jayaraman, V., and Sridharamurthi, K. R., 2002. Issues for a remote sensing policy and perspective of the Indian Remote

Sensing Programme. In *Proceedings from The First International Conference on the State of Remote Sensing Law*, pp. 47–61. United Nations, 1986. *Principles Relating to Remote Sensing of the Earth from Outer Space*. New York: United Nations.

## Cross-references

Cost Benefit Assessment  
Emerging Applications  
Observational Systems, Satellite  
Policies and Economics  
Public-Private Partnerships  
Radar, Synthetic Aperture

---

## COSMIC-RAY HYDROMETEOROLOGY

---

Darin Desilets<sup>1</sup> and Marek Zreda<sup>2</sup>

<sup>1</sup>Hydroinnova LLC, Albuquerque, NM, USA

<sup>2</sup>Department of Hydrology and Water Resources, University of Arizona, Tucson, AZ, USA

## Definitions

*Cosmic-ray hydrometeorology.* The science of measuring hydrologic variables through their effects on secondary cosmic-ray intensity.

*Primary cosmic ray.* A charged particle, usually a proton, traveling toward Earth at relativistic speed.

*Secondary cosmic ray.* An energetic proton, neutron, or other subatomic particle generated as a consequence of primary cosmic rays colliding with the Earth.

## Introduction

Cosmic rays continually bombard Earth, giving rise to a small but measurable flux of background neutrons at the land surface. These ambient neutrons respond strongly to the presence of land surface water in the form of soil moisture and snow or more specifically to the hydrogen which that water contains. The unique ability of hydrogen to influence neutron intensity has been known since the discovery of the neutron itself in the 1930s, when the mysterious nonionizing radiation was first identified through its ability to scatter hydrogen nuclei from paraffin (Chadwick, 1932), losing substantial fraction of its energy in the process. By the late 1950s, soil scientists began applying neutron scattering principles to the field determination of soil water content by lowering radioisotopic neutron sources and collocated neutron detectors down bore holes and measuring the intensity of backscattered neutrons (Gardner and Kirkham, 1952). It was later demonstrated that water content in the shallow subsurface and snow water equivalent depth could be obtained passively by measuring background cosmic-ray neutrons with detectors buried in the top meter of soil (Kodama et al., 1985), although the method was never widely adopted. More recently, Zreda et al. (2008) showed the feasibility of noninvasively measuring soil water content through

aboveground measurements of cosmic-ray neutron intensity. This technique operates at a scale of tens of hectares, which fills an important gap between the scales of invasive point measurements and satellite remote sensing footprint.

## Neutron interactions in soil

The transmission of fast neutrons through bulk matter is profoundly influenced by the presence of hydrogen, which at the land surface is present mainly in the form of liquid and solid water and plant carbohydrates. Hydrogen is uniquely effective in moderating (slowing) neutrons by virtue of its low mass and relatively large elastic scattering cross section, which is a measure of the probability of interacting elastically with a neutron. As with any two particles having the same mass, a fast neutron can theoretically be brought to rest through a single head-on collision with hydrogen (Glasstone and Edlund, 1952). The fewer collisions needed to moderate a fast neutron, the lower the fast neutron intensity will be. Elastic collisions with hydrogen and other light nuclei progressively moderate a fast neutron until it is either absorbed by a nucleus or is reduced to a velocity on the order of the thermal motions of surrounding molecules, at which point there is no net change in energy through subsequent collisions. A distinguishing characteristic of thermal neutrons is their strong tendency to be absorbed by nuclei. Common absorbing elements in the soil matrix include major elements such as Fe, Ca, K, and trace elements with unusually high absorption cross sections, such as B, Gd, and Sm.

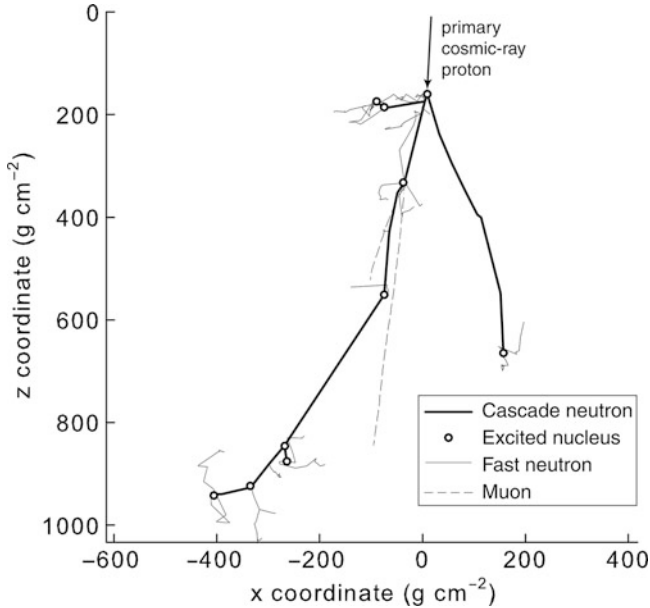
## Cosmic-ray neutrons

Cosmic-ray neutrons are an ever-present part of the land surface radiation environment. They are a by-product of chain reactions initiated at the top of the atmosphere by primary cosmic rays (Simpson, 1951) (A simulated particle cascade created by a 10 GeV primary interacting with nitrogen is shown in Figure 1). The primary radiation is composed of highly energetic particles, mainly protons and helium nuclei, which are believed to have been accelerated in shock waves associated with supernovas occurring throughout the Milky Way (Uchiyama et al., 2007). Energetic primaries collide with atmospheric gas molecules, unleashing cascades of secondary protons, neutrons, and other subatomic particles, some of which penetrate to sea level.

The neutrons utilized for passive water content measurements are generated mainly by cascade neutrons interacting with matter. Fast neutrons are produced in two types of interactions. A cascade neutron can transfer kinetic energy to an entire target nucleus, raising it to an excited energy state. The nucleus then cools off by “evaporation,” that is, the emission of fast neutrons in random directions. Cascade neutrons with higher energies will tend to interact at the surface of a nucleus, dislodging the outermost neutrons in a mostly forward direction (Krane, 1987). Regardless of how they are produced, fast neutrons

are scattered elastically in random directions until they are eventually absorbed by soil or atmospheric nuclei.

Fast neutron intensity at the land surface reflects the equilibrium between production, moderation, and absorption of neutrons in the ground and atmosphere (Figure 2).



**Cosmic-Ray Hydrometeorology, Figure 1** Atmospheric particle cascade simulated with the radiation transport code Monte Carlo N-Particle eXtended (MCNPX – Pelowitz, 2005). A 10 GeV primary cosmic-ray proton collides with atmospheric nitrogen, triggering a particle cascade that reaches sea level. Fast neutrons are generated at each collision marked by a circle. The fast neutrons are scattered in random directions as they are moderated and eventually become captured.

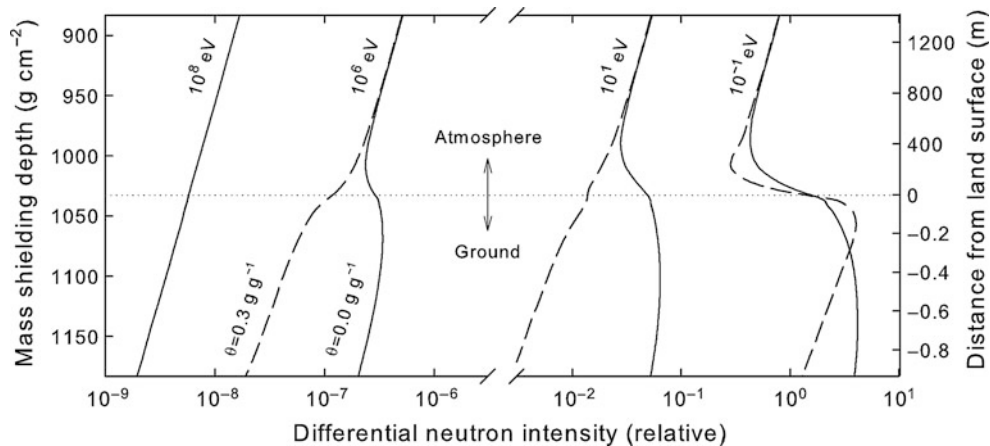
Neutrons are scattered between the ground, which tends to be the better moderator when wet, and the atmosphere, which is the better thermal neutron absorber. Any change in water content at the land surface disturbs this equilibrium. An increase in the amount of soil water or snow decreases the intensity in the fast to epithermal region because neutrons are more efficiently reduced to lower energies through collisions with hydrogen. Conversely, thermal neutron intensity first increases with increasing water content and then decreases monotonically. This behavior is explained by the competing roles of hydrogen as an absorber and moderator. Initially, a small increase in water content rapidly increases the rate of thermalization, which increases the thermal neutron flux. But above a few percent gravimetric soil moisture content, the role of hydrogen as a moderator is challenged by its tendency to absorb neutrons.

### Retrieval of soil moisture

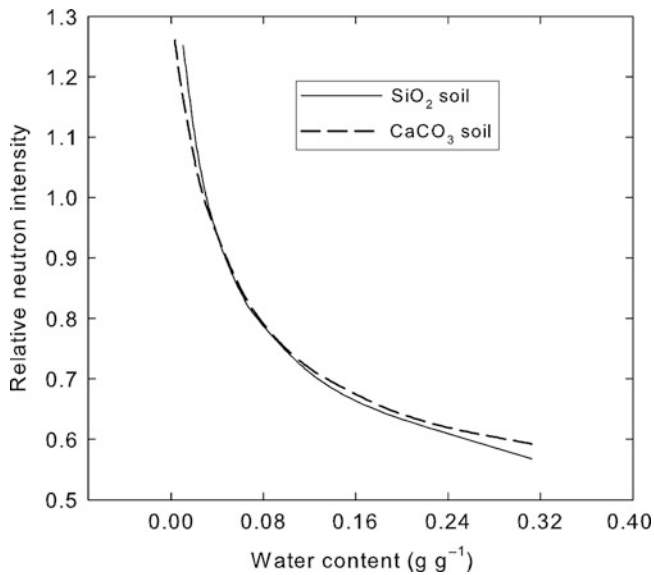
For a wide range of soil compositions, a “universal” shape-defining function can be used to convert neutron counting rates to soil water content for typical silica-dominated soils (Figure 3). This function is valid for neutrons in the epithermal to fast part of the spectrum ( $10^0$ – $10^6$  eV), where neutron absorption is minor. A calibration curve for soil water content has been obtained by fitting simulated ground-level neutron fluxes to the semiempirical shape-defining equation:

$$\theta(\phi/\phi_r) = \frac{1}{B} \left( \frac{A}{(\phi/\phi_r) - D} - C \right) \quad (1)$$

where  $(\phi/\phi_r)$  is the neutron intensity normalized to a reference soil moisture state. The dependence of land surface neutron intensity in the epithermal to fast energy range on gravimetric soil water content is represented in



**Cosmic-Ray Hydrometeorology, Figure 2** Depth profiles of neutron intensity near the land surface for different energies simulated with MCNPX. Between  $10^1$  and  $10^6$  eV, where elastic scattering interactions dominate, the shape of the profile and its sensitivity to soil moisture are remarkably constant. At lower energies ( $<10^{-1}$  eV), thermal neutron absorption becomes important and the shape of the profile reflects the strong contrast between the absorbing properties of the ground and atmosphere. At higher energies ( $>10^8$  eV) the profile reflects exponential attenuation expected for cascade neutrons.



**Cosmic-Ray Hydrometeorology, Figure 3** The dependence of neutron intensity on soil water content at 0–2 m above the ground according to MCNPX calculations for a soil matrix with pure  $\text{SiO}_2$ . For comparison, a curve for a pure  $\text{CaCO}_3$  soil matrix is also shown.

silica-dominated soils by  $A = 0.562$ ,  $B = 0.060$ ,  $C = 0.942$ ,  $D = 0.449$ , with the reference state dry soil. The shape of the function is not significantly altered by differences in soil texture, salinity, bulk density, or moderate amounts of carbonates or organic matter in soil.

Although the shape of the calibration function is largely invariant, the absolute “source” neutron intensity is highly variable across the surface of the Earth. In other words, the calibration function can translate on the intensity axis depending on location. Elevation differences are responsible for the biggest differences in source intensity. The elevation effect is more accurately described as a function of the mass shielding depth at a site, which is the product of atmospheric depth and air density and is expressed in units of  $\text{g cm}^{-2}$ . Local barometric pressure readings are usually an acceptable proxy for mass shielding depth. Neutron-generating cascades are attenuated exponentially as a function of mass shielding according to

$$\phi_2 = \phi_1 \exp[(x_1 - x_2)/\Lambda] \quad (2)$$

where  $\phi_1$  and  $\phi_2$  are the neutron intensities at depths  $x_1$  and  $x_2$  ( $\text{g cm}^{-2}$ ) and the attenuation length  $\Lambda$  is  $\sim 130 \text{ g cm}^{-2}$  at high to mid-latitudes (Desilets et al., 2006). According to this relationship, the neutron intensity at an elevation of 3,000 m ( $750 \text{ g cm}^{-2}$ ) is almost nine times greater than at sea level ( $1,033 \text{ g cm}^{-2}$ ). Neutron intensity decreases by about half from high and mid-latitudes to the equator due to stronger magnetic shielding of primary cosmic rays at lower geomagnetic latitude. The elemental composition of soil may also have some effect on neutron source intensity because of differences

between elements in the number of neutrons emitted following excitation.

The spatial variability in cosmic-ray intensity means that the calibration function must be normalized to the local neutron source strength. This can be accomplished by obtaining at least one field calibration point. Because the radius of influence is large, many field samples are usually needed in order to obtain an areally representative average moisture (e.g., Western and Blöschl, 1999; Famiglietti et al., 2008). Different strategies to obtaining this point may be employed. One consideration is that average soil water content is ideally in the middle of the anticipated moisture range. Another consideration is that samples should be collected when the distribution of soil moisture is expected to be fairly uniform, in order to reduce the number of samples required for representativeness. A calibration is transferrable to another site if the topography, biomass concentration, and soil composition are similar between the two sites and elevations and latitudes are similar. Differences in source neutron intensity related to elevation and latitude can be compensated for by applying published scaling factors for neutron intensity (e.g., Desilets et al., 2006).

Counting rates should also be corrected for fluctuations in neutron source intensity over time. These are related mainly to variations in barometric pressure and solar activity. Corrections for barometric pressure can be made with Equation 2 using local pressure data and the local attenuation length for neutron-generating cosmic rays. Changes related to solar activity can be corrected using publicly available data from the global network of neutron monitors (Kuwabara et al., 2006).

### Measuring neutron intensity

Neutron detectors tend to be most sensitive over a limited range of energies. The optimal sensitivity for soil moisture measurements is in the epithermal ( $10^0$ – $10^1$  eV) range because a reasonably high count rate can be achieved while sensitivity to neutron absorbers is minimized. Although the shape of the calibration function is nearly constant up to  $10^6$  eV, neutron intensity drops off rapidly with energy according to a  $1/E$  law (Glasstone and Edlund, 1952). Measurements at higher energies therefore require larger or more efficient detectors or longer averaging times in order to compensate for lower neutron intensity.

The analytical precision of soil moisture determinations is governed by Poissonian statistics, which assumes that neutron counts are uncorrelated. The coefficient of variation is given by  $N^{-0.5}$ , where  $N$  is the counting rate. A precision of better than 2–3 % for 1 h of counting is easily achieved at sea level using portable equipment.

### Sample volume

A major advantage of subaerial cosmic-ray measurements is that a large area can be sampled noninvasively from the ground or a low-flying aircraft. The radius of influence for 86 % (two e-fold drops) of the counts is 350 m at sea level

for a ground based, omnidirectionally sensitive neutron detector. Several factors are responsible for the large radius of influence: the neutron source is distributed across the land surface, the mean free path for atmospheric collisions is on the order of 30 m, and trajectories are randomized through collisions in the atmosphere. The footprint increases with elevation in proportion to the atmospheric collision mean free path length, which is inversely proportional to atmospheric pressure. The measurement depth depends strongly on soil moisture, ranging from 0.6 m in dry soil to 0.2 m in saturated soil for 86 % of the response.

### Summary

Soil water content can be inferred from subaerial measurements of cosmic-ray neutron intensity. The hydrogen in soil water dominates the moderating power in the land surface environment. Through its ability to moderate and absorb neutrons, hydrogen exerts a strong control on neutron fluxes in the fast to thermal energy range. Cosmic-ray measurements are passive, noninvasive, noncontact, and represent a sample area of tens of hectares and a depth of tens of centimeters. The method has moderate power demands and data processing and transmission requirements, which makes it particularly well suited for long-term monitoring and field campaigns. A promising direction for future research is coupling neutron observations to land surface models and possibly even inverting neutron data to obtain soil properties and evapotranspiration. Furthermore, advances in neutron detection technology, for example, in the area of directionally sensitive neutron detectors (Mascarenhas et al., 2006), have the potential to open new applications and spatial scales for hydrologic measurements.

### Bibliography

- Chadwick, J., 1932. Possible existence of a neutron. *Nature*, **129**, 312.
- Desilets, D., Zreda, M., and Prabu, T., 2006. Extended scaling factors for in situ cosmogenic nuclides: new measurements at low latitude. *Earth and Planetary Science Letters*, **246**, 25.
- Famiglietti, J. S., Ryu, D., Berg, A. A., Rodell, M., and Jackson, T. J., 2008. Field observations of soil moisture variability across scales. *Water Resources Research*, **44**, W01423.
- Gardner, W., and Kirkham, D., 1952. Determination of soil moisture by neutron scattering. *Soil Science*, **73**, 391.
- Glasstone, S., and Edlund, M. C., 1952. *Elements of Nuclear Reactor Theory*. Van Nostrand: Princeton, pp. 148–150.
- Kodama, M., Kudo, S., and Kosuge, T., 1985. Application of a mospheric neutrons to soil moisture measurement. *Soil Science*, **140**, 237.
- Krane, K. S., 1987. *Introductory Nuclear Physics*. New York: Wiley.
- Kuwabara, T., Bieber, J. W., Clem, J., Evenson, P., et al., 2006. Real-time cosmic ray monitoring system for space weather. *Space Weather: The International Journal of Research and Applications*, **4**, S08001.
- Mascarenhas, N., Brennan, J., Krenz, K., Lund, J., et al., 2006. Development of a neutron scatter camera for fission neutrons.

In *IEEE Nuclear Science Symposium*, Vol. 1, San Diego, CA, pp. 185–188.

- Pelowitz, D. B. (ed.). 2005. *MCNPX User's Manual, Version 5*. LA-CP-05-0369, Los Alamos National Laboratory.
- Simpson, J. A., 1951. Neutrons produced in the atmosphere by the cosmic radiations. *Physics Reviews*, **83**, 1175.
- Uchiyama, Y., Aharonian, F. A., Tanaka, T., Takahashi, T., and Maedo, Y., 2007. Extremely fast acceleration of cosmic rays in a supernova remnant. *Nature*, **449**, 576.
- Western, A. W., and Blöschl, G., 1999. On the spatial scaling of soil moisture. *Journal of Hydrology*, **217**, 203.
- Zreda, M., Desilets, D., Ferré, T. P. A., and Scott, R. L., 2008. Measuring water content non-invasively at intermediate spatial scale using cosmic-ray neutrons. *Geophysical Research Letters*, **35**, L21402.

---

## COST BENEFIT ASSESSMENT

---

Molly Macauley

Resources for the Future, Washington, DC, USA

### Synonyms

Cost savings; Economic benefit; Net benefit; Societal benefit; Value of information

### Definition

The “costs” of remote sensing usually refer to the direct monetary costs of designing, testing, constructing, deploying, operating, and maintaining the hardware (instruments, platforms, supporting infrastructure, communications networks) of remote sensing devices. These are typically the cameras, radar, lidar, or other instruments carried on aircraft or spacecraft for purposes of observing Earth processes (in situ remote sensing involves the hand-carrying of these devices). Costs also include the expenses of designing, testing, operating, and maintaining the software and other tools associated with using the data acquired from remote sensing instruments. Additional costs include those of personnel and may range from salaries of administrative and engineering experts to training and salaries of scientific researchers and the final “consumers” who use remote sensing for decision making. “Benefits” refer to the enhanced knowledge or scientific understanding gained from remote sensing as well as the practical applications which remote sensing data may contribute to. Benefits may be expressed in monetary measures or other quantitative measures such as “a percentage improvement in accuracy” or qualitative descriptions. “Cost benefit assessment” links costs and benefits in an attempt to measure the net gain from remote sensing – what benefits does it provide, after accounting for the costs incurred to glean those benefits?

## Introduction

A decision whether to invest in remote sensing can be informed by understanding its costs and benefits. These costs and benefits are relevant to many decision makers, ranging from public officials who invest in remote sensing systems to consumers of information, such as managers of natural and environmental resources and the public at large.

## Discussion

### Costs

Although measuring the costs of remote sensing systems may be thought to be straightforward, accounting for all costs may be difficult in practice. The costs of hardware, software, and personnel may not be easily identified if they are included within broad categories in some cost accounting systems, making it difficult to assign costs specifically to a remote sensing system. For many users of remote sensing, data may be provided freely or at a marginal cost of reproduction, in which case costs as reported in budget statements may not represent the full cost to society of investment in a remote sensing system. In addition, the costs incurred to use remote sensing data may include common resources, such as shared computers, communications devices, and personnel, for which the allocation of cost among uses of shared facilities is difficult. In a study of how remote sensing data are transformed into information for managers of natural and environmental resources, such as national or local agencies or agricultural or geologic exploration companies, the National Research Council (NRC, 2001) identifies a range of indirect costs of transforming “data” into useful “information.” One of the conclusions of the NRC (p. 16) is that “transforming technical data into a form that is meaningful to nontechnical users – a process often including either the integration of remote sensing data with other types of data or scientific research to characterize the data (or both) – is highly dependent on the information requirements of applied users and on the skills of technical experts.” The NRC concludes that this process is poorly developed and an impediment – a cost – in effective use of remote sensing.

### Benefits

Benefits of remote sensing include enhanced scientific understanding of the Earth and Earth processes, improved ability to make decisions in managing natural and environmental resources, and, arguably, the prestige-accorded demonstration of technological prowess in building and deploying a remote sensing system or even the benefits to national or regional security associated with remote sensing of Earth resources. Benefits can accrue to the private sector as well as the public sector; in fact, some remote sensing systems are owned and operated exclusively by the private sector or as

joint arrangements between the private and public sectors.

The National Research Council (NRC, 2008) discusses the enhanced scientific understanding of the Earth and Earth processes from remote sensing. These accomplishments (benefits) include monitoring global **stratospheric ozone** depletion, detecting tropospheric ozone, measuring the Earth’s radiation budget, generating synoptic weather imagery, assimilating data for sophisticated numerical weather prediction, discovering the dynamics of ice sheet flows, detecting mesoscale variability of **ocean surface topography** and its importance in ocean mixing, observing the role of the ocean in climate variability, monitoring agricultural lands for a famine early warning system, and determining the Earth reference frame with unprecedented accuracy (see NRC, 2008, Table S.1, p. 4).

Numerous case studies have examined the benefits of applications of remote sensing for managing environmental and natural resources (for instance, see Battese, 1988; Ning, 1996; Nelson, 1997; Dudhani, 2006; Ward, 2000). Most of these studies express the benefits of remote sensing in terms of percentage improvements in statistical measures of accuracy; fewer studies express benefits in monetary terms. The primary difficulty in attempting to monetize benefits of remote sensing is that the environmental and natural resources themselves are typically “public goods,” that is, resources which, unlike ordinary goods and services, are not exchanged in markets (see Macauley, 2006 for a discussion of the challenges in valuing “information” such as remote sensing). Accordingly, it is difficult to ascribe monetary value to remote sensing data about nonmarketed resources. Bouma and coauthors (2009) carry out a case study of the value of satellite remote sensing of water quality in the North Sea and are able to monetize benefits in terms of the costs saved by water managers. Williamson and coauthors describe the economic value of remote sensing in improving forecasts of natural disasters in terms of reducing loss of life, property damage, and other costs. These approaches thus illustrate ways in which to express benefits in financial terms, but this line of research remains small and fragmented. And, because remote sensing data can often serve multiple purposes (remote sensing of land use, for instance, can inform highway planning as well as forecasts of agricultural production), a “unit” of data may be undervalued if only one of many applications of the data is evaluated in a case study.

### Assessing costs and benefits

Few studies have attempted to assess the net benefits – that is, comparing both the costs and benefits of remote sensing and quantifying the extent to which benefits exceed costs. Given the difficulty in monetizing benefits, quantitatively relating benefits and costs is obviously even more difficult. In the few instances when benefits and costs are expressed in common units (say, dollars), the

comparison is easier. For example, if benefits are expressed in terms of costs saved, and if cost data are available, then benefits and costs can be compared (Bouma and coauthors make this comparison, for instance). If benefits and costs are combined, a general rule of thumb in benefit and cost assessment is that the *difference* between benefits and costs is preferred to the ratio between benefits and costs. Using the difference avoids the problem of whether a benefit is a negative cost, which can lead to ambiguous results when using the ratio rather than the numerical difference. (An example: In estimating the benefits of remote sensing in monitoring air pollution, is a reduction in pollution a benefit or an avoided cost? Expressing the reduction as a benefit or a cost will not affect the difference but will affect the result if benefits and costs are expressed as a ratio.)

## Conclusion

Assessing the benefits and costs of remote sensing is one of the challenges of ascertaining the appropriate amount of investment a society should undertake in remote sensing systems. When is the cost of these systems justified by the benefits they confer? For a variety of reasons, quantifying costs and benefits is difficult. Expressing benefits in financial terms is particularly difficult, as remote sensing data may confer benefits in the form of new knowledge or about natural resources (air, water, climate, land, oceans) and the environment (air and water quality, land use). Society values these benefits, but ascribing monetary value to them is quite difficult.

## Bibliography

- Battese, G. E., 1988. An error-components model for prediction of county crop areas using survey and satellite data. *Journal of the American Statistical Association*, **83**(401), 28–36.
- Bouma, J. A., van der Woerd, H. J., and Kuik, O. J., 2009. Assessing the value of information for water quality management in the North Sea. *Journal of Environmental Management*, **90**(2), 1280–1288.
- Dudhani, S., 2006. Assessment of small hydropower potential using remote sensing data for sustainable development in India. *Energy Policy*, **34**(17), 3195–3205.
- Macauley, M. K., 2006. The value of information: measuring the contribution of space-derived earth science data to resource management. *Space Policy*, **22**, 274–282.
- National Research Council, Committee on Scientific Accomplishments of Earth Observations from Space, 2008. *Earth Observations from Space: The First 50 Years of Scientific Accomplishments*. Washington, DC: The National Academies.
- National Research Council, Space Studies Board and Ocean Studies Board, 2001. *Transforming Remote Sensing Data into Information and Applications*. Washington, DC: The National Academies.
- Nelson, G. C., 1997. Do roads cause deforestation? Using satellite images in econometric analysis of land use. *American Journal of Agricultural Economics*, **79**(1), 80–88.
- Ning, S. K., 1996. Soil erosion and non-point source pollution impacts assessment with the aid of multi-temporal remote sensing images. *Journal of Environmental Management*, **79**(1), 88–101.
- Ward, D., 2000. Monitoring growth in rapidly urbanizing areas using remotely sensed data. *The Professional Geographer*, **52**(3), 371–386.
- Williamson, R. A., Hertzfel, H. R., Cordes, J., and Logsdon, J. M., 2002. The socioeconomic benefits of earth science and applications research: reducing the risks and costs of natural disasters in the USA. *Space Policy*, **18**(1), 57–66.

## Cross-references

[Commercial Remote Sensing Data Policies](#)  
[Emerging Applications](#)  
[Environmental Treaties](#)  
[Mission Operations, Science Applications/Requirements](#)

## CROP STRESS

Susan Moran  
 USDA ARS Southwest Watershed Research Center,  
 Tucson, AZ, USA

## Synonyms

Insect infestation; Nitrogen deficiency; Water deficiency; Weed infestation

## Definitions

*Crop stress*. Crop response to environmental factors that results in suboptimal crop production.

## Introduction

Crop stress is the plant response to environmental factors that ultimately results in suboptimal crop production. The environmental factors of primary interest to US corn, cotton, soybean, and wheat producers are water, nutrients, weeds, and insects. Not coincidentally, these are also the factors that are most easily managed through irrigation and applications of fertilizer, herbicides, and pesticides. Crops are generally managed to minimize crop stress within the constraints of producing a profitable yield and minimizing environmental impact. The day-to-day management decisions to achieve this delicate balance are based in part on information about the extent, duration, and cause of crop stress. The role of remote sensing in crop management is to provide such information about crop stress using sensors that acquire data in the visible (VIS), near-infrared (NIR), short-wave infrared (SWIR), thermal infrared (TIR), and synthetic aperture radar (SAR) wavelengths. A first step is to understand the physical plant manifestations associated with crop stress that are most easily detected with optical and microwave remote sensing.

## Plant manifestations of crop stress

Water stress affects the plant leaf canopy by two primary mechanisms (Rosenthal et al., 1987). The first involves the closure of leaf stomata, which results in a reduction in

photosynthesis and transpiration. The associated increase in leaf temperature can be detected using remote sensing in the thermal infrared wavelengths (Jackson et al., 1981). The second mechanism involves a decrease in leaf expansion and an increase in leaf senescence. The reduction in plant leaf canopy development in comparison to well-watered plants can be detected through estimates of LAI or ground cover made using remote sensing in the visible wavelengths (Maas and Rajan, 2008). The mechanism affecting leaf stomata is initiated when available soil water in the root zone falls below 30 %. In contrast, the mechanism affecting leaf expansion and senescence is initiated when available soil water in the root zone falls below 50 %. Thus, leaf expansion and senescence typically are affected by water stress before photosynthesis and transpiration. There are a number of secondary effects of water stress that are associated with the adaptation of plants to the decrease in water availability.

The crop physiological adaptations to transient water deficit range from changes in canopy architecture to adjustments in leaf osmotic potential (Turner, 1977). Many of these adaptations have a pronounced effect on spectral reflectance and SAR backscatter and the optical properties of plants that allow stress detection with remote sensing. Crops have the capacity for developmental plasticity to complete the life cycle before serious water deficits develop. For example, studies have shown that wheat can hasten maturity in response to mild water deficits at the critical time between flowering and maturity. To endure prolonged water deficit while maintaining high water potential, some crops reduce water loss through increased epidermal waxes of leaves and a reduction in general plant productivity. Other adaptations are to reduce the radiation absorbed by the plant through leaf movement (e.g., leaf cupping, paraheliotropism, or wilting) or to reduce leaf area through decreased leaf expansion, reduced tillering and branching, and leaf shedding. It is generally reported that leaves under water stress show a decrease in reflectance in the NIR spectrum and a reduced red absorption in the chlorophyll active band (0.68  $\mu\text{m}$ ); however, Guyot et al. (1984) found that it was necessary to have an extremely severe water stress to affect the leaf reflective properties. In the TIR, there is a direct link between the process of plant water evaporation and the plant thermal response (i.e., water evaporates and cools the leaves) explained by Jackson et al. (1981).

Like crop water stress, crop nutrient stress has a direct effect on crop growth and development. Nitrogen is frequently the major limiting nutrient in agricultural soils. Leaves deficient in nitrogen absorb less and scatter more visible light (Schepers et al., 1996). Due to the link between leaf chlorophyll and nitrogen concentrations (Daughtry et al., 2000), leaves marginally deficient in nitrogen may appear a lighter, less saturated shade of green, and more severely nitrogen-stressed leaves may appear yellowish green and chlorotic. Thomas and Oerther (1972) found that with nitrogen deficiency, the visible reflectance increased (due to decreasing

chlorophyll content) and the NIR and SWIR reflectances decreased (due to decreasing number of cell layers). Nutrient deficiencies in crop canopies have the potential to affect canopy architecture and the optical properties of not only the leaf but also the stem and flower/grain head. Manifestations of typical nutrient stresses generally appear initially as changes in the optical properties of leaves and only later as change in the canopy architecture and decreased canopy biomass. The position of the red edge (an abrupt, step increase in the leaf reflectance in the NIR around 0.72  $\mu\text{m}$  just outside the visible region) offers a robust metric for monitoring leaf and canopy nutrient status (Peñuelas and Filella, 1998). Recently, the concentration of epidermal polyphenolics, secondary metabolites in the leaf that may be measured using a commercially available clip-on UV absorption meter, has shown promise as a surrogate measure of leaf nitrogen status (see, for example, Tremblay et al., 2007; Demotes-Mainard et al., 2008; Meyer et al., 2006).

Crop stress due to weed interference has been attributed to many factors, including allelopathy and competition for sunlight, soil water, and nutrients (Sikkema and Dekker, 1987). The plant manifestation of weed-induced crop stress is generally reduced crop yields. Because weed distribution is influenced by drainage, topography, soil type, and microclimate, crop stress in weed-infested fields is highly variable. Variations in reflectance patterns and canopy temperatures over time and space may reveal crop stress associated with soil and topographic conditions (Wiles et al., 1992). In the early season, herbicide application is based simply on the presence or absence of plants, and remote sensing systems generally use the reflectance differences between relatively wide spectral bands in the visible and NIR spectra to make the distinction between plants and soil or rock (Medlin et al., 2000). Post-emergent herbicide applications require discrimination between weeds and crops, which is generally accomplished by using the difference between spectral signatures of crops and specific weeds or by acquiring images when weed coloring is particularly distinctive (Brown et al., 1994) or weed patches are comparatively large, dense, and/or tall (Pérez et al., 2000).

Remote sensing is not used to directly observe insects, but rather, to observe the damage to crop foliage and to detect plant canopy conditions that might be conducive to insect infestation. Early infestations of some insects are associated with leaf senescence or mortality, resulting in reduction in canopy density. Some crop pests not only cause physical damage to the leaf canopy but also cause a change in the spectral reflectance characteristics of the affected foliage. Aphids (*Aphididae*) deposit honeydew on cotton leaves which supports the growth of sooty mold (*Aspergillus* spp.), thus profoundly affected the reflectance characteristics of the leaves, particularly in the NIR (Maas, 1998). Other pests, such as spider mites (*Tetranychus* spp.), can cause changes in leaf reflectance that can be detected using remote sensing in the visible and NIR wavelengths (Fitzgerald et al., 2001, 2004). These spectral

signatures are distinct enough to differentiate them from water stress effects (Fitzgerald et al., 2000). Insects are sometimes attracted to areas within fields that contain the most vigorous plant growth. Areas of lush cotton growth in Louisiana were identified with spectral vegetation indices to direct scouting for the tarnished plant bug (*Lygus lineolaris*) and facilitate spatially variable insecticide applications (Willers et al., 2000).

### Remote sensing of crop stress

Readers are referred to recent reviews by Moran et al. (2004) and Hatfield et al. (2004) for an extensive summary of remote sensing applications and products for detecting crop stress associated with water and nutrient deficiencies and weed and insect infestations. The greatest progress has been made in crop water stress detection. The use of remote sensing in irrigation scheduling has been reviewed by Maas (2003). Some spectral crop water stress indices have been commercialized for irrigation scheduling (Jackson et al., 1981; Burke et al., 1988). Opportunities for deriving crop nutrient status and pest infestation from remote sensing have recently increased with the development of hyperspectral and narrowband multispectral imaging sensors (Gitelson et al., 2006; LaCapra et al., 1996). The production of fine-resolution digital elevation models (DEM) with high vertical accuracies from radar systems provides useful supplemental information for the management of large agricultural areas. Recent development and launches of multispectral sensors with fine resolution has stimulated efforts to observe the early stages of pest infestations and areas with potential for pest infestations in time for control measures (Fitzgerald et al., 2004).

### Conclusions

The technologies of the future will probably include sensors to measure natural and genetically induced fluorescence related to crop vigor (e.g., Liu et al., 1997), more focus on multispectral data fusion including SWIR, TIR, and microwave measurements (e.g., Jackson et al., 2004), and increased assimilation of remotely sensed data in crop yield models and decision support systems (e.g., Maas, 2005; Baez et al., 2005; Maas, 2005; Ko et al., 2005, 2006). The latter has the potential to address one of the greatest challenges to use of remote sensing as a source of information about crop stress – determining the cause of crop stress. It has been particularly difficult to discriminate crop stress due to water and nitrogen, which often produce similar plant manifestations but require different and costly management. Decision support systems based on crop growth theory can assimilate producer knowledge, management history, and remote sensing information to best determine the extent, magnitude, and cause of crop stress. This could lead to the turnkey solution called for by Hatfield et al. (2008) for application of remote sensing for agronomic decisions suited to both specialists and nonspecialists.

### Bibliography

- Baez, A. D., Kiniry, J., Maas, S. J., Tiscereno, M., Macias, J., Mendoza, J., Richardson, C., Salinas, G. J., and Manjarrez, J. R., 2005. Large-area maize yield forecasting using leaf area index based yield model. *Agronomy Journal*, **97**(2), 418–425.
- Brown, R. B., Steckler, J.-P. G. A., and Anderson, G. W., 1994. Remote sensing for identification of weeds in no-till corn. *Transactions of ASAE*, **37**, 297–302.
- Burke, J. J., Mahan, J. R., and Hatfield, J. L., 1988. Crop-specific thermal kinetic windows in relation to wheat and cotton biomass production. *Agronomy Journal*, **80**, 553–556.
- Daughtry, C. S. T., Walthall, C. L., Kim, M. S., deColstoun, E. B., and McMurtrey, J. E., 2000. Estimating corn leaf chlorophyll concentration from leaf and canopy reflectance. *Remote Sensing of Environment*, **74**, 229–239.
- Demotes-Mainard, S., Boumaza, R., Meyer, S., and Cerovic, Z. G., 2008. Indicators of nitrogen status for ornamental woody plants based on optical measurements of leaf epidermal polyphenol and chlorophyll contents. *Scientia Horticulturae*, **115**, 377–385.
- Fitzgerald, G. J., Maas, S. J., and DeTar, W. R., 2000. Assessing spider mite damage in cotton using multispectral remote sensing. In *Proceedings of the Beltwide Cotton Conference*, San Antonio, TX, Vol. 2, pp. 1342–1345.
- Fitzgerald, G. J., Maas, S. J., and DeTar, W. R., 2001. Spying on spider mites from on high. *California-Arizona-Texas Cotton Magazine*, **Fall**, 2001, 13–15.
- Fitzgerald, G. J., Maas, S. J., Pinter, P. J., Hunsaker, D. J., and Clarke, T. R., 2002. Spider mite damage mapping and cotton canopy biophysical characterization using spectral mixture analysis. In *Proceedings Symposium on American-Taiwan Agricultural Cooperative Projects*, Taipei, Taiwan, November 15, 2005.
- Fitzgerald, G. J., Maas, S. J., and DeTar, W. R., 2004. Spider mite detection and canopy component mapping in cotton using hyperspectral imagery and spectral mixture analysis. *Precision Agriculture*, **5**, 279–289.
- Gitelson, A. A., Keydan, G. P., and Merzlyak, M. N., 2006. Three-band model for noninvasive estimation of chlorophyll, carotenoids and anthocyanin contents in higher plant leaves. *Geophysical Research Letters*, **33**, 111402, doi:10.1029/2006G1026457.
- Guyot, G., Dupont, O., Joannes, H., Prieur, C., Huet, M., and Podaire, A., 1984. Investigation into the Mid-IR spectral band best suited to monitoring vegetation water content. In *Proceedings of 18th International Symposium on Remote Sensing of the Environment*, October 1–5, 1984, Paris, pp. 1049–1063.
- Hatfield, J. L., Prueger, J. H., Kustas, W., Hatfield, J. L., Prueger, J. H., and Kustas, W. P., 2004. In Ustin, S. (ed.), *Remote Sensing for Natural Resources Management and Environmental Monitoring: Manual of Remote Sensing*, 3rd edn. New York: Wiley, Vol. 4, pp. 531–568. Chap. 10.
- Hatfield, J. L., Gitelson, A. A., Schepers, J. S., Schepers, J. S., and Walthall, C. L., 2008. Application of spectral remote sensing for agronomic decisions. *Agronomy Journal*, **100**, S-117–S-131.
- Jackson, R. D., Idso, S. B., Reginato, R. J., and Pinter, P. J., Jr., 1981. Canopy temperature as a crop water stress indicator. *Water Resources Research*, **17**, 1133–1138.
- Jackson, T. J., Chen, D., Cosh, M., Li, F., Anderson, M., Walthall, C., Doraiswamy, P., and Hunt, E. R., 2004. Vegetation water content mapping using Landsat data derived normalized difference water index for corn and soybeans. *Remote Sensing of Environment*, **92**, 475–482.
- Ko, J., Maas, S. J., Lascano, R. J., and Wanjura, D., 2005. Modification of the GRAMI model for cotton. *Agronomy Journal*, **97**(5), 1374–1379.
- Ko, J., Maas, S. J., Mauget, S., Piccinni, G., and Wanjura, D., 2006. Modeling water-stressed cotton growth using within-season remote sensing data. *Agronomy Journal*, **98**, 1600–1609.

- LaCapra, V. C., Melack, J. M., Gastil, M., and Valeriano, D., 1996. Remote sensing of foliar chemistry of inundated rice with imaging spectrometry. *Remote Sensing of Environment*, **55**, 50–58.
- Liu, C., Muchhal, U. S., and Raghothama, K. G., 1997. Differential expression of TPS-11, a phosphate starvation-induced gene in tomato. *Plant Molecular Biology*, **33**, 867–874.
- Maas, S. J., 1998. Remote sensing: value in a bird's-eye view. In Wrona, A. F. (ed.), *Cotton Physiology Today*, 9th edn. Memphis: National Cotton Council, Vol. 2, pp. 13–15.
- Maas, S. J., 2003. Irrigation scheduling by remote sensing technologies. In Stewart, B. A., and Howell, T. A. (eds.), *Encyclopedia of Water Science*. New York: Marcel Dekker, pp. 523–527.
- Maas, S. J., 2005. An overview of interfacing models with remote sensing. In *Proceedings of the 35th Biological Systems Simulation Conference*. Phoenix, AZ, pp. 31–33.
- Maas, S. J., and Rajan, N., 2008. Estimating ground cover of field crops using medium-resolution multispectral satellite imagery. *Agronomy Journal*, **100**(2), 320–327.
- Maas, S., Lascano, R., Cooke, D., Richardson, C., Upchurch, D., Wanjura, D., Krieg, D., Mengel, S., Ko, J., Paynem, W., Rush, C., Brightbill, J., Bronson, K., Guo, W., and Rajapakse, S., 2004. Within-season estimation of evapotranspiration and soil moisture in the high plains using YieldTracker. In *Proceedings of the 2004 High Plains Groundwater Resources Conference*. Lubbock, TX, pp. 219–226.
- Medlin, C. R., Shaw, D. R., Gerard, P. D., and LaMastus, F. E., 2000. Using remote sensing to detect weed infestations in Glycine max. *Weed Science*, **48**, 393–398.
- Meyer, S., Cerovic, Z. G., Goulas, Y., Montpied, P., Demotes-Mainard, S., Bidet, L. P. R., Moya, I., and Dreyer, E., 2006. Relationships between optically assessed polyphenols and chlorophyll contents, and leaf mass per area ratio in woody plants: a signature of the carbon-nitrogen balance within leaves? *Plant, Cell & Environment*, **29**, 1338–1348.
- Moran, M. S., Maas, S. J., Vanderbilt, V. C., Barnes, E. M., Miller, S. N., and Clarke, T. R., 2004. Application of image-based remote sensing to irrigated agriculture. In Ustin, S. (ed.), *Remote Sensing for Natural Resources Management and Environmental Monitoring: Manual of Remote Sensing*, 3rd edn. New York: Wiley, Vol. 4, pp. 617–676. Chap. 12.
- Peñuelas, J., and Filella, I., 1998. Visible and near infrared reflectance techniques for diagnosing plant physiological status. *Trends in Plant Science*, **3**(4), 151–156.
- Pérez, A. J., López, F., Benlloch, J. V., and Christensen, S., 2000. Colour and shape analysis techniques for weed detection in cereal fields. *Computers and Electronics in Agriculture*, **25**, 197–212.
- Rosenthal, W., Arkin, G., Shouse, P., and Jordan, W., 1987. Water deficit effects on transpiration and leaf growth. *Agronomy Journal*, **79**, 1019–1026.
- Schepers, J. S., Blackmer, T. M., Wilhelm, W. W., and Resende, M., 1996. Transmittance and reflectance measurements of corn leaves from plants with different nitrogen and water supply. *Journal of Plant Physiology*, **148**, 523–529.
- Sikkema, P. H., and Dekker, J., 1987. Use of infrared thermometry in determining critical stress periods induced by quackgrass (*Agropyron repens*) in Soybeans (*Glycine max*). *Weed Science*, **35**, 784–791.
- Thomas, J. R., and Oerther, G. F., 1972. Estimating nitrogen content of sweet pepper leaves by reflectance measurements. *Agronomy Journal*, **64**, 11–13.
- Tremblay, N., Wang, Z., and Belec, C., 2007. Evaluation of the Dualex for the assessment of corn nitrogen status. *Journal of Plant Nutrition*, **30**, 1355–1369.
- Turner, N. C., 1977. Drought resistance and adaptation to water deficits in crop plants. In Mussell, H., and Staples, R. C. (eds.), *Stress Physiology in Crop Plants*. New York: Wiley, pp. 344–372.
- Wiles, L. J., Oliver, G. W., York, A. C., Gold, H. J., and Wilkerson, G. G., 1992. Spatial distribution of broadleaf weeds in North Carolina soybean (*Glycine max*) fields. *Weed Science*, **40**, 554–557.
- Willers, J. L., Seal, M. R., and Luttrell, R. G., 1999. Remote sensing, line-intercept sampling for tarnished plant bugs (Heteroptera: Miridae) in mid-South cotton. *Journal of Cotton Science*, **3**, 160–170.

## Cross-references

[Agriculture and Remote Sensing](#)  
[Data Assimilation](#)  
[Irrigation Management](#)  
[Precision Agriculture](#)  
[Soil Moisture](#)  
[Soil Properties](#)  
[Vegetation Indices](#)  
[Vegetation Phenology](#)

---

## CRYOSPHERE AND POLAR REGION OBSERVING SYSTEM

---

Mark Drinkwater

Mission Science Division, European Space Agency,  
 ESA/ESTEC, Noordwijk ZH, The Netherlands

## Definition

*Cryosphere*. It collectively describes elements of the Earth system containing water in its frozen state and includes sea ice, lake and river ice, snow cover, solid precipitation, glaciers, ice caps, ice sheets, permafrost, and seasonally frozen ground. Although a significant portion of the world's snow and ice is found in the polar regions, cryosphere exists at all latitudes and in about 100 countries.

*Polar regions*. Earth's polar regions are the areas of the globe surrounding the north and south poles typically encompassed by a line of latitude corresponding to 66° 34' north or south (i.e., between each pole and its corresponding polar circle), which is the approximate limit of the midnight sun and the polar night. Alternatively, it can be defined as the region where the average temperature for the warmest month (July) is below 10 °C (50 °F).

## Introduction

Knowledge of the state of the cryosphere is important for weather and climate prediction, assessment and prediction of [sea level rise](#), availability of freshwater resources, navigation, shipping, fishing, mineral resource exploration and exploitation, and in many other practical applications (IGOS, 2007). Changes to the cryosphere have far-reaching climate and socioeconomic consequences. The need for reliable global monitoring is essential to address the issues of climate and cryosphere within the Earth system. Despite its importance, the cryosphere remains one of

the most under-sampled domains in the Earth's climate system.

The *Cryosphere and Polar Region Observing System* (hereafter abbreviated as *CryOS*) shall provide a stable, long-term monitoring capability using a combination of in situ and remote sensing measurement capabilities (Drinkwater et al., 2008). The satellite remote sensing part of this system specifically fulfills the need for regular measurements of changes in the global cryosphere in response to climate variability and change. In particular, due to the logistical challenge of accessing the remote polar regions and high elevation cryosphere, together with the harsh weather conditions and extended winter-season darkness, satellites are the primary means of making year-round, day and night, weather-independent observations. Their advantage also lies in their ability to obtain uniform, consistent global sampling, including observations of the north and south polar ice-covered regions and lower-latitude mountain glaciers, permafrost, lake and river ice, and seasonally snow-covered areas.

The objectives of the satellite element of *CryOS* shall be to quantify snow- and ice-mass variability and mass, energy, freshwater, and gas exchanges between the cryosphere and the other elements of the Earth system (land, atmosphere, and ocean). This system element must respond to climate research and policy needs, socio-economic needs, and operational snow and ice service needs. Moreover, the resulting data shall be made easily and freely available and shall be integrated with data from airborne and in situ observing systems for the purpose of developing a comprehensive record on cryospheric variability (Drinkwater et al., 2008, 2010).

Satellites contributing to *CryOS* must comprise a broad range of capabilities and have the ability both to sample the primary aspects of the cryosphere. Due to the sensitivity of the cryosphere to temperature and corresponding short timescales on which snow and ice may change, the system must be capable of providing global coverage with daily sampling from broad-swath, low-resolution sensors, complemented by high-resolution satellite sensors with the ability to provide detailed local and regional information, as required by the specific application.

### Essential satellite elements of an observing system

The cryosphere and polar observing system must contain the following basic satellite capabilities:

- Daily, all-weather, global imaging
- High-resolution all-weather polar ice dynamics imaging
- Surface temperature and albedo change
- Ice topography/elevation/thickness change
- Gravity and mass distribution and exchange
- Position monitoring/navigation
- Telecommunications for data relay

Additionally, the geophysical products described in the list above require a source of independent measurement

data for product validation. Together these general capabilities are required to provide robust information on the main terrestrial and marine cryospheric domains.

### Terrestrial cryosphere

For the terrestrial cryosphere, *CryOS* shall provide a complete picture of the snow reserves and solid precipitation, river and lake ice, permafrost, seasonally frozen ground, glaciers, ice caps, and ice sheets. This element of the observing system bridges meteorological and hydrological applications and ensures incorporation of data on the appropriate cryospheric variables in the next generation of hydrological and climate models. The basic challenge is to provide global data with the accuracy required for water management and disaster mitigation (e.g., avalanches), for monitoring climate change and variability, and for the estimation of [sea level rise](#).

### Marine cryosphere

For the marine cryosphere, *CryOS* shall provide regular observations of sea ice and ice shelf characteristics and their dynamics. Ideally these data shall be supported by Global Ocean Observing System (GOOS) observations of ocean temperature, salinity, dynamic topography, and tides to understand the ocean-ice-atmosphere coupling processes responsible for variability and changes.

The following sections treat each of the cryospheric subdomains which require specific monitoring capabilities.

### Snow extent and water equivalent

Terrestrial snow cover has the largest geographic extent of the components of the cryosphere covering nearly 50 million km<sup>2</sup> of the Northern Hemisphere in winter. Snow, with its high albedo, influences surface water and energy fluxes, atmospheric dynamics and weather, frozen ground and permafrost, biogeochemical fluxes, and ecosystem dynamics.

In order to support water, weather, and climate applications, various observations of snow are required. Remote sensing observations focus on the daily geographic extent of snow cover and snow water equivalent (SWE; the total water content) since these two quantities have a fundamental control on hydrologic and ecosystem processes.

Point measurements of solid precipitation and snow depth on the ground are often unrepresentative of surrounding areas, and so satellite remote sensing data must be combined with these snow measurement sites to provide a consistent picture at regional or continental scale. Satellite measurements of snow extent are typically accomplished using visible and near-infrared sensors on satellites in either polar low Earth orbit (LEO) or geostationary orbit (GEO). Using such multispectral measurements from GOES, MSG/SEVIRI, AVHRR, MODIS, MERIS, MISR, and AATSR, it is possible to discriminate between snow- and cloud-covered regions and to establish

the extent of snow cover. Currently, these sensor data are complemented by all-weather SWE products produced from passive and active microwave data with appropriate frequencies such as SSM/I, AMSR-E, and ASCAT; QuikSCAT; and Oceansat-2 Scat though their low spatial resolution currently limits their use in hydrometeorological models. Future multiple-frequency (Ku- and X-band), high-resolution active microwave sensors such as synthetic aperture radars (SAR) (see entry [Data Processing, SAR Sensors](#)) must be developed specifically for measurement of SWE at the relevant sub-kilometer scale.

### Solid precipitation

To date satellite precipitation measurements have greatly increased our ability to monitor and observe liquid precipitation (i.e., rainfall) globally. However, a similar capability does not yet exist at high latitudes for solid precipitation (i.e., snow and hail). Thus, development of a robust snowfall measurement capability remains a high priority for the cryosphere, such that the contribution of this critical element of the high-latitude water cycle can be fully characterized.

### River and lake ice

Lake and river ice are a key component of the terrestrial cryosphere, and seasonal ice growth plays an important role in regulating physical, chemical, and biological processes. Long lake and river ice records serve as an indicator of high-latitude climate variability and serve as an important data source for initializing weather forecast and climate models (Jeffries et al., [in press](#)). Meanwhile, the presence of freshwater ice also has a number of socioeconomic implications ranging from transportation to the occurrence and damaging effects of ice-jam flooding.

The observing system must be able to monitor the seasonal distribution and duration of lake and river ice. Autumn freeze-up and spring time thaw may be monitored at high resolution (10–120 m) under daylight conditions using Landsat MSS or TM and SPOT HRV for small lakes and narrow rivers, whereas for larger features the detection of the presence of ice has more traditionally been accomplished using medium-resolution (250 m–1 km) visible and infrared AVHRR and MODIS products. Nonetheless, extensive cloud cover and periods of darkness in winter limit their use at high latitudes. For establishing freeze-up and break-up dates and for year-round monitoring of seasonal ice on smaller lakes and rivers, SAR image products from ERS-1 and ERS-2, RADARSAT-1 and RADARSAT-2, Envisat ASAR, ALOS PALSAR, and TerraSAR-X may be considered more optimal (Jeffries et al., [2005](#)). These are complemented by scatterometer and passive microwave monitoring of the largest lakes.

### Permafrost

Permafrost is subsurface soil which remains at or below the freezing point of water for 2 or more years.

Such permanently frozen ground and seasonally or intermittently frozen ground is widespread in the Arctic, subarctic, alpine, and high plateau regions, and in ice-free areas of the Antarctic and subantarctic. In the Northern Hemisphere, permafrost is estimated to cover approximately 23 million km<sup>2</sup> with up to 17 million km<sup>2</sup> of this underlying exposed land (Brown et al., [1997](#)). Seasonal and intermittently frozen ground together occupies approximately 56 million km<sup>2</sup> in the Northern Hemisphere and includes the “active layer” over permafrost (i.e., the layer which undergoes seasonal thawing) and soils outside permafrost regions (Zhang et al., [2003](#)).

Permafrost and the freeze-thaw state of land surfaces exert a critical influence on the surface energy balance, hydrologic cycle, ecosystems, biogeochemical fluxes, hydrology, and weather and climate systems. Further, permafrost thaw can have significant socioeconomic consequences through its direct impact on structures such as roads, buildings, railways, and pipelines.

The primary needs in permafrost areas are to determine the terrain and its changes over time (including topography and vegetation characteristics), in association with the thermal state of the surface. Near surface soil freeze-thaw state is a critical variable since it is a primary indicator in relation to the fluxes of energy, water, and carbon. Unlike other components of the terrestrial cryosphere, subsurface properties of permafrost terrain are not directly observable from remote sensing platforms. However, many surface features of permafrost terrain are observable with a variety of sensors ranging from aerial photography and high-resolution optical satellite imagery to synthetic aperture radar and satellite passive microwave radiometry (Duguay et al., [2005](#); Käab, [2008](#)).

Passive optical imaging radiometers operating at visible and infrared wavelengths have traditionally been used under cloud-free conditions to map changes in the characteristics and thermal condition of permafrost terrain. Very-high-resolution (0.2–5 m pixels), narrow swath optical sensors such as EO1 Hyperion, Ikonos, or QuickBird can provide extremely detailed information on small features of the landscape. For mapping the evolution of features over time, ASTER, ALOS PRISM, ALOS AVNIR-2, and SPOT image data (10–100 m pixels) can be used, with the advantage of availability of SPOT data since the mid-1980s. For large area land cover mapping, these are complemented by medium-resolution (250 m–1 km pixels) broader swath imaging instruments (such as MERIS, MODIS) providing regional to continental scale coverage on a daily basis. Low-resolution (12–25 km pixels) image data from passive microwave radiometers and scatterometers, for example, have the advantage of year-round, daily, weather-independent continental scale coverage, and may be used to monitor the circumpolar spatial and temporal details of freeze and thaw cycles.

In addition, digital terrain models (DTMs) are also essential for understanding and modeling permafrost and

its evolution. High-resolution and high vertical accuracy DTMs may be derived at high-latitude tundra permafrost from repeat-pass InSAR or tandem interferometry (i.e., ERS-2-Envisat ASAR cross interferometry, COSMO-SkyMed, or TanDEM-X) measurements. Meanwhile changes in permafrost terrain may be detected using differential InSAR or DInSAR (i.e., the calculation of ground deformation from the difference between two InSAR images). In addition to InSAR techniques, lower-precision optical DTMs can be derived from stereoscopic optical sensors, such as SPOT HRV, Cartosat-1, and ALOS PRISM, or using stereophotogrammetry.

### Ice sheets (topographic change, mass change, and sea level)

Ice sheets play a key role in the climate system, locking up vast amounts of freshwater in the form of snow and solid ice, and by their significant influence on the energy balance of the polar regions. The two major ice sheets remaining from the last ice age blanket most of Greenland and Antarctica. They contain enough freshwater, in the form of ice, to raise sea level by approximately 7.2 and 62 m, respectively (Alley et al., 2005). The inland ice rests on bedrock, while their floating ice shelf extensions link the ice sheet with the ocean. Ice is transported from the inland toward the ice shelves via fast-flowing ice streams and outlet glaciers.

Ice sheets undergo seasonal growth by snowfall and then wasting by summer melting, with accompanying release of freshwater into the ocean. The extent to which ice sheets and glaciers are changing is reported as “mass balance” by measuring the net inputs and net losses. The totals of precipitation and accumulation, ablation, melting, runoff, sublimation/evaporation, ice dynamics, and iceberg calving are reported over the course of each year and used to compute the net balance either as a gain in mass (positive) or negative loss of mass (negative). Ice sheets may lose mass by a combination of dynamical processes which govern ice stream flow across the grounding line, or by surface ablation, basal melting, and iceberg calving at the seaward margins of floating ice shelves. Exchange of mass between ice sheets and oceans as freshwater has a major impact on both ocean circulation and sea level and is currently estimated to contribute more than 0.3 mm/year (30 cm/century) to sea level.

Since the early 1990s, there are indications that rapid changes are taking place particularly around the margins of the Greenland and Antarctic ice sheets (Rignot et al., 2008; Van Den Broeke et al., 2009). A combination of remote sensing methods have highlighted that streaming ice flow (i.e., ice motion) is responsible for the largest proportion of mass loss from the ice sheets. By contrast, the central plateau of both ice sheets appears to be close to net neutral balance, with accumulation balancing ice-mass losses.

Remote sensing of ice sheet behavior relies on the ability of the sensors to acquire data over vast areas of terrain,

during day or night and also in all-weather conditions. Optical satellite data at visible wavelengths have been used since the 1960s to define changes in the ice margin and surface characteristics, with pairs of images acquired at different times used for motion of the surface and digital terrain model generation, the latter in stereographic mode.

Passive microwave radiometer or scatterometer images of ice sheets are often used to measure the onset, duration, and extent of ice sheet surface melt, since they are sensitive to the appearance of melt water in snow. Each has also been used to make estimates of mean annual snow accumulation.

Changes in ice sheet surface elevation averaged over large areas can be interpreted as a measure of changing ice sheet volume. Since 1978, successive radar altimeters have measured ice sheet and ice shelf surface elevation. Their primary limitation has been their ability to recover accurate data in the steep terrain around the edges of the ice sheets. Recently, this limitation has been addressed with the CryoSat-2 SAR interferometric radar altimeter. The ICESat laser altimeter has also recently acquired detailed topography around the sloping margins of the Greenland and Antarctic ice sheets. The advantage of the laser altimeter is its smaller measurement spot on the surface, allowing more accurate elevation data, albeit limited by optically thick cloud conditions.

SAR measurements complement the other remote sensing instrument data described above, through high-resolution observations. Since the early 1990s, SAR images have provided a wealth of new information on characteristics of the ice sheet surface, though the advent of SAR interferometry (InSAR) has enabled measurement of details of topography as well as precise details on the motion of ice (Rignot et al., 2011). In conjunction with ice sheet models, InSAR data provide a valuable means to study the impact of ice stream velocity on the net loss of ice mass.

Satellite gravity provides direct measurements of gravity anomalies due to ice sheet mass unloading or ice sheet mass change. Data from the GRACE satellite confirms other measurements which suggest that the Greenland and Antarctic ice sheets are losing mass around their margins over the last decade (Rignot et al., 2008; Van den Broeke et al., 2009). The high-resolution geoid and gravity anomaly data acquired by the GOCE satellite will serve as a precise reference for elevation changes and to understand the details of gravity anomalies due to isostatic adjustments to ice-mass unloading.

The observing system for quantifying ice sheet and glacier changes and their contribution to sea level include a number of contributing measurement capabilities (Wilson et al., 2010). Continued surveys by satellite radar and laser altimeters are needed to provide elevation changes over broad areas on a routine basis. These should ideally be coupled with continued time series of interferometric synthetic aperture radar (InSAR) measurements of glacier velocities to understand changes in ice thickness due to ice discharge. In addition, time series of satellite

gravimetric measurements of the static and time-varying components of the gravity field reveal net ice-mass changes over large regions and entire ice sheets. Periodic surveys by optical systems may also be beneficial as another means of mapping of changes in ice stream margins, ice shelves, or for complementary Digital Elevation Model generation.

### Sea ice extent and concentration

A significant fraction of the surface of the world's polar ocean is frozen at any given time. Sea ice grows seasonally from  $7$  to  $16 \times 10^6$  km<sup>2</sup> in the Northern Hemisphere and from  $3$  to  $19 \times 10^6$  km<sup>2</sup> in the Southern Hemisphere, covering up to about 10 % of the surface area of each hemisphere at the respective winter peak. Arctic sea ice observations over the last 30 years indicate significant decreases in total area and extent of sea ice, although regional patterns of change can be highly variable and indicate opposing patterns of growth or decay in extent on interannual to decadal timescales.

Polar sea ice has an important climate regulating impact by limiting exchanges of momentum, heat, and moisture between the ocean and atmosphere. Due to the large difference in albedo between ice and ocean, reductions in sea ice extent by melting result in more heat being absorbed by the ocean, thereby amplifying the effects of high-latitude warming. Sea ice redistributes salt and freshwater by rejecting brine when it freezes, transporting freshwater by ice drift, and ultimately by depositing this freshwater in the upper ocean during summer melt. Thus sea ice variability exerts a considerable impact on the regional energy and freshwater budgets, as well as directly impacting the temperature, salinity, and buoyancy of brine in the upper ocean.

Daily observations of sea ice extent and concentration (fractional coverage of ice in a given area) are required to understand the thermodynamic evolution of the sea ice cover on seasonal to interannual timescales (Breivik et al., 2010). Satellite passive microwave radiometer observations (from ESMR, SMMR, SSM/I, and AMSR-E) have traditionally been used for this purpose as they are capable of daily mapping of the entire sea ice cover of both polar regions. The 30 year continuous time series of dual-polarized, multifrequency passive microwave radiometer data spanning the period from 1979 until the present day (Cavalieri et al., 1996; Comiso et al., 2003) has become the backbone of the sea ice monitoring system (see <http://www.nsidc.org/sealice/>). More recently, radar scatterometer images have been used to complement these radiometer data (Long et al., 2001). Their combination helps to distinguish between seasonal and perennial, or multiyear, ice and to provide more robust information on ice conditions during surface melting conditions. This synergy allows more robust retrieval of sea ice characteristics in operational sea ice products (e.g., EUMETSAT sea ice products: <http://saf.met.no/p/ice>).

Daily passive microwave radiometer observations have been supplemented by continuous visible and infrared very-high-resolution radiometer (1 km pixels) data since the 1970s with the NOAA AVHRR instrument series and DMSP OLS. More recently, the NASA Moderate Resolution Imaging Spectroradiometer (MODIS) added to this capability. During cloud-free, sunlit periods, this class of sensors provides supplemental information on ice concentration and ice characteristics such as albedo and thickness from reflective characteristics. During the cold season, cloud-free infrared data may also be used to derive ice surface temperature using a split-window technique which employs two thermal bands (typically at 11 and 12  $\mu$ m).

The advent of SAR has revolutionized the capability to study sea ice at much higher resolution. Since the early 1990s, SAR has provided detailed images of sea ice at spatial resolutions of up to 30 m, including information fracture or lead locations/orientations with relatively thin ice, and information on ice ridging with relatively thicker, deformed ice. Wide-swath SAR (up to 500 km wide swath) has added the capability to deliver synoptic-scale coverage (up to 1,000 km) on timescales of 1–3 days, with complete Arctic coverage on a weekly basis (Kwok et al., 1999).

### Sea ice thickness and dynamics

In order to fully appreciate the variability in sea ice mass and volume in response to climate variability, it is also required to measure sea ice thickness and drift dynamics. Both variables are essential to partition the role of thermodynamic and dynamic contributions to ice thickness changes, or to quantify advective fluxes of freshwater in the form of ice.

Ice drift data are derived from image pairs of the same region typically spaced at intervals of one to several days, using a variety of computer tracking algorithms which measure displacement of ice features over time. Daily passive microwave radiometer and scatterometer products have been used as a basis for Arctic and Antarctic ice drift products (Breivik et al., 2010), with merging of the drift fields from these two instruments providing more reliable results over several day intervals (Laverne et al., 2010). Notably, the accuracy of these products is limited by the resolution of the sensor and the intervals between images, which prevents the details of ice drift to be recorded on short time (<2 days) and space (<10 km grid) scales. For this purpose wide-swath SAR data from RADARSAT and Envisat ASAR have been used to estimate ice drift on a much finer grid, limited only by the image resolution and pixel spacing of 100–150 m. Using consistent time series of such products, it is possible to resolve the details of ice drift velocity and divergence and convergence of the ice, together with the dynamical thickening and drift-related area flux of sea ice (Kwok, 2011).

Since data from active and passive microwave imaging sensors do not contain sea ice thickness information

content, it was necessary to develop this capability. Radar altimeter measurements of ice surface elevation or freeboard (i.e., the difference in elevation between the ice surface and sea level in leads), together with ice density and snow-loading information, allow conversion of freeboard to ice thickness along profiles across the ice surface. Both the ICESat lidar and CryoSat-2 radar altimeter missions, with their higher resolution and measurement precision, allow changes in thickness and volume of sea ice to be estimated over sea ice cover.

The final goal of combination of sea ice thickness, concentration, and dynamics data is to make a complete estimation of ice volume fluxes (Kwok et al., 2009; Kwok, 2011). Using time series of each of these quantities, it becomes possible to estimate the seasonal to interannual variability in ice fluxes and, thus, the variability in transport of freshwater from high to lower latitudes.

With the future combination of passive microwave radiometers such as SSM/I and JPSS/MIS, and C-band SAR such as RADARSAT-2 and RADARSAT-3, and GMES Sentinel-1, and SAR altimeters such as CryoSat-2 and GMES Sentinel-3, a robust sea ice observing system component is assured for the next decade or so.

### Albedo and surface temperature measurements

Observations of broadband albedo and surface temperature are required for characterizing surface-atmosphere radiation budgets and energy exchanges over polar snow, ice, land, and ocean surfaces. Albedo varies considerably for different snow and ice surface properties (from 35 % to 95 %), and changes dramatically with snow metamorphism due to temperature variability or melting, or underlying surface properties (Perovich et al., 2002). Broadband albedo measurements are accomplished by passive, multi-angle optical measurements in the visible and shortwave-infrared spectral range.

Surface temperature of snow, ice, ocean, or frozen ground is also important for the determination of energy exchanges and for understanding onset of processes such as snow metamorphism or freeze and thaw. Accurate temperature observations help constrain surface radiative and turbulent fluxes, and can help improve water and energy budgets for the cryosphere.

To date these measurements have been accomplished by passive visible and infrared radiometers operating in the visible and infrared range such as AVHRR, ASTER, ATSR, AATSR, MODIS, MISR, and MERIS instruments, with the future continuity in measurements secured with the future GMES Sentinel-3 OLCI and SLSTR instruments, and the NPP and JPSS VIIRS instrument successors to MODIS.

### Gravity and the geoid

The measurement of small spatial and temporal variations in the Earth's gravity and of the geoid (i.e., equipotential reference surface) are required to quantify snow- and ice-mass distribution and mass transports including

freshwater exchange between land, ocean, ice, and atmosphere and for constraining heat, energy, and freshwater cycling through the Earth system.

Since 2000, three missions have contributed valuable data to meet these needs. The CHAMP, GRACE, and GOCE satellites have sequentially improved knowledge of the static gravity and geoid, while GRACE has revolutionized our understanding of the time-variable component of the gravity field. The GOCE mission promises to deliver a revolutionary accuracy in the static geoid over its operating lifetime. Gravity gradients from its fundamentally new gradiometer instrument, coupled with precise orbit information, give access to approximately 2 cm geoid accuracy at 100 km spatial resolution. This geoid promises a uniform global reference level for altimeter detection of regional dynamic ocean topography or sub-centimeter eustatic sea level changes (see entry *Sea Level Rise*) (over a nominal satellite lifetime of several years) in response to ice sheet melting (Wilson et al., 2010).

The GRACE follow-on (GRACE-FO) mission, currently being prepared for launch in 2016, is designed to provide a gap-free succession of data between the current GRACE mission and an upgraded GRACE-II planned for launch in the 2020 timeframe. GRACE-FO will continue to map the Earth's gravitational field with regional resolution and monthly variability.

### Other infrastructure considerations

For the polar and cryospheric observing system to fulfill all essential needs, it is necessary to consider also a number of other critical issues which indirectly require other satellite remote sensing capabilities.

### Ground-based observations

As opposed to remote sensing measurements, in situ measurements are made in direct contact with the medium of interest and typically result in sparse or sporadic observations in space or time (i.e., by comparison to the satellite data). Independent in situ, surface-based measurements of known quality of the physical state of the relevant cryospheric subdomain, or atmosphere, land, or ocean are required to understand the physical processes at work and to validate the satellite data products. Reference observation networks of autonomous or manned stations are needed for this purpose. Capabilities include precipitation (solid/liquid); snow water equivalent; vertical profiles of temperature, physical, and dielectric properties; satellite-tracked buoys (ice/ocean); automatic weather stations; and glacier or ice sheet GNSS survey reference sites.

### Satellite communications and positioning

Operations in the polar regions and particular navigation in sea ice require a combination of satellite-based communications and accurate positioning. Many in situ observing measurement systems rely on some combination of

positioning, and satellite communications/data relay to operate successfully (e.g., autonomous drifting buoys).

Communications satellites are invaluable to telecommunications uses such as data relay in the polar regions. Modern communications satellites use a variety of orbits including geostationary orbits, elliptical (e.g., Molniya) orbits, and other and low (polar and nonpolar) Earth orbits. Communications satellites provide a microwave-based radio relay capability which today is used extensively for mobile applications such as communications to ships, aircraft, and handheld terminals, for which, in polar regions, alternative technologies do not exist. New highly elliptical orbiting polar communications and weather satellite systems such as the Canadian Polar Communications and Weather (PCW) and Russian Arktika satellites are currently in development to improve monitoring capability and high-latitude activities.

Today, accurate navigation and positioning has become dependent on satellite aids such as satellite navigation or Global Navigation Satellite Systems (GNSS) such as the currently operational US Global Positioning System (GPS) and the developing European GALILEO, the Russian GLONASS, and the Chinese BeiDou-2 (or COMPASS) systems.

### Measurement reference frames

An accurate and stable measurement reference frame is essential for most precise remote sensing measurement techniques such as the altimetry and InSAR techniques discussed earlier (Wilson et al., 2010). This requires the following:

- Sustained support for satellite remote sensing tools integral to the International Terrestrial Reference Frame (ITRF), including satellite laser ranging, very-long-baseline interferometry, DORIS, and GNSS
- Inclusion of observations of the static gravity field from GOCE and other stand-alone missions to determine a precise, high spatial resolution geoid
- ITRF accurate to approximately 1 mm and stable to approximately 0.1 mm/year or better, in order to be able to understand the consequences of a changing cryosphere upon the rate of sea level change

### Remote sensing product validation

One of the shortcomings in cryospheric remote sensing measurements is that algorithms used to retrieve geophysical data products may be sensitive to spatial variability, topography, atmospheric propagation, or other diurnally or seasonally driven physical effects. To check the robustness of measurements and veracity of the resulting products over time, it is necessary to perform product validation.

Independent validation measurement data are typically acquired during in situ experiments synchronized with the satellite overpass times, at specific carefully selected instrumented sites. In situ measurements must also be made at the appropriate time and space scale for

effective comparison with the satellite sampling. Comparison of well-calibrated in situ measurements with the satellite data products allows the evaluation of the consistency of measurements over time, and for the sources of uncertainties and biases in the satellite data to be rigorously quantified.

Validation of cryospheric products also relies on critical ancillary data provided by existing in situ measurement networks which report regularly via the Global Telecommunications System (GTS) or other satellite communication links. These networks include buoys in the ocean and sea ice pack, Global Observing System (GOS) weather stations and snow cover monitoring sites, and other terrestrial network sites comprising the Global Terrestrial Networks for Permafrost (GTN-P) and Glaciers (GTN-G).

### Summary

Due to the complex interrelationships between the terrestrial, alpine, and marine elements of the cryosphere, the space component of the cryospheric and polar region observing system (*CryOS*) is needed to provide comprehensive information on all cryospheric domains. Methods of remotely sensed observations may be common to these domains, and thus the principal challenge for *CryOS* is to identify ways to develop, coordinate, maintain, and sustain these remote sensing observations within the GEOSS framework (Drinkwater et al., 2008; Jezek and Drinkwater, 2010).

Notably, the cryospheric and polar region observing system is recognized to require more than remote sensing measurements of snow and ice properties from satellites or airborne platforms. It must also include complementary networks of ground-based instrumentation as well as other capabilities such as modeling, data assimilation, and reanalysis systems and comprehensive data archiving and management systems.

### Bibliography

- Alley, R. B., Clarke, P. U., Huybrechts, P., and Joughin, I., 2005. Ice-sheet and sea-level changes. *Science*, **310**(5747), 456–460.
- Breivik, L., Carrieres, T., Eastwood, S., Fleming, A., Girard-Ardhuin, F., Karvonen, J., Kwok, R., Meier, W., Mäkynen, M., Pedersen, L., Sandven, S., Similä, M., and Tonboe, R., 2010. Remote sensing of sea ice. In Hall, J., Harrison D. E., and Stammer, D. (eds.), *Proceedings of OceanObs'09: Sustained Ocean Observations and Information for Society*, Venice, September 21–25, 2009. ESA Publication, WPP-306, 2.
- Brown, J., Ferrians, Jr., O. J., Heginbottom, J. A., and Melnikov, E. S., 1997. *Circum-Arctic Map of Permafrost and Ground-Ice Conditions*. Washington, DC: U.S. Geological Survey in Cooperation with the Circum-Pacific Council for Energy and Mineral Resources. Circum-Pacific Map Series CP-45, scale 1:10,000,000, 1 sheet.
- Cavalieri, D., Parkinson, C., Gloersen, P., and Zwally, H. J., 1996. *Sea Ice Concentrations from Nimbus-7 SMMR and DMSP SSM/I-SSMIS Passive Microwave Data*. Boulder: National Snow and Ice Data Center. Digital Media.
- Comiso, J. C., Cavalieri, D. J., and Markus, T., 2003. Sea ice concentration, ice temperature, and snow depth using AMSR-E data.

- IEEE Transactions on Geoscience and Remote Sensing*, **41**(2), 243–252.
- Drinkwater, M. R., Jezek, K. C., and Key, J. R., 2008. Coordinated satellite observations during the international polar year 2007–2008: towards achieving a polar constellation. *Space Research Today*, **171**, 6–17.
- Drinkwater, M. R., Bonekamp, H., Bontempi, P., Chapron, B., Donlon, C., Fellous, J.-L., DiGiacomo, P., Harrison, E., LeTraon, P. Y., and Wilson, S., 2010. Status and outlook for the space component of an integrated ocean observing system. In Hall, J., Harrison, D. E., and Stammer, D. (eds.), *Proceedings of OceanObs'09: Sustained Ocean Observations and Informing for Society*, Venice, Italy, September 21–25, 2009, ESA Publication, WPP-306, 1.
- Duguay, C. R., Zhang, T., Leverington, D. W., and Romanovsky, V. E., 2005. Remote sensing of permafrost and seasonally frozen ground. In Duguay, C. R., and Pietroniro, A. (eds.), *Remote Sensing in Northern Hydrology: Measuring Environmental Change*. Washington, DC: American Geophysical Union. Geophysical Monograph, Vol. 163, pp. 91–118.
- IGOS, 2007. *Integrated Global Observing Strategy Cryosphere Theme Report – For the Monitoring of our Environment from Space and from Earth*. Geneva: World Meteorological Organization., WMO/TD-No. 1405.
- Jeffries, M. O., Morris, K., and Kozlenko, N., 2005. Ice characteristics and processes, and remote sensing of frozen rivers and lakes. In Duguay, C. R., and Pietroniro, A. (eds.), *Remote Sensing in Northern Hydrology: Measuring Environmental Change*. Washington, DC: American Geophysical Union. Geophysical Monograph, Vol. 163, pp. 63–90.
- Jeffries, M. O., Morris, K., and Duguay, C. R., (in press). Lake ice and river ice. In Williams, Jr., R. S., and Ferrigno, J. G. (eds.), *Satellite Image Atlas of Glaciers of the World – Review of the State of the Earth's Cryosphere*. U.S. Geological Survey Professional Paper 1386-A.
- Jezek, K. J., and Drinkwater, M. R., 2010. Satellite observations from the international polar year. *Eos, Transactions American Geophysical Union*, **91**(14), 125–126.
- Kääb, A., 2008. Remote sensing of permafrost-related problems and hazards. *Permafrost and Periglacial Processes*, **136**, 107–136.
- Kwok, R., 2011. Satellite remote sensing of sea ice thickness and kinematics: a review. *Journal of Glaciology*, **56**(200), 1129–1140.
- Kwok, R., Cunningham, G. F., LaBelle-Hamer, N., Holt, B., and Rothrock, D. A., 1999. Ice thickness derived from high-resolution SAR imagery. *Eos, Transactions American Geophysical Union*, **80**(42), 495–497.
- Kwok, R., Cunningham, G. F., Wensnahan, M., Rigor, I., Zwally, H. J., and Yi, D., 2009. Thinning and volume loss of the Arctic Ocean sea ice cover: 2003–2008. *Journal of Geophysical Research*, **114**, C07005, doi:10.1029/2009JC005312.
- Lavergne, T., Eastwood, S., Teffah, Z., Schyberg, H., and Breivik, L.-A., 2010. Sea ice motion from low-resolution satellite sensors: an alternative method and its validation in the Arctic. *Journal of Geophysical Research*, **115**, C10032, doi:10.1029/2009JC005958.
- Long, D. G., Drinkwater, M. R., Holt, B., Saatchi, S., and Bertoia, C., 2001. Global ice and land climate studies using scatterometer image data. *Eos, Transactions American Geophysical Union*, **82**(43), 503.
- Perovich, D. K., Grenfell, T. C., Light, B., and Hobbs, P. V., 2002. Seasonal evolution of the albedo of multiyear Arctic sea ice. *Journal of Geophysical Research*, **107**(C10), 8044, doi:10.1029/2000JC000438.
- Rignot, E., Bamber, J. L., van den Broeke, M., Davis, C., Li, Y., van de Berg, W. J., and van Meijgaard, E., 2008. Recent Antarctic ice mass loss from radar interferometry and regional climate modeling. *Nature Geoscience*, **1**, 105–110.
- Rignot, E., Mouginot, J., and Scheuchl, B., 2011. Ice flow of the Antarctic ice sheet. *Science*, **333**(6048), 1427–1430.
- Van Den Broeke, M., Bamber, J., Ettema, J., Rignot, E., Schrama, E., van de Berg, W. J., van Meijgaard, E., Velicogna, I., and Wouters, B., 2009. Partitioning recent greenland mass loss. *Science*, **326**(5955), 984–986.
- Wilson, W. S., Abdalati, W., Alsdorf, D., Benveniste, J., Bonekamp, H., Cogley, J. G., Drinkwater, M. R., Fu, L. L., Gross, R., Haines, B. J., Harrison, D. E., Johnson, G. C., Johnson, M., LaBrecque, J. L., Lindstrom, E. J., Merrifield, M. A., Miller, L., Pavlis, E. C., Petrovicz, S., Roemmich, D., Stammer, D., Thomas, R. H., Thouvenot, E., and Woodworth, P. L., 2010. Observing systems needed to address sea-level rise and variability. In Church, J. A., Woodworth, P. L., Aarup, T., and Wilson, W. S. (eds.), *Understanding Sea-Level Rise and Variability*. Oxford: Wiley-Blackwell, pp. 376–399.
- Zhang, T., Barry, R. G., Knowles, K., Ling, F., and Armstrong, R. L., 2003. Distribution of seasonally and perennially frozen ground in the Northern Hemisphere. In Phillips, M., Springman, S. M., and Arenson, L. U. (eds.), *Permafrost: Proceedings of the Eighth International Conference on Permafrost*, July 21–25, 2003, Zurich, Switzerland. Lisse, T Netherlands: A.A. Balkema.

## Cross-references

[Calibration and Validation](#)  
[Cryosphere, Climate Change Effects](#)  
[Cryosphere, Climate Change Feedbacks](#)  
[Cryosphere, Measurements and Applications](#)  
[Geodesy](#)  
[Global Climate Observing System](#)  
[Global Earth Observation System of Systems \(GEOSS\)](#)  
[Global Land Observing System](#)  
[Ice Sheets and Ice Volume](#)  
[Lidar Systems](#)  
[Microwave Radiometers](#)  
[Ocean Surface Topography](#)  
[Polar Ice Dynamics](#)  
[Radar, Altimeters](#)  
[Radar, Scatterometers](#)  
[Radar, Synthetic Aperture](#)  
[Sea Ice Albedo](#)  
[Sea Ice Concentration and Extent](#)  
[Sea Surface Temperature](#)  
[Sea Surface Wind/Stress Vector](#)  
[Terrestrial Snow](#)

---

## CRYOSPHERE, CLIMATE CHANGE EFFECTS

---

Aixue Hu  
 Climate and Global Dynamics Division, National Center  
 for Atmospheric Research, Boulder, CO, USA

## Synonyms

Frozen water sphere; Solid water sphere

## Definition

The cryosphere is defined as the part of the earth's surface where the water is in solid form. It includes the sea ice, lake and river ice, glaciers and mountain ice caps, ice sheets, snow cover, and the frozen ground (including permafrost). The cryosphere is important to global climate due to its high reflectivity (albedo) of the sun's rays. Changes in the cryosphere affect the global heat balance and thus modulate the global climate.

Albedo is the reflectivity of the earth's surface to the incoming solar radiation (sunlight).

## Introduction

The cryosphere is an integral part of the earth's climate system. It is closely linked to the earth's surface energy budget, the water cycle, sea level changes, and the surface gas exchanges. Presently, the cryosphere on land contains about 75 % of the world's freshwater, mostly in the Greenland ice sheet and the Antarctic ice sheet. The total melt of these two ice sheets would increase the global sea level by about 64 m. In the past million years, the cryosphere has gone through significant changes on different time scales, such as the Ice Age. When the global climate cools, the cryosphere expands, and when the global climate warms, the cryosphere shrinks. On the other hand, the cryosphere not only responds passively to changes in the global climate, it also actively modifies the global climate through the albedo feedback. In general, roughly 80–90 % of the sun's rays reaching the snow or ice surface are reflected back into space. In contrast, only 10 % of the sun's rays are reflected back to space from the ocean surface. In a colder climate, the growth of sea ice and the snow cover and ice sheets on land would increase the albedo, which reflects more of the sun's rays back into space and reduces the heat absorption by the earth's climate system, leading to a further cooling effect of the climate. In a warmer climate, the shrinkage of the cryosphere would reduce the global albedo, thus allowing more of the sun's rays to be absorbed by the earth's climate system and make the climate even warmer. This is a positive feedback.

## Present state of the cryosphere

### Mean state of the cryosphere

Currently, about 10 % of the earth's land area is covered by ice, mostly in the Antarctic and Greenland; only a tiny fraction lies in the ice caps and mountain glaciers. In the annual mean, sea ice covers about 7 % of the earth's ocean area. In the Northern Hemisphere, the maximum sea ice extent is about 15 million square kilometers in winter, with a minimum of about 3.6 million square kilometers in summer in the Arctic and the adjacent seas. In the Southern Hemisphere, the sea ice covers about 19 million square kilometers of ocean in winter and about 3 million square kilometers in summer. In the Northern Hemisphere winter

season, snow covers about 33 % of the land north of the equator and reaches 49 % in midwinter. Since the land area south of 40 °S is very small in the Southern Hemisphere, the region with snow cover in winter is small, except for Antarctica. The frozen ground (including both seasonally frozen ground and permafrost) covers about 51 % of the land area in the Northern Hemisphere in winter, of which about half is permafrost.

## Changes of the cryosphere during the twentieth century

Based on both historical and satellite observations, the snow cover has declined in spring and summer in the Northern Hemisphere since the early 1920s, especially since the late 1970s, but the changes are small in winter (Lemke et al., 2007). In the Southern Hemisphere, little or no long-term trend is found from the satellite observations for the last three decades, but there is substantial interannual variability.

For the river and lake ice, studies show that the freeze-up date in the late fall is later, with a rate of change of  $5.8 \pm 1.6$  days per century, and the break-up date is earlier, changing at a rate of  $6.5 \pm 1.2$  days per century for selected rivers and lakes in the Northern Hemisphere (Magnuson et al., 2000).

In terms of sea ice, the satellite observations show a significant declining trend ( $-7.4 \pm 2.4$  % per decade from 1979 to 2005) for the Northern Hemisphere summer sea ice extent (Comiso, 2003). The 2012 summer minimum sea ice extent was only about 3.6 million square kilometers, a dramatic reduction in comparison to the 1979–2000 average minimum of about seven million square kilometers. The winter sea ice cover is also shrinking in the Northern Hemisphere with a rate of about 44,000 km<sup>2</sup> per year since 1979. In the Southern Hemisphere, the sea ice cover increased slightly during the recent decade, but it is not statistically significant. On the other hand, from up-looking sonars on submarines and some moored instruments that measure sea ice thickness, a drastic thinning of the Arctic multiyear sea ice around the late 1980s is found (Johannessen et al., 2004). There is no trend before the late 1980s (Tucker et al., 2001).

The glaciers and ice caps which are not adjacent to the large ice sheets of Greenland and Antarctic occupy only a very small portion of the land surface. However, these glaciers and ice caps affect the river runoff since most of the large rivers originate there. Variations of the stability of these glaciers and ice caps would affect the river flow in spring and late summer. Studies show that the retreat of the glaciers and ice caps became evident globally as early as 1850 (Oerlemans, 2005). Regionally, the retreat of the glaciers and ice caps has been significant everywhere except in Europe and the Andes since 1960s (Dyrgerov and Meier, 2005). In Europe and the Andes, the glaciers and ice caps show evidence of retreat since the 1990s.

Since the Greenland and Antarctic ice sheets hold huge amounts of ice which could significantly raise the sea level if they were to fully melt, it is important to monitor the changes in the ice sheets and study the impact of these ice sheets on global climate in the future. In the Greenland ice sheets, about half of the ice loss is by surface melting and runoff into the sea. In the Antarctic, ice is drained by slow-moving ice at the center of the ice sheet and by faster-moving ice-walled ice streams or ice shelves and narrow ice tongues at the edges. Observations from multiple sources, including from remote sensing instruments, show that the Greenland ice sheet mass was balanced during most parts of the twentieth century, but the Greenland ice sheet started to lose mass since the early 1990s with an accelerating trend (Lemke et al., 2007). In the Antarctic, the ice sheet appears to be losing mass all the time which might be associated to the past forcing since portions of the ice sheet respond very slowly. Recent satellite observations indicate that there is a slight mass gain in the eastern Antarctic and a more significant mass loss in the west Antarctic (Rignot and Thomas, 2002; Zwally et al., 2006). The total contribution of the ice sheets, glaciers, and ice caps to the [sea level rise](#) has been about  $1.2 \pm 0.4$  mm/year from 1993 to 2003.

Observations show a warming of the permafrost all over the world in the twentieth century, especially in the late twentieth century when data are more abundant (Lemke et al., 2007). In some regions, this warming causes the permafrost to degrade. The degradation of the permafrost can cause significant problems for human activities. Thawing can induce the subsidence of the ground, a downward displacement of the surface, especially for the ice-rich permafrost. Typically, this subsidence does not happen uniformly; some regions would rise up and some regions would sink. Any man-made infrastructure standing on the thawing permafrost can be significantly damaged. On the coast of the Arctic, the permafrost degradation causes an erosion of the coastline by up to 3 m per year. For the seasonally frozen ground, the active layer which thaws and freezes on top of the permafrost becomes thicker, indicating a downward propagation of the surface warming signal. The area of the seasonally frozen ground outside of the permafrost region has shrunk about 7 % in the Northern Hemisphere during the last century.

### The cryosphere in past climates

In the past million years, the earth's climate has experienced a few cold-warm cycles – the glacial-interglacial cycle. Each of these cycles lasted about 100,000 years. The most recent interglacial started about 10,000 years ago. The cause of these glacial-interglacial cycles is not well understood, but strong evidence indicates that these are linked to regular variations of the earth's orbit around the sun, the so-called Milankovitch cycles. In each of these cycles, the amount of the solar radiation reaching the earth surface changes at each latitude in each season,

but may not change the annual mean value. Many studies suggest that the total amount of solar radiation reaching the North Hemisphere in summer is crucial for the starts and ends of this climate change cycle. If the snow in the previous winter can survive the following summer, snow cover would grow and ice sheets would grow due to the albedo feedback. A growing ice and snow cover on the earth's surface would reflect more sunlight into space and further cool the earth's climate, the ice sheets grow bigger, the glaciers and ice caps grow towards lower altitudes, and sea ice cover expands towards the equator. At the last glacial maximum (about 21,000 years before present), the global sea level dropped by about 120 m, or about 120 m of shallow ocean was turned onto land. The ice sheets covered a significant portion of the North America continent up to 45°N (called the Laurentide ice sheet), a large portion of Europe, and part of the western and middle Russia (called the Weichselian ice sheet) in the Northern Hemisphere and southern South America (called Patagonian ice sheet) and the Antarctic in the Southern Hemisphere. These ice sheets were, in general, about 3–4 km thick.

### Projected changes of cryosphere in future climate

In the recent report of the Intergovernmental Panel on Climate Change (IPCC, 2007), scientists using comprehensive state-of-the-art coupled climate models show that the status of the sea ice cover, snow cover, and frozen ground in the future climate depends heavily on how much CO<sub>2</sub> is emitted into the atmosphere by human activities. The Arctic could be seasonally ice-free in the mid-to-late twenty-first century if the CO<sub>2</sub> emission were high (Meehl et al., 2007). If so, human and marine life would be affected dramatically. Polar bears rely on the sea ice to hunt for food. If there is no sea ice at all in summer, polar bears would not be able to obtain enough nourishment. Model projections also show a significant reduction of the snow cover in the Northern Hemisphere, a poleward movement of the permafrost extent (indicating a shrinking in permafrost area), and an increase in the active layer thickness in the permafrost region. These changes would reduce the surface albedo, and the earth system would absorb more solar radiation which would warm the earth's climate even more.

In recent years, a slight inland thickening and strong marginal thinning of the Greenland ice sheet produce a net loss of the ice mass. A model-projected warming in the twenty-first century would suggest a continued mass loss of the Greenland ice sheet. One model projection indicates that the entire Greenland ice sheet could completely melt away in the next 3,000 years if the current warm climate persists (Ridley et al., 2005). This would raise the global sea level by half a meter per century at peak melting. The changes in the Antarctic ice sheet as a whole are uncertain. But the Western Antarctic ice sheet is likely to lose more mass, or even totally collapse, if the future climate is warmer; a complete collapse of the West

Antarctic ice sheet would cause a global [sea level rise](#) of 5 m. It is hard to project how long this process will take from present ice sheet models.

In general, if the future climate is warmer than now projected by the IPCC models, it is certain the glaciers and ice caps will become smaller. Based on model simulations of 17 glaciers, the volume of loss of the glaciers is projected to be up to 60 % by 2050. Since the disappearance of these glaciers and ice caps is much faster than a potential reglaciation, the loss of the glaciers and ice caps may be irreversible, at least in some regions. Because the total mass of the global glaciers and ice caps is much smaller than the ice sheets of Greenland and Antarctic, the melting of these glaciers and ice caps would not raise the global sea level by much. However, it potentially can significantly impact the river runoff and the availability of freshwater supply, hence adversely affecting human activities.

### Summary

The cryosphere is a very important part of the global climate system, and many important properties can be derived using remote sensing. The cryosphere played a significant role in the past changes of the earth's climate. Because of its high reflectivity (albedo) of solar radiation, shrinkage of the cryosphere coverage on the earth's surface would induce a higher absorption of the solar radiation by the earth's climate system which would enhance warming. A seasonal ice-free Arctic would enhance the hydrological cycle there, which will significantly affect human and marine life in the pan-Arctic region. A possible melt of the Greenland and West Antarctic ice sheets in the future would raise the global sea level markedly. Studies show that the climate was only a few degrees warmer during the last interglacial period than now and that the sea level was about 3–6 m higher. At that time, a very large portion of the Greenland ice sheet melted. If the sea level were to rise by 3 m in the next century or so, by the melting of the Greenland and West Antarctic ice sheets, human activities would be impacted in a momentous way.

### Bibliography

- Climate change – Wikipedia, the free encyclopedia.  
 Comiso, J. C., 2003. Large scale characteristics and variability of the global sea ice cover. In Thomas, D., and Dieckmann, G. S. (eds.), *Sea Ice – An Introduction to Its Physics, Biology, Chemistry, and Geology*. Oxford: Blackwell Science, pp. 112–142.  
 Cryosphere – Wikipedia, the free encyclopedia.  
 Dyurgerov, M., and Meier, M. F., 2005. Glaciers and the changing Earth system: a 2004 snapshot. *Occasional Paper 58, Institute of Arctic and Alpine Research*, University of Colorado, Boulder, CO, 118 pp.  
 Global Outlook for Ice and Snow Assessment on the state and future of the Cryosphere, UN Environment Programme, June 2007.  
 IPCC, 2007. Climate change 2007: the physical science basis. In Solomon, S., Qin, D., Manning, M., Chen, Z., Marquis, M., Averyt, K. B., Tignor, M., and Miller, H. L. (eds.), *Contribution of Working Group I to the Fourth Assessment Report of the*

- Intergovernmental Panel on Climate Change*. Cambridge/New York: Cambridge University Press, p. 996.  
 Johannessen, O. M., et al., 2004. Arctic climate change – observed and modelled temperature and sea ice. *Tellus*, **56A**, 328–341.  
 Lemke, P., et al., 2007. Observations: changes in snow, ice and frozen ground. In Solomon, S., Qin, D., Manning, M., Chen, Z., Marquis, M., Averyt, K. B., Tignor, M., and Miller, H. L. (eds.), *Climate Change 2007: The Physical Science Basis. Contribution of Working Group I to the Fourth Assessment Report of the Intergovernmental Panel on Climate Change*. Cambridge/New York: Cambridge University Press, pp. 337–383.  
 Magnuson, J. J., et al., 2000. Historical trends in lake and river ice cover in the Northern Hemisphere. *Science*, **289**, 1743–1746.  
 Meehl, G. A., et al., 2007. Global climate projections. In Solomon, S., Qin, D., Manning, M., Chen, Z., Marquis, M., Averyt, K. B., Tignor, M., and Miller, H. L. (eds.), *Climate Change 2007: The Physical Science Basis. Contribution of Working Group I to the Fourth Assessment Report of the Intergovernmental Panel on Climate Change*. Cambridge/New York: Cambridge University Press.  
 Oerlemans, J., 2005. Extracting a climate signal from 169 glacier records. *Science*, **308**, 675–677.  
 Ridley, J. K., Huybrechts, P., Gregory, J. M., and Lowe, J. A., 2005. Elimination of the Greenland ice sheet in a high CO<sub>2</sub> climate. *Journal of Climate*, **17**, 3409–3427.  
 Rignot, E., and Thomas, R. H., 2002. Mass balance of polar ice sheets. *Science*, **297**(5586), 1502–1506.  
 Tucker, W. B., III, et al., 2001. Evidence for the rapid thinning of sea ice in the western Arctic Ocean at the end of the 1980s. *Geophysical Research Letters*, **28**(14), 2851–2854.  
 Zwally, H. J., et al., 2006. Mass changes of the Greenland and Antarctic ice sheets and shelves and contributions to sea level rise: 1992–2002. *Journal of Glaciology*, **51**, 509–527.

### Cross-references

- [Cryosphere, Climate Change Feedbacks](#)  
[Cryosphere, Measurements and Applications](#)  
[Climate Data Records](#)  
[Climate Monitoring and Prediction](#)  
[Ice Sheets and Ice Volume](#)  
[Sea Ice Albedo](#)

---

## CRYOSPHERE, CLIMATE CHANGE FEEDBACKS

---

Peter J. Minnett  
 Rosenstiel School of Marine and Atmospheric Science,  
 University of Miami, Miami, FL, USA

### Definition

The term “feedback” is taken from electrical engineering and describes how a small part of the output of a circuit or a system, such as an amplifier, is fed back to become part of the input. A positive feedback loop results in a growth in the signal, or initial disturbance, and a negative feedback loop acts to diminish the effects of a disturbance, retaining the system close to a stable state. A positive feedback loop could push a hitherto stable system past a tipping point into another state. The concept of feedback loops is a very appealing idea for

geophysics and climate researchers, for example, as there are many levels of complexity that permit feedback loops of both signs that can stabilize the system to some disturbances or perturbations, and render it unstable to others (Bony et al., 2006).

### Climate feedbacks

In the climate system, the simplest approach is to consider the change in the equilibrium temperature of the earth, or of a particular region (the temperature change being written as  $\Delta T_d$ ), that results directly from a change in the radiative forcing ( $\Delta Q$ ):

$$\Delta T_d = \lambda \Delta Q$$

where  $\lambda$  represents a sensitivity factor. For the direct radiative forcing of the climate system,  $\lambda$  is determined by the physical law relating radiation and temperature (Stefan-Boltzmann's Law) and has a value of about  $0.25 \text{ K (Wm}^{-2}\text{)}^{-1}$  for temperatures typical of the middle atmosphere. Thus, a change in radiative forcing of  $4 \text{ Wm}^{-2}$  would lead to a temperature change of about 1 K.

In the more realistic case, the climate changes involve feedbacks which modify  $\Delta T_d$  to give the actual equilibrium temperature change ( $\Delta T$ ). Using the term "gain" ( $g$ ) to represent the fraction of  $\Delta T$  that is caused by feedback mechanisms, where  $g$  can be negative, but no larger than +1, then:

$$g = (\Delta T - \Delta T_d) / \Delta T$$

so that:

$$\Delta T = \Delta T_d / (1 - g)$$

Thus, a negative gain reduces the temperature change, and a value close to 1 leads to large amplification of the direct temperature change. There are generally several components in the climate gain factor which result from different physical mechanisms, and so the value of  $g$  is not a single value but varies according to the relative strengths of the different components, which in turn depend on the relative influence of the relevant parts of the climate system (NRC, 2003).

In the cryosphere, several feedbacks are also present in other parts of the climate system, but here they are rendered more extreme by the special characteristics of a region that are close to the freezing point of water. Several of the various components of the cryospheric feedbacks are accessible to satellite remote sensing, either directly through measurements of the critical variables, or through measurements of the consequences of the feedbacks.

In the polar regions, there are at least four major feedbacks that can, at least in principle, be monitored, or quantified, using remotely sensed data: the surface albedo-shortwave radiation feedback, the water-vapor feedback, the cloud radiative feedbacks, and the biogenic cloud condensation nuclei (CCN) feedback.

### Surface albedo-shortwave radiative feedback

The rapid loss of summertime Arctic Ocean ice cover in recent years has focused attention on possible mechanisms for the accelerated loss, and the surface albedo feedback is one that is frequently mentioned. When the ocean is covered by ice, most of the incident solar radiation is reflected back through the atmosphere and to space. The ratio of the total amount of reflected energy to the incoming sunlight is called the albedo of the surface. Dry, fresh snow on sea ice can reflect as much as 90 % of the incident sunlight. The reflectivity varies with wavelength of the radiation (Hanesiak et al., 2001). As the temperature rises and the snow or ice begins to moisten, the albedo decreases, resulting in more of the solar energy being absorbed, and this leads to more melting of snow and ice. When melt ponds form, the surface albedo falls further and more solar energy is absorbed, leading to accelerated melting. The melting sea ice reveals the dark sea surface which has an albedo of <10 %. The heat resulting from the absorption of solar energy can be moved laterally by surface currents and brought into contact with sea ice, which it can melt from the sides or from beneath.

The situation on land is similar: when snow and ice melt away, they are replaced by bare ground or vegetation which generally has lower albedo and therefore absorbs more energy, hastening the melting of the remaining snow and ice nearby.

The albedo shortwave radiation feedback is a positive one, as the melting of the snow and ice reduces the surface albedo, resulting in the absorption of more sunlight, leading to yet more snow and ice melt (Curry et al., 1995).

The extent of polar sea ice is monitored very effectively from polar orbiting satellites using microwave radiometers and the surface reflectivity, and hence albedo is measured by satellite imaging radiometers operating in the visible part of the electromagnetic spectrum.

### Water-vapor feedback

Water vapor in the atmosphere is a very potent greenhouse gas. This means the water molecules at a given height in the atmosphere absorb some of the infrared radiation emitted from the surface below and from the intervening atmosphere, radiation that would otherwise escape to space thereby cooling the planet; when that energy is reemitted, some of it propagates back toward the surface. The maximum amount of water vapor the atmosphere can hold without condensing is approximately exponentially dependent on the absolute temperature. Thus, as the temperature of the air rises, so does its ability to support an increasing water vapor burden and therefore its ability to intercept more of the outgoing infrared radiation. This is a positive feedback. The actual amount of water vapor in the atmosphere is also dependent on an available source of water, usually at the base of the atmosphere. A frozen surface is a poor source of moisture, so the atmosphere above is generally very dry, and the downward infrared radiation from the

atmospheric water vapor emission is small. Over open water, evaporation into the atmosphere leads to a moister atmosphere and increased downward infrared radiative heating of the surface. The advection of the moister atmosphere from over the open water to over sea-ice increases the radiative heating of the surface, leading to melting of the surface and increased evaporation – another positive feedback.

Although the atmospheric water vapor content, often called the precipitable water, can be measured quite accurately over the open oceans by microwave radiometers on spacecraft, the retrievals are not very accurate over land or over sea ice, or a surface comprised of mixed open water and ice. The atmospheric water vapor profile can be derived from measurements of infrared and microwave sounding radiometers, but again over land and over mixed ice and water surface, the retrievals are not very accurate. Thus the remote sensing of the water vapor and hence the direct quantification of this feedback is not possible using current remote sensing technology.

### Cloud radiative feedbacks

A consequence of the increased atmospheric water vapor content resulting from evaporation over open water in polar regions is increased cloud cover. Often the low-level clouds that form over leads and polynyas (areas of open water surrounded by ice; Smith and Barber, 2007) can be traced many kilometers downwind, and are apparent in satellite imagery (Dethleff, 1994). Over the polar regions, as elsewhere, clouds can be carried great distances by the winds. The presence of clouds has two consequences on the surface radiative energy budget: they heat the surface by increasing the infrared radiation incident at the surface, and they cool the surface by casting shadows, that is, by scattering sunlight back to space. The former is a positive feedback, and the latter a negative one (Curry et al., 1996). Both are present at the same time, and the combined effect depends on the relative strengths of each (Hanafin and Minnett, 2001). The infrared heating depends on the amount, type, thickness, and height of the clouds and is present both night and day. The short-wave cooling occurs only in daylight and depends on the amount, type of clouds, and also on the solar zenith angle, and whether there are clouds across the face of the sun (Minnett, 1999). In general, the negative feedback that results in the cooling of the surface occurs in the polar summer, when the sun is higher in the sky, whereas the positive feedbacks occur when the incident solar radiation is small, when the sun is close to the horizon, or absent, as in the winter (Intrieri et al., 2002; Vavrus, 2004).

Clouds can be identified in satellite images, although this is more readily done when the clouds are illuminated by sunlight against a dark background of open water or dark vegetation. Over a bright frozen surface, the automatic identification of clouds is difficult and appreciable errors can occur. Similarly at night, when the

identification of clouds relies on a temperature contrast with respect to the surface, problems of misidentification can arise. Relatively new techniques using space-borne cloud radars and lidars show promise in improving the confident identification and classification of clouds and consequent improvements in the study of the cloud radiative feedbacks in the polar regions.

### Biogenic cloud condensation nuclei (CCN) feedback

For clouds to form in the polar atmosphere, it is not sufficient that the water vapor content be at or above saturation, but also that there are small particles in the air that can act as cloud condensation nuclei. One group of CCNs over the oceans are minute salt crystals that result from the evaporation of spray droplets and another are derived from biological activity in the ocean. Airborne experiments over the Antarctic ice floes revealed bacteria and algal spores acting as CCNs (Saxena, 1983), and subsequently dimethylsulfide (DMS), a gas released from its precursor dimethyl sulfonium propionate (DMSP) at the ocean surface, have been found to be effective CCNs. DMSP is released when phytoplankton and algae die and decay. More recently, viruses, bacteria, and fragments of diatoms have been found to act as CCNs in the lower atmosphere over leads in the Arctic Ocean (Leck et al., 2004). The presence of biogenic material provides a possible feedback mechanism in the climate system: solar radiation is necessary for plankton to bloom, and when they die they release material that become CCNs, increasing the cloud amount, and this leads to a reduction in solar radiation reaching the surface – a negative feedback.

The presence of CCNs promotes not only cloud formation, but also influences the cloud properties. High concentrations of CCNs result in more and smaller droplets in the clouds, and this has two consequences. Firstly, the clouds have a higher albedo and therefore scatter more solar energy back to space, the Twomey Effect (initially described in terms of anthropogenic pollution in the atmosphere (Twomey, 1977)), and secondly, the smaller cloud droplets take longer to accrete to sizes that will lead to precipitation, so that the clouds live longer – the Albrecht Effect (Albrecht, 1989).

This biogenic negative feedback has been hypothesized to result in the appropriate amount of sunlight reaching the ocean surface to sustain the appropriate levels of biological activity. Too little sunlight reaching the surface, because of a local positive perturbation in the cloud cover, leads to less phytoplankton growth, fewer CCNs, and eventually more sunlight reaching the surface because fewer clouds are formed, or they have properties that are less effective in reducing the sunlight at the surface (Leck et al., 2004).

Unlike the other feedbacks, discussed briefly here, the biogenic feedback remains hypothetical and the links involved have not been quantitatively

substantiated. It remains a topic of research. The chlorophyll concentration in the upper ocean can be monitored using remotely sensed measurements of ocean color derived from reflected sunlight in the visible part of the spectrum, and clouds can be monitored from space, as mentioned above.

## Summary

Climate feedbacks in polar regions act to accelerate or delay the effects of global change, not only at high latitudes, but worldwide. Because of the remoteness of the polar regions, and the difficulty of gathering appropriate measurements using conventional instrumentation, the study and monitoring of many of the components of the feedback loops are feasible only by using satellite remote sensing.

## Bibliography

- Albrecht, B. A., 1989. Aerosols, cloud microphysics and fractional cloudiness. *Science*, **245**, 1227–1230.
- Bony, S., Colman, R., Kattsov, V. M., Allan, R. P., Bretherton, C. S., Dufresne, J.-L., Hall, A., Hallegatte, S., Holland, M. M., Ingram, W., Randall, D. A., Soden, B. J., Tselioudis, G., and Webb, M. J., 2006. How well do we understand and evaluate climate change feedback processes? *Journal of Climate*, **19**, 3445–3482.
- Curry, J. A., Schramm, J. L., and Ebert, E. E., 1995. Sea ice-albedo climate feedback mechanism. *Journal of Climate*, **8**, 240–247.
- Curry, J. A., Rossow, W. B., Randall, D., and Schram, J., 1996. Overview of Arctic cloud and radiation characteristics. *Journal of Climate*, **9**, 1731–1764.
- Dethleff, D., 1994. Polynyas as a possible source for enigmatic Bennett Island atmospheric plumes. In Johannessen, O. M., Muench, R. D., and Overland, J. E. (eds.), *Polar Oceans and their Role in Shaping the Global Environment*. Washington, DC: American Geophysical Union, Vol. 85, pp. 475–483.
- Hanafin, J. A., and Minnett, P. J., 2001. Cloud forcing of surface radiation in the North Water Polynya. *Atmosphere-Ocean*, **39**, 239–255.
- Hanesiak, J. M., Barber, D. G., deAbreu, R. A., and Yackel, J. J., 2001. Local and regional albedo observations of arctic first-year sea ice during melt ponding. *Journal of Geophysical Research*, **106**, 1005–1016.
- Intrieri, J. M., Fairall, C. W., Shupe, M. D., Persson, P. O. G., Andreas, E. L., Guest, P. S., and Moritz, R. E., 2002. An annual cycle of Arctic surface cloud forcing at SHEBA. *Journal of Geophysical Research*, **107**, 8039, doi:10.1029/2000JC000439.
- Leck, C., Tjernström, M., Matrai, P., Swietlicki, E., and Bigg, K., 2004. Can marine micro-organisms influence melting of the Arctic pack ice? *Eos Transactions, American Geophysical Union*, **85**, 25.
- Minnett, P. J., 1999. The influence of solar zenith angle and cloud type on cloud radiative forcing at the surface in the Arctic. *Journal of Climate*, **12**, 147–158.
- NRC, 2003. *Understanding Climate Change Feedbacks*. Washington, DC: National Academy of Sciences.
- Saxena, V. K., 1983. Evidence of the biogenic nuclei involvement in Antarctic coastal clouds. *Journal of Physical Chemistry*, **87**, 4130–4134.
- Smith, W. O., and Barber, D. G. (eds.), 2007. *Polynyas: Windows to the World*. Amsterdam: Elsevier. Elsevier Oceanography Series.
- Twomey, S. A., 1977. The influence of pollution on the shortwave albedo of clouds. *Journal of the Atmospheric Sciences*, **34**, 1149–1152.
- Vavrus, S., 2004. The impact of cloud feedbacks on arctic climate under greenhouse forcing. *Journal of Climate*, **17**, 603–615.

## Cross-references

[Climate Monitoring and Prediction](#)  
[Cloud Properties](#)  
[Cryosphere, Climate Change Effects](#)  
[Cryosphere, Measurements and Applications](#)  
[Emerging Technologies, Lidar](#)  
[Ice Sheets and Ice Volume](#)  
[Polar Ice Dynamics](#)  
[Sea Ice Albedo](#)  
[Sea Ice Concentration and Extent](#)  
[Terrestrial Snow](#)

---

## CRYOSPHERE, MEASUREMENTS AND APPLICATIONS

---

Roger Barry  
 National Snow and Ice Data Center, NSIDC 449 UCB,  
 University of Colorado, Boulder, CO, USA

## Definitions

*(Land)fast ice*. Sea ice attached to the shore or near-shore sea bed.

*Nunatak*. A mountain peak protruding through glacier ice.

## Introduction

Remote sensing of the cryosphere has a 50 year history. We begin with an historical overview of aerial photography of the cryosphere – mainly glaciers and ice caps – and then proceed to satellite imagery and data for each of the major components of the cryosphere. In turn, we consider glaciers, snow cover, freshwater ice, sea ice, ice sheets and ice shelves, icebergs, and frozen ground.

## Aerial photography

### Glaciers and ice caps

Remote sensing of the cryosphere began with both vertical and oblique aerial photography of glaciers and ice caps. A massive campaign to photograph the Canadian Arctic was undertaken in the late 1940s–1950s (Dunbar and Greenway, 1956) and the photography covered all land areas. The US Geological Survey (USGS) photographed numerous glaciers in western North America and Alaska beginning in the 1950s (Post, 2005: <http://earthweb.ess.washington.edu/EPIC/Collections/Post/index.htm>).

The Austin Post aerial photograph collection begins in 1957 and continued through the 1980s. About 100,000 images on microfilm became a part of the World Data Center (WDC) for Glaciology collection when the WDC was transferred to the USGS in Tacoma in 1970 and to

the University of Colorado, Boulder, in 1976. This collection of the USGS Ice and Climate Project is known as the Post-Mayo-Krimmel Collection.

Aerial photography has continued to find applications. For example, snow patches remaining in late July in the Canadian Arctic have been mapped from air photographs for 1948–1983 by Lauriol et al. (1986). They found a high (0.93) correlation between the residual snow and maximum late winter snow thickness.

### Satellite imagery and data

Aerial photography studies largely transitioned to satellite imaging from the Earth Resources Technology Satellite (ERTS) in July 1972 (renamed Landsat 1) and the subsequent Landsat series through Landsat 7 (15 m resolution) launched in 1999. The images are from a return beam vidicon (RBV) camera and multispectral scanner (MSS).

US military satellites in the CORONA and related programs collected over 800,000 diffraction-limited panoramic photographs with 2–7 m ground resolution from 1960 to 1972, which were declassified and made available for scientific use in the 1990s (McDonald, 1995). Mosaics of Greenland were developed from the Declassified Intelligence Satellite Photographs (DISP) by Zhou and Jezek (2002) in 1962 and 1963. Csatho et al. (2000) discuss the rectification of CORONA images for studying Greenland glacier motion and Altmaler and Kany (2002) use stereographic pairs for digital surface model generation.

In March 2002, the European Space Agency launched Envisat with the MEdium Resolution Imaging Spectrometer (MERIS) which has 15 channels in the 390–1,040 nm spectral range; a spatial resolution at nadir of 300 m is reduced on board to 1,200 m. In January 2006, the Japan Aerospace Exploration Agency (JAXA) launched the Advanced Land Observing Satellite (ALOS) with three remote sensing instruments: the Panchromatic Remote sensing Instrument for Stereo Mapping (PRISM) for digital elevation mapping with 2.5 m spatial resolution, the Advanced Visible and Near-Infrared Radiometer type 2 (AVNIR-2) for precise land coverage observation, and the Phased Array type L-band Synthetic Aperture Radar (PALSAR) for day-and-night and all-weather land observation. Imagery from commercial satellites has found occasional use but is too expensive for most research purposes. This includes data from the French Satellite Pour l'Observation de la Terre (SPOT) series, with SPOT 1 launched in 1986 and 5 in 2002 with 2.5–20 m resolution, the US Ikonos launched in 1999 with 1–4 m resolution and Quickbird launched in 2001 with 0.6–2.4 m resolution. The status of Russian environmental satellites in the METEOR, OKEAN, and RESURS series is reported by Asmus (2003).

### Glaciers

Glacier mapping from Landsat Thematic Mapper (TM) data has followed several approaches (Paul, 2000). These involve: (1) manually delineating the glacier outline by

cursor tracking, (2) segmentation of ratio images, and (3) unsupervised or supervised classification. The first approach has been used to determine glacier length changes (Hall et al., 1992, for example). Various combinations of ratios have been used. Bayr et al. (1994) derive a glacier mask by using thresholds with ratio images of raw digital numbers from TM channels 4 and 5. Rott and Markl (1989) use atmospherically corrected spectral images of TM3/TM5 and TM4/TM5, with the help of thresholds to obtain a glacier mask. Paul noted that classification methods, both supervised and unsupervised, proved not to be suitable for glacier mapping.

Beginning in 1978, a major effort was undertaken by Williams and Ferrigno (1988) of the US Geological Survey to compile a Satellite Image Atlas of Glaciers of the World. The authors used maps; aerial photographs; Landsat 1, 2, and 3 MSS images; and Landsat 2 and 3 RBV images to inventory the areal distribution of glacier ice between about 82° north and south latitudes. Some later contributors also used Landsat 4 and 5 MSS and Thematic Mapper (TM), Landsat 7 Enhanced Thematic Mapper-Plus (ETM+), and other satellite images. There are 10 regional chapters: Those concerning Antarctica (B); Greenland (C); Continental Europe (E); Asia (F); Turkey, Iran, and Africa (G); Irian Jaya, Indonesia, and New Zealand (H); South America (I); North America excluding Alaska (J); and Alaska (K). All chapters are now accessible at <http://pubs.usgs.gov/pp/p1386/>.

A NASA-funded project for Global Land Ice Measurements from Space (GLIMS) is under way at the National Snow and Ice Data Center (NSIDC) (Armstrong et al., 2005b; <http://www.glims.org/>). It is an international project involving 60 institutions worldwide, with the goal of surveying a majority of the world's estimated 103,000 glaciers (Bishop et al., 2004). Currently over 96,000 glacier outlines are in the GLIMS database. A supplemental globally complete inventory was developed for the IPCC AR5 report and is available as the Randolph Glacier Inventory RGI3.0 (April 2013) from GLIMS. GLIMS uses data collected primarily by the Advanced Spaceborne Thermal Emission and Reflection Radiometer (ASTER) instrument, aboard the Terra satellite, and the LANDSAT ETM+, along with historical observations. Analysis of changes in glacier extent using GLIMS data, earlier satellite imagery, and historical maps for the Eastern Pamir (Khromova et al., 2006) show that the glacier area decreased 7.8 % during 1978–1990, and 11.6 % in 1990–2001. In the Cordillera Blanca, Peru, Raup et al. (2007) show that glaciers receded by 11–30 % over the period 1962–2003; they also recognized inconsistencies in the earlier glacier mapping. Racoviteanu et al. (2008) use Spot 5 scenes from 2003 compared with aerial photography from 1970 for the Cordillera Blanca and report a 22.4 % loss in glacier area. High-resolution ALOS/PRISM data have been used for mapping glaciers in Eurasia and determining areal changes by comparison with earlier data by Aizen et al. (2007) and Surazakov et al. (2007).

There is still no single map of the world's glaciers. However, work is under way at the NSIDC to compile such a map using 500 m-resolution Moderate-Resolution Imaging Spectroradiometer (MODIS) images. The procedure involves determining whether a pixel has ever been snow free, by combining the lowest reflectance signatures for each pixel over several summer time periods in order to identify permanent snow and ice with the highest reflectance.

Glacier motion has been mapped with JERS-1 L-band SAR data. Strozzi et al. (2008) employ offset fields between pairs of JERS-1 satellite SAR data acquired in winter with 44 days time interval to estimate glacier motion on Svalbard, Novaya Zemlya, and Franz-Josef Land. The displacement maps show that the ice caps are divided into a number of clearly defined fast-flowing units with displacement larger than about 50 m/year with an estimated error on the order of 20 m/year.

Glacier mass balance has been estimated for three glaciers in the French Alps using a combination of SAR data and surface stakes (Dedieu et al., 2003). The essential key to using remote sensing is to obtain a high-resolution digital elevation model (DEM). This is possible from ASTER using stereoscopy, provided there are ground control points (GCPs) on and around the glaciers.

### Snow cover

Hemispheric analysis of snow cover began in the United States in October 1966 from the polar orbiting Very High Resolution Radiometer (VHRR), with 3 km resolution, and continued with the use of AVHRR, GOES, and other mainly visible-band satellite data. The National Oceanic Atmospheric Administration (NOAA) issued weekly snow cover maps of the Northern Hemisphere that, beginning in 1972, were analyzed from the Advanced Very High Resolution Radiometer (AVHRR) instrument with 1.1 km resolution. The NOAA snow maps were generated from a polar stereographic grid whose pixel size ranged from  $125 \times 125$ – $200 \times 200$  km depending on latitude. This now provides the longest time series of any satellite product. Since February 1997, it has been issued on a daily basis using the Interactive Multisensor Snow and Ice Mapping System (IMS) (Ramsay, 1998). Recent upgrades to the IMS are reported by Helfrich et al. (2007). They include: a 4 km-resolution grid output, ingest of an automated snow detection algorithm, expansion to global extent, and a static Digital Elevation Model for mapping based on elevation.

Global snow cover maps are now available from MODIS on Terra (February 2000–present) and Aqua (July 2002–present). There are daily, 8 day, and monthly global grids at 500 m and  $0.05^\circ$  resolution (<http://nsidc.org/data/modis/data.html>). Hall and Riggs (2007) provide an accuracy assessment for the Terra products. The overall absolute accuracy of the 500 m resolution swath and daily tile products is 93 %, but varies by land-cover type and

snow condition. The most frequent errors are due to snow/cloud discrimination problems; however, improvements in the MODIS cloud mask have occurred in each reprocessing. Detection of very thin snow (<1 cm thick) can also be problematic.

Global snow depth and water equivalent can be estimated from passive microwave data. One of the earliest algorithm applications was by Foster et al. (1980) using SMMR data for a hemispheric analysis. Chang et al. (1987, 1990) use the difference of the 18 and 37 GHz channels on SMMR to estimate snow volume in the Northern Hemisphere. The mean monthly snow volume ranges from about  $1.5 \times 10^{13}$  kg in summer to about  $300 \times 10^{13}$  kg in winter. Tait (1998) developed a series of algorithms for different land-cover types similar to those of Chang et al. (1987). Snow grain size, especially the presence of large depth hoar crystals, has a huge effect on microwave backscatter and so decreases the brightness temperature. Over the Canadian Prairies, operational analyses have been issued in near-real time since 1988/1989 using a vertically polarized gradient ratio algorithm  $(37-19 \text{ V})/18$  (Goodison and Walker (1994)). The algorithm was much improved by the use of a wet snow indicator. Foster et al. (1997) compare snow mass estimates from a prototype passive microwave snow algorithm, a revised algorithm, and a snow depth climatology.

Global maps of snow water equivalent from SMMR and SSM/I have been produced from 1978 to 2007 (with updates) by Armstrong et al. (2005a); (<http://nsidc.org/data/nsidc-0271.html>). The data are in 25 km grids but the radiometric information is from an area that is larger than  $625 \text{ km}^2$ , so the gridded value represents a mean Snow Water Equivalent (SWE) for this area. There is decreased confidence in the SWE reliability and possible under-measurement in the following cases:

1. Mountainous areas with large topographic variability return low SWE values. Samples from these areas contain a mixed signal from a large footprint.
2. Forested areas return low mean SWE values, because the mixed signal includes emission from trees and the snow canopy as well as the underlying surface.
3. Areas near coastlines return low or no SWE values, because the mixed signal includes frozen and unfrozen water and land.
4. Areas containing melting snow or wet snow packs typical of maritime snow conditions return low or no SWE values, because the microwave emission from liquid water overwhelms scattering from the snow pack.
5. Shallow or intermittent snow during fall and early winter typically does not result in sufficient microwave scattering to reliably detect SWE.

Further details are available at [http://nsidc.org/data/docs/daac/nsidc0271\\_ease\\_grid\\_swe\\_climatology.gd.html](http://nsidc.org/data/docs/daac/nsidc0271_ease_grid_swe_climatology.gd.html)

The Advanced Microwave Scanning Radiometer for the Earth Observing System (AMSR-E) was launched on Aqua in May 2002. It measured horizontally and vertically polarized brightness temperatures at 6.9, 10.7, 18.7, 23.8,

36.5, and 89.0 GHz. The spatial resolution of the individual measurements varied from 5.4 km at 89 GHz to 56 km at 6.9 GHz. Thus, it had twice the resolution of SSM/I. A snow cover algorithm has been developed and tested by Chang et al. (2003). AMSR-E (SWE) and MODIS (snow extent) are available at NSIDC. AMSR-E was decommissioned on October 4, 2011.

Regional analyses of snow cover extent and characteristics have been carried out using Landsat Thematic Mapper data (Dozier and Marks, 1987; Martinec and Rango, 1987).

Subsequently, Airborne Visible/Infrared Imaging Spectrometer (AVIRIS) data have been used to map grain size and other snow characteristics via spectral mixture analysis. AVIRIS has 224 contiguous spectral channels with wavelengths from 400 to 2,500 nm. The spatial resolution is 4–20 m. The classification algorithm is based on the multiple end-member approach to spectral mixture analysis in which the spectral endmembers and the number of endmembers can vary on a pixel-by-pixel basis. This approach accounts for surface cover heterogeneity within a scene. The mixture analysis is operated on endmembers from a library of snow, vegetation, rock, soil, and lake ice spectra. Snow end members of varying grain size were produced with a radiative-transfer model (Painter et al., 1998, 2003; Dozier and Painter, 2004).

Algorithms are available to map snow extent (Shi and Dozier, 1993; Rott and Nagler, 1993; Shi and Dozier, 1997) and snow depth and density (Shi and Dozier, 1996) using SAR data. These approaches are valuable for small areas in mountain terrain but the limited swath coverage makes them impractical for continental regions.

The Cold Land Processes Experiment (CLPX), funded by NASA, was a multisensor, multi-scale approach to assess terrestrial snow cover, providing a comprehensive data set necessary to address several experiment objectives. Within a framework of nested study areas in the Rocky Mountains of Colorado, ranging from 1 ha to 160,000 km<sup>2</sup>, intensive ground, airborne, and spaceborne observations were collected for mid-winter and spring intensive observation periods (IOPs) in 2002–2003. The three major questions of the mission (Cline et al., 1999) were as follows:

1. Can the components of the terrestrial cryosphere be observed from space accurately enough to identify meaningful climatic trends?
2. To what extent can snow and frozen ground information, deduced from remote sensing data, improve models of cold season processes, hydrologic forecasts, and forecasts of high-latitude ecosystem functions?
3. To what accuracy can SWE be estimated from remote sensing data, and is this sufficient for hydrological applications?

More specifically, the project aimed to:

- Evaluate and improve snow water equivalent retrieval algorithms for spaceborne passive microwave sensors such as SSM/I and AMSR-E

- Evaluate and improve radar retrieval algorithms for snow depth, density, and wetness, and soil freeze/thaw status
- Improve radar retrieval algorithms to enable discrimination of freeze/thaw status of snow, soil, and vegetation surfaces
- Examine the effects of spatial resolution on the skill of active and passive microwave remote sensing retrieval algorithms for snow and freeze/thaw status
- Examine the feasibility of coupling forward microwave radiative-transfer schemes to spatially distributed snow/soil models, to improve assimilation of microwave remote sensing data
- Examine the spatial variability of snow and frozen soil distributions in different environments and (a) improve the representation of subgrid-scale variability of snow and frozen soil in coupled and uncoupled land surface models, and (b) improve the representation of orographic precipitation (snowfall) in atmospheric models

Data collection focused on airborne measurements from five sensors each with a different spatial resolution. The NASA AIRSAR instrument collected synthetic aperture radar measurements at three frequencies (P-, L-, and C-bands) in both polarimetric and interferometric modes. The NASA POLSCAT instrument collected Ku-band scatterometer measurements. The NOAA PSR-A instrument collected passive microwave measurements at five frequencies ranging from 10.7 to 89 GHz. The similar Airborne Earth Science Microwave Imaging Radiometer (AESMIR) was flown during the 2003 campaigns to collect passive microwave measurements (at all AMSR-E frequencies from 6.9 to 89 GHz). The National Weather Service (NWS)/National Operational Hydrologic Remote Sensing Center (NOHRSC) airborne snow survey program also flew similar snow-detection sensors. An instrument measured terrestrial and atmospheric gamma radiation, which was used to determine snow water equivalent based on standard operational algorithms. At the two largest scales (33,000 and 142,000 km<sup>2</sup>), data collection focused on spaceborne measurements from several active and passive microwave and optical sensors.

Tedesco et al. (2005) show that airborne Polarimetric Scanning Radiometer data can be modeled by a log-normal distribution (Fraser, forested area) and by a bimodal distribution (North Park, patchy-snow, non-forested area). The brightness temperatures are resampled over a range of resolutions to study the effects of sensor resolution on the shape of the distribution, on the values of the average brightness temperatures, and on the standard deviations. The histograms become more uniform and the spatial information contained in the initial distribution is lost for a resolution >5,000 m in both areas. Tedesco et al. (2006) analyze the brightness temperatures of melting and refreezing snow using a truck-mounted radiometer at 6.7, 19, and 37 GHz and measuring brightness as a function of snow wetness. The physical model

reproduces brightness temperatures with a relative error of 3 % (8 K).

Haran (2003) provides MODIS radiances, reflectances, snow cover, and related grids for the CLPX IOPs in 2002–2003. Stankov and Gasiewski (2004) supply airborne multiband polarimetric brightness temperature images over three 25 × 25 km meso-scale study areas for both years. A listing of CLPX data sets is available at: <http://www.nsidc.org/data/clpx/#data>.

### Freshwater ice

Ice forms seasonally on lakes, reservoirs, and rivers. A major problem for detection is the small spatial scale of rivers and small lakes. Detection of ice cover by passive microwave data is possible on large lakes and ice conditions have been routinely mapped on Great Slave and Great Bear Lakes in Northern Canada since April 1992 (Walker and Davey, 1993). DMSP SSM/I data are acquired with a focus on ice freeze-up and breakup. It has been found possible to discriminate between areas of ice cover and open water using SSM/I 85 GHz data. Airborne SAR data were used by Leconte and Klassen (1991) to determine lake and river ice features in Northern Manitoba, and Radarsat SAR is used routinely for ice classification and mapping over the Great Lakes (Leshkevich et al., 1998). Wynne et al. (1998) determined lake ice breakup dates from 1980 to 1994 for 81 lakes and reservoirs in the US Upper Midwest and portions of Canada (60 °N, 105 °W to 40 °N, 85 °W). Analyses of images from the visible band of the GOES-VISSR were used. The objectives were to investigate the utility of monitoring ice phenology as a climate indicator and to assess regional trends in lake ice breakup dates. MODIS 250 m-resolution data have been used for a study of ice-out dates in the Brooks Range (Kukthuroja et al., 2006). An initial problem was to construct a lake mask using 30 m TM imagery. Duguay and Lafleur (2003) combine optical and SAR data analysis to map ice thickness on shallow sub-Arctic lakes.

### Sea ice

Sea ice in the Eurasian Arctic seas was routinely mapped by visual reconnaissance from aircraft flights in the Soviet Union starting in July 1933 and continuing until 1992 (Borodachev and Shilnikov, 2003). From the 1950s onward, 30–40 aircraft made 500–700 flights annually (Johannessen et al., 2007). The coverage was initially only in late summer, but by 1950, it was continuous throughout the year. Side-Looking Airborne Radar (SLAR) mapping was used from the mid-1960s and in 1983. SLR (Side-looking RADAR) was available from the Okean 01 series of satellites. Ice concentration and ice type were mapped at 10 to 30 day intervals. The chart records have been resumed since 1997 using satellite data. Early paper charts were digitized, and the entire series, including later charts that were produced entirely digitally, were converted to Sea Ice Grid (SIGRID) format at the Arctic and Antarctic Research Institute (AARI) in St. Petersburg, Russia.

NSIDC completed the conversion to EASE-Grid – a Lambert equal-area projection with 12.5 km cell size. Total ice concentration, as well as partial concentrations for multiyear, first-year, new/young ice, and fast ice, is available (Arctic and Antarctic Research Institute, 2007). Mahoney et al. (2008) analyzed sea ice extent in the Eurasian Arctic for 1933 to 2006 using the Soviet historical data.

The first aerial ice reconnaissance in Canada was completed during the winter of 1927–1928 by the Royal Canadian Air Force (RCAF) over Hudson Strait and Hudson Bay. In 1940, the Canadian Department of Transport Marine Services began an “Ice Patrol” in the Gulf of St. Lawrence. Summer patrols in the Arctic began in 1957. The first SLAR used for ice reconnaissance was installed in 1978; it had a 100 m resolution. SLAR measurements continue to be used along the eastern coast of Canada. Airborne Synthetic Aperture Radar (SAR) was introduced in 1990 with digital processing techniques and a resolution in the range of 5–30 m.

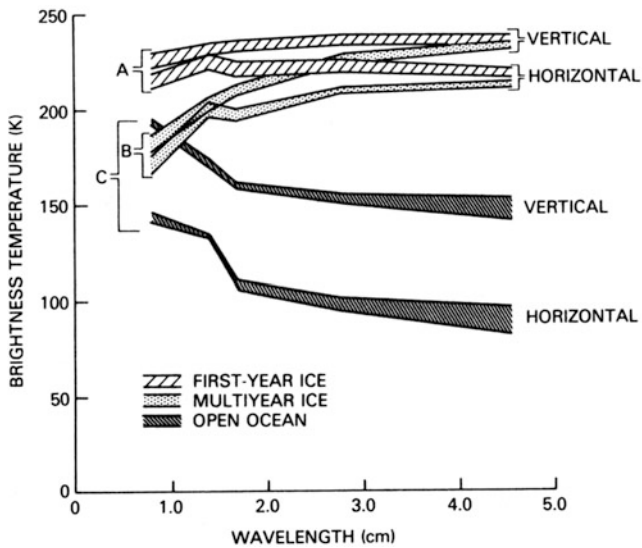
The use of satellite data from the visible and infrared Very High Resolution Radiometer (VHRR) began in 1966. In 1970, the National Oceanographic and Atmospheric Administration (NOAA) launched the first of a series of satellites with VHRR having an improved resolution of 1 km. In 1978, the first satellite carrying the improved Advanced Very High Resolution Radiometer (AVHRR) was launched. This series continues to this day.

Satellite reception at the Arctic and Antarctic Research Institute provides visible and infrared satellite images both from Russian (METEOR, OKEAN, RESURS) and US (NOAA) satellites. The OKEAN satellite also provides SLR and passive microwave data.

In December 1972, the National Aeronautics and Space Administration (NASA) launched the Electrically Scanning Microwave Radiometer (ESMR) on Nimbus 5. Until May 1977 this provided single channel horizontally polarized radiation at a frequency of 19 GHz. Its ability to operate in darkness and through cloud cover yielded the first comprehensive maps of polar sea ice extent for 1973–1976 (Zwally et al., 1983; Parkinson et al., 1987). The brightness temperature data gridded to 25 km (Parkinson et al., 1999) are available at: [http://nsidc.org/data/docs/daac/nsidc0077\\_esmr\\_tbs.gd.html](http://nsidc.org/data/docs/daac/nsidc0077_esmr_tbs.gd.html).

In October 1978, the Scanning Multichannel Microwave Radiometer (SMMR) was launched on Nimbus 7 and operated until August 1987. The instrument had three channels, two with dual polarization. Frequencies 18 and 37 GHz were used in various algorithms to derive sea ice concentrations for first-year and multiyear ice (Gloersen et al., 1992). The records continued with the Special Sensor Microwave Imager (SSM/I) on Defense Meteorological Program satellites. These instruments had five frequencies including 19 and 37 GHz.

Sea ice can be discriminated in the microwave regime through differences in the emissive characteristics between ice and ocean; in general, sea ice is more emissive than the open ocean. Use of combinations of frequencies



### Cryosphere, Measurements and Applications,

**Figure 1** Microwave brightness temperatures of sea ice and open water observed by Nimbus 7 SMMR in three regions of the Arctic, February 3–7, 1979. The regions A, B, and C are representative of first-year sea ice, multiyear ice, and open water, respectively. Hatched bands indicate  $\pm$  one standard deviation about the mean (From Cavalieri et al., 1984; courtesy of the American Geophysical Union).

allows more accurate discrimination between ice and ocean as well as the ability to estimate fractional ice cover within regions of mixed ice and water. The NASA Team algorithm (Cavalieri et al., 1984) uses a polarization ratio and a gradient ratio.

The polarization ratio is:

$$PR_{[19V/H]} = \frac{T_B[19V] - T_B[19H]}{T_B[19V] + T_B[19H]}$$

The gradient ratio is:

$$GR_{[37V/19V]} = \frac{T_B[37V] - T_B[19V]}{T_B[37V] + T_B[19V]}$$

The PR is small for ice and large for water while the GR is small for first-year ice but large for multiyear ice. **Figure 1** illustrates these points (Cavalieri et al., 1984). Combinations of PR and GR enable the  $T_B$  signatures to be interpreted as ice type and there are some eight or so algorithms in use for this purpose.

Another approach is used by the Bootstrap algorithm (Comiso, 1986), which employs linear combinations of 19 and 37 GHz frequencies at both horizontal and vertical polarizations to estimate fraction ice coverage. The NASA Team and Bootstrap, as well as other algorithms, require empirically derived “tie points,” or coefficients for pure surface types (100 % ice and 100 % water).

There are many uncertainties and limitations in using passive microwave data for sea ice detection. There are

errors due to ambiguous emissivity signals, particularly from surface melt water during summer and for thin ice. The available passive microwave frequencies can discriminate between at most three ice types, but often a region may have more than three unique microwave signatures. There can be erroneous ice retrievals over open water due to increased ocean surface emissivity from wind roughening. Atmospheric emission may be a factor in some conditions. Perhaps the major limitation is the low spatial resolution of passive microwave sensors, with footprints of 12–50 km. Thus, individual floes cannot be imaged and the ice edge location can be estimated to several kilometers accuracy at best. However, passive microwave data are a valuable source of sea ice information because it is sunlight independent and is generally not affected by clouds and other atmospheric sources. Also, passive microwave sensors have wide swaths and sun-synchronous orbits that provide frequent coverage of the polar regions. Thus, passive microwave data has provided a consistent and nearly complete daily record of sea ice conditions in both the Arctic and Antarctic since late 1978. Carsey (1992a) discusses the passive microwave properties of sea ice and the limitations of passive microwave remote sensing in more detail.

While the NASA Team and Bootstrap algorithm products are the most commonly used passive microwave sea ice estimates, several other algorithms have been developed, including the Cal/Val or AES York (Bjerkelund et al., 1990), Bristol (Hanna and Bamber, 2001), and Norsex (1983). All these algorithms make use of some combination of the 19 and 37 GHz channels. More recent algorithms have employed the higher frequency passive microwave channels on SSM/I and AMSR-E to obtain better spatial resolution and to resolve some of the surface ambiguities. These include the NASA Team 2 (Markus and Cavalieri, 2000) and the ARTIST (Spren et al., 2008). The NASA Team 2 algorithm is used for the AMSR-E standard sea ice product (Comiso et al., 2003).

A comparison of the NASA Team and the Bootstrap algorithms is given by Comiso et al. (1997) and of the NASA Team, NASA Team 2, and the Bootstrap algorithms by Stroeve et al. (2001). Partington (2000) compared NASA Team and Cal/Val estimates and discussed the potential for a combined product using data fusion. Meier (2005) compares four different algorithms with AVHRR data. He finds that the smallest mean errors are from the Cal/Val and NASA Team-2 algorithms; the former tends to overestimate and the latter underestimate ice concentration relative to AVHRR in three near-marginal ice zones of the Arctic. Andersen et al. (2007) compared several algorithms and found significant differences in long-term trends depending on the algorithm, indicating potentially important influence of atmospheric and surface properties on the various sea ice algorithms.

Comiso and Nishio (2008) combine SSMR, SSM/I, and Advanced Microwave Scanning Radiometer (AMSR)-E data to show that the trend in ice area through 2006 in the Arctic is now slightly more negative at  $-4.0 \pm 0.2$  % per

decade, respectively, while the corresponding trend in the Antarctic remains slightly positive at  $+1.7 \pm 0.3$  % per decade. The Arctic sea-ice cover, as revealed by microwave radiometry experienced a remarkable reduction in area in the summer of 2007, and again in 2012.

Carsey (1992a) provides a detailed and comprehensive treatment of sea ice remote sensing using both passive microwave and active radar remote sensing.

Passive microwave imagery is also useful for tracking large-scale sea ice motions using cross-correlated feature matching (e.g., Agnew et al., 1997; Kwok et al., 1998; Meier et al., 2000) or with a wavelet analysis approach (Liu and Cavalieri, 1998). SSM/I 85 GHz can estimate daily ice motions to within an RMS error of 6 km/day accuracy (Meier et al., 2000); averaging over longer time periods (Kwok et al., 1998) or using spatial interpolation (Meier et al., 2000) can reduce the error. Ice motion retrievals are limited during summer melt. Passive microwave sea ice motions have higher errors in the Antarctic (Kwok et al., 1998). The higher spatial resolution of AMSR-E can provide improved motion accuracy (Meier and Dai, 2006) and allow for better detection of summer motion through the use of the 18 GHz channel (Kwok, 2008). Because of the change in emissivity of sea ice during melt, passive microwave imagery is also useful for the determination of melt onset (Smith, 1998; Drobot and Anderson, 2001; Belchansky et al., 2004)

Radars that measure the power of the return pulse scattered back to the antenna can be used to derive geophysical parameters of the illuminated surface, or volume, based on the scattering principles of microwave electromagnetic radiation (Maurer, 2003). These instruments are known as “scatterometers.” The major instruments flown are the ESCAT, the European Space Agency’s (ESA) Earth Remote Sensing (ERS)-1 and -2 Active Microwave Instrument (C band, 3 GHz, V), the first of which operated between 1992 and 1996 and the second of which has been operating since 1996, and the NASA QuikSCAT SeaWinds instrument (Ku band, 13.6 GHz, V and H), flown from 1999 to present. Scatterometry is useful for measuring ice extent (Allen and Long, 2006; Anderson and Long, 2005; Remund and Long, 1999) and ice motion (Zhao et al., 2002; Haarpaintner, 2006). Resolution-enhanced scatterometer data using image reconstruction techniques have provided improved spatial resolution (Long et al., 1993), which potentially yields more precise ice edge position (Meier and Stroeve, 2008). Due to salinity differences between multiyear and first-year ice, scatterometer data can estimate seasonal and perennial ice coverage (e.g., Nghiem et al., 2007). Scatterometry is also useful for measuring the extent of snowmelt on sea ice due to its extreme sensitivity to the presence of liquid water.

Another active microwave sensor useful for sea ice studies is synthetic aperture radar. In contrast to scatterometers, it is an imaging radar that synthesizes images from multiple looks during the satellite’s motion in orbit to effectively create a large antenna and thus

obtain much higher spatial resolution. The Canadian RADARSAT-1 sensor has been providing SAR coverage of sea ice since 1995. RADARSAT-2 was launched in December 2007 and will take over SAR acquisition from RADARSAT-1. However, RADARSAT-2 is a purely commercial satellite and it is unlikely that data will be widely available to the science community. The resolution is high enough to capture small-scale ice motion and ice deformation events, allowing ice motion, ice age, ice volume, ice production, seasonal ice area to be estimated at fine spatial scales (Kwok and Cunningham, 2002; Kwok et al., 1995, 1998). The high-resolution, all-sky capabilities are particularly useful for operational analysis of sea ice, and SAR imagery is widely used by operational sea ice centers such as the Canadian Ice Service and the US National Ice Center (Bertoia et al., 2001). However, the narrow swath of SAR sensors limits repeat coverage to every 3–6 days in many regions of the Arctic. In addition, SAR imagery of sea ice can be difficult to interpret and efforts at automated analysis have been largely unsuccessful.

The determination of sea ice thickness remains a major challenge. Upward looking sonar (ULS) on submarines is the major source of ice thickness information in the Arctic (Rothrock et al., 1999). Ocean floor-mounted ULS have also provided ice thickness estimates but only in isolated locations (Vinje et al., 1998). Airborne electromagnetic induction instruments have been used experimentally and operationally since about 1990 (Haas and Eicken, 2001). Worby et al. (1999) describe its use over fast ice and pack ice in the Antarctic. More recently, autonomous underwater vehicles (AUVs) have been successfully employed to map the terrain of the underside of sea ice (Wadhams and Doble, 2008).

ERS radar altimetry has been used to estimate ice thickness in the Arctic (Laxon et al., 2003; Peacock and Laxon, 2004) and the Antarctic (Giles et al., 2008), but the coverage of the polar regions by the ERS orbit limits retrievals to the seasonal ice zones in the Arctic. Cryosat 2 with a radar altimeter was launched by ESA in April 2010 and is providing ice thickness and volume estimates for the Arctic (Laxon et al., 2012). The laser altimeter on the Ice, Cloud, and Land Elevation Satellite (ICESat) has been used to determine sea ice freeboard in the Arctic. Kwok et al. (2008) obtained average values of 43 cm over multiyear ice and 27 cm over first-year ice in February–March 2006. Uncertainties arise primarily through snow cover on the ice. Zwally et al. (2008) measured Antarctic ice thickness using ICESat.

There are considerable issues in determining sea ice thickness from altimeters and such measurements are still largely unvalidated. Because altimeters are measuring only freeboard, any errors in such estimates are magnified when deriving total ice thickness. The major uncertainty is snow thickness, which must be known to accurately account for its contribution to freeboard height (for laser altimeters that measure from the top of the snow surface) or for total freeboard density (for radar altimeters that

penetrate snow cover and measure from the snow/ice interface). However, while there is still considerable uncertainty in any absolute thickness estimates from altimeters, they appear to be able to capture seasonal and interannual variations well in sea ice thickness.

Lagrangian tracking of sea ice using passive microwave imagery and other sources provides a long history (since early 1980s) of ice age, a proxy for ice thickness (Maslanik et al., 2007); comparison with ICESat thickness indicates reasonable correlation between age and thickness on a basin scale up to ages of 9 years.

### Ice sheets

Ice sheet remote sensing involves all wavelengths of the electromagnetic spectrum. Initial work was done with Landsat MSS images in the 1980s. Williams et al. (1982) assembled 4,270 Landsat scenes covering Antarctica to about 82 °S latitude. A Landsat MSS mosaic of the Ronne-Filchner ice shelf and Coats Land was georeferenced using measured ground control points by Sievers et al. (1989). A SAR mosaic from ERS-1 was georeferenced and is thought to be accurate to 50 m (Roth et al., 1993). The images are co-registered by either (1) matching fixed points such as nunataks projecting through the ice or (2) using the furnished coordinates based on orbital parameters. Note that georeferencing using the ephemeris data (furnished coordinates) has an advantage in the ice sheet interiors, where large areas are devoid of fixed rock outcrops. There are two methods to determine the glacial velocities: an interactive one in which crevasse patterns are visually traced (Lucchitta et al., 1993) and an autocorrelation program developed by Scambos et al. (1992).

Polar Pathfinder AVHRR products are available twice daily at 5 km resolution in Equal-Area Scalable Earth (EASE) Grid format (<http://nsidc.org/data/avhrr/>) for July 1981 through June 2005, and for shorter periods at 1.25 and 25 km resolution. The products include: clear-sky surface broadband albedo and skin temperature, solar zenith angle, surface type mask, cloud mask, orbit mask, and ice motion vectors (Maslanik et al., 1998; Scambos et al., 2000). Laine (2008) used these data to analyze albedo changes in the Antarctic. All sectors show slight increasing spring–summer albedo trends. The steepest ice sheet albedo trend of  $0.0019 \pm 0.0009/\text{year}$  is found in the Ross Sea sector. The steepest sea ice albedo trend of  $0.0044 \pm 0.0017/\text{year}$  occurs in the Pacific Ocean sector.

Multi-angle Imaging SpectroRadiometer (MISR) data have been used to determine the ice albedo over Greenland (Nolin et al., 2001). Stroeve and Nolin (2002) use two different methods to derive the snow albedo: one based on the spectral information and one utilizing the angular information from the MISR instrument. The latter method is based on a statistical relationship between in situ albedo measurements and the MISR red channel reflectance at all MISR viewing angles and is found to

give good agreement with the ground-based measurements. The spectral method is more sensitive to instrument calibration and shows bidirectional reflectance distribution function models and narrowband-to-broadband albedo relationships. The MISR sensor's ability to map glacier facies and roughness was explored and documented by Nolin et al. (2002).

The VELMAP project at NSIDC (<http://nsidc.org/data/velmap/>) aims to compile all ice flow data for the Antarctic continent. The project includes Landsat 7 and ASTER ice velocity maps while the second and third Radarsat Antarctic Mapping Missions provide data north of 80 °S. There are currently more than 130,000 ice vectors in the database.

Changes in the West Antarctic ice sheet since 1963 have been identified using formerly classified Corona images and recent data by Bindschadler and Vornberger (1998). They find that ice stream B has widened at a rate much faster than expected and its movement also slowed down. The available data are reviewed and described in Bindschadler and Seider (1998). A mosaic of the 1962–1963 Antarctic coast and ice shelves was compiled, and a grounding line for that time was calculated, from these data (Kim et al., 2006).

In 1997, the Canadian RADARSAT-1 satellite was rotated in orbit, so that its synthetic aperture radar (SAR) antenna looked south toward Antarctica. This permitted the first high-resolution mapping of the entire Antarctic continent to be accomplished in less than 3 weeks. Swath images representing calibrated radar backscatter data have been assembled into 90 tiles at 25 m resolution and an image mosaic available at 125 m to 1 km resolutions. The RADARSAT Image Map of Antarctica, 1999, is the product of the RADARSAT-1 Antarctic Mapping Project (RAMP). The mosaic provides a detailed look at ice sheet morphology, rock outcrops, research infrastructure, the coastline, and other features. Accompanying this mosaic is the high-resolution RAMP Digital Elevation Model (DEM) that combines topographic data from a variety of non-SAR sources to provide consistent coverage of all of Antarctica. Version 2 improves upon the original version by incorporating new topographic data, error corrections, extended coverage, and other modifications. The RAMP DEM is gridded at 200, 400, and 1,000 m.

There are large-scale spatial variations in radar brightness. The bright portion of Marie Byrd Land and the eastern Ross Ice Shelf probably represents the region where significant melting and refreezing occurred during an early 1990s melt event. Most of the coastal areas and much of the Antarctic Peninsula appear bright also because of summer melt. Remaining strong variations in radar brightness are poorly understood. Thousands of kilometer long curvilinear features across East Antarctica appear to follow ice divides separating the large catchment areas. On an intermediate scale, the East Antarctic Ice Sheet appears to be very “rough.” The texturing is probably due to the flow of the ice over the Wilkes subglacial basin located in George V Land. There the imagery shows subtle

rounded shapes similar in appearance to the signature of subglacial lakes such as Lake Vostok. In Queen Maud Land, East Antarctica, there are extensive ice stream and ice stream-like features. An enormous ice stream fed by a funnel-shaped catchment, reaching at least 800 km into East Antarctica, feeds Recovery Glacier, which enters the Filchner Ice Shelf. Megadunes and wind glaze regions were first identified as local features in Landsat TM, but are fully visible for the first time in the RAMP mosaic. Megadunes cover approximately one million square kilometers of the plateau surface (Fahnestock et al., 2006).

Using interferometry with SAR imagery obtained during the 1997 Antarctic Mapping Mission, ice velocity vectors were obtained over the East Antarctic ice streams. The upstream velocity of the Recovery Glacier is about 100 m/year but near the grounding line there is a local peak velocity of about 900 m/year.

Two digital image maps of surface morphology and optical snow grain size that cover the Antarctic continent and its surrounding islands have been prepared by NSIDC and the University of New Hampshire (Haran et al., 2005). The MODIS Mosaic of Antarctica (MOA) image maps are derived from composites of 260 MODIS orbit swaths. The MOA provides a cloud-free view of the ice sheet, ice shelves, and land surfaces, and a quantitative measure of optical snow grain size for snow- or ice-covered areas. Scambos et al. (2007) use MOA to provide continent-wide surface morphology and snow grain size.

Recently, the USGS with the British Antarctic Survey, NASA, and the National Science Foundation have produced a Landsat Image Mosaic of Antarctica (LIMA) from over 1,000 scenes of ETM+ to latitude 82.5 °S at 15 m resolution ([http://lima.usgs.gov/view\\_lima.php](http://lima.usgs.gov/view_lima.php)). Both the mosaic and the individual original Landsat images used in the compilation (which are nearly completely cloud-free scenes of the surface) are available online for free.

For Greenland, there has been albedo mapping with AVHRR (Stroeve et al., 1997) and MODIS (Liang et al., 2005). Ice velocity in ice streams has been derived from interferometric SAR (InSAR) (Joughin et al., 2000) and C-band SAR data from ERS-1 have been used to map the different snow and ice facies of the ice sheet (Fahnestock et al., 1993). Snow melt over the ice sheet has been mapped using SSM/I data by Abdalati and Steffen (1996) and using SMMR and SSM/I data by Mote and Anderson (1995). The latter used a threshold value of the 37 GHz brightness temperature while Abdalati and Steffen used a cross-polarized gradient ratio (XPGR), which is a normalized difference between the 19 GHz horizontally polarized and 37 GHz vertically polarized brightness temperatures. The threshold of  $XPGR = -0.025$  is used to classify dry versus wet snow.

Changes in mass balance of the two major ice sheets have recently been derived from a variety of satellite measurements including the Gravity Recovery and Climate Experiment (GRACE) (Rignot and Thomas, 2002).

They show that the Greenland ice sheet is losing mass by near-coastal thinning. The West Antarctic ice sheet, with thickening in the west and thinning in the north, is probably thinning overall. The mass imbalance of the East Antarctic ice sheet is likely to be small, but even its sign is uncertain. The main objective of the laser altimetry data obtained from the Geoscience Laser Altimeter System (GLAS) on the Ice, Cloud, and land Elevation Satellite (ICESat) was to measure ice sheet elevations and changes in elevation (Schutz et al., 2005). GLAS provided global coverage between 86 °N and 86 °S. ICESat has seen wide use as a tool in investigating specific processes or regions, via profile comparisons over time. Among several results are the discovery of rapidly changing subglacial lake systems, which appear to fill and drain on short (month to year) timescales (Fricker et al., 2007; Shepherd and Wingham, 2007). Using satellite-derived surface elevation and velocity data, Howat et al. (2007) found large short-term variations in recent ice discharge and mass loss at two of Greenland's largest outlet glaciers (Howat et al., 2007).

### Ice shelves

Iceberg calving from the Ross and Filchner ice shelves has been observed via satellite by the National Ice Center (NIC) originally using DMSP Optical Line Scanner (OLS) with 2.7 km resolution and AVHRR and subsequently MODIS and Envisat. Ballantyne and Long (2002) use scatterometer data to show the increasing numbers of icebergs detected since 1976. Antarctic icebergs are designated by the NIC as originating in one of four quadrants: A 0–90 °W, B 90–180 °W, C 180–90 °E, and D 90–0 °E. Iceberg B-15 broke off the Ross Ice Shelf in late March, 2000. Among the largest ever observed, this iceberg was approximately 270 km long × 40 km wide, nearly as large as the state of Connecticut.

MODIS satellite imagery revealed that the northern section of the 220 m-thick Larsen B ice shelf, on the eastern side of the Antarctic Peninsula, shattered and separated from the continent. A total of about 3,250 km<sup>2</sup> of shelf area disintegrated in a 35 day period beginning on January 31, 2002. The shattered ice formed a plume of thousands of icebergs adrift in the Weddell Sea. Over the last 5 years, the shelf has lost a total of 5,700 km<sup>2</sup>, and is now about 40 % the size of its previous minimum stable extent. Glasser and Scambos (2008) found that ice-shelf breakup is not controlled simply by climate. A number of other atmospheric, oceanic, and glaciological factors are involved. The location and spacing of fractures on the ice shelf such as crevasses and rifts are very important because they determine the strength of the ice shelf.

On Ellesmere Island, Arctic Canada, the Ward Hunt Ice Shelf has undergone similar rapid changes since 2000. SAR imagery revealed an extensive serpentine crack, and secondary fractures, in 2002 (Mueller et al., 2003). In summer 2005, the Ayles Ice Shelf broke off forming an ice island (Copeland et al., 2007).

## Icebergs

Icebergs were originally tracked by airborne reconnaissance in the Canadian Eastern Arctic and sub-Arctic. During 1960–1968, the International Ice Patrol used visual aerial reconnaissance. From 1963 to 1982, the Ice Patrol made iceberg survey flights north along the Labrador coast and into Baffin Bay. Side-looking airborne radar (SLAR) was introduced in 1983 and continues to be used. Following the advent of Radarsat-1 SAR (Power et al., 2001) in November 1995, the costly airborne surveys were discontinued by the Canadian Ice Service.

The Antarctic Meteorological Research Center at the University of Wisconsin-Madison provides near-real-time and archived imagery of Antarctic icebergs (<http://amrc.ssec.wisc.edu/index.html>). The images are from NOAA Polar Orbiting visible and IR band data. Brigham Young University, Provo, UT, produced enhanced resolution scatterometer backscatter images during July–September 1978 (from Seasat), July 1996–June 1997 (from NSCAT), 1992–2001 (from ERS-1 and 2), and June 1999 up to present (from QuikSCAT). Images were obtained from the Scatterometer Climate Record Pathfinder (SCP) project (Stuart et al., 2007). The initial position for each iceberg is located based on either (1) a position reported by the National Ice Center's web page (<http://www.natice.noaa.gov/>) or (2) by the sighting of a moving iceberg in a time series of scatterometer images. Ballantyne and Long (2002) used the archive to produce a long-term analysis of Antarctic iceberg activity.

## Frozen ground

Frozen ground may be seasonal or perennial (permafrost). Permafrost is beneath the surface and not readily amenable to direct remote sensing (Zhang et al., 2004). However, the near-surface soil freeze/thaw status can be determined using satellite remote sensing data. SAR provides information on the timing, duration, and spatial progression of near-surface freeze/thaw in autumn and spring, for example. Freezing results in a large increase in the dielectric of soil and vegetation, which causes a large decrease in L-band (15–30 cm wavelength) and C-band (3.75–7.5 cm wavelength) radar backscatter (3 dB). Way et al. (1997) used the ERS-1 C-band instrument over central Canada, for example, to detect this. Passive microwave radiation (PMR) data offer similar information at lower spatial resolution. Frozen soils relative to unfrozen soils exhibit (1) lower thermal temperatures, (2) higher emissivity, and (3) lower brightness temperatures. The PMR algorithm for frozen soils is:

$$\frac{\partial}{\partial f} T_B(f) \leq P_{SG}$$

and

$$T_{B(37V)} \leq P_D$$

where the spectral gradient is in  $\text{K GHz}^{-1}$  and  $T_{B(37V)}$  is in K.  $P_{SG}$  and  $P_D$  are the cutoff spectral gradient and brightness temperature, respectively. Based on these equations, surfaces can be classified as frozen, dry (and hot), wet (and cool), and mixed (Zuerndorfer and England, 1992). A frozen surface has low brightness temperature (37 GHz) and a relatively low negative spectral gradient. Zhang and Armstrong (2001) and Zhang et al. (2003) analyzed soil freeze/thaw status over the contiguous United States and southern Canada in winter 1997/1998. They used a negative spectral gradient and a threshold value of  $P_{37} = 258.2$  K. They found that almost 80 % of the time, the near-surface soil was frozen before snow accumulated on the ground. They applied the validated frozen soil algorithm to investigate near-surface soil freeze/thaw status from 1978 through 2003 over the Northern Hemisphere (Zhang and Armstrong, 2003). The long-term average maximum area extent of seasonally frozen ground, including the active layer over permafrost, is approximately 50.5 % of the landmass in the Northern Hemisphere. Preliminary results indicate that the extent of seasonally frozen ground has decreased about 15–20 % during the past few decades.

Smith et al. (2004) developed a freeze/thaw algorithm for SSM/I data and applied it for high northern latitudes for 1988–2002. They found a trend toward later autumn freeze-up in evergreen conifer forests in North America by  $3.1 \pm 1.2$  days/decade while in Eurasia there was a trend toward earlier thaw dates in tundra ( $-3.3 \pm 1.8$  days/decade) and larch biomes ( $-4.5 \pm 1.8$  days/decade). Despite the trend toward earlier thaw dates in Eurasian larch forests, the growing season did not increase in length because of parallel changes in timing of the fall freeze ( $-5.4 \pm 2.1$  days/decade).

## Conclusions

Remote sensing of the cryosphere has made major advances over the last three decades and has become an indispensable tool for cryospheric research, given the remote locations and hostile environments involved in the spatial distribution of many cryospheric variables. Beginning with aerial photography of glaciers, optical remote sensing then came into use in the 1960s–1970s for mapping snow cover and sea ice. The advent of passive microwave remote sensing in the 1970s eliminated most of the problems of cloud cover and illumination, and this advantage continued with the much higher resolution airborne and satellite radar data in the 1980s. Spatial resolution of optical sensors became much enhanced in the 1990s, and the 2000s have seen the use of satellite laser altimeter and gravity measurements. Techniques have also advanced with the direct production of DEMs from satellite data and ice motion studies using Interferometric SAR.

## Bibliography

- Abdalati, W., and Steffen, K., 1996. Passive microwave-derived snow melt regions on the Greenland Ice Sheet. *Geophysical Research Letters*, **22**, 787–790.
- Agnew, T. A., Le, H., and Hirose, T., 1997. Estimation of large-scale sea-ice motion from SSM/I 85.5 GHz imagery. *Annals of Glaciology*, **25**, 305–311.
- Aizen, V. B., Aizen, E. M., and Kuzmichenok, V. A., 2007. Glaciers and hydrological changes in the Tien Shan: simulation and prediction. *Environmental Research Letters*, **2**, 045019, 10 pp.
- Allen, J. R., and Long, D. G., 2006. Microwave observations of daily Antarctic sea-ice edge expansion and contraction rates. *IEEE Geoscience and Remote Sensing Letters*, **3**(1), 54–58.
- Altmaler, A., and Kany, C., 2002. Digital surface model generation from CORONA satellite images. *Journal of Photogrammetry and Remote Sensing*, **56**, 221–235.
- Andersen, S., Tonboe, R., Kaleschke, L., Heygster, G., and Pedersen, L. T., 2007. Intercomparison of passivemicrowave sea ice concentration retrievals over high-concentration Arctic sea ice. *Journal of Geophysical Research*, **112**, C08004, doi:10.1029/2006JC003543.
- Anderson, H. S., and Long, D. G., 2005. Sea ice mapping method for SeaWinds. *IEEE Transactions on Geoscience and Remote Sensing*, **43**(3), 647–657.
- Arctic and Antarctic Research Institute, 2007. Sea ice charts of the Russian arctic in gridded format, 1933–2006. In Smolyanitsky, V., Borodachev, V., Mahoney, A., Fetterer, F., and Barry, R. (eds.), *Digital Media*. Boulder, CO: National Snow and Ice Data Center.
- Armstrong, R. L., et al., 2005a. *Global Monthly EASE-Grid Snow Water Equivalent Climatology*. *Digital Media*. Boulder, CO: National Snow and Ice Data Center.
- Armstrong, R., et al., 2005b. *GLIMS Glacier Database*. *Digital Media*. Boulder, CO: National Snow and Ice Data Center.
- Asmus, V., 2003. Russian environmental satellites: current status and development perspectives. In *Committee on Earth Observation Satellites, 17th Plenary Meeting Colorado Springs*, November 19–20, 2003, Colorado Springs, CO, Item 19.5.
- Ballantyne, J., and Long, D. G., 2002. A multidecadal study of the number of Antarctic icebergs using scatterometry data. In *Geoscience and Remote Sensing Symposium*, 2002. *IGARSS'02*, Vol. 5, pp. 3029–3031.
- Barry, R. G., and Gan, T. Y., 2011. *The global cryosphere: past, present and future*. Cambridge: Cambridge University Press, 498 pp.
- Bayr, K. J., Hall, D. K., and Kovalick, W. M., 1994. Observations on glaciers in the eastern Austrian Alps using satellite data. *International Journal of Remote Sensing*, **15**, 1733–1742.
- Belchansky, G. I., Douglas, D. C., and Platonov, N. G., 2004. Duration of the Arctic melt season: regional and interannual variability, 1979–2001. *Journal of Climate*, **17**, 67–80.
- Bertoia, C., Manore, M., and Andersen, H. S., 2001. Mapping ice covered waters from space. *Backscatter*, **12**, 14–21.
- Bindschadler, R., and Seider, W., 1998. *Declassified intelligence satellite photography (DISP) coverage of Antarctica*. NASA Technical Memorandum 1998–206879, 38 pp.
- Bindschadler, R., and Vornberger, P., 1998. Changes in the West Antarctic Ice Sheet since 1963 from declassified satellite photography. *Science*, **279**, 689–692.
- Bishop, M. P., et al., 2004. Global Land Ice Measurements from Space (GLIMS): Remote sensing and GIS investigations of the Earth's cryosphere. *Geocarto International*, **19**(2), 57–84.
- Bjerkelund, C. A., Ramseier, R. O., and Rubinstein, I. G., 1990. Validation of the SSM/I and AES/York algorithms for sea ice parameters. In Ackley, S. F., and Weeks, W. F. (eds.), *Sea Ice Properties and Processes*. Hannover, NH: USACE. U.S. Army Cold Regions Research and Engineering Laboratory Monograph, Vol. 90–91, pp. 206–208.
- Borodachev, B. E., and Shilnikov, V. I., 2003. *Istoriya L'dovoi Aviatsonnoi Razedki v Arktikei na Zamerzayushchikh Moryakh Rossii (1924–1993) [The History of Aerial Ice Reconnaissance in the Arctic and Ice-covered Seas of Russia, 1924–1993]*. St. Petersburg: Gidrometeoizdat, 441 pp.
- Carsey, F. (ed.), 1992a. *Microwave Remote Sensing of Sea Ice*. Washington, DC: American Geophysical Union. Geophysical Monograph, Vol. 68, 478 pp.
- Carsey, F., 1992b. Remote sensing of ice and snow: review and status. *International Journal of Remote Sensing*, **13**, 5–11.
- Cavalieri, D. J., Gloersen, P., and Campbell, W. J., 1984. Determination of sea ice parameters with Nimbus 7 SMMR. *Journal of Geophysical Research*, **89**(C3), 5355–5369.
- Chang, A. T. C., Foster, J. L., and Hall, D. K., 1987. Nimbus-7 SMMR derived global snow cover parameters. *Annals of Glaciology*, **9**, 39–44.
- Chang, A. T. C., Foster, J. L., and Hall, D. K., 1990. Satellite sensor estimates of northern hemisphere snow volume. *International Journal of Remote Sensing*, **11**, 167–171.
- Chang, A. T. C., et al., 2003. Global SWE monitoring using AMSR-E data. In *Proceedings of the International Geoscience and Remote Sensing Symposium (IGARSS)*, 2003, pp. 680–682.
- Cline, D., et al., 1999. *Cold Land Processes Mission (EX-7) Science and Technology Implementation Plan*. Report on the NASA Post-2002 Land Surface Hydrology Planning Workshop, Irvine, CA.
- Comiso, J. C., 1986. Characteristics of Arctic winter sea ice from satellite multispectral microwave observation. *Journal of Geophysical Research*, **91**(C1), 975–994.
- Comiso, J. C., and Nishio, F., 2008. Trends in the sea ice cover using enhanced and compatible AMSR-E, SSM/I, and SMMR data. *Journal of Geophysical Research*, **113**(C2), C02S07.
- Comiso, J. C., Cavalieri, D., Parkinson, C., and Gloersen, P., 1997. Passive microwave algorithms for sea ice concentrations: a comparison of two techniques. *Remote Sensing of Environment*, **60**(3), 357–384.
- Comiso, J. C., Cavalieri, D. J., and Markus, T., 2003. Sea ice concentration, ice temperature, and snow depth using AMSR-E data. *IEEE Transactions on Geoscience and Remote Sensing*, **42**, 243–252.
- Copeland, L., Mueller, D. R., and Weir, L., 2007. Rapid loss of the Ayles Ice Shelf, Ellesmere Island, Canada. *Geophysical Research Letters*, **34**, L21501.
- Csatho, B., et al., 2000. Investigating the longterm behavior of Greenland outlet glaciers using high-resolution satellite imagery. In *Proceedings of the IEEE International Geoscience and Remote Sensing Symposium (IGARRS)*, 2002, pp. 1047–1150.
- Dedieu, J. F., and et al., 2003. Glacier mass balance determination by remote sensing in the French Alps: Progress and limitation for time series monitoring. In *Proceedings of the Fourth International Geoscience and Remote Sensing Symposium (IGARSS)'03*, pp. 2602–2604.
- Dozier, J., and Marks, D., 1987. Snow mapping and classification from Landsat Thematic Mapper data. *Annals of Glaciology*, **9**, 97–103.
- Dozier, J., and Painter, T. H., 2004. Multispectral and hyperspectral remote sensing of alpine snow properties. *Annual Reviews of Earth and Planetary Sciences*, **32**, 465–494.
- Drobot, S. D., and Anderson, M. R., 2001. An improved method for determining snowmelt onset dates over Arctic sea ice using scanning multichannel microwave radiometer and special sensor microwave/imager data. *Journal of Geophysical Research*, **106** (D20), 24,033–24,050.
- Duguay, C. R., and Lafleur, P. M., 2003. Estimating depth and ice thickness of shallow subarctic lakes using spaceborne optical

- and SAR data. *International Journal of Remote Sensing*, **24**(3), 475–489.
- Dunbar, M. R., and Greenway, K. R., 1956. *Arctic Canada from the Air*. Ottawa: Defense Research Board, 541 pp.
- Fahnestock, M., et al., 1993. Greenland Ice Sheet surface properties and ice dynamics from ERS-1 SAR imagery. *Science*, **262**(5139), 1530–1534.
- Fahnestock, M., Scambos, T., Haran, T., and Bauer, R., 2006. *AWS data: characteristics of snow megadunes and their potential effect on ice core interpretation*. Digital media. Boulder, CO: National Snow and Ice Data Center.
- Foster, J. L., et al., 1980. Snowpack monitoring in North America and Eurasia using passive microwave satellite data. *Remote Sensing of Environment*, **10**, 285–298.
- Foster, J., Chang, A., and Hall, D., 1997. Comparison of snow mass estimates from a prototype passive microwave snow algorithm, a revised algorithm and a snow depth climatology. *Remote Sensing of Environment*, **62**, 132–142.
- Fricke, H. A., et al., 2007. An active subglacial water system in West Antarctica mapped from space. *Science*, **315**(5818), 1544–1548.
- Giles, K. A., Laxon, S. W., and Worby, A. P., 2008. Antarctic sea ice elevation from satellite radar altimetry. *Geophysical Research Letters*, **35**, L03503, doi:10.1029/2007GL031572.
- Glasser, N. F., and Scambos, T. A., 2008. A structural glaciological analysis of the 2002 Larsen B ice shelf collapse. *Journal of Glaciology*, **54**(184), 3–16.
- Gloersen, P., Campbell, W. J., Cavalieri, D. J., Comiso, J. C., Parkinson, C. L., and Zwally, H. J., 1992. *Arctic and Antarctic Sea Ice, 1978–1987: Satellite Passive-Microwave Observations and Analysis*. Washington, DC: NASA.
- Goodison, B. E., and Walker, A. E., 1994. Canadian development and use of snow cover information from passive microwave satellite data. In Choudhury, B. (ed.), *Passive Microwave Remote Sensing of Land-Atmosphere Interactions*. Utrecht: VSP VB, pp. 245–262.
- Haarpaintner, J., 2006. Arctic-wide operational sea ice drift from enhanced resolution QuikScat/SeaWinds scatterometry and its validation. *IEEE Transactions on Geoscience and Remote Sensing*, **42**, 1433–1443.
- Haas, C., and Eicken, H., 2001. Interannual variability of summer sea ice thickness in the Siberian and central Arctic under different atmospheric circulation regimes. *Journal of Geophysical Research*, **106**(C3), 4449–4462.
- Hall, D. K., and Riggs, G. A., 2007. Accuracy assessment of the MODIS snow products. *Hydrological Processes*, **21**, 1534–1547.
- Hall, D. K., Williams, R. S., Jr., and Bayr, K. J., 1992. Glacier recession in Iceland and Austria. *Eos, Transactions of the American Geophysical Union*, **73**, 129, 135 and 141.
- Hanna, E., and Bamber, J., 2001. Derivation and optimization of a new Antarctic sea-ice record. *International Journal of Remote Sensing*, **22**, 113–139.
- Haran, T. (ed.), 2003. *CLPX-Satellite: MODIS radiances, reflectances, snow cover and related grids*. Digital Media. Boulder, CO: National Snow and Ice Data Center.
- Haran, T., et al., 2005 updated 2006. *MODIS mosaic of Antarctica (MOA) image map*. Digital media. Boulder, CO: National Snow and Ice Data Center.
- Helfrich, S., et al., 2007. Enhancements to, and forthcoming developments in the Interactive Multisensor Snow and Ice Mapping System (IMS). *Hydrological Processes*, **21**, 1576–1586.
- Howat, I. M., Joughin, I., and Scambos, T. A., 2007. Rapid changes in ice discharge from Greenland outlet glaciers. *Science*, **315**(5818), 1559–1561.
- Johannessen, O. M., et al., 2007. *Remote Sensing of Sea Ice in the Northern SeaRoute: Studies and Applications*. Chichester: Springer, Praxis, p. 472.
- Joughin, I. R., Fahnestock, M. A., and Bamber, J. L., 2000. Ice flow in the northeast Greenland ice stream. *Annals of Glaciology*, **31**, 141–146.
- Khromova, T. E., et al., 2006. Changes in glacier extent in the eastern Pamir, Central Asia, determined from historical data and ASTER imagery. *Remote Sensing of Environment*, **102**, 24–32.
- Kim, K., Jezek, K., and Liu, H., 2006. Orthorectified image mosaic of Antarctica from 1963 Argon satellite photography: image processing and glaciological applications. *International Journal of Remote Sensing*, **28**(23), 5357–5373.
- Kukthuroja, N., White, M. A., and Luecke, C., 2006. *Using Daily MODIS 250 m Data to Monitor Lake Ice Out*. Department of Watershed Sciences, Utah State University, 5 pp.
- Kwok, R., 2008. Summer sea ice motion from the 18 GHz channel of AMSR-E and the exchange of sea ice between the Pacific and Atlantic sectors. *Geophysical Research Letters*, **35**, L03504, doi:10.1029/2007GL032692.
- Kwok, R., and Cunningham, G. F., 2002. Seasonal sea ice area and volume production of the Arctic Ocean: November 1996 through April 1997. *Journal of Geophysical Research*, **107**, 8038, doi:10.1029/2000JC000469.
- Kwok, R., et al., 1995. Determination of the age distribution of sea ice from Lagrangian observations of ice motion. *IEEE Transactions on Geoscience and Remote Sensing*, **33**, 392–400.
- Kwok, R., et al., 1998. Sea ice motion from satellite passive microwave imagery assessed with ERS SAR and buoy motions. *Journal of Geophysical Research*, **103**(C4), 8191–8214.
- Kwok, R., et al., 2008. Ice, Cloud, and Land Elevation Satellite (ICESat) over Arctic sea ice: retrieval of freeboard. *Journal of Geophysical Research*, **112**(1–19), C12013.
- Laine, V., 2008. Antarctic ice sheet and sea ice regional albedo and temperature change, 1981–2000, from AVHRR Polar Pathfinder data. *Remote Sensing of Environment*, **112**(3), 646–667.
- Lauriol, B., et al., 1986. The residual snow cover in the Canadian Arctic in July: a means to evaluate the regional maximum snow depth in winter. *Arctic*, **39**, 309–315.
- Laxon, S. W., Peacock, N., and Smith, D., 2003. High interannual variability of sea ice thickness in the Arctic region. *Nature*, **425**, 947–950.
- Laxon, S. W., et al., 2012. CryoSat 2 estimates of Arctic ice thickness and volume. *Geophysical Research Letters*, **40**, 732–737.
- Leconte, R., and Klassen, P. D., 1991. Lake and river ice investigations in northern Manitoba using airborne SAR imagery. *Arctic*, **44**(Suppl. 1), 153–163.
- Leshkevich, G. A., Ngiem, S. V., and Kwok, R. 1998. Algorithm development for satellite synthetic aperture radar (SAR) classification and mapping of Great Lakes ice cover. In *Proceedings, IEEE International Geoscience and Remote Sensing Symposium (IGARSS'98)*, Seattle, WA, 3 pp.
- Liang, S., Stroeve, J., and Box, J., 2005. MODIS-derived Greenland ice sheet albedo: the improved direct estimation algorithm. *Journal of Geophysical Research*, **110**, doi:10.1029/2004JD005493.
- Liu, A. K., and Cavalieri, D. J., 1998. On sea ice drift from the wavelet analysis of the Defense Meteorological Satellite Program (DMSP) Special Sensor Microwave Imager (SSM/I) data. *International Journal of Remote Sensing*, **19**, 1415–1423.
- Long, D. G., Hardin, P. J., and Whiting, P. T., 1993. Resolution enhancement of spaceborne scatterometer data. *IEEE Transactions on Geoscience and Remote Sensing*, **31**, 700–715.
- Lucchitta, B. K., et al., 1993. Antarctic glacial tongue velocities from Landsat images: first results. *Annals of Glaciology*, **17**, 356–366.
- Mahoney, A. R., et al., 2008. Observed sea ice extent in the Russian Arctic, 1933–2006. *Journal of Geophysical Research*, **113**, C110015.

- Markus, T., and Cavalieri, D., 2000. An enhancement of the NASA team sea ice algorithm. *IEEE Transactions on Geoscience and Remote Sensing*, **38**, 1387–1398.
- Martinec, J., and Rango, A., 1987. Interpretation and utilization of areal snow cover data from satellites. *Annals of Glaciology*, **9**, 166–169.
- Maslanik, J., et al., 1998. AVHRR-based polar pathfinder products for modeling applications. *Annals of Glaciology*, **25**, 388–392.
- Maslanik, J. A., et al., 2007. A younger, thinner Arctic ice cover: increased potential for rapid, extensive sea-ice loss. *Geophysical Research Letters*, **34**, L24501, doi:10.1029/2007GL032043.
- Maurer, J., 2003. Spaceborne scatterometry of the cryosphere: a review. [http://cires.colorado.edu/maurerj/scatterometry/scatterometry\\_cryosphere](http://cires.colorado.edu/maurerj/scatterometry/scatterometry_cryosphere)
- McDonald, R. M., 1995. Opening the cold war sky to the public: declassifying satellite reconnaissance imagery. *Photogrammetric Engineering and Remote Sensing*, **61**, 485–490.
- Meier, W. M., 2005. Comparison of passive microwave ice concentration algorithm retrievals with AVHRR imagery in Arctic peripheral seas. *IEEE Transactions in Geoscience and Remote Sensing*, **43**(6), 1324–1337.
- Meier, W. N., and Dai, M., 2006. High-resolution sea-ice motions from AMSR-E imagery. *Annals of Glaciology*, **44**, 353–356.
- Meier, W. N., and Stroeve, J., 2008. Comparison of sea-ice extent and ice-edge location estimates from passive microwave and enhanced-resolution scatterometer data. *Annals of Glaciology*, **48**, 65–70.
- Meier, W. N., Maslanik, J. A., and Fowler, C. W., 2000. Error analysis and assimilation of remotely sensed ice motion within an Arctic sea ice model. *Journal of Geophysical Research*, **105**, 3339–3356.
- Mote, T. L., and Anderson, M. R., 1995. Variations in snowpack melt on the Greenland ice sheet based on passive-microwave measurements. *Journal of Glaciology*, **41**(137), 51–60.
- Mueller, D. R., Vincent, W. F., and Jeffries, M. O., 2003. Ice shelf break-up and ecosystem loss in the Canadian High Arctic. *Eos, Transactions American Geophysical Union*, **84**(49), 548–552.
- Nghiem, S. V., et al., 2007. Rapid reduction of Arctic perennial sea ice. *Geophysical Research Letters*, **34**, L19504, doi:10.1029/2007GL031138.
- Nolin, A. W., et al., 2001. Cryospheric applications of MISR data. In *Proceedings of the Third IEEE International Geoscience and Remote Sensing Symposium (IGARRS) 2001*. New York: IEEE, pp. 1219–1221.
- Nolin, A., Fetterer, F., and Scambos, T., 2002. Surface roughness characterizations of sea ice and ice sheets: case studies with MISR data. *IEEE Transactions of Geophysics and Remote Sensing*, **40**(7), 1605–1615.
- NORSEX Group, 1983. Norwegian remote sensing experiment in a marginal ice zone. *Science*, **220**(4599), 781–787.
- Painter, T. H., Roberts, D. A., Green, R. O., and Dozier, J., 1998. The effect of grain size on spectral mixture analysis of snow-covered area with AVIRIS data. *Remote Sensing of Environment*, **65**, 320–332.
- Painter, T. H., Dozier, J., Roberts, D. A., Davis, R. E., and Green, R. O., 2003. Retrieval of subpixel snow-covered area and grain size from imaging spectrometer data. *Remote Sensing of Environment*, **85**, 64–77.
- Parkinson, C. L., et al., 1987. *Antarctic sea ice, 1973–1976: satellite passive-microwave observations*. Washington, DC: NASA, SP 489, 296 pp.
- Parkinson, C., Comiso, J., and Zwally, H. J., 1999. *Nimbus-5 ESMR daily polar gridded brightness temperatures*. Digital media. Boulder, CO: National Snow and Ice Data Center.
- Partington, K. C., 2000. A data fusion algorithm for mapping sea-ice concentrations from Special Sensor Microwave/Imager data. *IEEE Transactions on Geoscience and Remote Sensing*, **38**, 1947–1958.
- Paul, F., 2000. Evaluation of different methods for glacier mapping using Landsat TM. In *Proceedings, EARSeL-SIG Workshop*. Dresden: Land ice and Snow.
- Peacock, N. R., and Laxon, S. W., 2004. Sea surface height determination in the arctic ocean from ERS altimetry. *Journal of Geophysical Research*, **109**, C07001, doi:10.1029/2001JC001026.
- Power, D., et al., 2001. Iceberg detection capabilities of RADARSAT synthetic aperture radar. *Canadian Journal of Remote Sensing*, **27**(5), 476–486.
- Racoviteanu, A., et al., 2008. Decadal changes in glacier parameters in the Cordillera Blanca, Peru, derived from remote sensing. *Journal of Glaciology*, **56**(186), 499–510.
- Ramsay, B. H., 1998. Interactive Multisensor Snow and Ice Mapping System (IMS). *Hydrological Processes*, **12**, 1537–1546.
- Raup, B., et al., 2007. The GLIMS geospatial glacier database: a new tool for studying glacier change. *Global and Planetary Change*, **56**, 101–110.
- Remund, Q. P., and Long, D. G., 1999. Sea ice extent mapping using Ku band scatterometer data. *Journal of Geophysical Research*, **104**(C5), 11,515–11,527.
- Rignot, E., and Thomas, R. H., 2002. Mass balance of polar ice sheets. *Science*, **297**(5586), 1502–1506.
- Roth, A., et al., 1993. Experiences with ERS-1 SAR compositional accuracy. *Proceedings of the Third IEEE Transactions Geoscience. Remote Sensing, IGARRS Symposium*, 1993, Tokyo, Japan, pp. 1450–1452.
- Rothrock, D. A., Yu, Y., and Maykut, G. A., 1999. Thinning of the Arctic sea-ice cover. *Geophysical Research Letters*, **26**(23), 3469–3472.
- Rott, H., and Markl, G., 1989. Improved snow and glacier monitoring by the Landsat Thematic Mapper. In *Proceedings of a Workshop on Landsat Thematic Mapper Applications*, ESA-SP-1102, European Space Agency, pp. 3–12.
- Rott, H., and Nagler, T., 1993. Capabilities of ERS-1 SAR for snow and glacier monitoring in alpine areas. In *Proceedings, Second ERS-1 Symposium*. Noordwijk: ESA Publications Division, ESA SP-361, pp. 1–6.
- Scambos, T. A., et al., 1992. Application of image cross-correlation to the measurement of glacial velocity using satellite image data. *Remote Sensing of Environment*, **42**, 177–186.
- Scambos, T., et al. 2000, updated 2002. *AVHRR Polar Pathfinder Twice-Daily 1.25 km EASE-Grid Composites*. Digital Media. Boulder, CO: National Snow and Ice Data Center.
- Scambos, T., et al., 2007. MODIS-based Mosaic of Antarctica (MOA) data sets: continent-wide surface morphology and snow grain size. *Remote Sensing of Environment*, **111**, 242–257.
- Schutz, B., et al., 2005. ICESat mission overview and history. *Geophysical Research Letters*, **32**, L21S01.
- Shepherd, A., and Wingham, D., 2007. Recent sea-level contributions of the Antarctic and Greenland ice sheets. *Science*, **315**, 1529–1532.
- Shi, J. C., and Dozier, J., 1993. Measurements of snow- and glacier-covered areas with single polarization SAR. *Annals of Glaciology*, **17**, 72–76.
- Shi, J. C., and Dozier, J., 1996. Estimation of snow water equivalence using SISR-C/X-SAR. In *Proceedings IGARRS 96*, IEEE No. 96, Chap. 35875, pp. 2002–2004.
- Shi, J. C., and Dozier, J., 1997. Mapping seasonal snow with SIR-C/X-SAR in mountainous areas. *Remote Sensing of Environment*, **59**, 294–307.
- Shi, J. C., Dozier, J., and Rott, H., 1994. Snow mapping in alpine regions with synthetic aperture radar. *IEEE Transactions on Geoscience and Remote Sensing*, **32**, 152–158.
- Sievers, J., Grindel, A., and Meier, W., 1989. Digital satellite image mapping of Antarctica. *Polarforschung*, **59**, 23–33.

- Smith, D. M., 1998. Observation of perennial Arctic sea ice melt and freeze-up using passive microwave data. *Journal of Geophysical Research*, **103**(C12), 27,753–769.
- Smith, N. V., Saatchi, S. S., and Randerson, J. T., 2004. Trends in high northern latitudes soil freeze and thaw cycles from 1988 to 2002. *Journal of Geophysical Research*, **109**, D12101.
- Spreen, G., Kaleschke, L., and Heygster, G., 2008. Sea ice remote sensing using AMSR-E 89-GHz channels. *Journal of Geophysical Research*, **113**, C02S03, doi:10.1029/2005JC003384.
- Stankov, B., and Gasiewski, A., 2004. *CLPX-Airborne multiband Polarimetric Scanning Radiometer (PSR) Imagery. Digital Media*. Boulder, CO: National Snow and Ice Data Center.
- Stroeve, J., and Nolin, A. W., 2002. New methods to infer snow albedo from the MISR instrument with applications to the Greenland ice sheet. *IEEE Transactions Geoscience and Remote Sensing*, **40**, 1616–1625.
- Stroeve, J., Nolin, A., and Steffen, K., 1997. Comparison of AVHRR-derived and in situ surface albedo over the Greenland ice sheet. *Remote Sensing of Environment*, **62**, 262–276.
- Stroeve, J., Markus, T., and Maslanik, J., 2001. Sensitivity analysis of operational passive microwave sea-ice algorithms. In *Proceedings of the IEEE International Geoscience and Remote Sensing Symposium (IGARRS)*, 2001, pp. 1798–1800.
- Strozzi, T., et al., 2008. Estimation of Arctic glacier motion with satellite L-band SAR data. *Remote Sensing of Environment*, **112**(3), 636–645.
- Stuart, K., et al., 2007. The Antarctic iceberg tracking database. <http://www.scp.byu.edu/data/iceberg/database1.html>
- Surazakov, A. B., et al., 2007. Glacier changes in the Siberian Altai Mountains, Ob River basin, (1952–2006) estimated with high resolution satellite imagery. *Environmental Research Letters*, **2**, 045017, 7 pp.
- Tait, A., 1998. Estimation of snow water equivalent using passive = microwave radiation data. *Remote Sensing of the Environment*, **64**, 286–291.
- Tedesco, M., et al., 2005. Analysis of multiscale radiometric data collected during the Cold Land Processes Experiment-1 (CLPX-1). *Geophysical Research Letters*, **32**, L18501.
- Tedesco, M., et al., 2006. Brightness temperatures of snow melting/refreezing cycles: observations and modeling using a multilayer dense medium theory-based model. *IEEE Transactions on Geoscience and Remote Sensing*, **44**(12), 3563–3572.
- Vinje, T., Nordlund, N., and Kvambekk, A. 1998. Monitoring ice thickness in Fram Strait. *Journal of Geophysical Research*, **103** (C5), doi:10.1029/97JC03360.
- Wadhams, P., and Doble, M. J., 2008. Digital terrain mapping of the underside of sea ice from a small AUV. *Geophysical Research Letters*, **35**, L01501, doi:10.1029/2007GL031921.
- Walker, A. E., and Davey, M. R., 1993. Observation of Great Slave Lake ice freeze-up and break-up processes using passive microwave satellite data. In *Proceedings of the 16th Canadian Symposium on Remote Sensing*, Sherbrooke, QC, pp. 233–238.
- Way, J. B., et al., 1997. Winter and spring thaw as observed with imaging radar at BOREAS. *Journal of Geophysical Research*, **102**(29), 671–684.
- Williams Jr., R. S., and Ferrigno, J. G. (eds.), 1988. *Satellite Image Atlas of Glaciers of the World, Antarctica*. U.S. Geological Survey Professional Paper 1386-B, 288 pp.
- Williams, R. S., Jr., et al., 1982. Landsat images and mosaics of Antarctica for mapping and glaciological studies. *Annals of Glaciology*, **3**, 321–326.
- Worby, A., et al., 1999. On the use of electromagnetic induction sounding to determine winter and spring sea ice thickness in the Antarctic. *Cold Regions Science and Technology*, **29**, 49–58.
- Wynne, R. H., et al., 1998. Satellite monitoring of lake ice breakup on the Laurentian shield (1980–1994). *Photogrammetric Engineering and Remote Sensing*, **64**, 607–617.
- Zhang, T., and Armstrong, R. L., 2001. Soil freeze/thaw cycles over snow-free land detected by passive microwave remote sensing. *Geophysical Research Letters*, **28**(5), 763–766.
- Zhang, T., and Armstrong, R., 2003 updated 2005. *Arctic Soil Freeze/Thaw Status from SMMR and SSM/I, Version 2. Digital Media*. Boulder, CO: National Snow and Ice Data Center/World Data Center for Glaciology.
- Zhang, T., Armstrong, R. L., and Smith, J., 2003. Investigation of the near-surface soil freeze/thaw cycle in the contiguous United States: algorithm development and validation. *Journal of Geophysical Research*, **108**(D22), 8860, doi:10.1029/2003JD003530.
- Zhang, T., Barry, R. G., and Armstrong, R. L., 2004. Application of satellite remote sensing techniques to frozen ground studies. *Polar Geography*, **28**(3), 163–196.
- Zhao, Y., Liu, A. K., and Long, D. G., 2002. Validation of sea ice motion from QuikSCAT with those from SSM/I and buoy. *IEEE Transactions on Geoscience and Remote Sensing*, **40**, 1241–1246.
- Zhou, G., and Jezek, K., 2002. *DISP Yearly Satellite Photographic Mosaics of Greenland 1962–1963. Digital Media*. Boulder, CO: National Snow and Ice Data Center.
- Zuerndorfer, B., and England, A. W., 1992. Radio brightness decision criteria for frozen ground boundaries. *IEEE Transactions on Geoscience and Remote Sensing*, **30L**, 89–102.
- Zwally, H. J., et al., 1983. *Antarctic Sea Ice, 1973–1976; Satellite Passive-Microwave Observations*. Washington, DC: NASA, SP 459, 206 pp.
- Zwally, H. J., et al., 2008. ICESat measurements of sea ice freeboard and estimates of sea ice thickness in the Weddell Sea. *Journal of Geophysical Research*, **113**, C02S15, doi:10.1029/2007JC004284.

## Cross-references

[Cryosphere and Polar Region Observing System](#)  
[Ice Sheets and Ice Volume](#)  
[Icebergs](#)  
[Polar Ice Dynamics](#)  
[Sea Ice Concentration and Extent](#)